PONTIFÍCIA UNIVERSIDADE CATÓLICA
DO RIO DE JANEIRO

Pedro Nieckele Azevedo

Lyophilized microfluidic monodisperse microbubbles as an ultrasound contrast agent

Tese de doutorado

Thesis presented to the Programa de Pós–graduação em Engenharia Mecânica, do Departamento de Engenharia Mecânica da PUC-Rio in partial fulfillment of the requirements for the degree of Doutor em Engenharia Mecânica..

Advisor: Prof. Márcio da Silveira Carvalho
Co-Advisor: Prof. Arnaud Tourin
Co-advisor: Prof. Patrick Tabeling

Rio de Janeiro
December 7th, 2022

Pontifícia Universidade Católica
do Rio de Janeiro

Pedro Nieckele Azevedo

Lyophilized microfluidic monodisperse microbubbles as an ultrasound contrast agent

Tese de doutorado

Thesis presented to the Programa de Pós–graduação em Engenharia Mecânica da PUC-Rio in partial fulfillment of the requirements for the degree of Doutor em Engenharia Mecânica. Approved by the Examination Committee:

Prof. Márcio da Silveira Carvalho
Advisor
Departamento de Engenharia Mecânica – PUC-Rio

Prof. Arnaud Tourin
Co-advisor
PSL - ESPCI Paris

Prof. Patrick Tabeling
Co-advisor
ESPCI-Paris

Prof. Philippe Marmottant
Laboratoire Interdisciplinaire de Physique Grenoble

Prof. Julien de Rosny
ESPCI-Paris

Prof. Arthur Martins Barbosa Braga
Departamento de Engenharia Mecânica – PUC-Rio

Prof. Lucimara Gaziola de la Torre
UNICAMP

Rio de Janeiro, December 7th, 2022

Pedro Nieckele Azevedo

Holds a master's degree (2016), and a bachelor's degree (2013) in mechanical engineering, both from Pontifícia Universidade Católica do Rio de Janeiro (PUC-Rio). He worked as doctorate student on the microfluidic group from the Mechanical Engineering department from PUC-RIO under the advisory of Prof. Márcio da Silveira Carvalho. As part of co-tutelage agreement with ESPCI-Paris, the author conducted studies in the field of ultrasound, acoustics, and microfluidic at the Institut Pierre-Gilles de Gennes under the advisory of Profs. Arnaud Tourin e Patrick Tabeling.

Bibliographic data

Azevedo, Pedro Nieckele

Lyophilized microfluidic monodisperse microbubbles as an ultrasound contrast agent / Pedro Nieckele Azevedo ; advisors: Márcio da Silveira Carvalho, Arnaud Tourin ; co-advisor: Patrick Tabeling. – 2022.
210 f. : il. color. ; 30 cm

Tese (doutorado)–Pontifícia Universidade Católica do Rio de Janeiro, Departamento de Engenharia Mecânica, 2022.
Inclui bibliografia

1. Engenharia Mecânica – Teses. 2. Microbolhas. 3. Microfluidica. 4. Liofilização. 5. Monodisperso. 6. Ultrassom. I. Carvalho, Márcio da Silveira. II. Tourin, Arnaud. III. Tabeling, Patrick. IV. Pontifícia Universidade Católica do Rio de Janeiro. Departamento de Engenharia Mecânica. V. Título.

CDD: 621

Aknowledgments

First, I would like to thank the support from PUC-Rio and ESPCI-Paris, who provided all the means that made this project possible. CAPES Print, with financial backing, made my arrival in France a reality. This study was financed in part by the Coordenação de Aperfeiçoamento de Pessoal de Nível Superior - Brasil (CAPES) - Finance Code 001.

My advisors, Marcio Carvalho, Arnaud Tourin, and Patrick Tabeling, contributed with their knowledge, experience, and efforts to construct this complex, challenging, and interesting multidisciplinary subject.

I want to thank the Institut Pierre-Gilles de Gennes team for welcoming me with kindness and availability to pass and teach their skills in the microfluidic sector. A special thanks to Ugur Soysal, who worked side by side with me on this project. His guidance and support made us achieve outstanding progress and success.

I would like to thank Flavien Bureau and Alexandre Aubry from Institut Langevin for making possible the realization of the Ultrasound matrix experiment, which resulted in a great addition to the thesis outcome.

A special thanks to Igor de Paula from PUC-Rio, who shared all his knowledge on signal processing, becoming a guide throughout my experiments.

I want to thank my father, Luis Fernando Alzuguir Azevedo, and my mother, Angela Ourivio Nieckele. They helped me not only with their love and appraisal but also with the thesis, providing tips, instructions, and suggestions.

Finally, I would like to thank Luiza Chaloub, my greater supporter. She was always showing me the possibilities of what I could reach. Her love, passion, and vision were a guiding star for my life and, as a consequence, this thesis.

Abstract

Azevedo, Pedro Nieckele; Carvalho, Marcio da Silveira (Advisor); Tourin, Arnaud (Advisor); Tabeling, Patrick (Co-advisor). **Lyophilized microfluidic monodisperse microbubbles as an ultrasound contrast agent**. Rio de Janeiro, 2022. 210p. Tese de Doutorado – Departamento de Engenharia Mecanica, Potificia Universidade Catolica do Rio de Janeiro.

In recent years, the advantages of using ultrasound contrast agents (UCA) with monodisperse size distribution have been highlighted. Characterized by a coefficient of variation (CV) lower than 5%, monodisperse microbubbles have the potential to improve the quality of ultrasound images (improving signal-to-noise ratio and reducing shadowing effects. It also facilitates microbubble resonance frequency monitoring, opening possibilities in the areas of molecular imaging and non-invasive pressure measurements. In addition, monodisperse bubbles can optimize the drugs, genes, and therapeutic gas delivery (e.g. sonotrombolysis, sonoporation, blood-brain barrier opening).

However, thus far, contrarily to polydisperse bubbles, freeze-drying monodisperse populations of fresh microbubbles, without deteriorating their monodispersity, remains a challenge. Thereby, today, monodisperse bubbles can neither be stored nor transported. This represents a bottleneck for their use in clinical applications. Attempts made to solve the problem have used toxic solvents, raising regulatory issues

The objective of the present work was to develop a new freeze-drying technique for monodisperse microbubbles that did not degrade their size distribution, or their acoustic properties, without the use of toxic solvents. As the first step of the project, flow-focusing microfluidic devices were fabricated to produce microbubbles with highly monodisperse size distribution (CV<5%). During this step, the optimization of the microbubble formulation and cryoprotectant materials was performed. Geometric characterization of two of microbubbles with mean diameters of 40µm and 5µm was performed. With the use of a high-speed camera coupled to

an optical microscope, images of all stages of the freeze-drying process of the microbubbles were captured and analyzed, aiming to control the size distribution and production rate of the microbubbles. The steps of the freeze-drying process consisted of production, collection, freezing, lyophilization, and resuspension. The development of a new retrieval technique, where the microbubbles were stored in monolayers, resulted in a drastic reduction of the interaction between the bubbles during lyophilization. In this way, it was possible to preserve the monodispersity during the freeze-drying process, resulting in a CV <6% for the resuspended microbubble population. Environmental scanning electron microscope (ESEM) assays demonstrated uniformity in the shells of the freeze-dried microbubbles with an estimated wall thickness of 70nm.

In the second stage of the project, a characterization of the backscatter acoustic response of the freeze-dried monodisperse PVA-shelled microbubbles, in comparison with freshly produced microbubbles, and commercially available polydisperse microbubbles SonovueTM was conducted. Firstly, the backscatter acoustic response of the microbubbles was evaluated in two different setups: the centimetric cell (large container - 45mmx10mmx30mm), and the ‘milli-channel’ (confined system in which the liquid is at rest - 10 mmx35 mmx1 mm). Using a focused acoustic transducer with a frequency of 2.25MHz, the acoustic responses of the microbubbles, in the form of the fundamental resonance frequency and amplitude, before and after the freeze-drying process was compared for the bubble population of 5µm diameter. It was found that the variation of amplitude and fundamental resonance frequency of the bubbles were within the experimental uncertainty range, suggesting that their acoustic properties were preserved. We also observed, in agreement with the literature, that there is a linear dependence between the concentration of the microbubble population (without freeze-drying) and the amplitude of the backscatter coefficient. Subsequently, a comparison of the acoustic backscatter response was performed for monodisperse and polydisperse bubbles. Also, in agreement with the literature, we observed an amplitude in the response signal of the monodispersed bubbles of 8 to 10 times higher than that for the polydispersed ones, for the same in vitro concentration. It was also possible to observe the lower uncertainty in monitoring the fundamental resonance peak of the bubbles and a smaller bandwidth for the monodispersed bubble population. Finally, using the universal ultrasound matrix imaging approach, developed at Institut

Langevin, the backscatter acoustic response of the freeze-dried monodisperse and polydisperse population was evaluated in a phantom mimicking tissue. The preliminary results reinforce the findings from the backscatter acoustic measurements in the centimetric cell and the milli-channel, in which the monodisperse population presented a significantly reduced bandwidth in comparison with the wide bandwidth of the polydisperse population.

The present work successfully presented a new technique developed to freeze-dry monodisperse microbubbles without degrading their geometrical and acoustic properties. Thus, we proposed a new generation of ultrasound contrast agents in the form of a stable freeze-dried powder that can be transported and stored for months and resuspended for use in clinical applications

Keywords

Microbubbles; microfluidic; lyophilized; monodisperse; ultrasound; polyvinyl alcohol

Résumé

Azevedo, Pedro Nieckele; Carvalho, Marcio da Silveira; Tourin, Arnaud; Tabeling, Patrick. **Microbulles monodispersées microfluidiques lyophilisées comme agent de contraste ultrasonore.** Rio de Janeiro, 2022. 210p. Thèse de Doctorat – Departamento de Engenharia Mecanica, Potificia Universidade Catolica do Rio de Janeiro.

Ces dernières années, les avantages de l'utilisation d'agents de contraste ultrasonores (ACU) à distribution de taille monodisperse ont été mis en évidence. Caractérisées par un coefficient de variation (CV) de leur diamètre inférieur à 5%, les microbulles monodisperses ont le potentiel d'améliorer la qualité des images ultrasonores (amélioration du rapport signal/bruit et réduction des effets d'ombre). Elles facilitent également le contrôle de la fréquence de résonance des microbulles, ouvrant des possibilités dans les domaines de l'imagerie moléculaire et des mesures de pression non invasives. En outre, les bulles monodisperses peuvent optimiser l'administration de médicaments, de gènes et de gaz thérapeutiques (par exemple, sonotrombolyse, sonoporation, ouverture de la barrière hémato-encéphalique).

Cependant, jusqu'à présent, contrairement aux bulles polydisperses, la lyophilisation de populations monodisperses de microbulles fraîches, sans détérioration de leur monodispersité, reste un défi. Ainsi, aujourd'hui, les bulles monodisperses ne peuvent être ni stockées ni transportées. Cela représente un goulot d'étranglement pour leur utilisation dans des applications cliniques. Les tentatives faites pour résoudre ce problème ont utilisé des solvants toxiques, ce qui soulève des problèmes de réglementation.

L'objectif du présent travail était de développer une nouvelle technique de lyophilisation des microbulles monodisperses qui ne dégrade pas leur distribution de taille, ni leurs propriétés acoustiques, et ce sans utiliser de solvants toxiques. La première étape du projet a consisté à fabriquer des dispositifs microfluidiques de focalisation du flux pour produire des microbulles avec une distribution de taille hautement monodisperse (CV<5%). Au cours de cette étape, l'optimisation de la formulation des microbulles et des matériaux cryoprotecteurs a été réalisée. La caractérisation géométrique de deux microbulles avec des diamètres moyens de 40µm et 5µm a été menée. A l'aide d'une caméra à haute vitesse couplée à un

microscope optique, des images de toutes les étapes du processus de lyophilisation des microbulles ont été capturées et analysées, dans le but de contrôler la distribution de taille et le taux de production des microbulles. Les étapes du processus de lyophilisation comprenaient la production, la collecte, la congélation, la lyophilisation et la remise en suspension. Le développement d'une nouvelle technique de récupération, où les microbulles étaient stockées en monocouches, a permis de réduire considérablement l'interaction entre les bulles pendant la lyophilisation. De cette manière, il a été possible de préserver la monodispersité pendant le processus de lyophilisation, ce qui a permis d'obtenir un CV <6% pour la population de microbulles remise en suspension. Les analyses au microscope électronique à balayage environnemental (ESEM) ont démontré l'uniformité des enveloppes des microbulles lyophilisées avec une épaisseur de paroi estimée à 70nm.

Dans la deuxième étape du projet, une caractérisation de la réponse acoustique (en rétrodiffusion) des microbulles monodisperses lyophilisées et enveloppées de PVA a été réalisée et comparée avec celles de microbulles fraîchement produites et de microbulles polydisperses disponibles dans le commerce (SonovueTM). Tout d'abord, la réponse acoustique en rétrodiffusion des microbulles a été évaluée dans deux configurations différentes : la cellule centimétrique (grand récipient - 45mmx10mmx30mm), et le "milli-channel" (système confiné dans lequel le liquide est au repos - 10 mmx35 mmx1 mm). En utilisant un transducteur acoustique focalisé avec une fréquence de 2.25MHz, les réponses acoustiques des microbulles (fréquence de résonance fondamentale et amplitude) avant et après le processus de lyophilisation ont été comparées pour la population de bulles de 5µm de diamètre. Il a été constaté que la variation de l'amplitude et de la fréquence de résonance fondamentale des bulles se situait dans la plage d'incertitude expérimentale, ce qui suggère que leurs propriétés acoustiques ont été préservées. Nous avons également observé, en accord avec la littérature, qu'il existe une dépendance linéaire entre la concentration de la population de microbulles (sans lyophilisation) et l'amplitude du coefficient de rétrodiffusion. Par la suite, une comparaison de la réponse acoustique a été effectuée pour des bulles monodisperses et polydisperses. Aussi, en accord avec la littérature, nous avons observé une amplitude du signal de réponse des bulles monodisperses de 8 à 10 fois supérieure à celle des bulles polydisperses, pour une même concentration in vitro. Il a également été possible d'observer une plus faible incertitude dans le suivi du pic de résonance des bulles et une plus petite largeur de bande pour la population de bulles monodisperses. Enfin, en utilisant une approche originale dite « d'imagerie

matricielle par ultrasons », développée à l'Institut Langevin, la réponse acoustique de la population lyophilisée monodispersée et polydispersée a été évaluée dans un fantôme simulant les tissus. Les résultats préliminaires renforcent les conclusions des mesures acoustiques menées dans la cellule centimétrique et le canal millimétrique, dans lesquelles la population monodisperse présente une largeur de bande significativement réduite par rapport à la grande largeur de bande de la population polydisperse.

Le présent travail a permis le développement d’une nouvelle technique pour lyophiliser des microbulles monodispersées sans dégrader leurs propriétés géométriques et acoustiques. Ainsi, nous avons proposé une nouvelle génération d'agents de contraste ultrasonores se présentant sous la forme d'une poudre lyophilisée stable qui peut être transportée et stockée pendant des mois et remise en suspension pour être utilisée dans des applications cliniques.

Mots Clés

Microbulles; microfluidique; lyophilisees; monodisperse; ultrason; alcool polyvinylique

Resumo

Azevedo, Pedro Nieckele; Carvalho, Marcio da Silveira; Tourin, Arnaud; Tabeling, Patrick. **Microbolhas monodispersas microfluídicas liofilizadas como agente de contraste de ultrassom**. Rio de Janeiro, 2022. 210p. Tese de Doutorado – Departamento de Engenharia Mecanica, Potificia Universidade Catolica do Rio de Janeiro.

Nos últimos anos, as vantagens do uso de agentes de contraste de ultrassom (UCA) com distribuição de tamanho monodisperso foram destacadas. Caracterizadas por um coeficiente de variação (CV) inferior a 5%, as microbolhas monodispersas têm o potencial de melhorar a qualidade das imagens de ultrassom (melhorando a relação sinal/ruído e reduzindo os efeitos de sombra). Também facilita o monitoramento da freqüência de ressonância das microbolhas, abrindo possibilidades nas áreas de imagem molecular e medições de pressão não-invasiva. Além disso, as bolhas monodispersas podem otimizar a entrega de drogas, genes e gases terapêuticos (por exemplo, sonotrombólise, sonoporação, abertura da barreira hemato-encefálica).

No entanto, até agora, ao contrário das bolhas polidispersas, a liofilização de populações monodispersas de microbolhas, sem deteriorar sua monodispersividade, continuam sendo um desafio. Assim, hoje, as bolhas monodispersas não podem ser armazenadas nem transportadas. Isto representa um gargalo para seu uso em aplicações clínicas. Tentativas feitas para resolver o problema têm usado solventes tóxicos, levantando questões regulatórias

O objetivo do presente trabalho foi de desenvolver uma nova técnica de liofilização para microbolhas monodispersas que não degradassem sua distribuição de tamanho, ou suas propriedades acústicas, sem o uso de solventes tóxicos. Como primeira etapa do projeto, foram fabricados dispositivos microfluídicos com focalização de escoamento (*flow-focusing*) para produzir microbolhas com distribuição de tamanho altamente monodispersa (CV<5%). Durante esta etapa, foi realizada a otimização da formulação das microbolhas e dos materiais crioprotetores. Foi realizada a caracterização geométrica de duas populações de microbolhas com

diâmetros médios de 40µm e 5µm. Com o uso de uma câmera de alta velocidade acoplada a um microscópio ótico, imagens de todas as etapas do processo de liofilização das microbolhas foram capturadas e analisadas, visando controlar a distribuição de tamanho e a taxa de produção das microbolhas. As etapas do processo de liofilização consistiram na produção, coleta, congelamento, liofilização e ressuspensão. O desenvolvimento de uma nova técnica de recuperação, onde as microbolhas eram armazenadas em monocamadas, resultou em uma redução drástica da interação entre as bolhas durante a liofilização. Desta forma, foi possível preservar a monodispersão durante o processo de liofilização, resultando em um CV <6% para a população de microbolhas ressuspensas. Os ensaios de microscópio eletrônico de varredura ambiental (ESEM) demonstraram uniformidade nas cascas das microbolhas liofilizadas com uma espessura de parede estimada em 70nm.

Na segunda etapa do projeto, foi realizada uma caracterização da resposta acústica de retrodifusão das microbolhas liofilizadas em forma de PVA, em comparação com as microbolhas recém produzidas e as microbolhas polidispersa Sonovue^{TM} disponíveis comercialmente. Primeiramente, a resposta acústica de retrodifusão das microbolhas foi avaliada em duas configurações diferentes: a célula centimétrica (recipiente grande - 45mmx10mmx30mm), e o "milli-canal" (sistema confinado no qual o líquido está em repouso - 10 mmx35 mmx1 mm). Usando um transdutor acústico focalizado com frequência de 2,25MHz, as respostas acústicas das microbolhas, na forma de frequência e amplitude de ressonância fundamental, antes e depois do processo de liofilização, foram comparadas para a população de bolhas de 5µm de diâmetro. Verificou-se que a variação de amplitude e frequência de ressonância fundamental das bolhas estava dentro da faixa de incerteza experimental, sugerindo que suas propriedades acústicas foram preservadas. Observamos também, de acordo com a literatura, que existe uma dependência linear entre a concentração da população de microbolhas (sem liofilização) e a amplitude do coeficiente de retrodifusão. Posteriormente, foi feita uma comparação da resposta de retrodispersão acústica para bolhas monodispersas e polidispersas. Também, de acordo com a literatura, observamos uma amplitude no sinal de resposta das bolhas monodispersas de 8 a 10 vezes maior que a das bolhas polidispersas, para a mesma concentração *in vitro*. Também foi possível observar a menor incerteza no monitoramento do pico de ressonância fundamental das bolhas e uma menor largura de banda para a população de bolhas monodispersas. Finalmente, utilizando a

abordagem de imagens de matriz universal de ultrassom, desenvolvida no *Institut Langevin*, a resposta acústica de retrodifusão da população monodispersa liofilizada e polidispersa foi avaliada em um tecido artificial com impedância acústica similar ao tecido humano. Os resultados preliminares reforçam os resultados das medições acústicas de retrodifusão na célula centimétrica e no milicanal, nos quais a população monodispersa apresentou uma largura de banda significativamente reduzida em comparação com a ampla largura de banda da população polidispersa.

O presente trabalho apresentou com sucesso uma nova técnica desenvolvida para liofilizar as microbolhas monodispersas sem degradar suas propriedades geométricas e acústicas. Assim, propusemos uma nova geração de agentes de contraste ultrassom na forma de um pó liofilizado estável que pode ser transportado e armazenado por meses e ressuspenso para uso em aplicações clínicas.

Palavras-chave

Microbolhas; microfluídica; liofilizado; monodisperso; ultrassom; álcool poli-vinílico

List of Tables

List of Figures

List of Symbols

A	Cross section area
A_s	Surface area
Bi	Biot number
C	Solubility
$\mathrm{C_p}$	Heat capacity at constant pressure
c	Gas concentration; thermal capacity; speed of sound
Ca	Capillarity number
D	Characteristic dimension; Diffusion coefficient
$\mathrm{D_w}$	Diffusivity constant
d_s	Shell thickness
E^s	Dilatational surface elasticity
E_s	Shell elasticity
f	Frequency; saturation level factor
f_r	Resonance frequency
f_0	Eigenfrequency
G_s	Shell shear modulus
h	Height; enthalpy; film thickness
H	Ostwald coefficient
h_c	Convective heat transfer
h_g	Gas permeability
$I_i(\omega)$	Incident sound intensity
I	Acoustic intensity
J	Effective permeability
k	Thermal conductivity; adiabatic bulk modulus of elasticity; wave-number
k_b	Boltzmann constant
K_H	Molar Henry’s constant

L	Length
l_D	Thermal diffusion Length
M	Mach number
M_e	Effective elastic modulus
M_w	Molecular weight
m	Mass
n_v	Particle density in volume
n_s	Number of scatterers
n_i	Moles of gas i
P	Calescence probability
p	Pressure
$\bar{p}^*$	Excess pressure
P_e	Scattered and absorbed power
p_L	Pressure at the bubble’s surface
p_0	External pressure
$\mathrm{p}_i(t)$	Driving acoustic pressure
$\mathrm{p}_s(t)$	Scattered pressure; scattered power
Pe	Peclet number
Q	Volumetric flow rate
R	Bubble radius; reflection intensity
R_{shell}	Shell resistance to mass transfer
S_p	Shell elasticity
S_f	Shell viscosity
SSr	Secondary scattering ratio
s	Stiffness
T	Absolute temperature; period; transmission coefficient
T_g	Glass transition temperature
T_{front}	Temperature at the transition front
t	Time
$t_{collapse}$	Collapse time of thin thread
u	Velocity

$u_{collapse}$	Speed of collapse
V	Velocity; Volume
V_m	Molar volume
w	Width
w_m	Minimum width of the thread of gas
Z	Acoustic impedance

Greek Symbols

$\alpha(\omega)$	Attenuation coefficient
β	Damping
γ	Adiabatic constant
Γ^{vis}	Viscous damping
δ	Damping coefficient; Thickness of encapsulation
η_e	Viscosity of the thinning film
η	Viscosity
$\eta(f)$	Backscatter/scatter coefficient
κ	Polytropic exponent of the gas
λ	Wavelength
μ	Dynamic viscosity
ν	Kinematic viscosity
ξ	Small displacement at bubble's surface
ρ	Mass density
$\Re$	Universal gas constant
σ	Interfacial tension
σ_a	Absorption cross-section
σ_b	Scattering strength
σ_e	Extinction cross-section
σ_s	Scattering cross-section
τ_d	Drainage time
τ_c	Contact time
χ	Shell elasticity

Ω_n	Mass transfer resistance
ω	Angular frequency

Subscripts

c	Critical
i	Inside; initial
o	Outside
or	Orifice
rad	Radiation
s	At the surface; shell
Th	Thermal
tot	total
0	Initial
η	Viscous

Contents

1. INTRODUCTION

Since the 1970s, ultrasound has been the most frequently applied medical imaging modality. It provides low-risk and portable imaging, creates real-time images that can be obtained at the patient's bedside, and is less costly than computed tomography (CT) and magnetic resonance imaging (MRI). The technology is based on capturing the scattering and reflection of transmitted ultrasonic waves at surfaces and tissue inhomogeneities with distinct acoustic impedances. The time of travel and the amplitude of the received echos can be used to create an ultrasound image. The most common ultrasonic frequencies employed are in the 1 to 50 MHz range, with higher frequencies resulting in higher spatial resolution due to their shorter wavelength. However, attenuation reduces penetration depth at higher frequencies, which grows linearly with frequency. As a result, the optimal imaging frequency is always a compromise between resolution and imaging depth. Acoustic inhomogeneities on bodily tissues scatter ultrasound which makes the ultrasound image brighter. Contrarily, ultrasound scattering from blood is substantially less than scattering from other tissues, often 30 to 60 dB weaker. However, the Doppler effect generates a frequency change in the echoes of flowing blood, and these weak signals can be distinguished from tissue echoes. This is utilized in different diagnostic ultrasound Doppler procedures to measure the velocity and direction of blood flow. The introduction of contrast agents is intended to enhance the scattering of sound from the blood. This will be utilized to boost the information content of ultrasound images and gather diagnostic information that would otherwise be unavailable.

1.1. Ultrasound Contrast Agents

Ultrasound contrast agents (UCA) are constituted of encapsulated microbubbles with diameters ranging from 1 to 10 µm that are filled with a gas that is insoluble in water (e.g., perfluorocarbon, nitrogen). They are administered into the systemic circulation intravenously; therefore, they must be less than 10 µm in diameter to pass through pulmonary circulation and microcirculation, which is equivalent to the size of red blood cells (6-8 µm). Free uncoated air microbubbles of this size could dissolve in the blood rapidly, in less than 1 second due to the surface tension (Stride, 2009). Thus, the microbubbles are coated with a shell of surface-active molecules (lipids or polymers), which counteracts surface tension, reduces gas diffusion into the surrounding environment, and extends the microbubbles' lifespan for imaging (> 10 minutes).

UCA offers excellent contrast between flowing or stagnant blood and surrounding tissue when injected into the circulatory system. Because the gas core is very compressible, UCA experiences volumetric oscillations and emits pressure waves when exposed to an acoustic field. Due to the pressure waves generated during volumetric oscillations, UCA have a small geometric scattering cross-section, but are extremely echogenic. As a consequence, the US Food and Drug Administration (FDA) has authorized UCA for use in cardiology.

1.2. History of Ultrasound Contrast Agents

Ultrasound contrast agents have been researched for over 40 years since it was first discovered by Gramiak and Shah (1968) by accident. They observed that saline infusion into the ascending aorta improved echo signals for echocardiography. This effect was then attributed to the formation of microbubbles that were found to scatter ultrasound efficiently. The first microbubbles could not travel through the lungs and could only be used to obstruct the right ventricle (Becher *et al.*, 1988). The discovery of tiny, stable, and highly echogenic microbubbles in the 1980s (e.g., gelatin-encapsulated nitrogen microbubbles (Carroll *et al.*, 1980) and human serum albumin-coated air bubbles (Feinstein *et al.*, 1984) sparked the commercialization of UCA. Echovist® (1982), produced by Schering AG (Berlin, Germany), was the first commercially marketed UCA, followed by Levovist® (1985). Albunex was the first UCA authorized by the FDA in 1994. It was created by Molecular Biosystems Inc. (MBI, San Diego, CA). Albunex is made by sonicating a 5% human serum albumin solution. These agents are from the first generation of UCA, and their microbubbles are generally filled with air. Because of their high solubility and diffusibility, air seeps out of the microbubbles as they travel through the pulmonary circulation, reducing their size.

In the early 1990s, high-molecular-weight gases (e.g., perfluorocarbon, nitrogen) were added to the second-generation UCA to address this issue. These gases can decrease gas diffusion to the surrounding medium, enhancing microbubble stability and lifespan. These agents have been shown to improve contrast imaging in various settings (e.g., echocardiography). Optison® (GE

Healthcare, Princeton, NJ) was approved by the FDA in 1998 and is made up of perfluoro gas microbubbles coated with human serum albumin. SonoVue® (Bracco Diagnostics, Inc., Princeton, NJ) uses another gas with a limited solubility: sulfur hexafluoride. Definity® (Lantheus Medical Imaging, Inc., N Billerica, MA), one of the most popular agents, was authorized by the FDA in 2001. They are perfluoro-filled lipid-coated microbubbles. However, in the United States, the FDA has only authorized Optison® and Definity® for left ventricular (LV) opacification (Kaul, 2008). Echogen® (Sonus Pharmaceuticals, Bothell, WA) (Grayburn, 1997) is a phase-shift colloid containing dodecafluoropentane (DDFP) liquid in the dispersion phase that transforms from liquid to gas phase at body temperature and creates microbubbles. A list of commercially available ultrasound contrast agents can be found in Kaul (2008) and Frinking *et al.* (2020).

1.3. Applications of Ultrasound Contrast Agents

UCA are commonly employed in ultrasound imaging due to their strong echogenicity and nonlinear response to acoustic stimulation. Microbubbles oscillate nonlinearly when insonified by ultrasound at frequency f. Thus, harmonic (2f, 3f, ...), subharmonic (f/2, f/3, ...), and ultra-harmonic (3f/2, 5f/2, ...) components can be formed depending on the shell characteristics, driving frequency, and pressure. Based on these characteristics, multiple techniques have been developed to increase the imaging sensitivity and contrast-to-tissue ratios (CTR), such as second harmonic imaging (Kaul, 2002), super-harmonic imaging (van Neer *et al.,* 2010), subharmonic imaging (Gong *et al.,* 2006; Couture *et al.,* 2009), pulse inversion (Simpson *et al.,* 1999), pulse inversion Doppler (Mahue *et al.,* 2011), dual-frequency modulation (Su *et al.,* 2008) and coded-pulse imaging (Gong *et al.,* 2007; Li *et al.,* 2010).

UCA is mainly used in echocardiography (Kaul, 2008), where it is used to detect ventricular opacification, delineate endocardial boundaries, measure systolic function and left ventricular volume, and identify myocardial infarction and coronary artery stenoses (Stride, 2009). Contrast-enhanced imaging is also utilized to identify and characterize liver tumors, assess brain strokes and other organs (e.g., kidney, breast, prostate, etc.).

Ultrasound has lately shown potential as an imaging modality for molecular imaging (Hamilton *et al.,* 2002; Leong-Poi *et al.,* 2003; Weller *et al.,* 2003; Bloch *et al.,* 2004; Hamilton *et al.,* 2004; Rychak, *et al.,* 2006; Dayton and Rychak 2007; Klibanov, 2007). In this method, UCAs coupled with particular antibodies or peptide sequences are directed towards membrane-bound ligand receptors produced during illness development. Diagnostic ultrasound pictures of the bound UCA are collected and employed to examine the disease's anatomy and pathology. UCA with all bubbles having the same frequency response would be ideal for molecular imaging applications. This would allow imaging to be performed at frequencies tuned to the resonance or harmonics of the bound bubbles, increasing the system's sensitivity to identify the targeted UCA.

In addition to diagnostic applications, UCA has been studied for therapeutic applications such as drug delivery (Larina *et al.,* 2005), gene therapy (Liu *et al.,* 2006; Phillips *et al.,* 2009), sonothrombolysis, blood-brain barrier (BBB) opening (Choi *et al.,* 2007), High Intensity Focused Ultrasound (HIFU) (Luo *et al.,* 2006; Kim *et al.,* 2008), functional ultrasound imaging (Macé *et al*., 2011), and super-resolution ultrasound imaging with ultrasound localization microscopy (ULM) (Errico et al., 2015, and Demené et al., 2021).

1.4. Monodisperse Ultrasound Contrast Agents

Since the inaugural use of free gas bubbles as ultrasonic contrast agents in 1968 (Gramiak and Shah, 1968), much effort has been made to enhance the stability, safety, and echogenicity of UCAs. Today, UCAs with a shell that encapsulates a heavy gas are created by sonication and agitation of a surfactant solution containing lipids, proteins, or polymers (Frinking *et al.*, 2020). Current manufacturing approaches produce the required structure, but give little control over microbubble size, resulting in polydisperse contrast agents.

Polydisperse microbubbles have a practical benefit. They cover both low and high frequencies, allowing the visualization of images of a deep or shallow structure. A single product might thus serve several purposes. However, limits caused by size polydispersity have been highlighted in recent years. Because the resonance frequency of microbubbles is inversely related to their size (Minnaert, 1933), the resonance spectrum in polydisperse UCAs will be broad (Tremblay-Darveau *et al.,* 2014; Hoff *et al.,* 2000). In a polydisperse population, ultrasound scanners used in clinics generally produce acoustic pulses with a restricted frequency bandwidth, exciting just a tiny percentage of the bubbles near their resonance (Segers *et al.,* 2016). As a result, polydispersity is not optimum in terms of signal-to-noise ratio (Stride *et al.*, 2020). Furthermore, (Segers *et al.,* 2018b) demonstrated that polydispersity makes it difficult to fully use the non-linear properties that allow for the reduction of shadowing effects in deep tissue imaging.

The use of polydisperse bubbles also inhibits quantitative measures that might be useful in therapeutic settings, such as detecting local pressure (Fairbank and Scully, 1977; Ishihara *et al.,* 1988; Tremblay-Darveau *et al.,* 2014; Segers *et al.,* 2018a). According to Minnaert's law, local pressure influences the resonance frequency. If the bubble population is monodisperse, a route connecting resonance measurements to local pressure can be established. However, polydisperse bubbles provide a broad resonance range from which it is challenging to derive quantitative pressure information. For example, the needed clinical sensitivity for diagnosing portal vein hypertension is ±2 kPa. The readings are supposed to be repeatable in a monodisperse population, with a coefficient of variation (CV) of 6%. (Tremblay-Darveau *et al.,* 2014). Attempts to use subharmonics have also been proposed (Shi *et al.,* 1999; Esposito *et al.,* 2020), but on a purely empirical basis, impairing the measurement's reliability.

In molecular diagnostics, the bubbles can be functionalized to acquire an affinity with certain antigens, causing them to preferentially settle in specific parts of the circulation, disclosing the presence of the targeted molecules (Leong-Poi *et al.,* 2003), as mentioned in the previous section. The amount of bubbles that reach their destinations is small, resulting in weak echoes (Frinking *et al.,* 2012). Polydisperse bubbles lack the high sensitivity of the resonance frequency shift for distinguishing freely circulating and confined bubbles (Overvelde *et al.*, 2011).

Drugs, genes, and therapeutic gases can also be transported via microbubbles (Hernot and Klibanov, 2008; Sutton *et al.,* 2014; Kooiman *et al.,* 2020). When bubbles reach specified regions, they might break, releasing the charge locally. Nonetheless, polydisperse bubbles necessitate high ultrasonic intensities for effective breaking, which might lead to clinical issues. To produce a regulated and efficient burst, monodisperse bubbles must be used (Roovers *et al.*, 2019). The fine control of monodisperse bubbles can also enhance therapeutic applications such as sonothrombolysis (Dixon *et al.*, 2019) and temporary blood-brain opening (Choi *et al.*, 2010).

Functional ultrasound imaging (fUS) is a breakthrough technology that uses ultrafast frame rates to map changes in local cerebral blood volume induced by neural activity (Macé *et al.*, 2011). However, skull bones attenuate and distort ultrasound waves in the MHz range (Pinton et al., 2012), which hinders the fully noninvasive potential of fUS imaging. A potential solution to compensate for skull attenuation is to augment the source of contrast in fUS – red blood cells – by administering UCA into the blood stream. Maresca *et al.*, (2020) used gas vesicles (GVs), genetically encodable ultrasound contrast agents derived from buoyant photosynthetic microorganisms, characterized by being monodisperse. They showed that intravenously infused GVs enhance ultrafast Doppler ultrasound contrast and visually-evoked hemodynamic contrast in transcranial fUS of the mouse brain. The enhancement leads to a more effective functional signal amplification compared to the commercial microbubbles which are polydisperse.

Recently, super-resolution ultrasound imaging with ultrasound localization microscopy (ULM) has received much attention (Errico *et al.,* 2015, and Demené *et al*., 2021). In ULM, the microvasculature is imaged by tracking the microbubbles that are confined within the capillaries. ULM requires a sparse distribution of microbubbles in the microvasculature, which ensures the separation of their point spread functions. By tracking the centroids of these point spread functions as the microbubbles flow through the capillaries, the microvasculature and its flow field (magnitude and direction) are mapped. Blanken *et al*., (2022) presented an alternative super-resolution approach, based on direct deconvolution of single-channel ultrasound radio-frequency signals with a one-dimensional dilated convolutional neural network (CNN). They showed a better performance for monodisperse bubbles compared to polydisperse bubbles, which was attributed to a lower degree of kernel variability. In other words, the individual bubble echoes varied less in amplitude and shape.

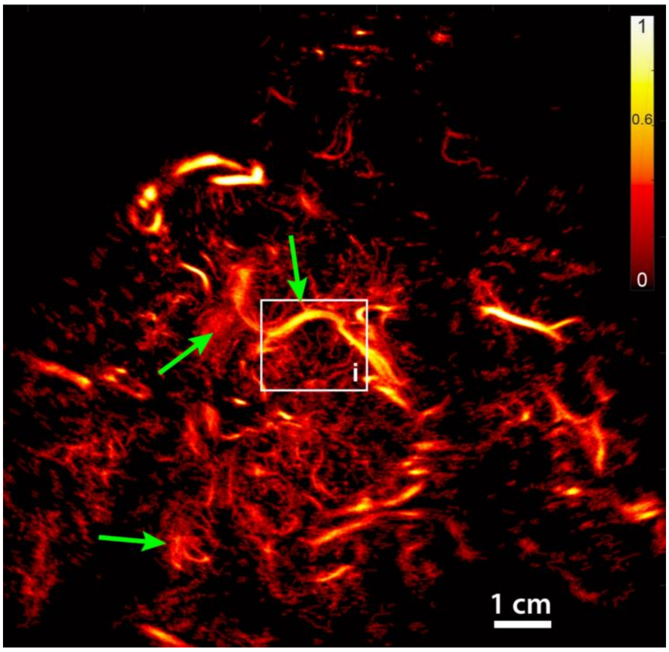

Figure 1.1 - Transcranial Ultrasound Localization Microscopy of deep brain vessels in patients using microbubbles. (figure adapted from Demené *et al.*, 2021).

In vitro, phospholipid-shelled microfluidic monodisperse microbubbles were shown to have 2-3 orders of magnitude more acoustic sensitivity than polydisperse microbubbles (Segers *et al.,* 2018b). Similarly, the acoustic sensitivity of monodisperse bubbles was found to be between 10 and 15 times (in rats) greater than that of clinical polydisperse bubbles like SonoVue, Definity, and Optison (Helbert *et al.,* 2020).

Based on these findings, one might conclude that monodisperse bubbles are particularly beneficial in therapeutic applications. Monodisperse bubbles bring new possibilities for diagnostics, pressure sensing, and treatment. Highly monodisperse bubbles are nowadays produced with microfluidics (Peyman *et al.,* 2012; Abou-Saleh *et al.,* 2021). However, to transport and store them, they must be freeze-dried without losing their qualities, which is currently a difficulty. The issue is that coalescence and ripening events decrease monodispersity during the freeze-drying process. Freeze-drying without compromising size uniformity remains a hurdle in the industry, preventing the use of monodisperse microfluidic bubbles in clinical applications.

Attempts have been undertaken in the past to obtain freeze-dried bubbles with restricted size ranges. For stability concerns (bubbles are more challenging to handle than droplets), the fabrication of monodisperse oil-water or air-oil-water emulsions was the starting point (Böhmer *et al.*, 2006; Song *et al.*, 2018; Lee *et al.*, 2011). These droplets were freeze-dried or evaporated to produce microbubbles with polymer shells (Kooiman *et al.*, 2009; Chlon *et al.*, 2009). These procedures need the removal of a solvent (e.g., dichloromethane, cyclododecane, dodecane) at some point throughout the process. This task, which is never guaranteed to be accomplished completely, poses regulatory concerns. Another approach is to size-filter polydisperse bubbles using mechanical (Streeter *et al.,* 2010), centrifugal (Feshitan *et al.,* 2009), or acoustic sorting (Segers *et al.,* 2018b), then freeze-dry them using the same method as commercial bubbles. These procedures resulted in a CV of 10% to 20%. Although sorting may be tailored to specific applications, the monodispersity produced with this method is insufficient for non-invasive pressure monitoring (Tremblay-Darveau *et al.*, 2014). Thus, to obtain a CV of less than 5%, allowing for such measurements and the other tasks outlined above, microfluidic bubble generation followed by freeze-drying is required. Monodisperse bubbles can be produced on-site using portable and automated microfluidic devices (Abou-Saleh *et al.*, 2021; van Elburg *et al.*, 2021). However, matching clinical limits and encouraging doctors to make bubbles themselves with this strategy is difficult (Schneider *et al.,* 1995; Sontum, 2008). Finally, this discussion suggests that freeze-drying directly shell-encapsulated monodisperse bubbles created in microfluidic devices is an ideal solution for addressing storage and transportation issues. These facts raise the possibility that, one day, monodisperse bubbles will be employed in clinics.

In this work, we succeeded in producing freeze-dried microfluidic-generated monodisperse microbubbles without degrading their monodispersity. The gas bubbles are encapsulated with nanometric polyvinyl alcohol (PVA) shell. Their size can be tuned from 4 to 50 µm in diameter with a narrow size distribution, i.e., less than 5% in CV. The lyophylisate we produced in the present work represents a new generation of contrast agents that can be stored for months and transported at any place, resuspended, and used directly in clinical applications.

1.5. Outline of the Thesis

This dissertation presents a general introduction of ultrasound contrast agents, their history, application, and limitations in the Introduction chapter. The thesis is then divided into two main sections.

Section 1 focuses on the freeze-drying of a microfluidic monodisperse microbubble population. First, we provide a detailed literature review regarding microbubble stability, microfluidics, and freeze-drying. After, the materials and techniques used to produce and freeze-dry PVA-shelled PFC-filled monodisperse microbubbles and their characterization methods are described. Finally, the results and discussion regarding size distribution and stability of two different size microbubble populations are presented.

Section 2 focuses on the backscatter acoustic characterization of the freeze-dried microfluidic monodisperse microbubbles population. First, we provide a detailed literature review of the fundamentals of ultrasound imaging, ultrasound contrast agents, and acoustic characterization of UCAs. The setups and methods used to characterize the freshly generated PVA-shelled monodisperse microbubbles, the Freeze-dried PVA-shelled monodisperse microbubbles, and the commercially available polydisperse microbubbles are presented. At last, we present the results and discussion for the backscattering acoustic characterization of the different bubble populations, comparing the effects of freeze-drying, size distribution, materials, and concentration.

Concluding remarks and suggestions for further studies are presented in the last chapter.

2. FREEZE-DRIED MONODISPERSE MICROBUBBLES

This chapter provides, at first, a literature review of the main mechanisms that affect microbubble’s stability (coalescence, Ostwald ripening, and bubble dissolution), presenting models that were developed through the years. In the following, a review of microfluidics and monodisperse microbubble production through the use of a flow-focusing microfluidic device is presented. At last, the physics behind the freeze-drying process is described and the parameters that play a role in the quality of the technique are discussed.

By understanding the parameter that influences microbubble stability, monodispersity, and freeze-drying, we were able to propose and develop a new lyophilization technique that does not degrade the monodispersity of a microbubble’s population.

2.1. Microbubble Stability Fundamentals

The stability of the microbubbles over time is vital for their applications as ultrasound contrast-enhancing agents and as therapeutic agents. The microbubble suspension must be stable in body fluids (*in vivo* stability) and during storage (shelf-stability). As defined by Dalvi *et al.* (2018), shelf-stability of a microbubble population is the period in which no significant change in the bubbles' size distribution and concentration (number/milliliter) is observed. Multiple factors can play a role in the instability of a microbubble suspension, such as coalescence, Ostwald ripening, and diffusion of the gas core out of the microbubbles.

2.1.1. Coalescence

One of the main processes that can affect the stability of microbubbles is coalescence. In the ultrasound contrast agent domain, the formation of large microbubbles is undesirable because it can lead to blood flow blockage and embolism, which can result in fatalities.

The most popular theory or criteria proposed for the coalescence process is the film drainage model (Shinnar and Church, 1960; Vrij, 1966). The process is divided into three manageable subprocesses. First, two bubbles dispersed in a liquid phase approach each other, forming a thin film (a quasi-equilibrium film thickness of typically 1-10µm between them. This phenomenon is governed by the hydrodynamics of the bulk liquid phase (Oolman and Blanch, 1986). At second, a drainage process due to capillary forces occurs, increasingly thinning the liquid film. In that phase, the system properties such as surface tension and viscosity also influence the thinning process. After reaching a thickness of approximately 100nm, Van der Waals attraction starts to increase the drainage rate, competing with electrostatic double-layer forces that try to reduce it. Around 50-10nm, some films become metastable or collapse. Metastability is reached when forces of attraction (border suction and van der Waals) equilibrate with repulsive force (double layer). When the attractive forces overcome the repulsive ones, instability appears. A spontaneous rupture of the unstable film occurs at a characteristic critical thickness. The rupture of the film (around 10nm) leads to the coalescence of the bubbles.

Since the rupture step happens at a much faster rate than the thinning of the liquid film between bubbles, coalescence is mainly controlled by the drainage rate. Therefore, bubble coalescence can be described as a probabilistic process governed by two characteristic time scales: the drainage time τ_d and the contact time τ_c, as follows (Coulaloglou, 1975; Segers, 2017):

$$P = \exp(-\tau_d / \tau_c) \tag{2-1}$$

where P is the coalescence probability. The drainage time is the time required for a thin film between two bubbles of initial thickness to reach a critical value, at which the bubble wall destabilize and rupture.

Various regimes of film drainage might be distinguished according to the rigidity of the particle surface (deformable or non-deformable, Figure 2.1), and the mobility of the contact interfaces (immobile, partially mobile, fully mobile, Figure 2.2) (Lee and Hodgson, 1968; Liao et al., 2010). The majority of the models found in the literature use the lubrication theory to derive a thinning equation. For simple boundary conditions (e.g., constant interaction force or constant approach velocity), the drainage time can be obtained by integrating the film thinning equation.

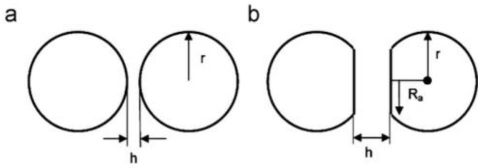

Figure 2.1 – (a) Non deformable surfaces ; (b) Deformable surfaces. Simon (2004).

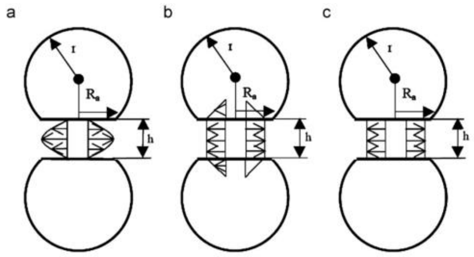

Figure 2.2– (a) Immobile interfaces; (b) Partially mobile interfaces; (c) Fully mobile interfaces. Simon (2004).

For the case of ultrasound contrast agents, where the bubbles have a diameter much smaller than 1mm, at a large distance, their interfaces are slightly deformed and they can be considered as nearly rigid spherical particles. For two non-deformable spheres with equal sizes, the drainage time was derived by Chesters (1991) by using the Poiseuille relation (Segers *et al.*, 2017, Liao *et al.*, 2010).

$$\tau_d = \frac{3\,\pi\,\eta_e\,R^2}{2\,F}\ln\left(\frac{h_i}{h_c}\right) \tag{2-2}$$

where η_e is the viscosity of the thinning film, R is the radius of the bubble, h_i is the initial thickness of the thin film between the bubbles, h_c is the critical thickness at which the thin film ruptures, F is the difference between compressive force F_d, and surface forces F_s originating from intermolecular interaction.

Coalescence is avoided when the contact time between two bubbles is smaller than the thinning time. For that reason, the focus of the coalescence mechanism is the drainage rate of the thin film between bubbles. Five main factors that influence the thinning rate are described in the literature:

1- Gravity and capillarity are the main forces influencing the drainage rate. Therefore, the mobility of the bubble surface, the physical properties of the continuous phase (surface tension gradients, viscosity, and surface viscosity) and the difference between the density of gas and liquid phases are the drivers of this process. Jeffreys and Davis (1971) showed that higher surface tensions lead to higher resistance to deformation of the bubble wall, resulting in a smaller drainage film area, increasing, as consequence, the speed of coalescence.

2- The electro-viscous effect, described by Elton and Pickness (1957) is shown to inhibit gas bubble coalescence. These phenomena appear in electrolyte solutions, where the formation of an electrical double layer at the bubbles interface retards the thinning of the film in between bubbles, by immobilizing their interfaces. This mechanism is more noticeable when the size of the electrical double layer has the same order of magnitude as the drainage film thickness.

3- The coalescence can be also inhibited by having surface-active agents in the aqueous solution. These agents consist of organic molecules with hydrophilic groups (-OH, >CO, -COOH, etc.) and a hydrophobic part (hydrocarbon structural group) (Keitel and Onken, 1982). They act in decreasing the surface tension and increasing the surface viscosity, which slows the thinning rate of the liquid film between bubbles, resulting in a reduction of the probability of rupture of the bubbles wall. Surface active molecules will adsorb to the gas-liquid interface forming a monolayer. The stability of this configuration depends on the type of surfactant, size of the molecule, and concentration. Moreover, these molecules have hydrophilic and hydrophobic parts, which will be aligned in the liquid and gas phase, respectively, making the surface around the bubble electrically charged. The polarization resulting from this phenomenon generates repulsive forces that contribute to reducing coalescence.

4- Diffusion can also play an important role in the drainage rate of the liquid film. Processes such as diffusion of the film to the liquid-gas interface or diffusion from solutes in the continuous liquid phase to the film between bubbles are examples of this phenomenon.

5- Chemical reactions of the gas core can lead to changes in the size of the bubbles, leading to an increase or decrease of the coalescence probability. This type of event can also change the size distribution of the bubble's population, even without coalescence.

The importance of the previously mentioned factors on coalescence will be defined by the type of system that the bubble is inserted. The systems are typically divided into four major groups where the liquid phase consists of a non-Newtonian fluid, a solution of electrolytes, a pure solvent (or a mixture of non-polar solvents), or a solution containing inorganic or organic surface-active agents. Based on that, multiple theoretical models were developed over the years aiming to obtain a quantitative description of the thin film drainage rate. Theoretical models and experimental data regarding the coalescence mechanism are described in deeper details by Chaudhari and Hofmann (1994).

More recently, the exposure of microbubbles to ultrasound fields was found to contribute to coalescence events of UCA populations as described by Postema *et al.* (2004). When exposed to the ultrasound field, the bubbles expand resulting in a flattening of the surface of the bubble before contact. Then, drainage of the liquid film occurs until reaching a critical thickness, followed by the rupture of the liquid film, leading to the formation of a single larger bubble. The study shows that the coalescence mechanism for colliding bubbles can be also applied for expanding bubbles but at a faster rate.

Liao *et al.* (2010) provided a detailed literature review on the mechanisms and models of coalescence of fluid particles. Figure 2.3 shows a flowchart with the main models available in the literature. The authors first distinguish the models in two categories, namely, physical models and empirical models.

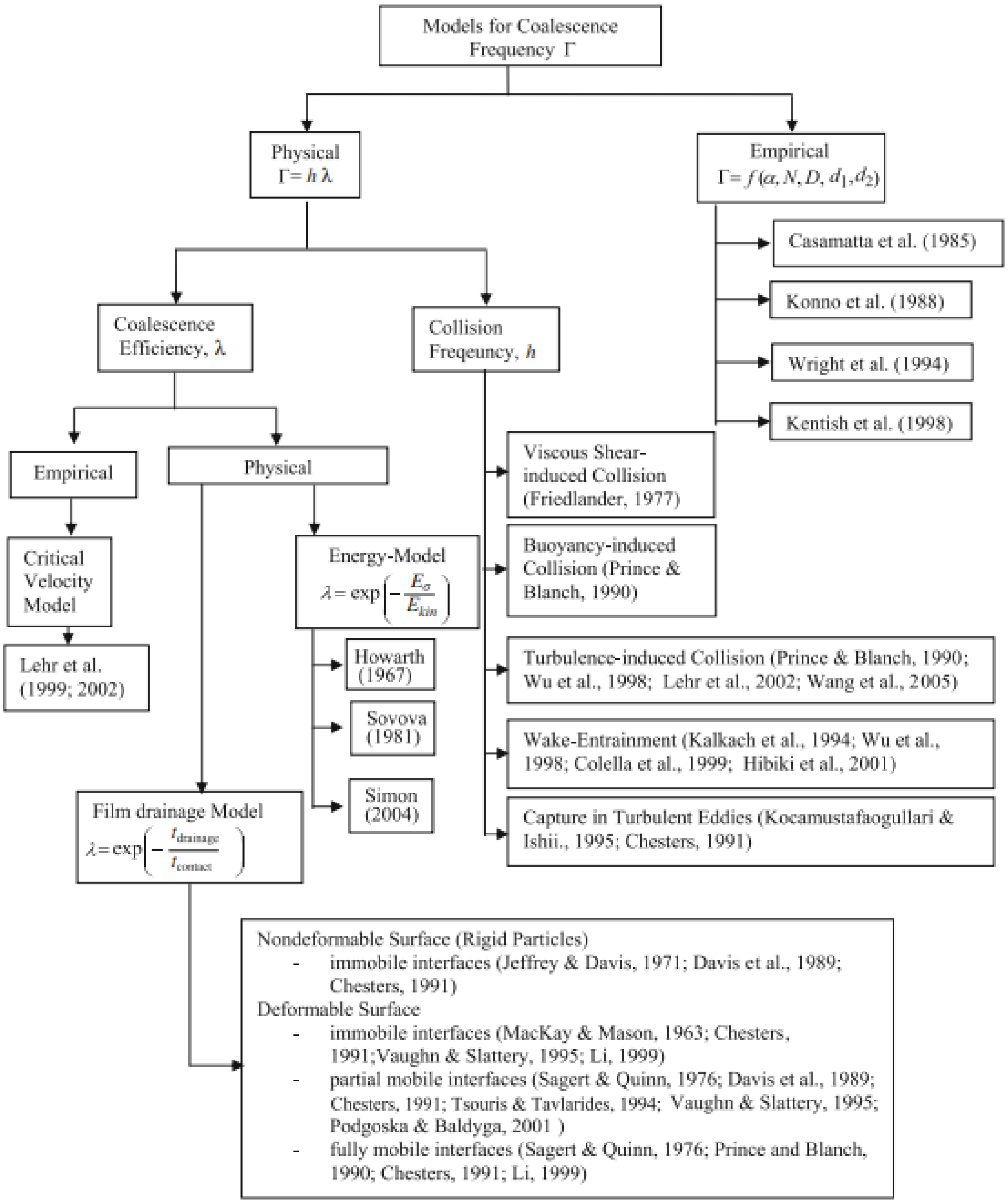

Figure 2.3 – Classification of Theories and Models in the literature (Liao et al., 2010).

The physical models calculate the coalescence frequency based on both collision frequency and coalescence efficiency. The collision frequency is caused by the relative velocity of the bubbles. Liao and colleagues summarize the five main parameters in a turbulent flow that contributes to the bubble's collision: viscous shear-induced collision, buoyancy-induced collision, turbulence-induced collision, wake interaction or zigzag trajectories, and bubbles captured in a turbulent eddy.

Since not all collisions lead to coalescence, the concept of coalescence efficiency is introduced. There are three main theories or criteria that aim to describe the coalescence process. First, the most popular one is the film drainage model (previously described), proposed initially by Shinnar and Church (1960). Second, is the Energy model proposed by Howarth (1964), where the main parameter that drives coalescence is the impact of colliding bubbles. He argues that the attraction force between two colliding bubbles (usually induced by molecular nature) is too weak when compared to forces imposed by the turbulent flow. The last one originates from the empirical models, where the concept of critical velocity is introduced. The concept arises from the experimental observation of Doubliez (1991) and Duineveld (1994), where they observed that small approach velocities result in higher coalescence efficiency. Most of these empirical models use a power-law function with empirically adjusted parameters.

2.1.2. Ostwald ripening

A second mechanism that can irreversibly decrease the monodispersity of a microbubble population is the Ostwald ripening phenomenon. In a polydisperse particles suspension, larger particles grow at the expense of smaller ones, whereas the small particles will diminish until completely disappear. Due to a lower surface-to-volume ratio, the larger particles are thermodynamically more stable than smaller particles. In the second stage, a differentiation in the size of the large particles takes place. This process arises because of the Kelvin effect, where the solubility of the substance inside the spherical particle increases with the reduction of size. In a system having one component disperse phase, the equation first proposed by Kelvin (1871) is the following:

$$C(r) = C(\infty) \cdot \exp\left(\frac{2\,\sigma\,V_m}{\Re\,T\,r}\right) \approx C(\infty) \cdot \left(1 + \frac{2\,\sigma\,V_m}{\Re\,T\,r}\right) \tag{2-3}$$

where σ is the interfacial tension, V_m is the molar volume of the substance of the disperse phase, r is the radius, $C(r)$ is the solubility, and $C(\infty)$ is the solubility when $r = \infty$ (the bulk phase solubility) of the spherical particle, $\Re$ is the universal gas constant, and T is the absolute temperature. The solubility of the gas inside the bubble is inversely proportional to the bubble's radius, and temperature, while it is directly proportional to the surface tension. Kabalnov and Shchukin (1992) reported a detailed description of the Ostwald ripening mechanism for fluorocarbon emulsions.

For the specific case of microbubbles in a polydisperse suspension, the mechanism basically results from the Laplace pressure differential giving rise to concentration gradients for bubbles of different sizes. The pressure inside the bubble is as follows:

$$p_i - p_o = \frac{2\sigma}{r} \tag{2-4}$$

where p_i and p_o are the pressure inside and outside the bubble, respectively. The bubbles radius is inversely proportional to the internal pressure, resulting in smaller p_i for the larger bubbles in comparison to smaller ones. This configuration generates a driving force for mass transfer of core gas from smaller bubbles to larger ones, which results in an increase of larger microbubbles. Figure 2.4 shows a typical case in which microbubbles experience Ostwald ripening. Talu *et al.* (2008) observed the growth of bigger microbubbles at the expanse of the smaller ones, as previously described, for PFB-air lipid-encapsulated microbubbles.

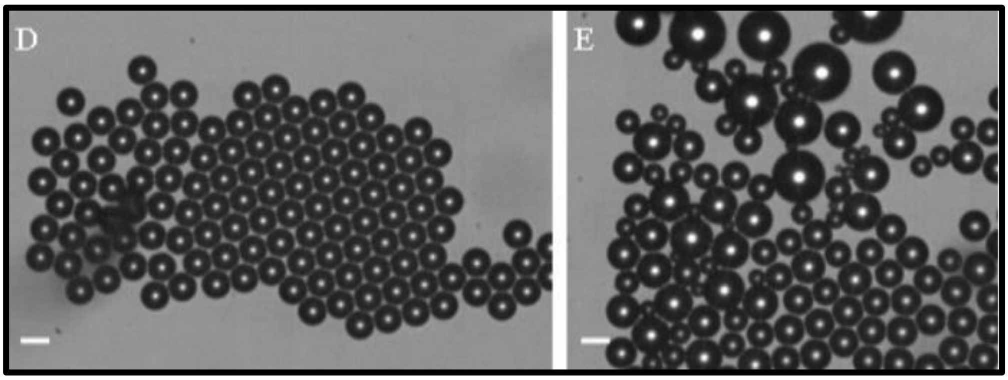

Figure 2.4 – Example of Ostwald ripening for PFB-air lipid-encapsulated microbubbles. (D) under the cover glass, and (E) microbubbles under the cover glass after 3 min. Scale bar represents 10 μm. Figure adapted from Talu et al. (2008).

It is impossible to increase the stabilization of microbubbles population infinitely through the choice of surfactants. Despite the usage of an optimized surfactant system, the degradation rate, which is slightly dependent on the emulsifying system, and highly dependent on the properties and composition of the disperse phase, is still a problem. In this type of system, which is sufficiently stabilized against coalescence, Ostwald ripening plays a major role in the bubbles population degradation (Kabalnov and Shchukin, 1992).

In 2008, Dressaire *et al.* demonstrate that it is possible to achieve stabilization of microbubble dispersion for more than 1 year, through the reduction of surface tension, and increase in the viscosity of the bulk phase. The mean size of the microbubble population increased from 0.7 to 3.5 µm over the studied period, meaning that bubble growth due to Ostwald ripening was reduced.

A theoretical study conducted by Hu and Le (2018) shows the influence of particle size distribution on the lifetime stability of Ostwald ripening of supported particles. Their results highlight the importance of both size and monodispersity in particle size distribution on the ripening stability.

The reduction of the Ostwald ripening effect due to monodispersity of microbubbles was also verified by Weaire and Hutzler (1999) and Zuniga and Aguilera (2009). In a monodisperse bubble suspension, the Laplace pressure through the bubble population is very similar, resulting in a very small pressure gradient between different bubbles. This configuration reduces the mass transfer between the bubbles, which enhances the stability of the bubble population.

Dagastine *et al.* (2020) conducted a study where they quantified gas transfer between two adjacent microbubbles separated by a thin film, far less than 100 nm, with and without surface-active species. They observed that an anionic surfactant does not provide a barrier to mass transfer but does enhance mass transfer above the critical micelle concentration. In contrast, a polymer monolayer (i.e., Polydiallyldimethylammonium chloride - PDADMAC) at the interface does restrict mass transfer, yielding higher stability to the bubbles.

Another parameter that could extend the stability of the bubble's population against Ostwald ripening is the bubbles concentration. Feshitan *et al.* (2009), through the use of differential centrifugation, were able to isolate from a polydisperse lipid-shell microbubble population, a 1–2 and 4–5 µm diameter fractions. They observed that the smaller size population (1-2 µm) was more stable over time than the larger population. They attributed this counter-intuitive behavior to the fact that the smaller population was 1 order of magnitude more concentrated than the 4-5µm population. They argue that the higher population led to a thicker cake coating the top surface that buffered, reducing film rupture and gas release at the surface ("popping").

2.1.3. Microbubble dissolution

The stability of the bubbles is affected by the microbubble's core gas diffusion into the surrounding medium. This process can lead to the collapse of the microbubbles. Therefore, when designing microbubbles, the encapsulated gas properties (solubility in aqueous medium and molecular weight) should be evaluated. Also, the permeability of the shell material to gas diffusion plays an important role in the dissolution process. The main parameters that influence the permeability of the shell are thickness, the nature of shell material, and the molecular configuration inside the shell (Dalvi and Joshi, 2015; Upadhyay and Dalvi, 2018).

In this chapter, a brief review of the models available in the literature for microbubble dissolution is presented. There are three main categories where the models fit in: single bubbles dissolution in a gas saturated aqueous medium, single bubble dissolution in a multigas environment, and stability of microbubbles population in aqueous suspension.

2.1.3.1. Single bubbles dissolution in gas saturated aqueous medium

The models described in this segment are typically suited to describe the bubble’s stability when stored in vials before their use in biomedical applications. The origin of these models is the Epstein-Plesset formulation from 1950. By assuming the gas inside the bubble as an ideal gas, and using the diffusion equation, they developed an expression for the concentration profile of a dissolving bubble in an aqueous medium. This equation was then differentiated in order to obtain the molar flux at the bubble’s surface. Then, the molar balance over the bubble was coupled with the molar flux equation, leading to the equation for the variation of the microbubble’s radius over time.

$$\dot{R} = \frac{D_w(c_i - c_s)\mathfrak{R}\, T}{M_w\left(p_0 + \frac{4\sigma}{3R}\right)}\left(\frac{1}{R} + \frac{1}{\sqrt{\pi D_w t}}\right) \tag{2-5}$$

where R is the bubble radius and $\dot{R}$ its time derivative, D_w is the diffusivity constant for the interface at a given temperature and pressure, c_i is the initial dissolved gas concentration in the liquid, c_s is the gas concentration at the bubble surface, $\mathfrak{R}$ is the universal gas constant, T the absolute temperature, σ is the interfacial surface tension, R_0 the initial bubble radius, p_0 the ambient pressure, M_w the molecular weight of the gas and t is time. Figure 2.5 shows the radius-time relation for dissolving bubbles. The chart shows the microbubbles dissolution curves for bubbles with diameters of 1, 3, and 5 µm. The dissolution time, respectively, for the air-filled bubbles were approximately 2, 25, and 90ms. The curves show a considerably shorter dissolution time for the smaller bubble, which is a consequence of the higher Laplace's pressure. It is also possible to see that the bubbles follow the exact same curve when they reach the same size. The comparison between the air and SF_6-filled microbubbles shows a four times higher dissolution time for the bubble containing the high-molecular-weight gas (SF_6).

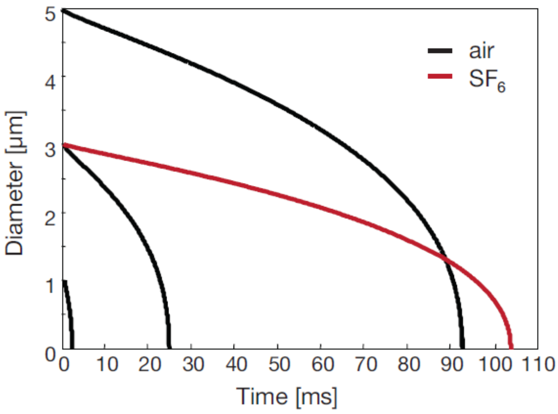

Figure 2.5 – Microbubble dissolution curves. A 5 μm air bubble in water dissolves in approximately 90 ms. A 3 μm and a 1 μm air bubble dissolve in 25 ms and 2 ms, respectively. Exchanging the gas core of the 3 μm bubble by a high-molecular-weight gas (SF6) shows a fourfold increase in its lifetime (Segers, 2015).

It is important to state that the Epstein-Plesset model takes into consideration the surface tension effects and the gas saturation of the aqueous solution, but does not account for the shell's permeability. D'Arrigo *et al.* (1992) showed experimentally that lipid-coated air-filled microbubbles of 1-5 µm diameter were stable in an air-saturated aqueous solution for up to one year. In the same direction, Soetanto *et al.* (1997) showed that sodium-laurate-coated air microbubbles dissolved much more slowly in a degassed medium than would be theoretically predicted for an air microbubble with no shell. Therefore, in scenarios where the microbubble shell provides high resistance to mass transfer, this classical Epstein-Plesset model is not suitable.

In the study of Borden and Longo (2002), they proposed a model for microbubble dissolution (Eq. 2-6) in a degassed medium considering both surface tension reduction and shell resistance to gas permeation and compared it to experimental data for lipid-coated, air-filled microbubbles.

$$-\dot{R} = \frac{H}{\frac{R}{D_w}+R_{shell}}\left(\frac{\left(1+\frac{2\sigma}{p_0 R}\right)-f}{1+\frac{4\sigma}{3p_0 R}}\right) \qquad (2\text{-}6)$$

where H is the Ostwald coefficient and is equal to the ratio of the gas concentration in the aqueous phase to that in the gas phase, f is the saturation level factor, and R_{shell} is the shell resistance to mass transfer. The gas molecules exiting the gas core of a dissolving bubble must permeate through three layers (illustrated by Figure 2.6), including the lipid monolayer, the grafted PEG brush layer, and the bulk aqueous medium. This makes the shell resistance to mass transfer to become the sum of the resistance of the individual layers. For the case in which shell resistance is negligible (free-gas bubbles), the equation reduces to the steady-state model from Epstein-Plesset, Eq. (2-5).

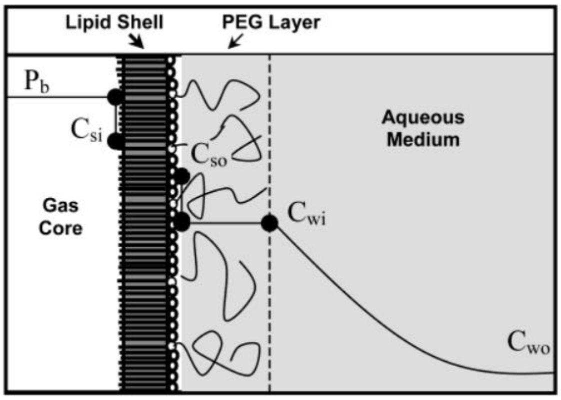

Figure 2.6 – Schematic of the concentration profile of gas molecules exiting the gas core of a lipid-coated microbubble (Borden and Longo, 2002).

The authors assumed in their model that the shell material was inelastic, leading to constant values of surface tension and shell resistance through the dissolution process. As a result, they observed that shell resistance is the primary stabilization mechanism for microbubbles coated with gel-state lipids. Further, the study concluded that the lipids with longer carbon chains resulted in higher shell resistance to gas diffusion.

In 2009, Sarkar *et al.* proposed a modification to the model, where they included the elasticity of the shell. The elasticity is modeled using a Gibbs elasticity type constitutive model, where a dilatational surface elasticity E^s term appears as derivative of surface tension with respect to the fractional change in the interfacial area (A/A_0).

$$E^s = \frac{d\sigma}{dA/A_0},$$

$$\sigma(R) = \begin{cases} \sigma_0 + E^s\left[\left(\frac{R}{R_0}\right)^2 - 1\right],\ for\ \sigma_0 + E^s\left[\left(\frac{R}{R_0}\right)^2 - 1\right] > 0 \\ 0,\ for\ \sigma_0 + E^s\left[\left(\frac{R}{R_0}\right)^2 - 1\right] \le 0 \end{cases} \tag{2-7}$$

The authors assume that R_0 is the initial bubble's radius that corresponds to a stress-free configuration. From Eq. (2-7), if the bubbles radius increases, the surface tension increases as well. The higher tension created at the interface tries to bring the surface back to a stress-free configuration. The opposite occurs as well. A decrease in the bubble's radius makes the second term in Eq. (2-7) to become negative. The compression generates a stress that tries to bring the radius back to the stress-free value. Due to a discontinuity in $d\sigma/d\,R$ at $R = R_0(1-\sigma_0/E^s)^{1/2}$, the model proposed by Sarkar *et al.* (2009) yields:

$$\dot{R} = -\frac{3H_gD_g}{\left(\frac{D_g}{h_g}+R\right)}\left[\frac{p_{atm}(1-f)+\frac{2\sigma_0}{R}+\frac{2E^s}{R}\left\{\left(\frac{R}{R_0}\right)^2-1\right\}}{3p_{atm}+\frac{4\sigma_0}{R}+\frac{4E^s}{R}\left\{2\left(\frac{R}{R_0}\right)^2-1\right\}}\right], for\ \sigma_0+E^s\left[\left(\frac{R}{R_0}\right)^2-1\right]>0.$$

$$\dot{R} = \frac{-H_gD_g}{\left(\frac{D_g}{h_g}+R\right)}(1-f), \qquad for\ \sigma(R)=0. \tag{2-8}$$

Note that for the case where the gas permeability h_g goes to infinity, and the dilatational surface, E^s, goes to zero, the model becomes the Epstein-Plesset equation, Eq. (2-5).

In summary, the author assumed the surface tension as variable, but the shell resistance was still constant. Their finding shows that the dissolution rate of microbubbles decreases significantly after reaching an equilibrium size. They attribute this behavior to the shell elasticity. With the gas diffusion from the core of the microbubbles, the shell material is compressed, leading to a hardening of the shell, and consequently, to a higher resistance to mass transfer.

More recently, a mathematical model for the microbubble's dissolution time was proposed by Dalvi and Joshi (2015). By using experimental data available in the literature for dissolution in a single-gas medium, they were able to fit their model and estimate shell elasticity and shell resistance. Differing from the before exposed models, the authors considered as variables the shell elasticity, the shell resistance, and surface tension. The surface tension was found to vary linearly with time, while the shell resistance increased linearly with time, for different levels of gas saturation of the medium. The authors attribute this behavior mainly to the elastic nature of the microbubbles shell material.

Table 2.1 from Dalvi and Upadhyay (2018) summarizes the 5 models presented in this chapter, highlighting the differences between them.

Table 2.1: Summary microbubbles dissolution models. Dalvi and Upadhyay (2018).

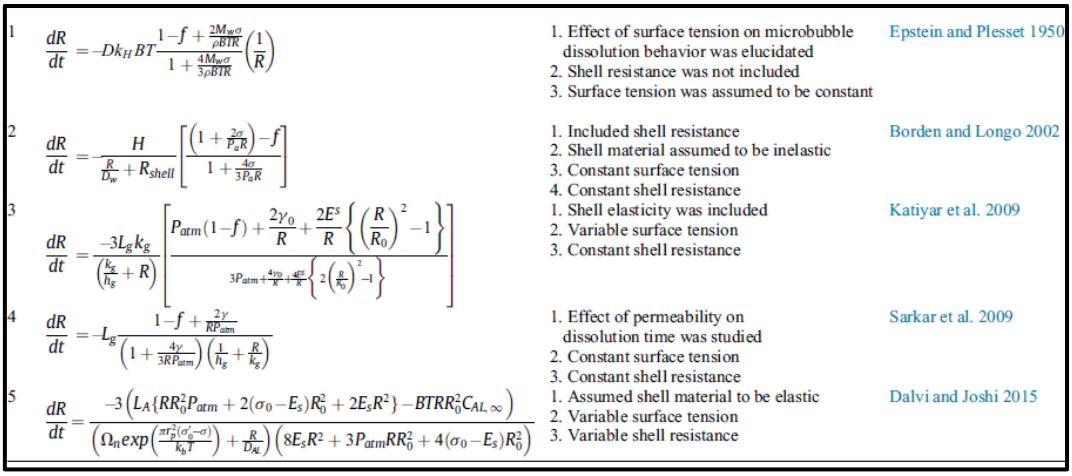

1	$\frac{dR}{dt} = -Dk_H BT \frac{1-f+\frac{2M_w\sigma}{\rho BTR}}{1+\frac{4M_w\sigma}{3\rho BTR}}\left(\frac{1}{R}\right)$	1. Effect of surface tension on microbubble dissolution behavior was elucidated 2. Shell resistance was not included 3. Surface tension was assumed to be constant	Epstein and Plesset 1950
2	$\frac{dR}{dt} = -\frac{H}{\frac{R}{D_w}+R_{shell}}\left[\frac{\left(1+\frac{2\sigma}{P_a R}\right)-f}{1+\frac{4\sigma}{3P_a R}}\right]$	1. Included shell resistance 2. Shell material assumed to be inelastic 3. Constant surface tension 4. Constant shell resistance	Borden and Longo 2002
3	$\frac{dR}{dt} = \frac{-3L_g k_g}{\left(\frac{k_g}{h_g}+R\right)}\left[\frac{P_{atm}(1-f)+\frac{2\gamma_0}{R}+\frac{2E^s}{R}\left\{\left(\frac{R}{R_0}\right)^2-1\right\}}{3P_{atm}+\frac{4\gamma_0}{R}+\frac{4E^s}{R}\left\{2\left(\frac{R}{R_0}\right)^2-1\right\}}\right]$	1. Shell elasticity was included 2. Variable surface tension 3. Constant shell resistance	Katiyar et al. 2009
4	$\frac{dR}{dt} = -L_g \frac{1-f+\frac{2\gamma}{RP_{atm}}}{\left(1+\frac{4\gamma}{3RP_{atm}}\right)\left(\frac{1}{h_g}+\frac{R}{k_g}\right)}$	1. Effect of permeability on dissolution time was studied 2. Constant surface tension 3. Constant shell resistance	Sarkar et al. 2009
5	$\frac{dR}{dt} = \frac{-3\left(L_A\{RR_0^2P_{atm}+2(\sigma_0-E_s)R_0^2+2E_sR^2\}-BTRR_0^2C_{AL,\infty}\right)}{\left(\Omega_n exp\left(\frac{\pi r_p^2(\sigma_0'-\sigma)}{k_bT}\right)+\frac{R}{D_{AL}}\right)\left(8E_sR^2+3P_{atm}RR_0^2+4(\sigma_0-E_s)R_0^2\right)}$	1. Assumed shell material to be elastic 2. Variable surface tension 3. Variable shell resistance	Dalvi and Joshi 2015

2.1.3.2. Microbubble dissolution in a multigas environment

Differently from the aqueous medium described in the chapter before, blood is a medium saturated by multiple gases (mainly O_2, and N_2 with traces of CO_2 and H_2O vapor). Therefore, models considering multiple gas effects over the dissolution time of the bubbles were proposed to more accurately describe the bubble's stability after being intravenously injected.

The model proposed by Epstein-Plesset for the kinetics of the dissolution process of bubbles (Eq. 2-5) can be adapted for the bloodstream as follows:

$$\dot{R} = -D_w H \frac{\bar{p}^* + 2\sigma/\Re}{p_{atm} + 4\sigma/3R}\left\{\frac{1}{R} + \frac{1}{\sqrt{\pi D_w t}}\right\} \tag{2-9}$$

where $\bar{p}^*$ is the excess pressure, which has a contribution from both the systemic blood pressure and the oxygen metabolism.

It is clear to see that bubbles filled with gas with a low Ostwald coefficient will have a lower dissolution rate. However, this feature comes at the expense of lower vapor pressure, which can potentially lead to a condensation of the gas into liquid, and loss of contrast in the ultrasound images.

The ultrasound contrast agents are typically filled by a single gas with a low Ostwald coefficient, which would make the model applicable for the stability prediction of microbubbles suspended in blood. However, when passing through the lungs, the bubbles will experience swelling in air, becoming multicomponent (Burkard and Van Liew, 1994; Van Liew and Burkard, 1995). In this scenario, the theory is not strict due to the big difference in the Ostwald coefficient and diffusivity of the gas in the bubble's core.

In 1998, Kabalnov *et al.* (1998) proposed a model for the dissolution of a microbubble in the bloodstream, where the bubble was assumed to be filled by an osmotic agent and air, characterized by Ostwald coefficients $H_F << H_A$ and water diffusivities D_F and D_A, respectively. The numerical simulation conducted by the authors are presented in the Figure 2.7.

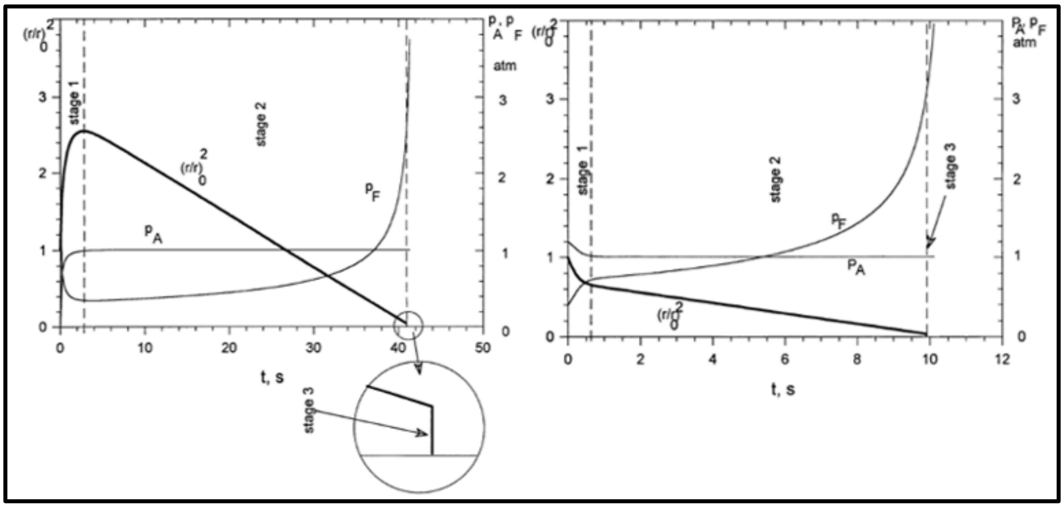

Figure 2.7 – Dissolution of n-C4F10-filled bubble. $\sigma = 70$ mN/m; $\overline{p}^* = 4300\ Par_0 = 2.5\ \mu m$. Left: initial mole fractions, $X_F = 1$; Right $X_F = 0.25$. Kabalnov et al. (1998).

The authors observed three defined stages for the dissolution process of the bubbles. The first stage was characterized by a quick swelling of the bubbles in air. They correlated the swelling ratio to the blood pressure, level of oxygen metabolism, surface tension, and the osmotic agent's initial mole fraction. In stage 2, they observed a slow diffusion of the osmotic agent out of the bubble. It was observed a decrease of the square of the bubble's radius nearly linearly with time, at a rate proportional to the osmotic agent's Ostwald coefficient and diffusivity. In the last stage, an elevation of the partial pressure of the osmotic agent led to its condensation into liquid. They conclude that in order to prolong the life of a 5 µm bubble in the bloodstream, the ideal osmotic gas should have a low Ostwald coefficient and a high saturated vapor pressure at body temperature. The model considered the effects of the Laplace pressure and systemic blood pressure, but the bubble's shell was assumed to be inelastic, with a constant shell resistance.

More recently a model predicting the molar flux of each gas at the bubble-liquid interface in a multigas environment was proposed by Sarkar *et al.,* 2009. The gas diffusion from encapsulated microbubbles was modeled using an explicit linear relation for gas permeation through the shell. The boundary conditions include the shell membrane permeability, yielding that the flux at the liquid side matches the diffusion through the shell. The model considers the diffusion through the membrane as being proportional to the concentration difference across the membrane, where C_w is the gas concentration at the inner wall of the membrane in contact with the gas inside (Figure 2.8),

$$-\mathcal{D}_g \left.\frac{\partial C}{\partial r}\right|_R = h_g[C_w - C(R)] \tag{2-10}$$

where $\mathcal{D}_g$ is the coefficient of diffusivity of the gas through the liquid. The mass flux through the encapsulation is modeled by a coefficient h_g which can be thought of as $h_g \cong \mathcal{D}_g^e/\delta$, where $\mathcal{D}_g^e$ is the diffusivity of the gas through the encapsulation and δ, the thickness of encapsulation.

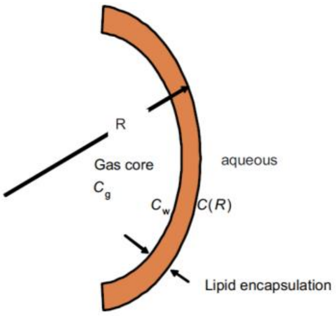

Figure 2.8 – Schematic for an encapsulated microbubble (Sakar et al., 2009).

These equations were coupled with a mole balance over the microbubble to obtain a model equation for a change in microbubble size.

Sarkar *et al.* (2009) numerically simulated the dissolution time of encapsulated 2.5 µm diameter bubble filled by Octafluoropropane (OFP) in air-saturated medium (Figure 2.9).

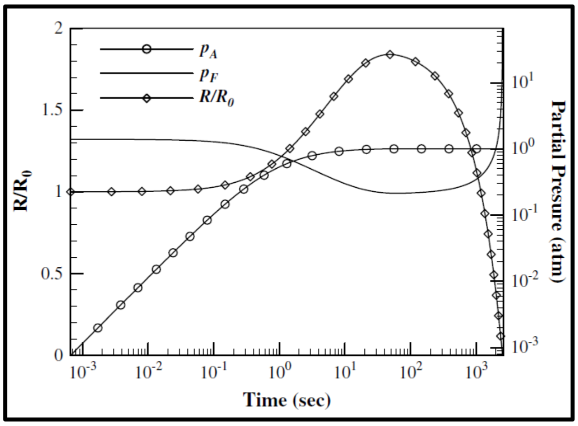

Figure 2.9 – Dissolution of an encapsulated 2.5 µm OFP bubble in an air-saturated medium (Sarkar et al., 2009).

By comparing the dissolution time presented in the study made by Kabalnov *et al.* (1998b) and Sarkar *et al.* (2009), it was possible to observe a lifetime 60 times longer for the encapsulated bubble, despite the OFP-filled bubble having half the size and a perfluorocarbon with smaller chain.

The authors found, in agreement with previous studies, that a perfluorocarbon-filled contrast microbubble experiences a transient growth due to air infusion before dissolving. However, the growth phase will only occur for bubbles containing a critical value of the initial mole fraction of the osmotic gas relative to air. They also investigated the diffusion time of bubbles filled by perfluorocarbon (PFC) and sulfur hexafluoride (SF_6). The results showed that PFC (a gas with larger molecules), had a lower solubility and diffusivity, and therefore a longer dissolution time in comparison with SF_6. Also, an increase in the number of carbon molecules in the PFC gases resulted in a significant increase in the dissolution time (Figure 2.10).

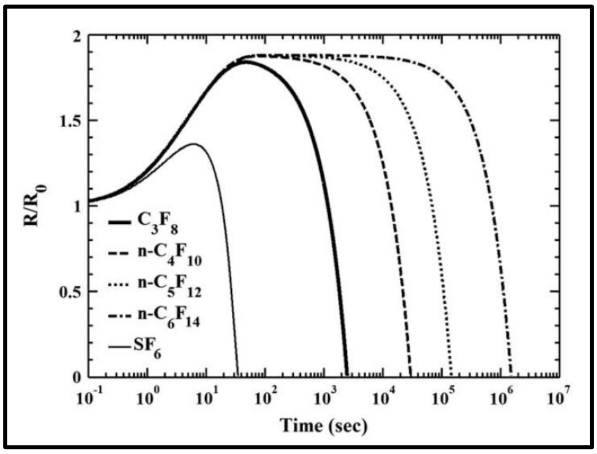

Figure 2.10 – Variation of R/R_0 with time for an encapsulated 2.5-micron-diameter bubble with different gas content in an air-saturated medium (Sarkar et al., 2009).

The proposed model also considered an inelastic shell material, with constant surface tension and shell resistance through the whole dissolution process.

In the same year, Katiyar *et al.* (2009) modified their earlier model by considering the shell elasticity (E_s), as already mentioned in the previous chapter (Eq. 2-7 and 2-8)

However, for the case of a multigas environment, where two gases (A – air, and F – perfluorocarbon) were studied, the authors considered the pressure balance across the gas-liquid interface to be:

$$p_A + p_F = (C_A + C_F)\Re T = p_{atm} + \frac{2\sigma(R)}{R} \qquad (2\text{-}11)$$

Yielding the following equation for the bubble's radius variation over time:

$$\dot{R} = \frac{\Re T}{R^2\left(3\,p_{atm}+\frac{4\sigma}{R}+2\frac{d\sigma}{dR}\right)}\left[\frac{d(R^3C_A)}{dt}+\frac{d(R^3C_F)}{dt}\right] \tag{2-12}$$

Therefore, Katiyar *et al.* (2009) estimated the variation of the perfluorocarbon-filled microbubbles radius as a function of time for a saturated liquid medium ($f = 1$) using the relation E_s/σ_0 equals to 1.6 and 0.4, as shown in Figure 2.11.

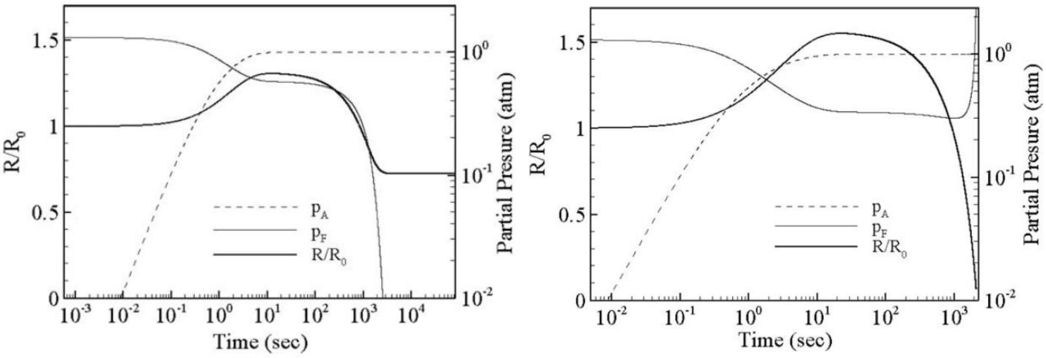

(a) E_s/σ_0=1.6 (b) E_s/σ_0=0.4

Figure 2.11 – Radius evolution of an encapsulated PFC bubble of 2.5 µm diameter in an air-saturated medium ($f = 1$) (Katiyar et al., 2009).

For cases where the relation $E_s/\sigma_0 > 1$, the bubbles are expected to reach a stable size in the long-time limit. As observed before, initially the bubble will experience a rapid swelling due to air diffusion into the bubble, until the air partial pressure equilibrates with the medium. Afterward, the osmotic gas diffusion controls the bubble behavior, and the bubble radius reduces. The radius reduction below the stress-free configuration will generate an elastic stress that counterbalances the surface tension, leading to an equilibrium radius which is 61% of R_0. It took approximately 3000 s for the bubble to reach this state for the $E_s/\sigma_0 = 1.6$ case. After reaching the stable state, the osmotic gas has dissipated completely, making the bubble to be only air-filled.

For the $E_s/\sigma_0 = 0.4$ configuration, the bubble behaves similarly to the previous case, where a quick growth due to air intake occurs. However, the bubble dissolves due to the outward diffusion of both air and the osmotic gas in approximately 1000 s. It was also observed a sharp pressure increase of the osmotic gas inside the bubble despite the reduction in the osmotic gas content.

As expected, the cases of low elasticity ($E_s/\sigma_0 < 1$) resulted in bubble dissolution, and the case of high elasticity (E_s/σ_0 >1) resulted in a stable radius for the bubble. Despite considering the shell material to be elastic, and hence, the surface tension as variable, the model proposed by Katiyar *et al.* (2009) assumed the shell resistance to be constant throughout the whole dissolution of the microbubbles. Also, their study was not compared to experimental data for microbubble dissolution.

Kwan and Borden (2010a, 2010b) proposed a model for microbubble dissolution in a multigas environment. They considered air as being a mixture of two gases (N_2 and O_2). The change in the microbubble radius was estimated through a material balance over the entire bubble. By assuming the gases inside the bubble were ideal, and considering the shell material to be inelastic, they obtained the following equation for bubble dissolution over time:

$$\frac{dn_i}{dt} = -4\pi R \mathcal{D}_i K_{H,i} \left(\frac{2\sigma}{R} - p_{\infty,i} f_i + p_H - \frac{3\Re T}{4\pi R^3} \sum_{j=1}^{N} n_j\right), \text{where } j \neq i. \qquad (2\text{-}13)$$

where n_i is the moles of the gas i, t is time, R is the microbubbles radius, $\mathcal{D}$ is the diffusivity, K_H is molar Henry's constant (correlates partial pressure to gas concentration), σ is the surface tension, p_∞ is the saturation pressure far from the bubble, f is the saturation fraction, p_H is the hydrostatic pressure, $\Re$ is the ideal gas constant, and T is the temperature.

Applying the ideal gas law to the microbubbles pressure given by Laplace's equation, yields:

$$0 = 2\sigma R^2 + p_H R^3 - \frac{3\,\Re\,T}{4\pi} \sum_{i=1}^{N} n_i \qquad (2\text{-}14)$$

Equations (2-13) and (2-14) were used by the authors to construct the numerical model, which can be solved by N number of gases. For the case where only one gas is taken into consideration, the model reduces to the before-mentioned single-gas Epstein-Plesset model, Eq. (2-5).

With a microscope, Kwan and Borden (2010a, 2010b) experimentally investigated the dissolution process for SF_6-filled microbubbles, coated by sodium dodecyl sulfate (SDS) in an air-saturated medium. The experimental dissolution data was compared to the predicted values obtained by the before-mentioned model for the same conditions. The dissolution time comparison resulted in a correction factor of 1.5, which was applied in order to consider the increase in the solubility of gases in the aqueous solution when exposed to SDS.

In agreement with previous studies, and their model's prediction, Kwan and Borden (2010a, 2010b) observed an initial growth phase as a result of the inflow of O_2 and N_2 (Figure 2.12). They observed a higher initial influx of N_2 than O_2 due to the higher N_2 concentration dissolved in water. Both gases contributed to diluting the SF_6, reducing the concentration gradient, and thus the bubble's dissolution rate. The initial bubble growth plays a role in reducing the Laplace pressure, due to the inverse proportionality of the pressure with the bubble's radius. The combination of these two phenomena resulted in a reduction in the outward flux of the SF_6 with time. When the bubble is completely depleted of the SF_6, it becomes an air-filled microbubble, as predicted by Sarkar *et al.* (2009). At this stage, the microbubble's diameter as a function of time curve follows the quasi-single gas model proposed by Epstein-Plesset. The gas core of the microbubble is exchanged within seconds after immersion, indicating that the concept of osmotic gas used as O_2 substitute may only be appropriate when the bubbles are initially submerged. The author's observed a maximum growth velocity of 1.7µm/s, which is several orders of magnitude slower than the diffusion velocity of a single SF_6 molecule (approximately 560µm/s assuming random walk diffusive velocity dynamics). Therefore, the assumption of a fully developed diffusion profile (quasi-static) surrounding the microbubbles during growth and dissolution was valid.

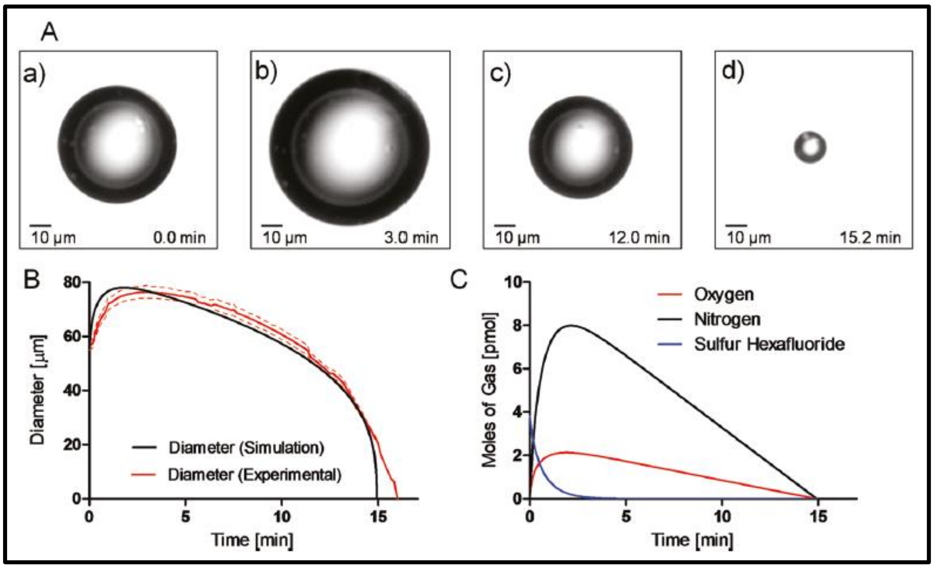

Figure 2.12 – Dissolution and growth of a SF_6-filled SDS-coated microbubbles after being exposed to an air-saturated environment. (A) Microscopy images of the bubbles growth and dissolution. (B) Experimental and theoretical diameter as function of time curves. (C) Predicted gas content inside the microbubble. Kwan and Borden (2010).

Kwan and Borden (2010a, 2010b) proceeded to run the same experience, but for a lipid-coated SF_6-filled microbubble in the air-saturated medium. They observed a shorter growth period in comparison to the previous case. They attributed the resistance to expansion to a large dynamic surface tension, which they further made as a fitting parameter of their model. Figure 2.13 shows the effective surface tension of the lipid-coated microbubble as a function of time, as the fitted diameter-time curve. A 7-fold larger effective surface tension in comparison to an air-water interface was found. This behavior was credited to the break-up tension, which is a tension that resists the lipid monolayer expansion from its fully condensate state. This mechanism was first proposed and studied by Marmottant *et al.* (2005), where the break-up was modeled by critical shell-tension above which gas is directly exposed to water. Despite the model proposed by Kwan and Borden (2010) assuming a varying surface tension, the shell resistance is considered constant.

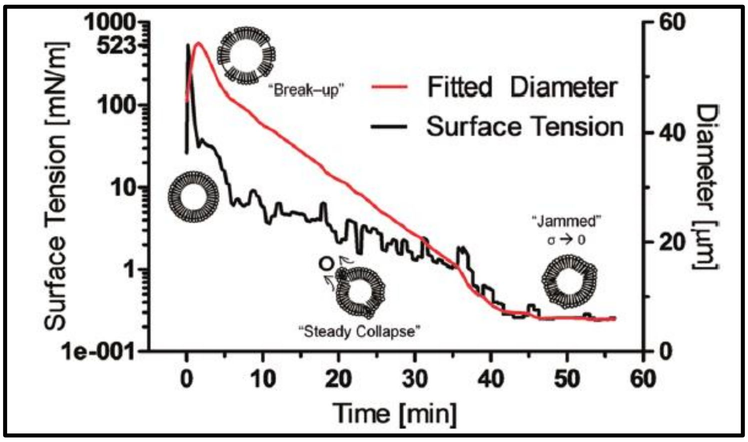

Figure 2.13 – Effective surface tension of lipid-coated microbubbles shown in Figure 2.3. The schematic drawings aim to illustrate the behavior of the lipid monolayer shell (Kwan and Borden 2010).

Later, in 2015, a mathematical model for microbubble dissolution in a multigas saturated aqueous medium, that considered the effect of shell resistance, shell elasticity, and surface tension was proposed by Dalvi and Joshi (2015). Their work also aimed to address the lack of accuracy and availability of shell parameter values in the literature, which were often assumed arbitrarily for estimation of the microbubble's dissolution kinetics.

The authors start with simplifying assumptions for the model. First, they considered that there is no convection in the microbubble's storage or aqueous medium. They assumed that the microbubble's shell is fully hydrated, allowing the gas solubility of the shell to be calculated through Herny's Law/Ostwald ripening coefficient. The gas inside the microbubble was considered an ideal gas. And, finally, they considered that the liquid phase controls the microbubbles dissolution process.

Figure 2.14 shows a schematic drawing of a microbubble and the concentration profiles inside and in the close vicinity of a microbubble, dissolving in a medium saturated by multiple gases. The tow-way mass transfer approach considers a microbubble comprising of gas A (e.g., SF_6) exposed to an aqueous medium saturated by a gas B (e.g. air, (N_2 and O_2)).

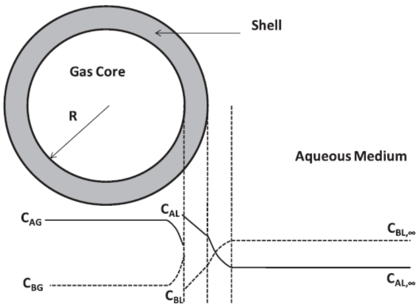

Figure 2.14 – Schematic drawing of a microbubble dissolving in a multigas environment (Dalvi and Joshi, 2015).

Dalvi and Joshi fitted a polynomial trend line to the experimental data for microbubble dissolution that was available in the literature. Afterward, they differentiate the polynomial equation with respect to time to obtain the radius-time relation. In order to estimates the values of shell elasticity (E_s), shell resistance (Ω_S), and surface tension, the differential equations were calculated at $t = 0$, $t = t$, and $t = t_{diss}$, resulting in the following non-linear equations:

At $t = t_{diss}, R = 0$, hence,

$$\dot{R} = \frac{-3H_A}{2\Omega_n \exp\left(\frac{\pi r_p^2 E_s}{k_b T}\right)}$$

At $t = 0, R = R_0$, hence,

$$\dot{R} = \frac{-3(H_A\{R_0^3 p_{atm} + 2(\sigma_0 - E_s)R_0^2 + 2E_s R_0^2\} - \Re T R_0^3 C_{AL,\infty})}{\left(\Omega_n + \frac{R_0}{\mathcal{D}_{AL}}\right)(3p_{atm}R_0^3 + 4(\sigma_0 - E_s)R_0^2 + 8E_s R_0^2)}$$

At $t = t, R = R$, hence

$$\dot{R} = \frac{-3(H_A\{RR_0^3 p_{atm} + 2(\sigma_0 - E_s)R_0^2 + 2E_s R^2\} - \Re T R R_0^2 C_{AL,\infty})}{\left(\Omega_n \exp\left(\frac{\pi r_p^2(\sigma_0' - \sigma)}{k_b T}\right) + \frac{R}{\mathcal{D}_{AL}}\right)(3p_{atm}RR_0^2 + 4(\sigma_0 - E_s)R_0^2 + 8E_s R^2)}$$

(2-15)

The above-mentioned equations were solved simultaneously and the values of the elasticity of the shell material, E_s, the mass transfer resistance to gas pre-exponential factor, Ω_n, and the surface tension in the gas-liquid interface, σ_0 were estimated. The Ω_n originates from an estimate using energy barrier model for the mass transfer resistance to gas A through a microbubble shell, $\Omega_{s,A}$.

$$\Omega_{s,A} = \Omega_n \exp\left(\frac{\pi r_p^2(\sigma_0' - \sigma)}{k_b T}\right) \tag{2-16}$$

where k_b is the Boltzmann constant, T is the absolute temperature and r_p is the radius of the transferring species, σ_0' is the surface tension at the bare gas–liquid interface.

They observed inconsistency between the values obtained in the literature in comparison with their model, for shell resistance values. The disparity in the values was attributed to the fact that the values in the literature were estimated without including shell elasticity or shell resistance variation over time.

Through the use of the estimated values, they found a better fitting between the theoretical and experimental calculations, yielding R^2 values ranging from 0.94 to 0.98 for the dissolution kinetic of the system in their study (Figure 2.15).

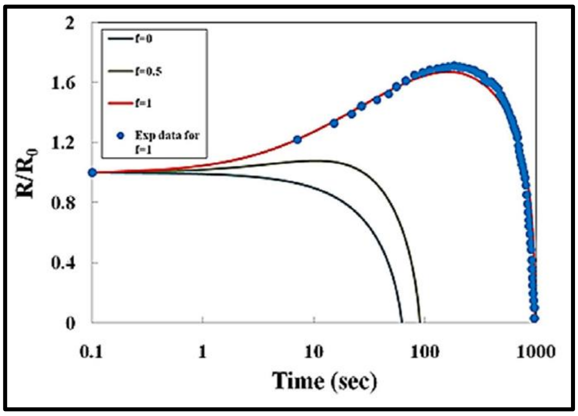

Figure 2.15 – Numerical prediction of the variation $R/R_0$for dissolution of SDS-coated SF6 microbubbles in water saturated with air, for different levels of saturation. Dalvi and Josh (2015).

For a one-way mass transfer scenario, where the aqueous medium is saturated by the same gas inside the bubble, their model predicted a decrease almost linear for the surface tension as a function of time, and an increase almost linear for the shell resistance (Figure 2.16). During the microbubble dissolution, the shell material molecules get close, becoming fully compressed, which leads to an increase in the shell rigidity. This behavior results in a decrease in surface tension. However, the compression also reduces the pore sizes in the bubble shell, yielding an increase in shell resistance to mass transfer.

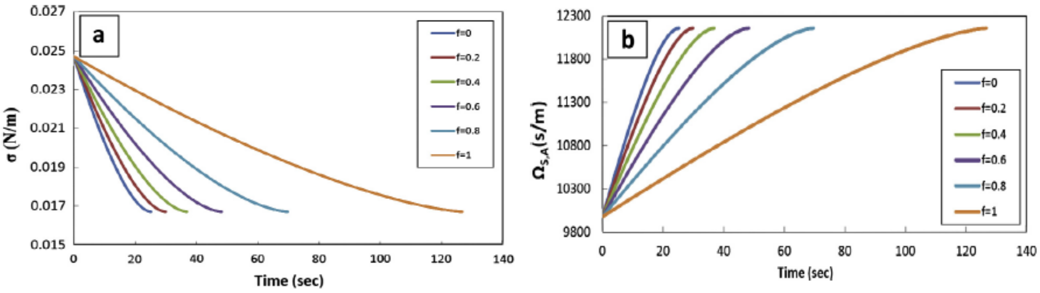

Figure 2.16 – Time evolution of one-way transfer Variation in (a) surface tension and (b) shell resistance at different saturated conditions. Dalvi and Josh (2015).

However, for the two-way mass transfer case, where the gas inside the bubble is different from the gas saturating the aqueous medium (Figure 2.17), the surface tension at the gas-liquid interface presents a maximum value. Contrarily, the shell resistance to the mass transfer of SF_6 and air shows a minimum during the dissolution process. During the growth stage, the molecules of the shell material move away from each other, becoming decompressed, and therefore, reducing the rigidity of the shell. This reduction leads to a decrease in the interaction between the molecules of the shell, resulting in an increase in surface tension. On the other hand, during the shrinking stage, as the bubble get dissolved, the molecules get compressed, repeating the behavior above mentioned for one-way mass transfer, leading to a decrease in surface tension with time. The shell resistance presents the exactly opposite behavior than the surface tension during the growth and shrinking stages. Growth leads to bigger gaps between shell molecules, leading to increasing gas permeability through the shell. When shrinking, the molecules present a tighter packing, which reduces the defect in the shell structure, yielding a higher gas diffusion restriction through the shell.

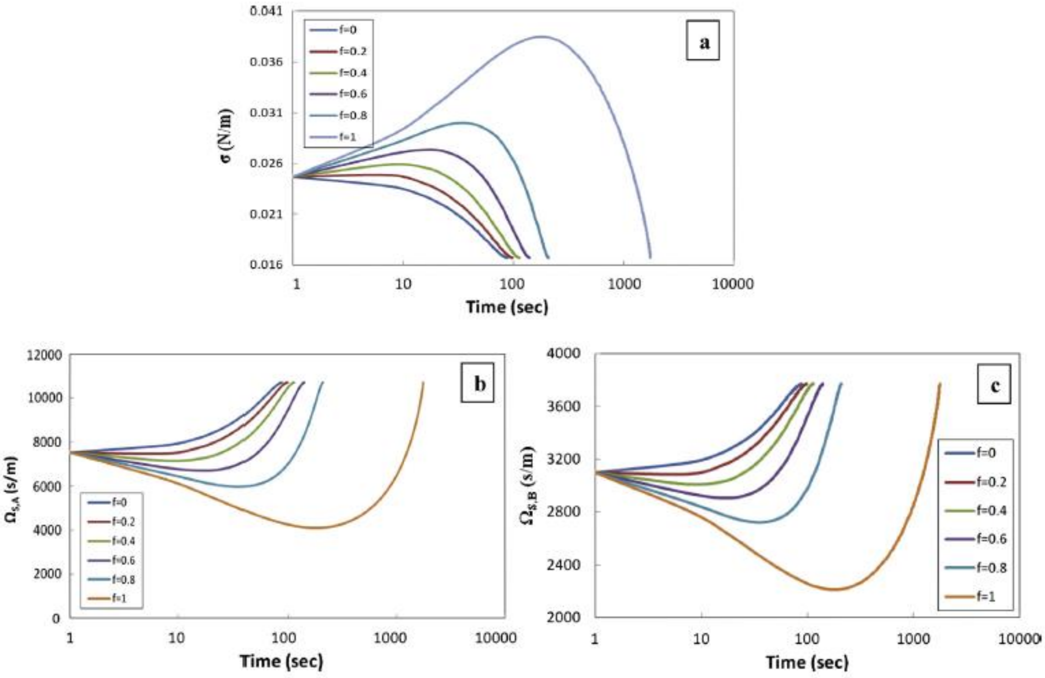

Figure 2.17 – Two-way mass transfer time evolution. (a)Variation of the surface tension, and (b and c) variation in the shell resistance for SF6 and air at different saturation conditions. Dalvi and Josh (2015).

The authors also compared the shell elasticity of lipid and SDS, finding that the SDS shell has an elasticity at least by 2 orders of magnitude lower than the lipids (Di12 PC to Di22 PC). They observed that shell elasticity was the most influential parameter in the model. Lower values resulted in negligible variations of both surface tension and shell resistance (observed in the SDS case), whereas higher shell elasticity led to larger variations in surface tension and shell resistance during bubble dissolution. The results presented by Dalvi and Joshi (2015) were in contrast with previous studies in the literature (Farook *et al.*, 2009; Feshitan *et al.* 2009; Lee *et al.* 2015; Stride and Edirisinghe, 2008), where they considered the shell properties to be constant or negligible, and therefore, their contribution in the model for microbubble dissolution/stability was neglected.

Table 2.2 from Dalvi and Upadhyay (2018), summarizes the 5 models presented in this chapter, highlighting the difference between them.

Table 2.2: Summary microbubbles dissolution models for multigas saturated aqueous medium. Dalvi and Upadhyay (2018)

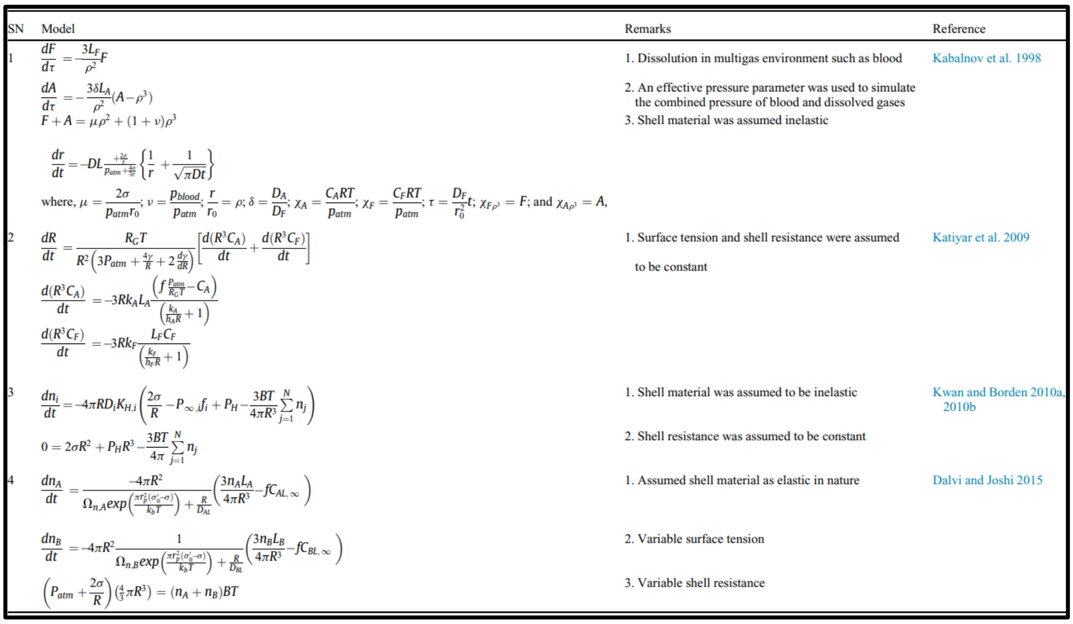

SN	Model	Remarks	Reference
1	$\frac{dF}{d\tau} = -\frac{3L_F}{\rho^2}F$ $\frac{dA}{d\tau} = -\frac{3\delta L_A}{\rho^2}(A-\rho^3)$ $F + A = \mu\rho^2 + (1+\nu)\rho^3$ $\frac{dr}{dt} = -DL\frac{+\frac{2\sigma}{r}}{p_{atm}+\frac{4\sigma}{3r}}\left\{\frac{1}{r} + \frac{1}{\sqrt{\pi D t}}\right\}$ where, $\mu = \frac{2\sigma}{p_{atm}r_0}$; $\nu = \frac{p_{blood}}{p_{atm}}$; $\frac{r}{r_0} = \rho$; $\delta = \frac{D_A}{D_F}$; $\chi_A = \frac{C_A RT}{p_{atm}}$; $\chi_F = \frac{C_F RT}{p_{atm}}$; $\tau = \frac{D_F}{r_0^2}t$; $\chi_{F\rho^3} = F$; and $\chi_{A\rho^3} = A$,	1. Dissolution in multigas environment such as blood 2. An effective pressure parameter was used to simulate the combined pressure of blood and dissolved gases 3. Shell material was assumed inelastic	Kabalnov et al. 1998
2	$\frac{dR}{dt} = \frac{R_G T}{R^2\left(3P_{atm} + \frac{4\gamma}{R} + 2\frac{d\gamma}{dR}\right)}\left[\frac{d(R^3C_A)}{dt} + \frac{d(R^3C_F)}{dt}\right]$ $\frac{d(R^3C_A)}{dt} = -3Rk_A L_A\frac{\left(f\frac{P_{atm}}{R_G T} - C_A\right)}{\left(\frac{k_A}{h_A R} + 1\right)}$ $\frac{d(R^3C_F)}{dt} = -3Rk_F\frac{L_F C_F}{\left(\frac{k_F}{h_F R} + 1\right)}$	1. Surface tension and shell resistance were assumed to be constant	Katiyar et al. 2009
3	$\frac{dn_i}{dt} = -4\pi R D_i K_{H,i}\left(\frac{2\sigma}{R} - P_{\infty,i}f_i + P_H - \frac{3BT}{4\pi R^3}\sum_{j=1}^{N} n_j\right)$ $0 = 2\sigma R^2 + P_H R^3 - \frac{3BT}{4\pi}\sum_{j=1}^{N} n_j$	1. Shell material was assumed to be inelastic 2. Shell resistance was assumed to be constant	Kwan and Borden 2010a, 2010b
4	$\frac{dn_A}{dt} = \frac{-4\pi R^2}{\Omega_{n,A}exp\left(\frac{\pi r_p^2(\sigma_0' - \sigma)}{k_b T}\right) + \frac{R}{D_{AL}}}\left(\frac{3n_A L_A}{4\pi R^3} - fC_{AL,\infty}\right)$ $\frac{dn_B}{dt} = -4\pi R^2\frac{1}{\Omega_{n,B}exp\left(\frac{\pi r_p^2(\sigma_0' - \sigma)}{k_b T}\right) + \frac{R}{D_{BL}}}\left(\frac{3n_B L_B}{4\pi R^3} - fC_{BL,\infty}\right)$ $\left(P_{atm} + \frac{2\sigma}{R}\right)\left(\frac{4}{3}\pi R^3\right) = (n_A + n_B)BT$	1. Assumed shell material as elastic in nature 2. Variable surface tension 3. Variable shell resistance	Dalvi and Joshi 2015

2.1.3.3. Model for estimation of the shelf life of microbubble

The capacity of a microbubble suspension to be stable over a long period of time is key for medical application. The microbubble must sustain its concentration (number of bubbles per volume of solution), and size distribution during the period of storage. Therefore, models to predict the microbubbles' suspension stability storage in an aqueous medium were proposed.

Lemlinch (1978) presented a model describing the change in the bubble size distribution as a result of the diffusion of gas between bubbles of liquid foam. The author first states that the gas diffuses to the liquid medium before entering another bubble. From Henry's Law, he correlates the concentration of the gas dissolved in the liquid to the gas pressure in the liquid. Using Laplace's equation, this equivalent pressure can be viewed as a fictitious spherical bubble of radius r. By combining Laplace's equation, with a molar balance over the bubble, the author derives the following equation:

$$\dot{R} = \frac{2J\sigma\,\Re\,T}{p_a}\left(\frac{1}{r_{21}} - \frac{1}{r}\right) \tag{2-17}$$

where J is the effective permeability, and r_{21} is a critical radius value. Equation (2-17) basically shows that bubbles with a radius greater r_{21} will grow and bubbles with $r < r_{21}$ will shrink.

Lemlinch (1978) then estimates the size distribution of the bubble population at various times, based on the number of bubbles present at t=0, and based on the number of bubbles in each time (Figure 2.18). However, he did not consider the effects of shell elasticity, the shell resistance to mass transfer, the variation in the shell resistance, or the variation of the surface tension during the dissolution process of the microbubbles.

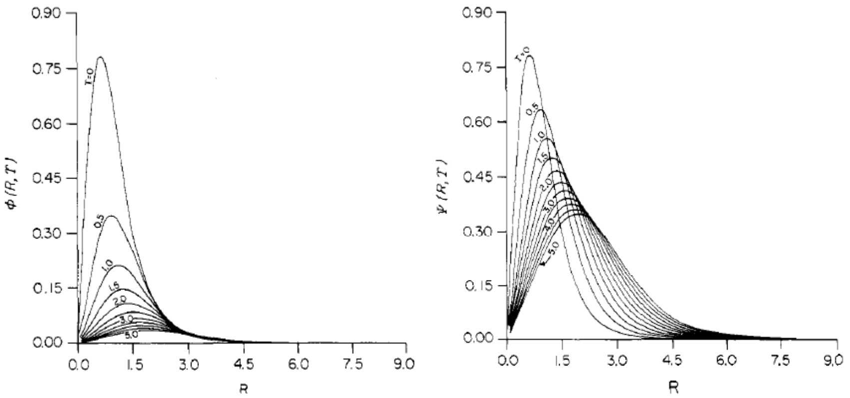

Figure 2.18 – Distribution of dimensionless radii of bubbles at various successive dimensionless times, based on the number of bubbles presents at (a) zero time, and (b) each dimensionless time. Lemlinch (1978).

Later on, Sridhar *et al.* (2015) proposed a model for the microbubble suspension stability during storage in an aqueous medium. They based their model on the work made by Lemlinch (1978), however, they considered the effects of shell elasticity, shell resistance, solution viscosity, surface tension, and the initial microbubbles size distribution. The model aimed to estimate the half-life of the microbubble population, in other words, the time that would take for the suspension to have half the initial number of bubbles,

$$\dot{R} = \frac{6\,R_0\,h_A\,\mathcal{D}_{AL}\left[(\sigma_0 - E_S)\left[\frac{1}{R_C} - \frac{1}{R}\right] + \frac{E_S(R_C - R)}{R_0^2}\right]}{H_A[Rh_A + \mathcal{D}_{AL}]\left[8\,E_S\,R^2 + 3\,R_0^2\,p_{atm}\,R + 4(\sigma_0 - E_S)R_0^2\right]} \tag{2-18}$$

where R_c is the critical size of the bubble suspension, which was called r_{21} in the Lemlinch (1978) work.

Sridhar *et al.* (2015) estimated the variation of the microbubble's size distribution as a function of time in an aqueous suspension (Figure 2.19). They observed that the shell resistance was the parameter that most influences the storage stability of the microbubbles. An increase of these variable values resulted in a larger half-life of the microbubbles population. Also, as expected, low values of surface tension were also found to enhance the bubble's stability. The parameter that had the least effect on the microbubble's population was the elasticity of the shell material. In addition, the authors estimated the effect of gas in the bubble's core on the microbubble's stability. They observed, in agreement with the literature, that gas with low liquid-phase diffusivity and low Ostwald Coefficient are prone to enhance the stability of a microbubble suspension.

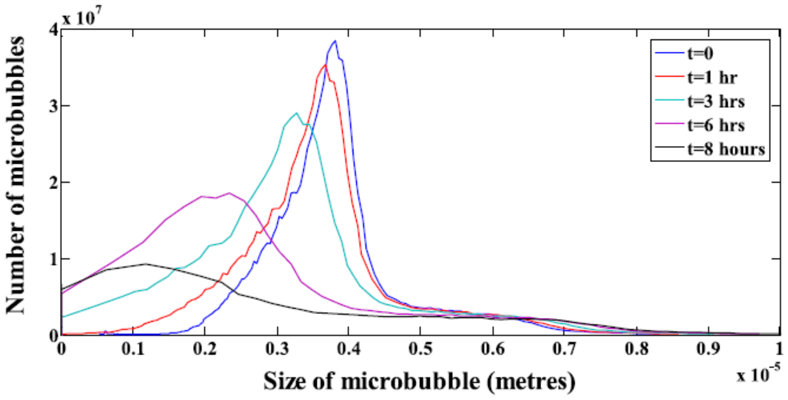

Figure 2.19 –Variation in size distribution as function of time for O2-filled microbubbles for $\sigma_0 = 0.02\ N/m$, $E_s = 0.001\ N/m$, and $\Omega_n = 107\ s/m$ (Sridhar et al. 2016).

Their model could be further modified in order to include the effects of saturating the aqueous medium where the bubbles will be stored by the same gas in the bubble core. In summary, the model proposed by Sridhar *et al.* (2015) can be a useful tool to design the microbubbles suspension to obtain optimal stability.

2.1.4. Importance of modeling microbubble behavior

As already stated, the stability of microbubble's population over time is of major importance to the medical community. The usefulness of microbubbles for different applications is imposed by the *in vivo* and shelf stabilities. Most of the mechanisms that affect the bubble stability (coalescence, Ostwald ripening; diffusion of core gas, etc.) are significantly affected by the core gas, the aqueous medium, and the properties of the material that composes the shell. Thus, mathematically modeling the effect of the different parameters in the bubble stability is of great importance. By simulating the different contributions, one can better understand the physical phenomena and, therefore, can directly improve the design of the microbubble's formulation.

The models available in the literature, and presented here, are mainly a variation of the Epstein-Plesset model, but they achieved a degree of complexity that many of the important parameters for the bubble dissolution process are considered, namely shell resistance, surface tension, and shell elasticity. Also, more sophisticated models accounting for the variation in the surface tension and shell resistance due to the changes in the bubble's size, and arrangement of shell molecules at the gas-liquid interface, were proposed with success. However, the models presented were only validated for microbubbles comprising of lipid shells. Hence, the importance of expanding the research to include different shell materials such as polymers or proteins.

The models presented are also limited because they consider a single microbubble dissolving in an infinity medium. We know that, in reality, the microbubbles will experience dissolution in the vicinity of multiple microbubbles, which will affect the mass transfer process.

The models presented in the previous subsection tried to access and model this condition to a certain degree, but improvements are still necessary in order to correctly consider the exact effect of a large number of microbubbles dissolving together.

Finally, convection effects induced by the bubbles flow (in the bloodstream for example), need to be considered in future models, so we could have a more complete understanding of microbubbles dissolution when injected into the body.

2.2. Monodisperse microbubbles with microfluidics

Microfluidics can be defined as the science that studies fluids that are geometrically constrained to small scales (sub-millimeter), where surface forces dominate over volumetric ones. This technological field offers the possibility of integrating multidisciplinary systems and performing separations and detections with high resolution and sensitivity, besides favoring the use of a reduced number of samples and reagents and allowing the reduction of experimental analysis time (Convery and Gadegaard, 2019; Ma *et al.*, 2017; Squires and Quake, 2005; Whitesides, 2006).

Microfluidic systems are characterized by particular hydrodynamic properties, such as laminar flow. This feature allows greater predictability and control over spatial-temporal fluid dynamics (Qian *et al.*, 2019; Sackmann, Fulton and Beebe, 2014), and molecular transport. In addition, the surface area/volume ratio, many times higher than in other conventional systems, makes it possible to reduce the resistances involved in mass and energy transfer in microfluidic processes (Convery and Gadegaard, 2019; Lee *et al.*, 2011).

This chapter aims to describe the fundamentals of flows at microscale, and to present the physics behind monodisperse microbubble production through the use of flow-focusing devices.

2.2.1. Fundamentals of micro-scale flows

In order to understand the microfluidics systems and their applications and possibilities, it is important to comprehend the physics that govern these microscale systems. One of the main effects of scaling down the geometry of the fluidic system is that the viscous forces will dominate over the inertial forces. The dimensionless Reynolds number (Re) is one of the most important parameters in fluid mechanics, which is given by:

$$Re = \rho VD/\mu \tag{2-19}$$

where ρ is the density of the fluid, V is the velocity, D is a characteristic dimension of the system, and μ is the dynamic viscosity. The Reynolds number is often described as the ratio between the inertial forces and viscous forces. It is possible to see that a decrease in the dimensions of the systems results in a smaller Re. Usually, in systems with Re values smaller than 2000, the flow behaves in a very orderly manner characterized by high momentum diffusion and low momentum convection. This regime is called the laminar flow regime, and it is distinguished by a highly predictable flow pattern and predictable kinetics of molecular transport. Most of microfluidics systems are characterized by small Re numbers, and therefore, they are always in the laminar flow regime. Another important parameter that provides information of the mass transport to the system is the dimensionless Peclet Number, which is defined as:

$$Pe = V\,D/\mathcal{D} \tag{2-20}$$

where $\mathcal{D}$ is the coefficient of diffusion, V is the velocity and D is a characteristic dimension of the system. In the mass transfer context, Pe is defined as the ratio between advective and diffusive transport of molecules in a fluid. Therefore, the reduction in the system dimension results in a smaller Pe number, which shows the dominance of diffusion over advection in the microfluidic system, yielding a more predictable mixing process.

Another very important parameter in microfluidic systems is the capillary number (Ca), which describes the relative effect of viscous forces over surface tension (or interfacial tension) forces acting across an interface liquid-gas or immiscible liquid-liquid.

$$Ca = \mu V/\sigma \tag{2-21}$$

where σ is the surface or interfacial tension between the two fluid phases. Surface tension describes the tendency of a fluid to modify the surface-gas interface by reducing the free energy, while interfacial tension is the same phenomenon, but applied for immiscible fluids (such as water and oil, for example) (Convery and Gadegaard, 2019; Sackmann, Fulton and Beebe, 2014). Microfluidics systems are often characterized by low Ca, which indicates that capillary forces dominate gravitational forces at the microscale (Tabeling, 2009). Capillarity is a surface tension phenomenon defined as the force that promotes the movement of a fluid through porous media or narrow capillaries, allowing fluid to rise in the direction opposite to gravity (Convery and Gadegaard, 2019; Squires and Quake, 2005). Thus, low values of Ca result in spherical droplets due to the greater influence of surface or interfacial tension (Oliveira *et al.*, 2016). These unique hydrodynamic properties allow microfluidic platforms to be employed in different research fields in order to streamline complex experimental protocols, significantly reduce the volume of investigated samples, reduce the cost with reagents and offer benefits in the development of diagnostics and new research tools (Gale *et al.*, 2018; Sackmann, Fulton and Beebe, 2014; Zhang, Zhu, and Shen, 2018).

Advances in microfabrication allow such systems to be produced with different materials and specific geometries for application in several areas. For biological applications, the materials used in microfluidics must have characteristics such as biocompatibility, chemical, and physical stability, and low toxicity. Among them, we highlight glass and some polymers, such as polydimethylsiloxane (PDMS) and polymethylmethacrylate (PMMA), which are widely used for the manufacture of microdevices, besides having transparency, which facilitates monitoring by microscopy. Microfabrication techniques include, among others, printing and hot stamping, photolithography, laser ablation, and X-ray lithography, commonly applied in the fabrication of microchannels in microdevices constructed with PDMS (Convery and Gadegaard, 2019; Gale *et al.*, 2018).

The flexibility to manipulate different materials for specific applications has made microfluidic devices important tools for the areas of nanomedicine and biotechnology, from the development of micro-bioreactors and separation processes to obtaining particles for therapeutic purposes (Björnmalm, Yan and Caruso, 2014; Zhang, Zhu, and Shen, 2018).

2.2.2. Microfluidic Monodisperse microbubble formation

This chapter aims to describe the controlled formation of microbubbles in a microfluidic flow-focusing device having a typical dimension of channels on the order of tens to hundreds of micrometers. The description is related to flows in planar geometries characterized by low values of Reynolds and Capillary numbers (Whiteside, 2005).

A schematic illustration of a typical flow-focusing system used by (Whiteside, 2005) in their studies is presented in Figure 2.20. The channels were fabricated by soft-lithography, and they were characterized by a height h, which is smaller in comparison with the lateral dimension of the channels (width and length). Typically, h values are smaller than 30µm, while width ranges from tens to hundreds of micrometers, and length ranges from hundreds of micrometers to a few millimeters. In order to sustain a stable production, the continuous phase must wet the channel's walls to ensure an ordered flow pattern. Therefore, the walls of the microfluidic device must be hydrophilic.

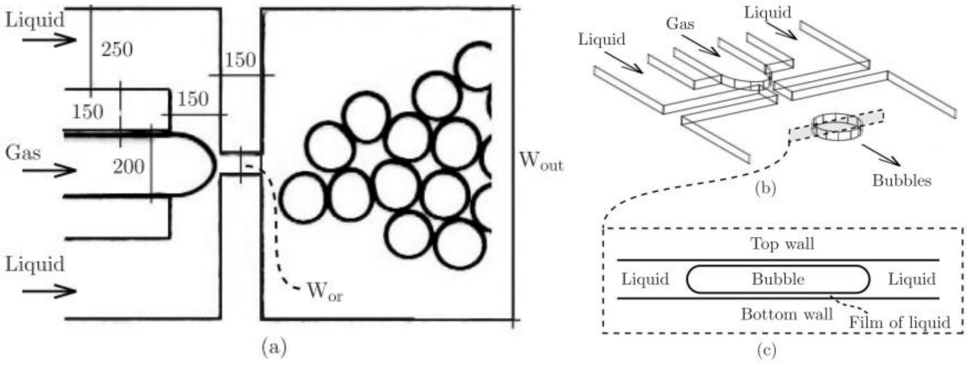

Figure 2.20 – Schematic drawing of the flow-focusing device used by (Whiteside, 2005). (a) The dimensions in the plane of the device; (b) Shows the aspect ratio of the height of the device to the widths of the various channels; (c) The walls of the device have to be preferentially wetted by the continuous. The gas-liquid interface is always separated from the walls by thin, wetting films of the carrier fluid.

The operation of the flow-focusing device can be described as follows. The gas (or disperse) phase flows through the central channel, while the liquid (or continuous) phase flows through the two outer channels. The three flows meet at the junction of these channels upstream of the orifice (or nozzle). Due to a pressure drop along the axis of the system, the fluid is forced through the nozzle. The gas stream tip enters the orifice, where it expands downstream of the orifice generating a gas cavity. The gas cavity is a growing bubble that displaces the liquid phase in the outlet channel downstream of the nozzle. The growing bubble is connected to the inlet gas by a thin thread, which eventually breaks, releasing the bubble in the outlet channel. It was observed by the authors that the system repeats this process in a periodic state for a wide range of pressures (p) applied to the gas stream, and volumetric flow rates (Q) for the liquid. Hence, the bubbles formed are uniform in size, with a coefficient of variation (CV) smaller than 5%, the CV being defined as the ratio of the measured standard deviation of the bubbles diameters to the diameter mean value of the bubble population.

By experimentally exploring the size of the microbubble's dependence on p, Q, μ (dynamic viscosity of the liquid), and σ (interfacial tension between the two phases) the following relation was obtained from Figure 2.21a:

$$\frac{\forall}{\forall_{or}} \propto \left(\frac{p}{Q\mu\left(\frac{h^3}{L}\right)}\right) \tag{2-22}$$

where $\forall$ is the volume of the bubble, $\forall_{or}$ is the volume of the orifice, h, w, and L are the height, width, and length of the outlet channel, respectively.

From the relation exposed above, it is possible to tailor the size of the microbubbles being produced. For a constant p, an increase in Q will result in a decrease in the bubble size. Contrarily, by fixing Q, and increasing p, a larger bubble size can be obtained.

Further, from Figure 2.21, it was found an approximate empirical relation for the bubbles production frequency, f, as a function of p and Q:

$$f \propto p\,Q \tag{2-23}$$

Therefore, for a given viscosity of the liquid, the size of the bubble is a function of the ratio of p to Q, while the frequency of bubble production is a function of the product of p and Q. By making a transformation of variables from $(p, Q) -> (\forall, f)$ it is possible to control the volume of the microbubble and the generation frequency simultaneously and independently. Hence, for any fixed size of bubble, and by keeping p/Q as constant, one can control the volume fraction (A) of the disperse phase, which can be expressed as follows:

$$A = f\forall/(f\forall + Q) \tag{2-24}$$

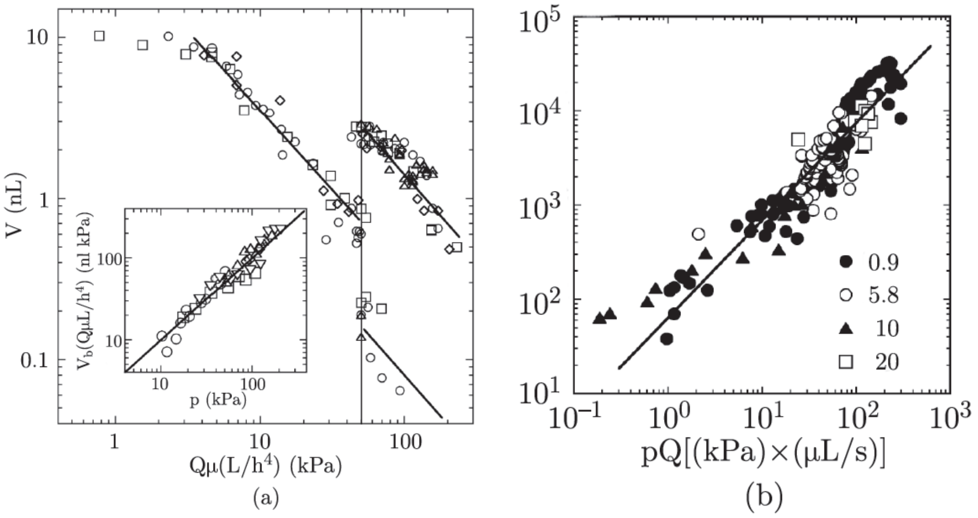

Figure 2.21 –The volume of bubbles created in a planar microfluidic device was plotted against the product of the rate of flow Q and liquid viscosity μ, and was scaled to pressure units by multiplying by L/h^4, where L is the length of the outlet channel and h is its height. Adapted from Garstecki et al., 2004, and Garstecki et al., 2005).

It is interesting to note that the work by Whiteside *et al.* (2005) was conducted at low Ca values, ranging from 10^{-3} to 10^{-1}, indicating that interfacial forces should be dominant over the shear stress. However, both Eqs. (2-.21) and (2-22) do not include interface tension values, showing that both $\forall$ and f are independent of this parameter.

Garstecki *et al.* (2005) proceed to study experimentally the dynamics of the break-up of the gas stream into bubbles. Figure 2.22 shows a schematic drawing of the tip of a stream of gas in a flow-focusing device. As described by the authors, the breakup dynamics start with the tip of the gas stream entering the orifice. The gas fills almost completely the nozzle, and the gas-liquid interface lays on the walls of the orifice, only separated by a thin liquid film wetting the surface. This stage is characterized by a minimum width of the thread of gas (w_m) of a similar size as the width of the orifice, w_{0r}. The flow of the continuous phase in the thin film is associated with high-pressure gradients, that can be approximated by the lubrication theory by (Stone, 2005):

$$\Delta p \propto \forall^{-1} \tag{2-25}$$

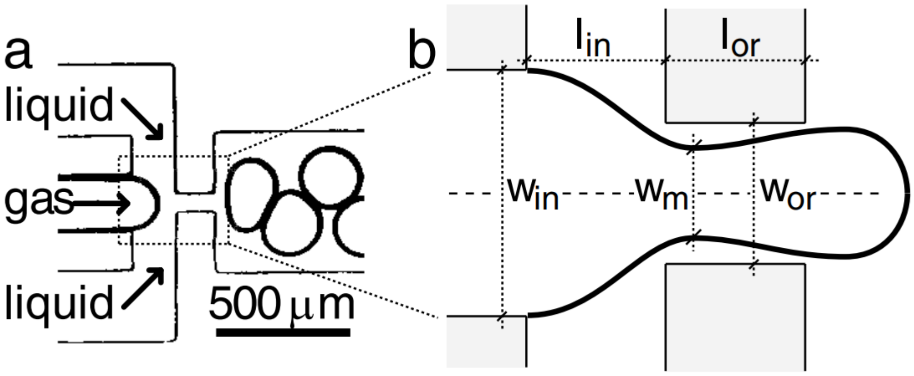

Figure 2.22 – Schematics of the orifice region and the gas-liquid interface (Garstecki et al., 2005).

The liquid is pumped into the orifice region at a constant flow rate, which leads to an increase in the pressure of the liquid upstream, resulting in a displacement of the gas at a rate proportional to its volumetric flow rate. The thread of gas connecting the inlet channel gas to the growing bubble in the outlet starts to get thinner, and w_m decreases approximately linearly with time. At the last stage, the growing bubble becomes unstable due to a Rayleigh-Plateau type of instability, and the thread breaks rapidly. The tip of the stream of gas retracts upstream, and the bubble is pushed away downstream. The whole process then repeats periodically as before mentioned. The rate at which the w_m decreases in the second stage is used to define the “speed of collapse” $u_{collapse}$ of the gas stream that forms the microbubble. It was found that the rate does not vary either with p, μ or σ, only linearly with Q:

$$u_{collapse} \approx dw_m/dt \propto Q \tag{2-26}$$

The speed of collapse measured in their experiments was compared to the “natural” speed of collapse from a classic capillary instability of gas thread. The estimates of the natural speed of collapse were one to three orders of magnitude larger than the $u_{collapse}$ measured. They conclude that the gas thread is stable against interfacial instabilities throughout almost the entirety of the collapse, which is not driven by surface tension.

The time that the thin thread takes to collapse, $t_{collapse}$, is on the order of ratio $Q/\forall_{or}$. This mechanism of break-up is characterized an $u_{collapse}$ much smaller than the typical rates of relaxation of the interface’s curvature. All the fluctuations in the system’s parameters such as flow rate, pressure, temperature is equilibrated at a much shorter timescale in comparison to the $t_{collapse}$. This difference between time scales of break-up and the time-scale of equilibration of pressure fields in the liquid and the curvature of the interface yields a very reproducible break-up, hence, the highly uniform size distribution of bubbles population.

It is important to state that this mechanism of a reproducible breakup, is specific for microfluidics systems, where the before-explained interfacial dynamics are highly affected by the presence of the device's wall. This condition is only observed for low capillary number, and in large ratios of the capillary lengths ($Lc = \sqrt{\sigma/(\rho\, g)}$) in comparison with typical length scales of the device, such as orifice width.

The production of monodisperse microbubbles, in a flow-focusing microfluidic device, is a proven versatile tool for production of highly monodisperse microbubble populations (Figure 2.23) (Gañan-Calvo *et al.*, 2001; Anna *et al.*, 2003; Garstecki *et al.* 2005). However, to match the needs for medical application of monodisperse microbubbles, we must attain a production rate in the order of 10^5 to 10^6 bubbles/s (Segers *et al.*, 2016), in order to obtain a clinically relevant microbubbles count in the suspension. Moreover, it was reported before that, the stability of monodisperse microbubbles produced by microfluidics at high production rates was very low (Shih *et al.*, 2013; Talu *et al.*, 2008).

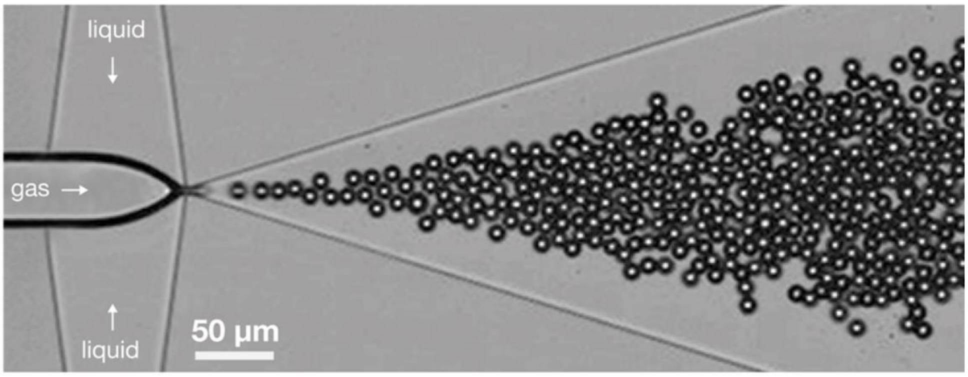

Figure 2.23 - Bubble formation at a rate of 6 × 10^4 bubbles/s from a flow-focusing geometry (Sergers et al. 2016).

In more recent studies conducted by (Sergers *et al.* 2016; van Elburg *et al.*, 2021), long-term size stability of perfluorobutane C_4F_{10} gas-filled lipid-shelled bubbles produced in a flow-focusing device at high production rates was characterized. The authors were able to obtain a production rate up to 10^6 bubbles/s, without losing the monodispersity of the bubbles, for microbubbles with radii of 2 to 10 µm. They showed that the lipid adsorption process reaches equilibrium prior to the pinche-off of the bubbles in the microfluidic nozzle. It was observed that the number of phospholipids on the bubble surface remains constant after formation, during dissolution or expansion. These highly stable elevated production rate opens a route to industrial and bedside production of clinical-grade ultrasound contrast agents.

2.3. Freeze-drying Process

Different groups have studied extensively the stability of microbubbles, verifying the importance of parameters such as the core gas type, shell composition, saturation of the liquid medium, in the bubble's lifetime as demonstrated in previous chapter. Microbubbles can often be stable for a few hours in controlled conditions. However, this lifetime is still short to meet the need for therapeutic and contrast-enhancing applications, meaning that treatment protocols would require bubbles to be produced directly before their use in clinics. The need to stabilize the size distribution and concentration is further increased when dealing with monodisperse bubble populations.

Microbubble freeze-drying has been widely used to increase the shelf life of commercially available ultrasound contrast agents. The microbubbles are freeze-dried at production and subsequently reconstituted at the point of use, resulting in better control of the bubble's population properties, with simpler protocols for administration, and lower production costs (Abou-Saleh, *et al.*, 2020). However, prior to this work, the freeze-drying of monodisperse microbubbles populations, without degrading their monodispersity was not achieved.

Despite being a relatively straightforward process, it is crucial to ensure that the reconstituted product preserver all the properties and characteristics of the starting one.

The freeze-drying process is usually segmented in the literature into three stages: (1) freezing, (2) primary drying, and (3) secondary drying (Franks, 1998; Jennings, 1999; Van Winden, 2003, Tang and Pikal, 2005). The final product quality is determined by the formulation of the sample being lyophilized and the parameters used in each phase. Therefore, this chapter aims to provide an overview of the basic principles behind the freeze-drying process.

2.3.1. Freezing phase

In the freezing phase, freezing to completion requires the removal of more than 99% water from an initially dilute solution. The cooling of the sample results in the formation of ice crystals, which also leads to a rapid increase in the total solute concentration. This process called “freeze-concentration” is a function of the temperature only, being independent of the initial solution concentration (Van Winden, 2003, Frank; 1998). At this stage, three processes can affect the stability of the microbubbles. First, the growth of ice crystals generates stress over the bubbles, potentially leading to ruptures. A secondary consequence relates to the acceleration of chemical reaction rates in the residual solution phase (Hatley et al, 1986). A phenomenon referred to in the literature as “freeze denaturation” or “concentration denaturation” (Frank, 1998). Also, during freeze-concentration, eutectic phase separation occurs for all solvents in a mixture, where each solvent precipitates when its respective solubility is reached. The different precipitations will cause major pH shifts that can be damaging for the microbubbles.

With the use of excipients called lyoprotectants or cryoprotectants (Bhattacharya, 2018; Frank, 1998), it is possible to prevent undesirable precipitation processes. This substance does not readily crystalize from a frozen solution, and depending on the concentration, it will inhibit salts precipitation, allowing for a longer freeze-concentration process, above the natural limit of saturation solubility. In this condition, the freezing process of the solution continues but at a slower rate, due to the increase in the supersaturation degree together with the decrease in temperature. Therefore, the viscosity of the solution rises with increasing rates, leading to a stop in the ice crystal’s growth. In this phase, the solution has the mechanical properties of an amorphous solid with the molecular structure of a liquid. The temperature at which this low molecular mobility configuration occurs is called the glass transition temperature of the freeze-concentrated solution, T_g (Figure 2.24). As explained by (Frank, 1998 and Van Widen, 2003) the T_g is a key parameter for the drying process, and the product should be frozen usually at 5°C below the T_g in order to avoid collapse of the structures. The solution containing the lyoprotectant and some minimal amount of buffer components will determine the glass transition temperature.

Another essential factor in the freezing phase is the cooling rate of the samples. For the cases where the samples to be freeze-dried are placed in a vial, quick cooling (on a prechilled shelf or in boiling nitrogen) can be detrimental (Frank, 1998 and Van Widen, 2003, Van Widen *et al.*, 1997). The high cooling rate can result in the formation of dendritic ice crystals that grow from the bottom to the top of the vial. This pushes up the freeze-concentrate, forming an amorphous layer at the top of the samples, where almost any ice crystals have been formed. Thus, a crust, with a limited number of pores, is formed on top of the cake, reducing the escape rate of water vapor from the sample.

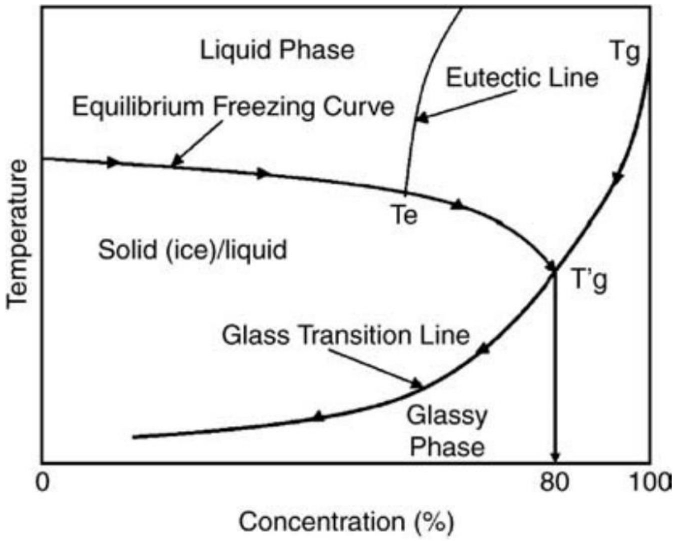

Figure 2.24 - Phase diagram for a binary system of sucrose–water showing T_g (Abdelwahed et al., 2006).

A slow cooling (e.g. – 0.5°C/min) technique is preferred in this situation, because it allows undercooling the sample. In other words, the sample can reach values below 0°C without immediate ice formation. When freezing occurs, the sample is nearly instantaneously frozen as a whole, yielding crystals of similar size throughout the product. The pores that will be created, reduce the resistance for the scaping of water vapor during sublimation (Searles, *et al.* 2001).

2.3.2. Primary Drying

At the primary drying phase, the ice crystals formed in the freezing phase are sublimated, creating a porous cake-like structure of the freeze-concentrated matrix. In order to preserve this newly formed structure from degradation, the temperature at the sublimation front (T_{front}) should be kept at 4°C below the T_g. In this way, ice crystals can be removed without collapsing the porous cake structure. On the other hand, if the T_{front} is kept above the T_g, a collapse of the cake structure occurs, leading to an increase in the water content and in the time required for reconstitution. In this scenario, the microbubbles may fuse, which leads to leakage of part of their content during rehydration (Van Widen, 2003).

The local pressure in the primary drying is the key parameter to determine the solution temperature at the sublimation front. Therefore, the pressure in the freeze-drying chamber should be controlled following the ice vapor pressure-temperature curve, having a corresponding temperature of 4°C below the T_g. However, in order to guarantee a heat transfer to the sublimation front, the shelf temperature should be set to a value higher than the ice temperature. For that reason, the difference in the water vapor pressure between the freeze-drier chamber (condenser) and the sublimation front is the dominant driving force in the drying process.

The heat transfer to the sublimation front is a limiting factor for the drying process as shown by (Pika, 1990, and Ybema *et al.*, 1995). In order to have more heat being transferred, the chamber's pressure should be increased. However, increasing the pressure leads to a higher temperature, which is limited by the T_g of the sample.

The geometry of the sample container, as the volume of the sample being freeze-dried, plays an important role in the drying process. For example, depending on the vial configuration, the drying process can lead to an increase in the thickness of the dried cake, which creates a higher resistance for water vapor, leading to a higher local pressure at the sublimation front. In case the pressure surpasses the chamber pressure, T_{front} can exceed T_g, which will jeopardize the product structure. Therefore, to avoid a long drying process, a maximal filling height of 30% of the vial is suggested (Van Widen, 2003).

In summary, the main parameters of the drying process are the chamber pressure, the shelf temperature, and the sample's temperature T_g. These variables should be carefully controlled in order to successfully freeze-dry the product.

2.3.3. Secondary Drying

The secondary drying phase starts after the sample temperature reach the shelf temperature, which leads to a further decrease in the water content in the amorphous matrix, and all the ice has been sublimated.

The reduction in the water content in the porous cake results in an increase in the T_g of the sample. In that scenario, the chamber's pressure is reduced to a minimal value and the temperature of the shelf is elevated slowly, to obtain a low residual water content.

Low water content is usually correlated with a higher stability of the dried product. However, some complex physical processes can occur during the freeze-drying of the porous cake. Van Winden and Crommelin (1999) have shown that for the freeze-drying of dipalmitoyl phosphatidylcholine (DPPC) liposomes, the T_g of the intraliposomal matrix can have a different value compared to the T_g of the extraliposomal matrix. This phenomenon occurs due to the higher concentration of the encapsulated compound. In this particular case, it was observed a chemical degradation of the liposomes in a process at temperatures well below the T_g of the amorphous matrix.

The freeze-drying is complete after closing the vial either under vacuum or with a chosen filling gas (nitrogen, argon, or perfluorhexane). In order to store the final product, usually, the air is avoided as a vial filler because it can lead to oxidation of the sample, as was shown by N. J. Zuidam for phospholipids microbubbles.

2.3.4. Ultrasound Contrast agents freeze-drying

Freeze-drying is a common technique used in the preparation of microbubbles for contrast-enhanced ultrasound imaging (Abou-Saleh *et al.*, 2020). The Bracco company produces a clinically used contrast agent, called SonoVue, using freeze-drying or spray-drying of lipids. Before being used, the product is mechanically agitated in the presence of a low solubility gas and aqueous carrier to create microbubbles with size in the 0.5−10 μm range (polydisperse population) (Schneider *et al.*, 1997). The contrast agent Sonozoid, which is produced by GE Healthcare, uses sucrose during the lyophilization of lipid-coated perfluorobutane microspheres (Figure 2.25) (Sontum, 2008). The product is resuspended prior to use in a similar method as Sonovue.

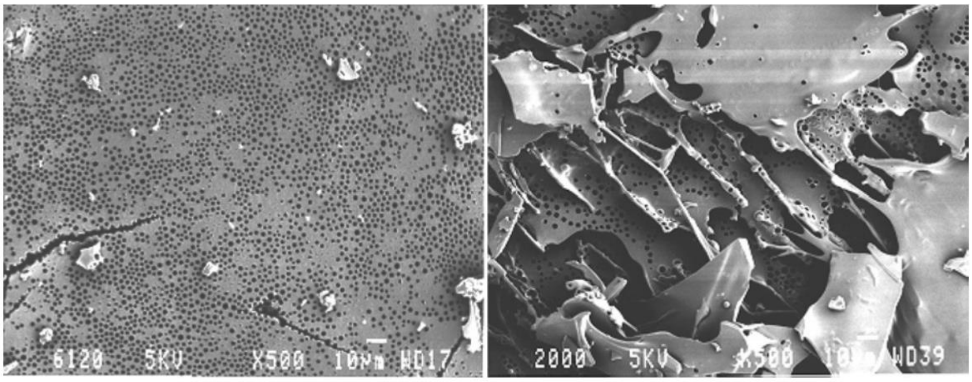

Figure 2.25 — Typical images from SEM on SonazoidTM powder. Surface view (right) of lyophilized cake. Size bars are 10 μm (Sontum, 2008).

In order to preserve the microbubbles, the freeze-drying technique was used in the presence of cryoprotectant or lyoprotectant. The process generated cavities in the cryoprotectant matrix, which were filled with an appropriated gas, that was chosen to refill the vial (Abou-Saleh *et al.*, 2020). The bubbles are formed upon rehydration, before being used. Wheatley *et al.* (2015) used this method in surfactant-based contrast agents (e.g. SE61, composed of Span60 and water-soluble vitamin E) to change the octa-fluoropropane gas core to O2 to increase the O2 level in hypoxic tissue upon delivery (Wheatley *et al.*, 2015) and, by the same group, to preserve the integrity of contrast agents with the nonionic ST68 (Wheatley *et al.*, 2010). Polymeric bubbles also benefited from the freeze-drying process. The study by Ojha *et al.* (2019) demonstrated that sucrose was better than glucose and other cryoprotectants for rhodamine-B dye loading. They observed that for the case of sucrose, all of the dye was retained after lyophilization with no leakage in the aqueous suspension. In pharmaceutical preservation, non-diffusible synthetic polymers are commonly used to provide ridge cryoprotection of the biological cells within. For example, polyvinyl alcohol (PVA), PEG, hydroxyethyl starch has a good tendency to decrease the size of ice crystals during the freezing stage (Bhattacharya 2018).

Despite all the progress and knowledge regarding the freeze-drying of microbubbles to be used as ultrasound contrast agents, sustaining the monodispersity of a microbubble population still poses a challenge.

By combining the knowledge of microbubbles stability, microfluidics for monodisperse microbubbles production, and freeze-drying techniques, we were able to unlock the bottleneck of the sector, by successfully freeze-drying monodisperse microbubble population, without degrading their properties.

3. MATERIALS AND EXPERIMENTAL DESCRIPTION

This chapter aims to describe the materials and methods used to produce the monodisperse microbubbles, as well as the method developed to lyophilize them without compromising their properties. The lyophilization of monodisperse microbubbles experiments were planned and conducted for two sizes of microbubbles population (40 µm and 5 µm mean diameter). Due to physical issues that followed the 8 times reduction of the bubble's diameter, two different designs of microfluidic devices were used. First, we will describe the microfluidic designs used, followed by the procedures for microfabrication and assembly of the microfluidic device.

3.1. Microfluidic Device Design

The microfluidics devices were manufactured from polydimethylsiloxane (PDMS) using soft lithography technology (Tabeling, 2005).

3.1.1. 40µm flow-focusing microfluidic device

In order to produce the 40 µm monodisperse microbubbles population, we followed the classical design for a microfluidic flow-focusing device (Garsteck *et al.*, 2004, Tabeling, 2005, Whiteside *et al.*, 2005). Three main microchannels characterize this device: gas-phase flow inlet, continuous liquid-phase flow inlet, and microbubbles flow outlet (Figure 3.1). The liquid channel separates into two channels to converge with the gas flow, focusing their streams towards the microbubble's outlet channel. A rectangular cross-section with a 16 µm height characterizes all the channels. The width of the liquid channel is 100 µm and the gas channel is 50 µm, while the nozzle width is 20 µm. The focusing orifice expands into the microbubble's outlet chamber with a width of 300 µm, to reduce the contact between the microbubbles yielding a smaller coalescence probability. All the inlets have a filtering system consisting of pillars to prevent clogging due to large particles or agglomerates suspended in the solution.

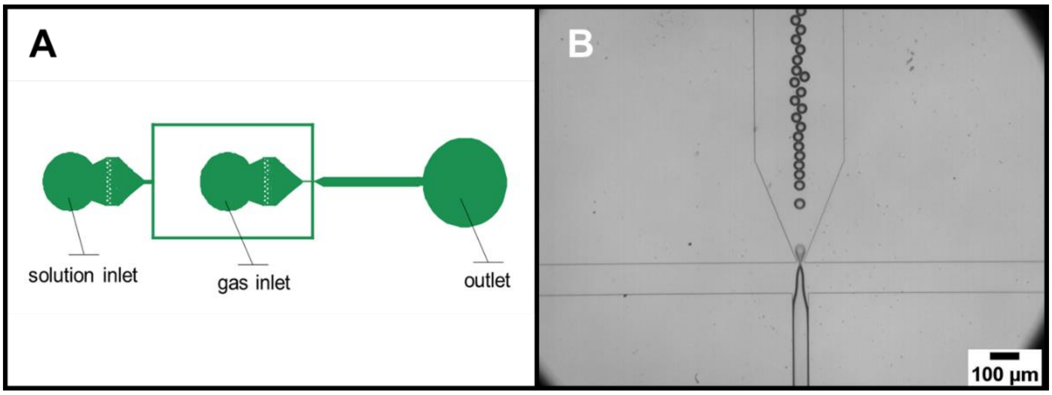

Figure 3.1 – Design of the flow-focusing microfluidic device for 40µm bubbles productions. A) Shows the design made with the Clewin software. B) Typical optical image with 10x magnification of the microbubbles production.

3.1.2. 5µm Flow-Focusing Microfluidic Device

The device used to produce the 5µm microbubbles, presented in Figure 3.2, has some particularities that differentiate its design from the one exposed in the previous chapter. First, this device contains two inlets for liquid phase injection, two outlets for the recovery of excessive material (i.e., an anti-clogging system), one gas inlet, and one bubble outlet for collecting the generated bubbles (Mallogi *et al.* 2010). The height and width of the flow-focusing geometry are 5µm. To reduce the hydrodynamic resistance and increase the microbubble's production throughput, a step-emulsification geometry was used upward of the nozzle orifice (height of 20µm). The small dimensions of the flow-focusing geometry would make the device prone to clogging due to large aggregates or contaminants. Therefore, an anti-clogging system (tangential filtering) was included in the design to assure a prolonged and stable microbubbles production (Malloggi *et al.* 2010). The liquid phase flow channel has a 20µm height and 100 µm width that bifurcates into the 5x5µm flow-focusing channel and a low hydrodynamic resistance outlet where the large aggregates are driven. The addition of the anti-clogging system resulted in only a small fraction of the liquid phase flow being driven to the production of the bubbles, which led to agglomeration of microbubbles and further coalescence. Therefore, the bubble outlet design consists of a lateral tube aligned along the axis of the collection channel (e.g., lateral collection), and a liquid phase inlet (e.g., pusher) that allows to increase the flow rate of the continuous phase and hence tune the bubble concentration.

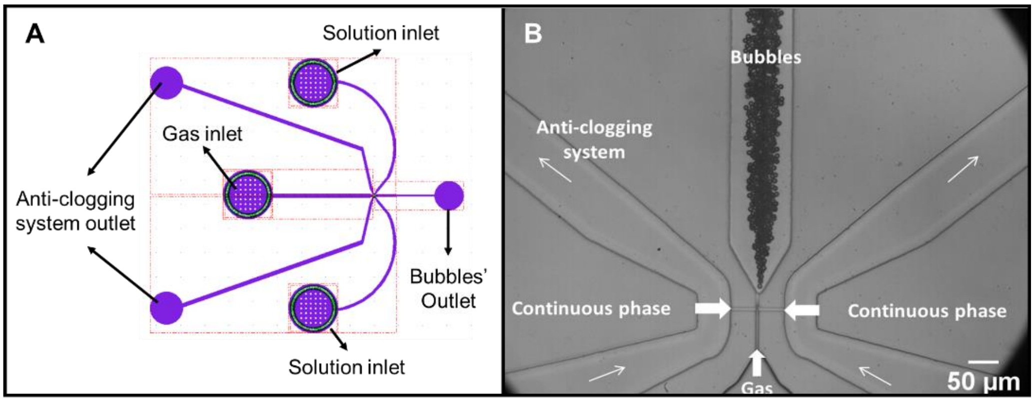

Figure 3.2 – Design of the flow-focusing microfluidic device for 5 µm bubbles productions. A) Design made with the Clewin software. B) Typical optical image with 20x magnification of the microbubbles production.

3.2. Microbubble Production

An 8%w/w Polyvinyl Alcohol (PVA) and 10mM Phosphate buffered saline (PBS) solution flows through the liquid phase channel while Perfluorohexane (PFC) is pushed through the gas phase channel. The central gas flow is pushed into the orifice (40µm or 5µm) by the two lateral liquid flows that come from a perpendicular direction. Due to the instability created by the liquid phase over the gas phase, the microbubbles are pinched off after the focusing orifice. Since the gas and the liquid flow are maintained constant, it is possible to obtain bubbles with narrow size distribution (as described in chapter 2.2).

The microbubbles production rate, as well as the mean diameter size of the bubble, can be controlled by the gas and liquid phase flow rates. The flow rate of both phases was pressure-driven by an MFCS-100 pressure controller system (MFCS-100, Fluigent, France). For the 5µm device, the “pusher” flow rate was controlled by a syringe pump (Standard Infusion Only Pump 11 Elite Syringe Pumps, Harvard Apparatus, USA).

In situ microbubble generation was recorded using a high-speed camera (Photron SA3, Japan) connected to an optical microscope (Zeiss Observer A1, USA) at 20x and 40x magnifications. The recordings were analyzed to obtain the size distribution and the generation rate of the bubbles in MATLAB using the *imfindcircles* function, which uses a Circular Hough Transform (CHT) based algorithm, more specifically an Atherton and Kerbyson's phase coding method (Atherton and Kerbyson, 1999).

3.3. Microfluidic device fabrication and assembly

The polydimethylsiloxane (PDMS)/glass chips were fabricated by applying standard soft lithography techniques (Duffy *et al.*, 1998, Tabeling, 2005). The designs described in the previous chapter were made using the CleWin software. In a clean room, the SU-8 photoresist was spin-coated onto a silicon wafer and UV-exposed using a photomask of the microfluidic design and a mask aligner MJB4 (SUSS Microtec, Germany). For the 40µm design, a lower resolution is necessary; therefore, we used a standard plastic photomask. To measure the vertical profile of the produced devices, we used Dektak Surface Profilometer (Veeco, USA). Afterward, the mold was replicated using PDMS (Sylgard 184 elastomer kit, Dow Corning, Germany), mixed in a 1:10 cross-linker/polymer ratio. After gently pouring the mixture into the mold, we placed it under a vacuum for 1h to remove small air bubbles that could jeopardize the geometry of the microchip. The mold was then cured inside an oven at 70 °C for 4 h, cut into the desired shape, and punched to make inlet and outlet holes. The PDMS device and a microscope glass slide were treated with an Oxygen plasma (The CUTE, Femto Science Inc., Republic of Korea) and irreversibly bonded.

For the 5µm design, we used a double layer technique to fabricate the step-emulsification geometry where a two-step UV exposure was conducted. First, we spin-coated the SU-8 photoresist over the molding silicon wafer and carried a UV exposure in order to obtain the flow-focusing microchannel with 5µm height and width. Since the nozzle was smaller than 20µm, a higher resolution mask was required for this geometry; hence, for the 5µm design, we printed and applied chrome photomasks to ensure the precision of the mold. Then, the second layer of SU-8 photoresist was spin-coated onto the silicon wafer, and a second UV exposure was made, after a careful alignment of the second mask, which contained the design of channels with a rectangular cross-section of 20µm height. The mold replication and the succeeding bonding to the microscope glass slide were conducted following the same procedures prior to exposure to the 40µm microchip. Finally, plastic tubes (PEEK Tubing 0.25mm inner diameter, Cluzeau Info Labo, France) were connected to the inlet and outlet of the device. In order to keep the inner wall of microchannels hydrophilic, oxygen plasma was carried out before microbubble production.

3.4. Microbubble composition (Why PVA?)

Microbubbles for ultrasound imaging have been created using a variety of materials. Commercially available microbubbles are based on air-filled denatured albumin microcapsules, phospholipids, and liposomes containing gaseous SF6 or perfluorocarbons (Ferrara *et al*., 2007). Polymeric microbubbles have been used in diagnostic imaging (Liu *et al.,* 2006, and Gao *et al.*, 2007) and as drug/gene carriers for controlled delivery (Peyratout *et al*., 2004, Hernot and Klibanov, 2008; Sutton *et al.,* 2014; Kooiman *et al.,* 2020, Tu *et al*., 2021). This method is associated with transient cell membrane permeabilization (sonoporation) and the release of encapsulated pharmaceutical agents at a specific location. Biologically relevant molecules can also be incorporated into the membrane that stabilizes the microbubbles; charged drugs can be electrostatically stabilized in or on the surfaces of bubbles (Unger *et al.,* 2001). The fusion of *in vivo* diagnostics and therapeutic applications (theranostics) at the cellular level necessitated the development of novel gas-encapsulated polymeric microbubbles with optimized properties. Controlled size and shell thickness distribution, persistence in circulation, gas core protection, long-term storage stability, and elasticity for controlling ultrasound damping behavior are among the essential characteristics of efficient theranostic microbubble materials (Wei *et al*., 2021). Because of its inherent nontoxicity, non-carcinogenicity, good biocompatibility, and physical properties such as compliance, elasticity, and resistance to mechanical stress, poly(vinyl alcohol) (PVA) became a polymer of great interest for various pharmaceutical and biomedical applications. PVA hydrogels are used to make contact lenses, wound dressing, coatings for sutures and catheters, and as synthetic articular cartilage (Paradossi *et al*., 2010). In 2008, Tzvetkov znd collegues produced air-filled microbubbles from a cross-linking reaction at the telechelic PVA solutions' air/water interface. The bubbles had an average diameter of 4.6±0.4 µm and a shelf life of several months (Tzvetkov *et al.,* 2008). An investigation into the ultrasound properties of PVA-based microbubbles revealed the value of the pressure threshold at which the bubble shells cracked upon insonification. It was discovered that it was within the mechanical index (MI) recommended for biomedical applications.

Furthermore, these microbubbles have been successfully decorated on the external surface with molecules such as oligopeptides, amino acids, oligosaccharides, and polysaccharides (Cavalieri *et al.,* 2006), allowing ligand attachment to the surface of the microbubbles (Klibanov 2005). Furthermore, it was shown that PVA-shelled microbubbles could be loaded with nitric oxide, NO, and the gas's *in vitro* release was evaluated, revealing its efficacy as an anticlotting agent (Cavalieri *et al*., 2008). In conclusion, PVA-shelled microbubbles as UCAs (Paradossi *et al.* 2010) are more echogenic (Grishenkov et al. 2011) and stable (Oddo et al. 2017) than lipid-based UCAs; the material is FDA (United States Food and Drug Administration) approved, and a series of preclinical tests revealed no toxicity (Cerroni et al. 2018). As a result, PVA-based microbubbles are an auspicious material for theranostics and imaging.

As the gas phase, perfluorohexane (C_6F_{14}) (Alfa Aesar Perfluorohexanes, 98+ percent, Fisher Scientific, USA) or sulfur hexafluoride (SF6) (Air Liquide, 99 percent, France) were utilized, which means that the bubbles are filled with C6F14 or SF6. Such gases are more hydrophobic, less soluble, and heavier than air in aqueous solutions. That is why they were chosen for the second generation of microbubbles (Podell *et al.* 1999, Schneider, 1999), since the bubble shell is characterized by high permeability, allowing gas to escape and eventually result in the bubbles dissolving quickly. As a result, such gases were chosen to increase the duration of the bubbles.

The liquid phase is a 10 mM Phosphate-Buffered Saline (PBS) (Sigma-Aldrich, Germany) solution in Milli-Q water containing an aqueous solution of PVA (Mw 13,000-23,000, 87-89 percent hydrolyzed, Sigma-Aldrich). PVA was agitated in an aqueous solution overnight at 80°C before being employed as the continuous phase. PVA functions as a surfactant and a shell material due to the surfactant's ability to produce a shell around the bubbles. To avoid the destruction of the bubbles during the rigorous freeze-drying process, which is linked with freezing, dehydration, and solid-liquid interfacial tensions (Abdelwahed *et al.* 2006, Date *et al.* 2010), a cryoprotectant is necessary (Mensink*et al.* 2017). The cryoprotectant and surfactant are both present in the external fluid. PVA serves as a surfactant and a cryoprotectant in our innovative, easy-to-prepare formulation. Although PVA is not currently employed as a cryoprotectant for freeze-drying microbubbles, it has attracted attention as an emerging cryoprotectant for droplets and pharmaceutical goods (Song *et al.* 2018, Mitchell *et al.* 2019).

3.5. Microbubble Size control and distribution

The geometrical characteristics of the microbubbles were evaluated by using an inverted optical microscope (Axio Observer Z1, Zeiss, Germany). A field lens was used to couple a 40X magnification microscope objective to a high-speed camera (FASTCAM SA3, Photron, USA) capable of capturing images with a 1024x1024 pixels resolution at 1000 frames per second (fps), and up to 60,000 fps at lower resolution. In order to determine the size, the dispersity, and the generation frequency of the microbubbles we used the MATLAB software for image treatment. First, a standard background subtraction by threshold technique was used followed by an image binarization by the threshold to enhance the contrast between the bubbles and the background. Afterward, we used the MATLAB's *imfindcircles* function, which uses a Circular Hough Transform (CHT) based algorithm, more specifically an Atherton and Kerbyson's phase coding method (Atherton and Kerbyson, 1999) to identify and measure the microbubble's size. The coefficient of variation (CV) was then calculated by the ratio between the standard deviation and the mean diameter of a population of microbubbles.

To measure the production rate of the microbubbles, pictures of the bubbles being produced in the nozzle of the microfluidic flow-focusing device were taken with a 20.000 fps recording speed. Differently, to characterize the produced and resuspended microbubbles, a sample of approximately 10µl was deposited on top of a microscope glass slide and covered with a thin glass coverslip for immobilization and to maintain the bubbles at the same plane of view.

3.6. Monolayer bubble collection and freeze-drying protocol

Figure 3.3 depicts the procedure employed to collect and freeze-dry the bubbles produced. Microfluidic bubbles are transported along lateral outlet tube. Bubbles produced milky suspension droplets at the tip of the tube at the concentrations we used. Each 2 to 10 µl drop was placed on a hydrophilic glass slide that had been treated with O2 plasma (75 mm x 25 mm). Bubbles create monolayers grouped into discrete places on a glass slide in this manner (see Figure 3.3). We usually obtained one hundred spots, consisting of 5 µm in diameter and made up of 10^4 bubbles, in each one.

Furthermore, bubbles were pre-frozen for at least 2 hours at –25°C, significantly below the glass transition temperature (T_g) of the cryoprotectant employed (80°C). Finally, the frozen bubbles were transported for 4 hours to a freeze-dryer (FreeZone Labconco, USA) with a shelf temperature of -50°C. Subsequently, each freeze-dried spot was hydrated on the glass slide in a PFC ambient with a gas-saturated PBS solution. In case the monodisperse bubbles were gathered in large drops, resulting in the creation of multilayers, the bubbles would interact before being frozen, the lyophilizate would be multilayer, and the resuspended microbubble population would be polydisperse.

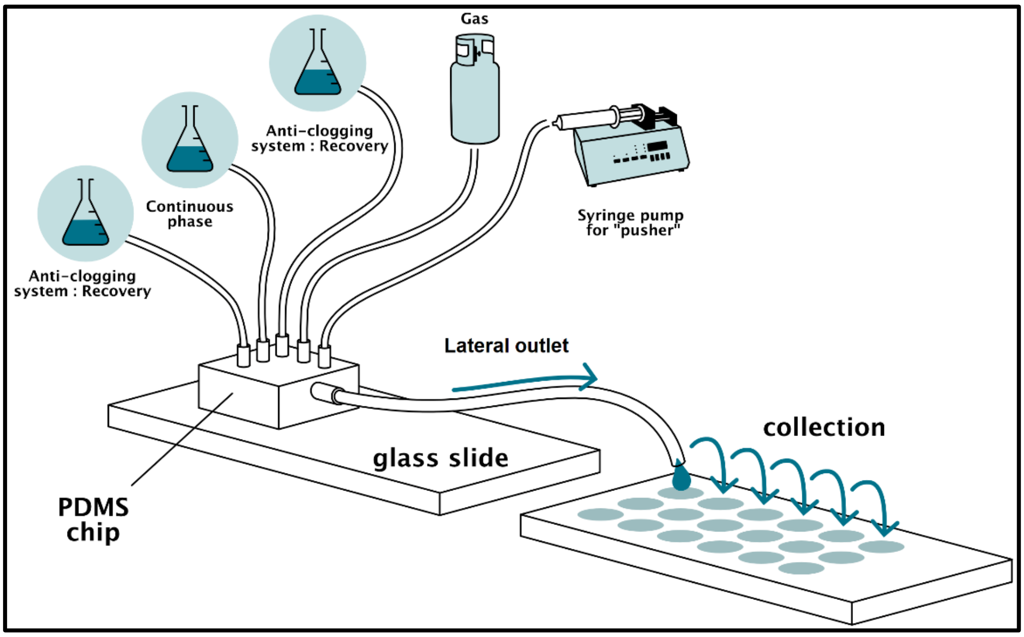

Figure 3.3 - An illustration of the microfluidic production showing required elements to operate the system and a spot-based collection of bubbles in a drop on a glass slide.

3.7. Method of observation of the lyophilisates

An environmental scanning electron microscope (ESEM) was utilized to assess the homogeneity of the freeze-dried microbubble population. The equipment was also used to obtain an estimate of the bubble’s shell thickness. A sample holder was used to hold the freeze-dried bubbles on a piece of a microscope glass slide. Even though the glass slide is not conductive, the sample was stimulated with a modest electron accelerating voltage (5kV) to prevent the background charging effect. The photos were taken with a 20° tilt and without metallic coating to prevent the shells' alterations, resulting in one side turning white owing to the charging effect.

3.8. Continuous Phase Surface Tension Measurements

The surface tension of the continuous phase used to produce the bubbles was measured by the pendant drop technique, using a Drop Shape Analyzer DSA30 (KRUSS GmbH, Germany). First, we filled a 1mL plastic syringe coupled with a needle adaptor (20 ga x ½” Luer stubs, PHYMEP, France) with the PVA solution. The results are presented as triplicates with the standard deviation. Deionized water at 25°C was measured as a reference.

3.9. Monodisperse microbubbles stability over time

The stability of a monodisperse microbubble population with a mean diameter of approximately 5 µm of was measured over time. The freshly generated PVA-shelled microbubbles were collected over a microscope glass slide and pictures of the population were taken at every minute for 1 hour. The microbubbles' size distribution was estimated using a Matlab code as described in chapter 3.5. The mean diameter and the coefficient of variation of the bubble population were compared for different time periods, to assess the stability of the PVA microbubbles.

4. RESULTS AND DISCUSSION: MICROFLUIDIC

This chapter aims to investigate the synthesis of monodisperse PVA-shelled microbubbles to be used as ultrasound contrast agents. Two different sizes of microbubbles population (40 µm and 5 µm mean diameter) were characterized optically in five stages of the lyophilization process: production, collection, freeze-thawing, lyophilizate, and resuspension.

4.1. Microfluidic flow-focusing 40µm microbubbles production

The flow-focusing microfluidic device with a nozzle size of 20µm was capable of producing monodisperse microbubbles. The production of microbubbles could be divided into five different regimes (Dhanaliwala, 2014), four of which are illustrated in Figure 4.1. First, the Overpressure regime is characterized by a gas pressure that overwhelms the liquid flow rate, resulting in a continuous gas stream, without bubble formation. The second regime, called Cylindrical, results in the production of non-spherical microbubbles that are larger than the microfluidic channel's height. The following regime, named Stable (or bubbling regime - Gañán-Calvo *et al.*, 2006, and Garstecki *et al.*, 2006) is characterized by a steady and stable production of microbubbles with a diameter smaller than the height of the channel, but bigger than the nozzle's width. The fourth regime, named Unstable, is distinguished by an unstable microbubble production, in which doublet formation can occur. The bubbles are produced in quick succession, generating pairs of bubbles of different sizes (one big and one satellite), followed by a delay in microbubbles production. In this configuration, the bubbles are found to have a size smaller than the nozzle's width. At last, the Underpressure regime is characterized by a liquid flow that overwhelms the gas pressure, yielding no bubble production. The gas pressure of the systems dictates the flow rate limits that define this regime. Generally, a gas pressure increase results in an increase in the minimum liquid flow rate in which the regime begins. Also, it broadens the range of liquid flow rates over which the regimes happen. For a given liquid flow rate, the variation of the gas pressure allows one to pass through all the regimes, as shown in the figure below from Dhanaliwala, 2014.

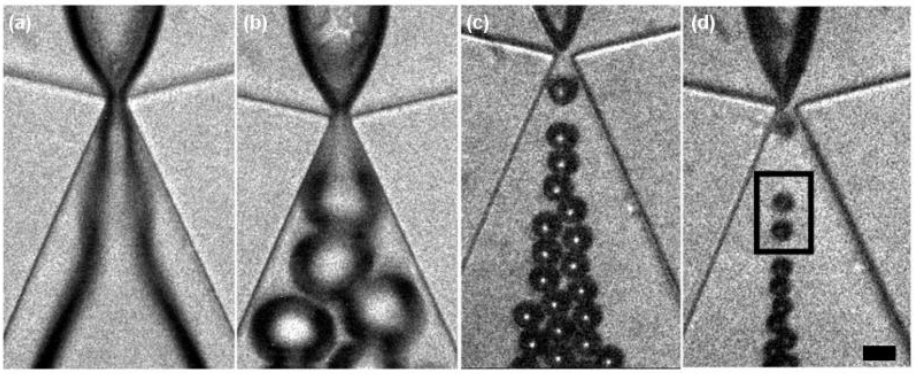

Figure 4.1 – Microbubble production regimes with a flow-focusing microfluidic device from the work of Dhanaliwala (2014). Scale bar 10 µm for all figures. (a)I: Overpressure (<34 µL/min), the gas pressure overwhelms the liquid flow rate and no microbubbles are produced. (b) II: Cylindrical (34-60 µL/min), microbubbles are larger than the height of the microfluidic channel resulting in the production of non-spherical microbubbles. (c) III: Stable (60-80 µL/min), microbubbles with diameters less than the height of the channel but greater than the nozzle width are stably produced. (d) IV: Unstable (80-92 µL/min), microbubbles production becomes unstable and can result in doublet formation (i.e. two microbubbles in quick succession followed by a delay in microbubbles production, black box) and microbubbles with a diameter less than the nozzle width.

The production of the microbubbles in the Unstable regime mentioned before was possible, yielding bubbles with a diameter smaller than the nozzle's width. However, the production couldn't be sustained, resulting in a rapid decrease in the microbubble production rate. In addition, the multiplet formation of the bubbles resulted in an increase in the polydispersity of the microbubbles population. For that reason, the only regime that will be characterized in the present work is the before mentioned Stable regime.

As presented in chapter 3.1, we developed a microfluidic flow-focusing device with a nozzle with a width of 20µm and a height of 16µm, and an expanded reservoir configuration, to reduce the hydrodynamic resistance downstream, ensuring continuous production of the microbubbles (Figure 4.2). In order to guarantee an optimized, reproducible, and stable production, we simultaneously controlled the liquid and gas flow rates with a syringe pump (Standard Infusion Only Pump 11 Elite Syringe Pumps, Harvard Apparatus, USA), and a MFCS-100 pressure controller system (MFCS-100, Fluigent, France, respectively. Figure 4.2A shows the bubbles production downstream of the nozzle, while Figure 4.2C shows the microbubbles closer to the outlet of the microfluidic device. The stable production regime was sustained for a PFC pressure of 1445 mbar and 20µl/min flow rater for the continuous phase (8% PVA + 10mM PBS). Figure 4.2B and D shows the size distribution of microbubbles in the different regions of the microfluidic chip. For Figure 4.2C, we selected the area of analysis marked by the red rectangle, to guarantee that all the bubbles analyzed are in the same focal plane.

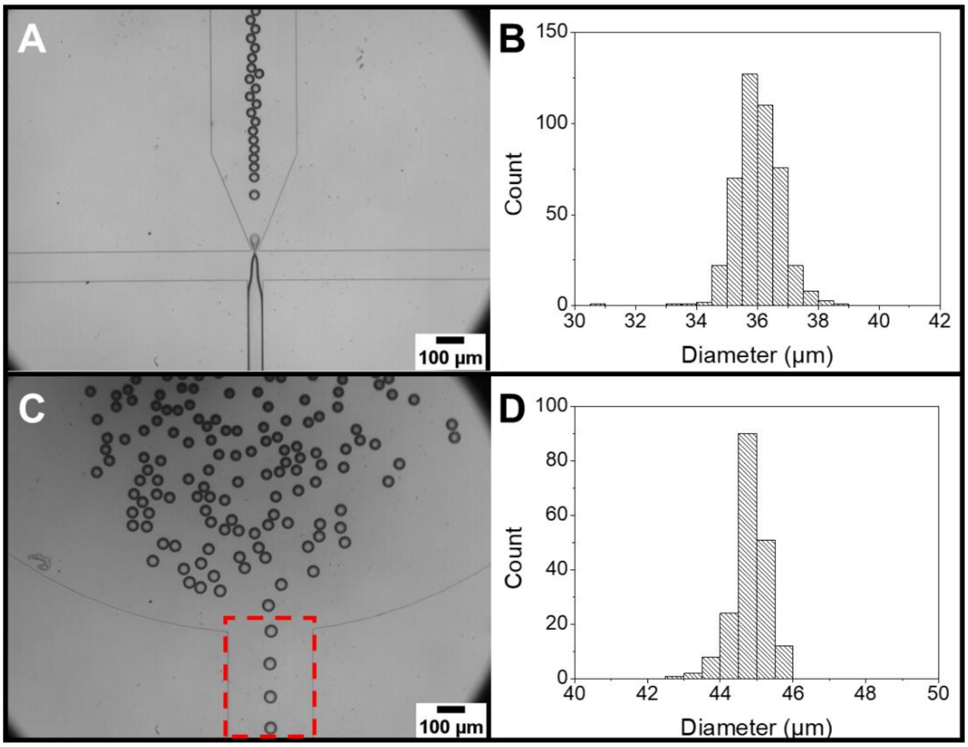

Figure 4.2 – Typical production of microbubbles in a flow-focusing microfluidic device with a nozzle of 20µm width and 16µm height. (A) image of the production of monodisperse microbubble population at the nozzle of the flow-focusing device. (B) The size distribution of the microbubbles downstream of the nozzle. Bubbles presented a mean diameter of 36.0±0.1 µm, a standard deviation of 1.0µm, and a CV of 2.9%. (C) Images of the monodisperse microbubble close to the outlet of the microfluidic device. The red rectangle is the selected area of analysis where the bubbles are in the same plane, and (D) shows the size distribution of the microbubbles close to the outlet. They presented a mean diameter of 44.7±0.2 µm, a standard deviation of 1.4 µm, and a CV of 3.2%.

As shown in Figure 4.2 A, and B, the bubbles produced with the flow-focusing device were monodisperse with high reproducibility. The recently formed bubbles presented a mean diameter of 36.0±0.1 µm, a standard deviation of 1.0µm, and a CV of 2.9%, demonstrating the monodispersity of the bubbles. The same bubble production measured at the outlet of the microchip presented a mean diameter of 44.7±0.2 µm, a standard deviation of 1.4 µm, and a CV of 3.2%. The 24% increase in the diameter can be explained by the decrease in the ambient pressure surrounding the bubbles while approaching the outlet of the chip (closer to atmospheric pressure).

Figure 4.3 shows qualitatively how the pressure inside of the microfluidic flow-focusing device behaves as a function of the position. The mean size distribution for positions A, B, and C in the schematic drawing are 39.0±0.1 (CV of 2.7%), 36.0±0.1 µm (CV of 2.9%), and 44.7±0.2 µm (CV of 3.2%), respectively. Due to the low solubility of the gas core, and high molecular weight of the PFC, together with the reduction of the surface tension, and the lower gas permeability provided by the PVA-shell, the diffusion of the gas core time scale is of the order of minutes. We can estimate the average speed of the bubble based on the known dimensions of the channel, and the recording speed of the bubble's production (1000 fps). The time of residency of the bubble can be derived as the length of the outlet channel (3.2 mm) divided by the estimated velocity of the bubbles (26 mm/s), yielding 0.12s. Therefore, we could assume that after formation, the mass of PFC inside the bubble is constant during its journey inside the channel. Based on this assumption, the size variation is mainly controlled by the ambient pressure inside the channel, hence the variation observed in Figure 4.3 while sustaining a similar CV.

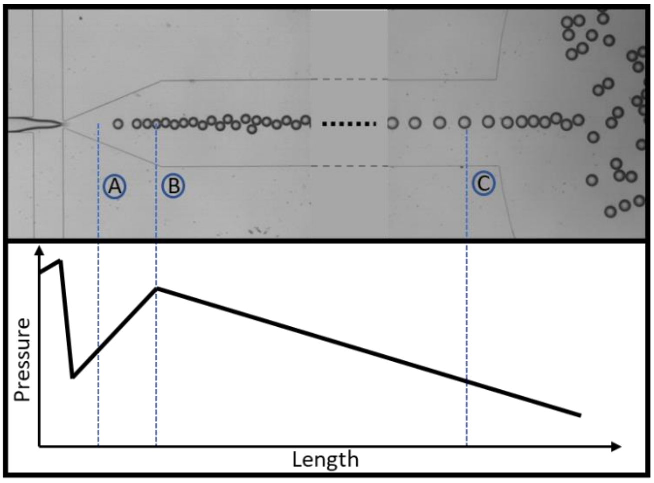

Figure 4.3 – Schematic illustration of the pressure variation in the microchip. Regions A, B, and C presented in the image have a mean size distribution of 39.0±0.1 (CV of 2.7%), 36.0±0.1 µm (CV of 2.9%), and 44.7±0.2 µm (CV of 3.2%), respectively.

Figure 4.4 shows a typical collection of microbubbles over a glass slide. The figure shows the size distribution for the population with a mean diameter of 52.7±0.2 µm, a standard deviation of 1.6 µm, and a CV of 3.1%, demonstrating once again the monodispersity of the population, and a further increase in the mean diameter due to the reduction of the ambient pressure to 1 atm.

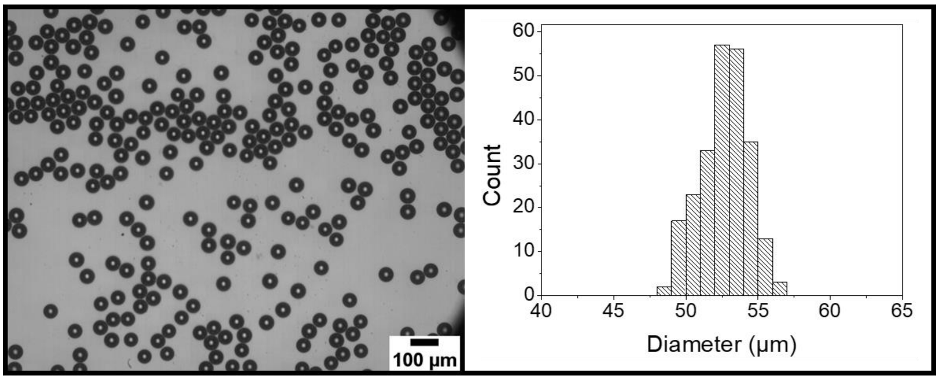

Figure 4.4 – The image on the left shows a typical collection of the produced microbubbles over a microscope glass slide. The image on the right shows the size distribution of the collected microbubbles.

4.2. Freeze-dried monodisperse 40 µm bubble population

This chapter aims to present the geometrical characterization of the freeze-dried microbubbles population, providing a comparison between bulk collection (multilayer configuration), and the monolayer method (described in chapter 3.6).

4.2.1. Bulk and multilayer freeze-drying

A population of monodisperse microbubbles was produced according to the procedure exposed in chapter 3.2. For the bulk freeze-drying, a glass vial was connected with the outlet tubing of the microfluidic device. The produced bubbles, that were pushed out of the chip by the continuous phase, were collected during 4 min with a production rate of 10^4 bubbles/s. The glass vial was then sealed with parafilm to avoid possible contaminations. The vial was placed in the freezer at -25°C, below the glass transition temperature of the PVA (80 °C) for 2h. Before introducing the vial into the freeze-drier, holes in the parafilm cover were pierced to allow water vapor to exit the vial during sublimation. The frozen microbubble population was submitted to the freeze-drying process overnight, at a constant temperature of -45°C and ambient pressure of 0.1 mbar.

Figure 4.5 shows the bulk lyophilizate cake formed during the above-mentioned process. The Figure 4.5E shows the size distribution of the resuspended population with a mean diameter of 56.9 ±1.2 µm, a standard deviation of 17 µm, and a CV of 29%. Qualitative access of the lyophilizate cake before resuspension (Figure 4.5C), shows that bubbles were already polydisperse in this configuration, suggesting that the degradation process happened before the rehydration of the bubbles.

By taking as a reference the mean diameter of the population collected (Figure 4.4) of approximately 52 µm, one can estimate the maximum rising time of a bubble in the bulk, through the use of the Stoke law for drag force. The assumption of no interference between particles on which Stokes' law relies is not perfectly verified for the microbubbles configuration that we have, but it can still provide an order of magnitude that we need for this analysis. A simple force balance can be made over the bubbles, accounting for buoyancy (F_b), weight (F_w), and drag (F_d) as follows:

$$F_b = \rho_l \, \forall_b \, g \qquad ; \qquad F_w = \rho_g \forall_b \, g \qquad ; \qquad F_d = 3\,\pi\,\mu\,D\,u \qquad (4\text{-}1)$$

$$\sum F = m\,\frac{du}{dt} \rightarrow \rho_g \forall_b\,\frac{du}{dt} = \left(\rho_l - \rho_g\right)\forall_b\, g - 3\,\pi\,\mu\,D\,u \qquad (4\text{-}2)$$

where $\rho_g (\sim 1\frac{kg}{m^3})$ is the PFC density, $\forall_b$ is the bubble volume, u is the bubble speed, $\rho_l\,(\sim 1000\frac{kg}{m^3})$ is the continuous phase density, $g\,(9.81\frac{m}{s^2})$ is the gravitational acceleration, $\mu\,(\sim 0.01\,Pa.s)$ is the liquid viscosity, and $D\,(\sim 52\,\mu m)$ is the bubble's diameter. By integrating the second-order differential equation we obtained:

$$x = U_t\,t + \frac{U_t}{\left(\frac{18\mu}{\rho_g D^2}\right)}\left[\exp\left(-\frac{18\mu}{\rho_g D^2}t\right) - 1\right] \quad ; \quad U_t = \left(\frac{\rho_l}{\rho_g} - 1\right)\frac{\rho_g\,g}{18\,\mu}\,D^2 \qquad (4\text{-}3)$$

where U_t is the terminal velocity of the bubbles. Therefore, the maximum time that a bubble would take to rise to the top of the liquid volume inside the vial ($h \approx 5\,mm$) is approximately **34 ms.**

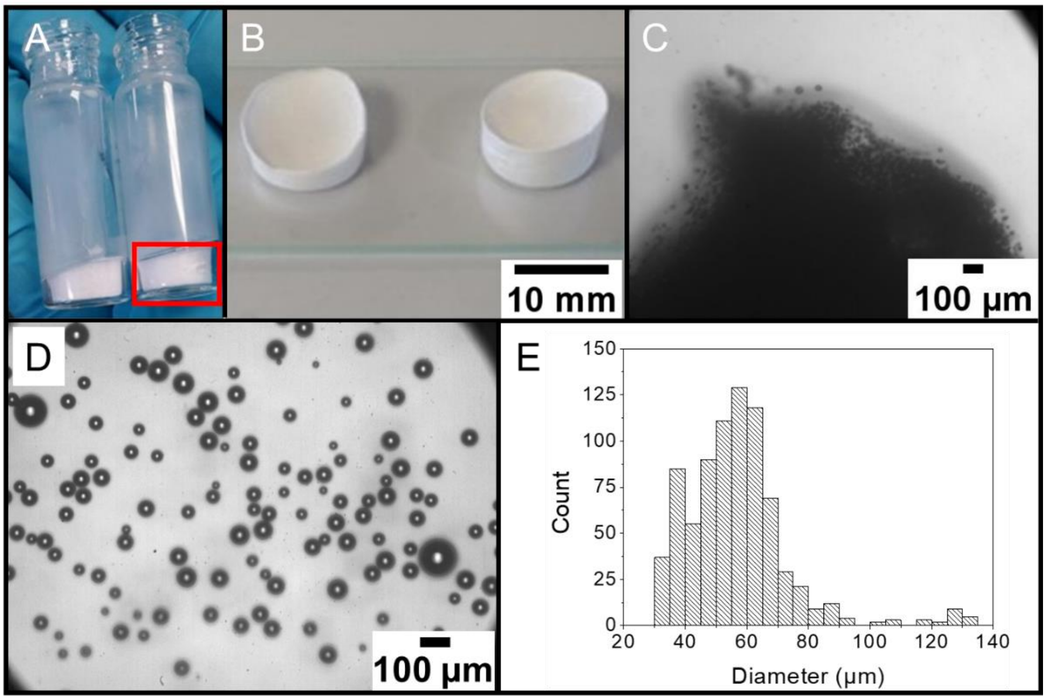

Figure 4.5 – Typical image of the freeze-dried cake collected in bulk before resuspension with a buffer saline solution (10mM PBS). A) Shows the cake inside of the glass vial, B) shows the freeze-dried cake over a microscope glass slide, and C) shows an optical image of the cake powder, with the presence of microbubbles. D) Shows an image of the freeze-dried population after resuspension, and E) show its size distribution with a mean diameter of 56.9 ±1.2 µm, a standard deviation of 17 µm, and a CV of 29%. Qualitative access of the lyophilizate cake before resuspension, shows that bubbles were already polydisperse in this configuration, suggesting that the degradation process happened before the rehydration of the bubbles.

The next step is to make a comparison with the time required for the whole volume of bubbles suspension inside the vial to freeze. First, we calculated the dimensionless Biot number for the suspension, to obtain the ratio of the thermal resistance inside of the body and at its surface

$$Bi = \frac{h_c L}{k} \tag{4-4}$$

The thermal conductivity, k, for water at 25°C is approximately 0.6 W/(mK), and the characteristic length L of the vial is 0.005 m (ratio between the body volume, ∀, and its surface area, A_s). The convective heat transfer, h_c, for air in free convection can vary from 2.5 to 25 W/(m^{2}K). For the case in which h_c takes its maximum value, the Biot number is 0.2 (Bi < 1), meaning that the diffusion inside the body is much higher than the convective heat exchange. Thus, we can consider the temperature gradients inside the body to be negligible, yielding the simplifying assumption that the temperature inside the body is spatially uniform. By making a global energy balance over the suspension volume we obtain the following equation:

$$\frac{T - T_\infty}{T_0 - T_\infty} = \exp\left[-\left(\frac{h_c\ A_S}{\rho\ \forall\ c}\right) t\right] \tag{4-5}$$

where T is the temperature of the solution at time t, T_∞ is the temperature in the freezer, T_0 is the initial temperature of the solution, and c is the thermal capacity of the liquid. We proceed to estimate that the time that would take for the volume of liquid to start to freeze (T=0°C). For the following parameters h_c=25, $T_\infty = -25°C, T_0 = 25°C,\ A_s = 314\, mm^2,\ \rho = 1000\, kg/m^3$,∀=1570 mm^3, and c= 4179 J/(kg K), the starting freezing time of the volume is $\boldsymbol{t \approx 580\, s}$**.**

It is thus possible to conclude that the time taken by the bubbles to rise to the surface is approximately four orders of magnitude smaller than the time that the solution, where the bubbles are suspended, takes to start freezing. Thus, a creaming effect (agglomeration of the bubbles on the surface) occurs, leading to a degradation of the monodispersity, due to coalescence and Ostwald ripening phenomena, which explains the polydispersity before the freeze-drying process.

For the multilayer freeze-drying, a population of monodisperse microbubbles was produced according to the procedure exposed in chapter 3.2. The microbubbles were collected as spots over a microscope glass slide in a manner similar to the one described in chapter 3.6 for the monolayer. The difference lays in the fact that the glass slide was not exposed to the O_2 plasma treatment, making the glass less hydrophilic, therefore reducing the capacity of the bubbles to spread on the surface. Also, the collection time for each spot was bigger, yielding bigger droplets, thus resulting in a multilayer configuration. The glass slide was placed in the freezer at -25°C, below the glass transition temperature of the PVA (80 °C) for 2h. The frozen microbubble population was submitted to the freeze-drying process overnight, at a constant temperature of -45°C and ambient pressure of 0.1 mbar.

Figure 4.6 shows a typical multilayer collection of microbubbles over a glass slide, and its size distribution after resuspension. The insert shows the size distribution for the population with a mean diameter of 41.5±2.2 µm, a standard deviation of 23.8 µm, and a CV of 57%.

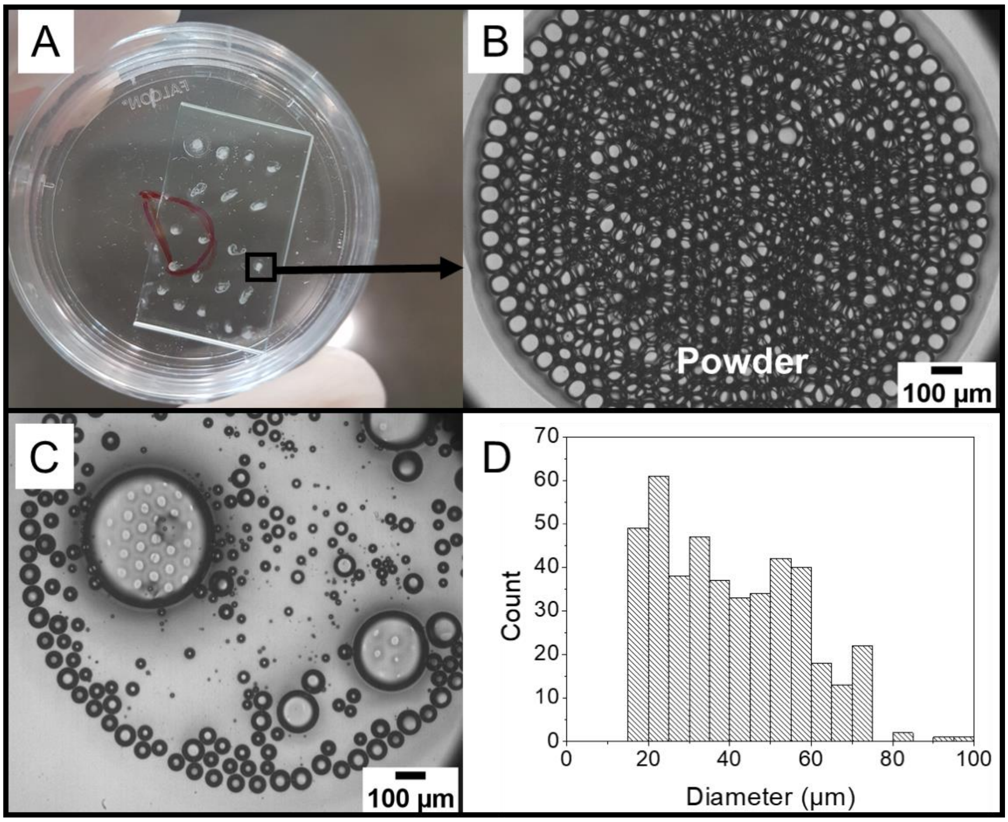

Figure 4.6 – This set of images shows the effect of a double layer collection of monodisperse microbubbles population over their polydispersity during freeze-drying. (A) The typical image of freeze-dried spots over a glass slide, (B) A freeze-dried powder of microbubbles in a double-layer configuration, (C) Freeze-dried population after resuspension, and (D) shows the size distribution of the resuspended microbubbles. The population presented a mean diameter of 41.5±2.2 µm, a standard deviation of 23.8 µm, and a CV of 57%

Even though the reduction in the liquid volume reduces the freezing time, the interactions between the microbubbles in the multilayer configuration is still detrimental to the stability of bubbles during the freeze-drying process. The origin of the in-plane interactions resulting from the close-packed state is not fully understood. However, it reinforces the idea that reducing the interaction between the bubbles is key to preserving its monodispersity during freezing and freeze-drying.

4.2.2. Monolayer collection of monodisperse bubbles

The lyophilisates we obtained, in the process described in Material and Methods (Chapter 3), were uniform in size as shown in Figure 4.7. Figure 4.7A and Figure 4.7C show bubble populations before and after rehydration and resuspension in PBS solutions, respectively. The detachment from the glass slide and, thus, resuspension of the bubbles took only a few seconds. After this time, bubbles started to freely float in PBS. The initial size distribution was measured when they were still located on the glass. It remains unchanged during the floating.

The inserts show the size distribution for the lyophilizate with a mean diameter of 42 µm, a standard deviation of 4 µm, and a CV of 9%, and the size distribution for the resuspended bubbles with a mean diameter of 44 µm, a standard deviation of 3 µm, and a CV of 6%.

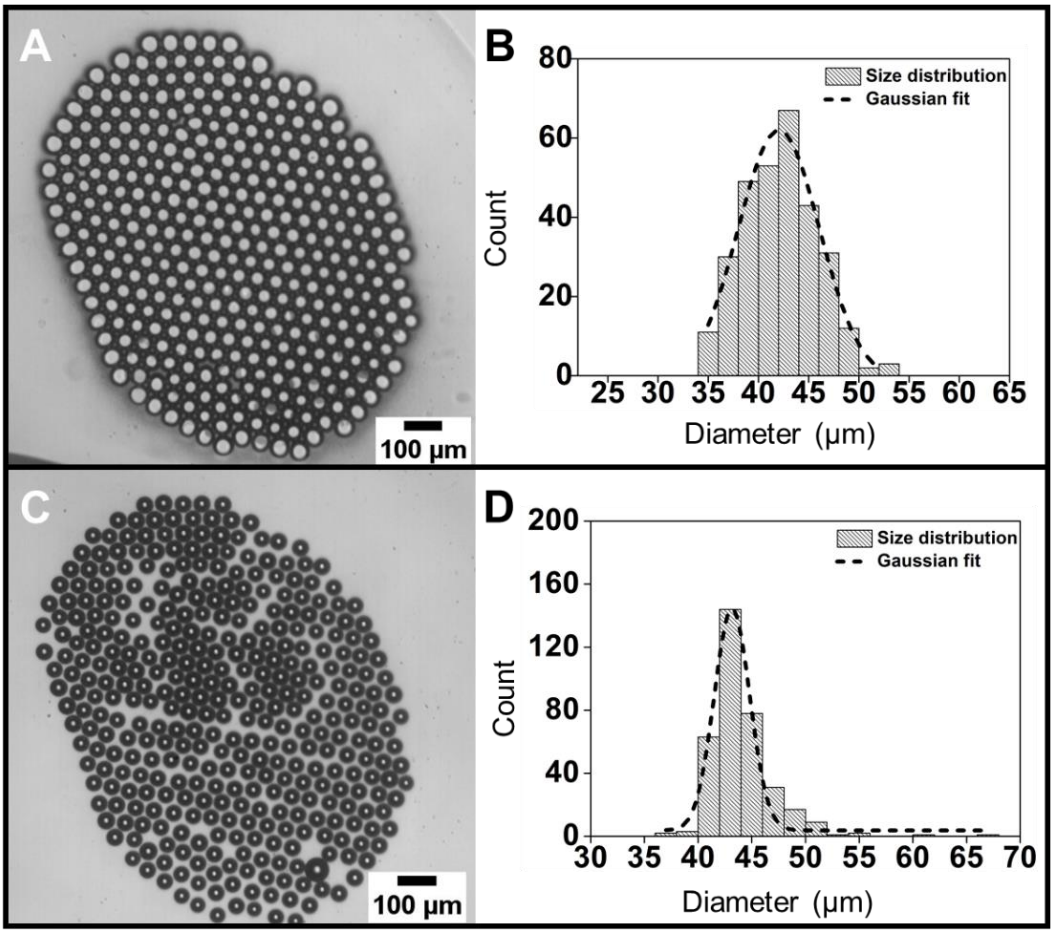

Figure 4.7 – The images and size distribution (bars represent the size distribution and dots represent Gaussian fits) of lyophilisates and resuspended bubbles. (A) Optical images of one spot of the lyophilizate, consisting of freeze-dried bubbles deposited onto glass slides. (B) Size distribution of the lyophilisates 42 µm, with a standard deviation of 4 µm, and a CV of 9%, in average diameters of the lyophilisates. (C) Resuspended bubbles and (D) their size distributions (insets): the average diameter of the bubbles is 44 µm, with a standard deviation of 3 µm and a CV of 6%.

The bubbles shown in Figure 4.7A form a closed-packed structure. This is because, with the concentrations at hand, the system stands above the jamming transition (Furuta *et al.* 2016). Increasing the volume fraction of the bubbles leads to close-packed states, as shown in Figure 4.7A, whereas increasing the volume fraction of the liquid by decreasing the size of the bubbles for the same population unjams the system (as shown will be presented in chapter 4.3). The size distribution measured for the resuspended bubbles shows a monodispersity larger than the 3% dispersion of the initial fresh bubble population, but still low. The reason originates from the fact that freeze-dried bubbles interact and undergo deformation due to the close packing. This behavior also indicates that, by forcing bubbles to be collected as a single monolayer and freeze-dried in such a configuration, even though in-plane interactions exist, they slightly degrade the size uniformity but do not destroy the monodispersity.

It is possible to see that there is a reduction of 16% in the mean size distribution from the collected bubbles, and the bubbles that were resuspended after freeze-drying.

We can conclude that in the process presented for freeze-drying the monodisperse bubbles population was successfully achieved, yielding a CV of 3% and 6% before and after the freeze-drying process, respectively.

4.3. Microfluidic flow-focusing 5 µm microbubbles production

As presented in chapter 3.1.2, we developed a microfluidic flow-focusing device with a nozzle of 5µm width and 5µm height, and an expanded reservoir configuration, to reduce the hydrodynamic resistance downstream, ensuring continuous production of the microbubbles (Figure 3.2). Due to the reduction in the nozzle’s size, clogging of the system by PVA aggregates made it impossible to sustain a stable production of monodisperse microbubbles. Thus, we introduced some modifications to the classical flow-focusing device used in the chapter before, namely the anti-clogging system (tangential filtering), step emulsification (reduce resistance downstream the nozzle), and a “pusher” (a system developed to push de bubbles out of the microfluidic device in a controlled concentration). The anti-clogging system is designed to deflect the majority of the continuous phase flow from the flow-focusing channel, to deviate large aggregates through inertia. On the other hand, the amount of continuous phase that is displaced for the bubble production becomes very small; leading to the aggregation of the microbubbles in the channel’s outlet, yielding coalescence of the population. Therefore, the implementation of a tubing inlet close to the outlet of the device, to push the bubbles out of the system, became mandatory. Thus, the addition of a “lateral collection” system, comprising the positioning of a tube axially aligned with the production channel of the microfluidic device. The incorporation of all these features, which are described in details in chapter 3.1.2, made it possible to sustain a stable monodisperse microbubble’s production for at least 16 continuous hours.

Figure 4.8A shows the bubbles production in the 5µm microfluidic device, in which we were able to obtain a 10-15kHz bubbles production. The stable production regime was sustained for a PFC pressure of 2300 mbar, continuous phase (8% PVA + 10mM PBS) pressure of 4200 mbar, and 2µl/min flow rater for the pusher (8% PVA + 10mM PBS). Figure 4.8B shows a typical microbubble collection with a mean diameter of 5.70±0.01 µm, a standard deviation of 0.2 µm, and a CV of 3.8%, demonstrating the monodispersity of the bubbles’ population.

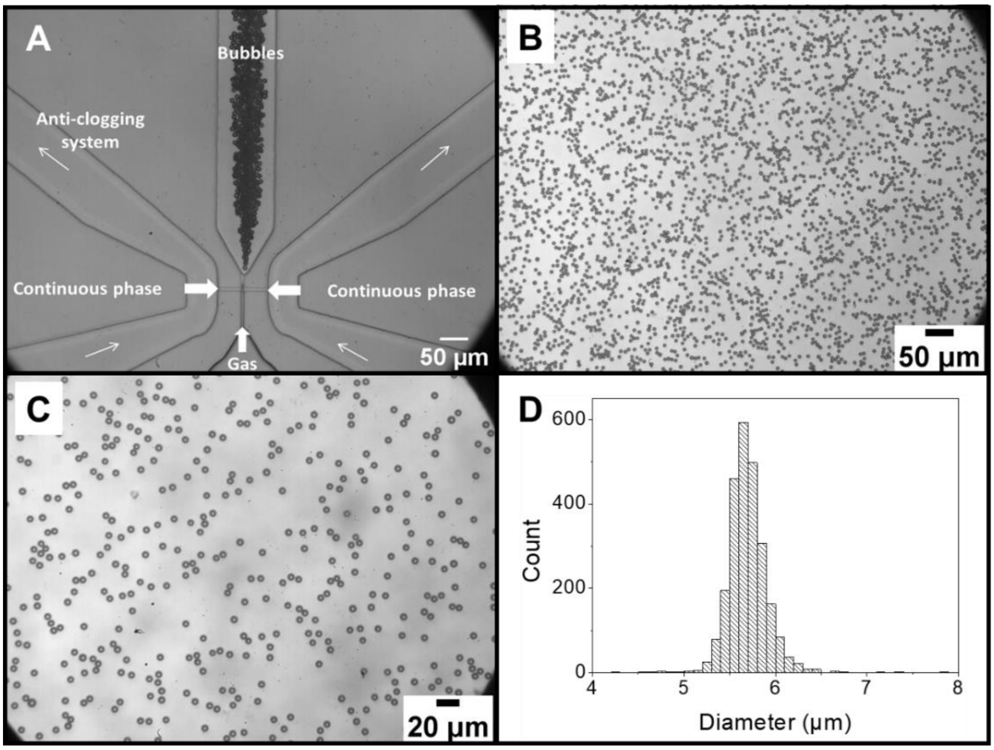

Figure 4.8 – Microfluidic generation of 5 µm in diameter poly(vinyl alcohol) (PVA) ‘fresh’ microbubbles (i.e., directly coming out of the microfluidic device and thereby not resuspended from a lyophilisate). (A) Monodisperse bubbles were generated in the central channel located between the “river” channels (i.e., anti-clogging system or tangential filtering) and after the gas channel. Bubbles exited the device without any coalescence. (B) Optical images with 20x magnification of freshly generated bubbles were collected in a monolayer manner on a glass slide, (C) is the optical image with 40x magnification of the same microbubble population. (D) Shows the size distribution of the collected bubbles showing average sizes, standard deviation, and coefficient of variation (CV) respectively equal to 5.70±0.01 µm, 0.2 µm, and 3.8%.

The reduction of one other magnitude of the bubbles size increased the rising time for the bubble. Using the same parameters described before, for a 5µm diameter bubble we obtain a maximum rising time of approximately 3.1 seconds, which is 100 times larger than the rising time of the 50 µm bubbles. However, it is still 2 orders of magnitude smaller than the time that it takes for the bulk volume to start freezing. Thus, the assumption of coalescence and Ostwald ripening prior to freezing is still valid for the 5µm bubbles case. In addition, the size reduction contributes to a more unstable bubbles' population, as it possible to verify, as an approximation, by using the Epstein-Plesset equation for free gas bubbles dissolution over time. The 50 µm bubble takes approximately 20 seconds to get dissolved while the 5µm bubble dissolves in approximately 100 ms, leading to 2 orders of magnitude faster dissolution. These factors reinforce the need for the monolayer collection, in which faster freezing occurs, and a reduced bubble to bubble interaction is obtained.

Figure 4.9 shows typical optical imaging of the central part of a lyophilizate spot, comprising freeze-dried bubbles deposited in a glass slide. The measured average diameter of the population was 5.80±0.03, with a standard deviation of 0.3µm and CV of 5%. During the freeze-drying process, water is removed from the samples, together with the gas content inside the microbubble, which puts the microbubbles in a surface tension-free configuration. Therefore, it is possible to see that the surface of the bubbles in the lyophilisate are not uniform circles. The digital imaging process technique used to evaluate the microbubbles' size distribution is based on the Circle Hough Transform (CHT) extraction. The algorithm basically works by finding circle candidates by "voting" in the Hough parameter space and then selecting local maxima in an accumulator matrix. The limitation is that non-circular objects are interpreted as circles, leading to a bigger estimation of the size of the bubbles, which would explain the increase in the mean diameter for the lyophilisate population.

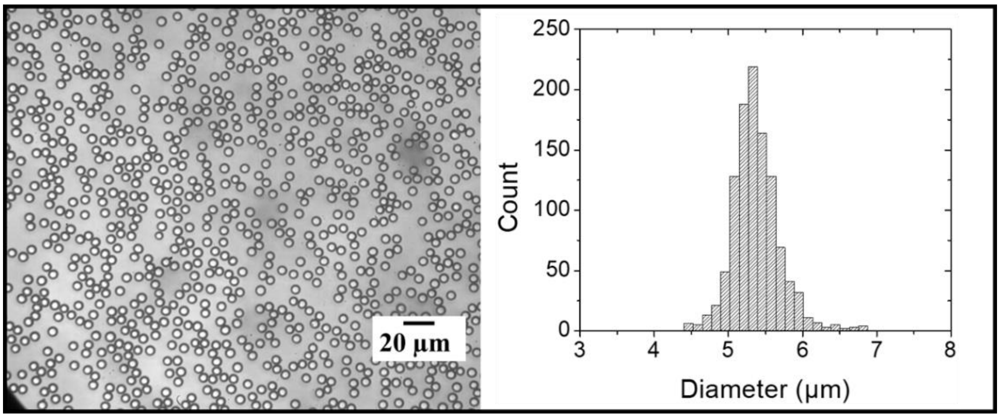

Figure 4.9 – The images and size distribution of lyophilisates and resuspended bubbles. (Left) The optical images of the central part of a lyophilisate spot consist of freeze-dried bubbles deposited on a glass slide. (Right) Shows the size distribution of the lyophilisate as 5.8±0.03 (standard deviation of 0.3 and CV of 5%) µm in average diameter.

Figure 4.10 shows typical environmental scanning electron microscopy (ESEM) images of the 5 µm freeze-dried microbubbles population. As mentioned above, it is possible to see that in these stress-free configurations the microbubbles do not present a uniform spherical shape. However, the shells look uniform, which suggests acceptable homogeneity of the lyophilization conditions across the population. Figure 4.10B shows a broken bubble in an ESEM image. Its shell thickness was estimated as ~70 nm as shown in the inset and the illustration of Figure 4.10B. This is smaller, but still consistent with (Poehlmann *et al.* 2013), who reported PVA shell thicknesses ranging between 120 nm and 230 nm. That difference can be explained by the fact that Poehlmann used a PVA with longer chains in their formulation, with a molecular weight of 70 kg/mol, which is almost 3 times larger than the one used in this study (13-23 kg/mol).

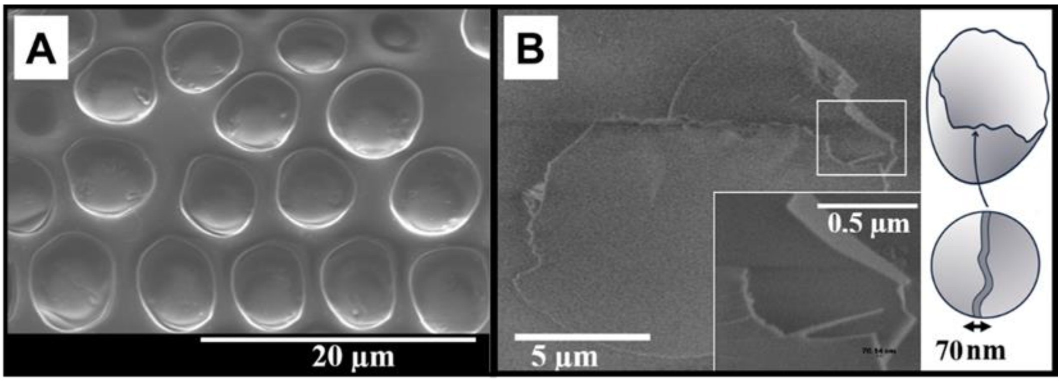

Figure 4.10 – A) Environmental scanning electron microscopy (ESEM) of the 5 µm lyophilisate. (B) Scanning electron microscopy (SEM) image shows a broken bubble and the magnified image, shown as an inset and an illustration (right-hand side), measuring the thickness of the shell as ~70 nm.

Figure 4.11 shows a typical optical image of the freeze-dried microbubbles after resuspension with a PBS solution. The measured mean diameter was 5.48±0.01 µm, a standard deviation of 0.3 µm, and a CV of 5.7%. Despite an increase in the CV of the resuspended bubbles in comparison with freshly generated, the population remains monodisperse. We may conclude that the monodispersity of the size is accurately conserved by the collection and freeze-drying process.

It is interesting to observe that the mean diameter of the microbubbles' population was reduced by approximately 4%, which is a much smaller variation compared to the 40 µm microbubbles population (20% reduction in size).

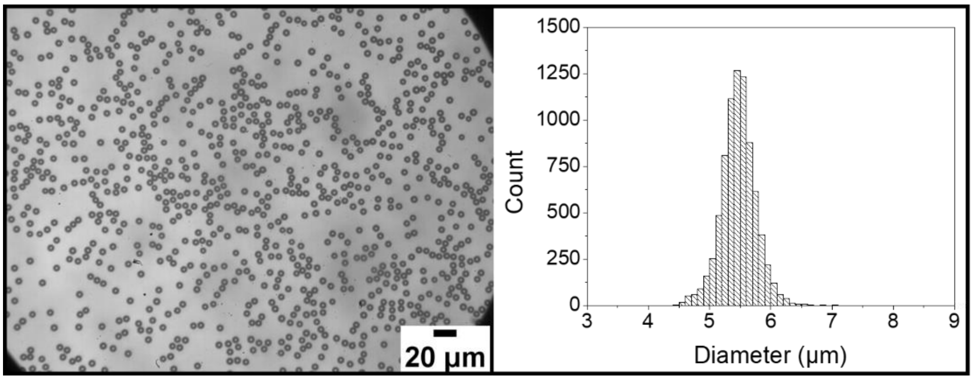

Figure 4.11 – The images and size distribution of resuspended bubbles. The insert shows the average diameter of the bubbles as 5.48±0.01 µm, a standard deviation of 0.3 µm, and a CV of 5.7%.

4.4. Microbubbles Stability

4.4.1. Surface tension measurement

The presence of surfactants in the encapsulating shell aims to stabilize the bubbles against coalescence, diminishing the surface tension and, therefore, reducing the gas dissolution from the core into the surrounding medium (Ferrara *et al.*, 2007). Thus, we measured the surface tension (γ) at the liquid-air interface of the PVA solution, comprising of 8wt% PVA and 10mM PBS. The results were compared with the measurements made by Pessoa *et al.* (2020), for the lipid composition of DSPC: DSPE-PEG2000 (9:1 molar), with different liquid phases. The lipid composition was chosen due to its proven stabilization of microbubbles (Gnyawali *et al.*, 2017; Talu *et al.*, 2007).

Figure 4.12 shows that the PVA reduces the surface tension by 30 mN/m, to the value of 42.70±0.59 mN/m. When comparing the PVA solution with the lipid formulations, it is possible to see that the SoyPC:DSPE-PEG: PCDA presented a lower surface tension (37.1± 0.6 mN/m). The author (Pessoa *et al.,* 2020) concludes that the small surface tension value is correlated with the addition of PCDA. However, the stability of the shell comes at the expense of a UV-polymerization post-treatment process that polymerizes the lipid shell around the microbubble. Thus, when thinking about an industrialization process, this technique would not be the most efficient. These results emphasize the improved surface tension of the PVA-shelled microbubbles in comparison with typical lipid bubbles, which are reported to be similar to the FDA-approved commercial products DEFINITY® (Lantheus Medical Imaging, USA) (Gnyawali *et al.*, 2017) and SonoVue® (Bracco Diagnostics, USA) (Kooiman *et al.*, 2014).

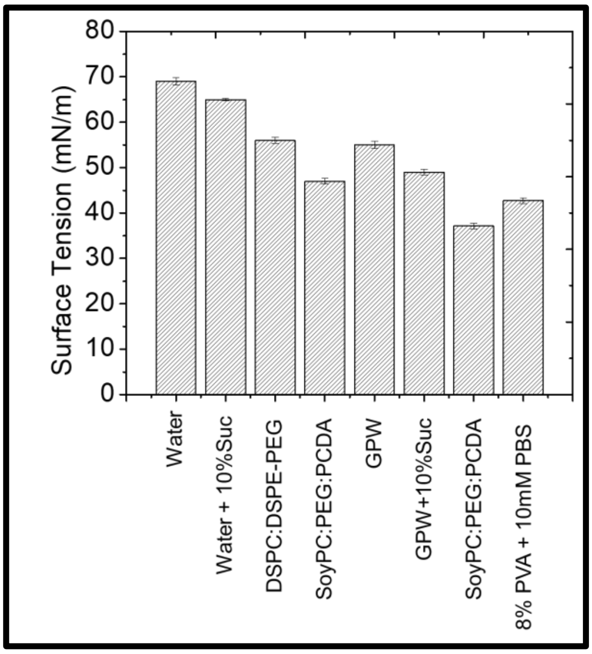

Figure 4.12 – Surface tension measurements using the pendant drop technique. The results extracted from Pessoa *et al.,* (2020) were combined with the measured surface tension for the 8% PVA + 10mM PBS continuous phase.

4.4.2. Microbubble stability

For the 5µm bubbles population, we measured their stability over time after production. The bubbles were collected on top of a microscope glass slide, and images of the suspension were taken over time. The size distribution of the microbubbles was measured for each time frame and the monodispersity of the population was verified as a function of time. Figure 4.13 shows the microscopic images and size distribution histograms at different time periods.

The microbubble's mean diameter at the start of the experiment (t=0 min) was 5.20±0.02 µm, with a standard deviation of 0.1 µm, and a CV of 2.0%. The CV was sustained below 5% during the first 10 minutes, reaching 7.8% at the 15 minutes mark. Some groups have established the term 'quasi-monodisperse' for particles that have CV values below 16% (Izumida *et al.*, 2005, De La Veja *et al.*, 2013). After 30 minutes, the microbubbles reached a CV of 17%, exiting the quasi-monodisperse configuration, becoming polydisperse. It is possible to see that Ostwald ripening was the main mechanism contributing to making the population polydisperse, through the growth of bigger bubbles at expense of the smaller ones.

The study of Paradossi *et al.* (2005) for PVA-shelled microbubbles reports a shelf life of a few months, and much higher stability compared to the bubbles produced in this study. This major difference is due to multiple factors. First, the authors use in their formulation a higher molecular weight PVA (70kg/mol), followed by a cross-linking process. This approach results in a microbubble of approximately 3µm, with a shell thickness of 0.7µm, a value 10 times bigger than the one obtained for our polymeric bubbles. The increase in stability comes at the expense of the echogenicity of the microbubble when exposed to an ultrasound field. The bubble becomes stiffer, increasing the damping of the emitted ultrasound pulse (mechanism will be described in detail in chapter 5.2.2), which works against the main purpose of the microbubbles in this study, of being an ultrasound contrast agent. Lastly, the authors are not tracking the monodispersity of the microbubble's population, since their original sample was already polydisperse.

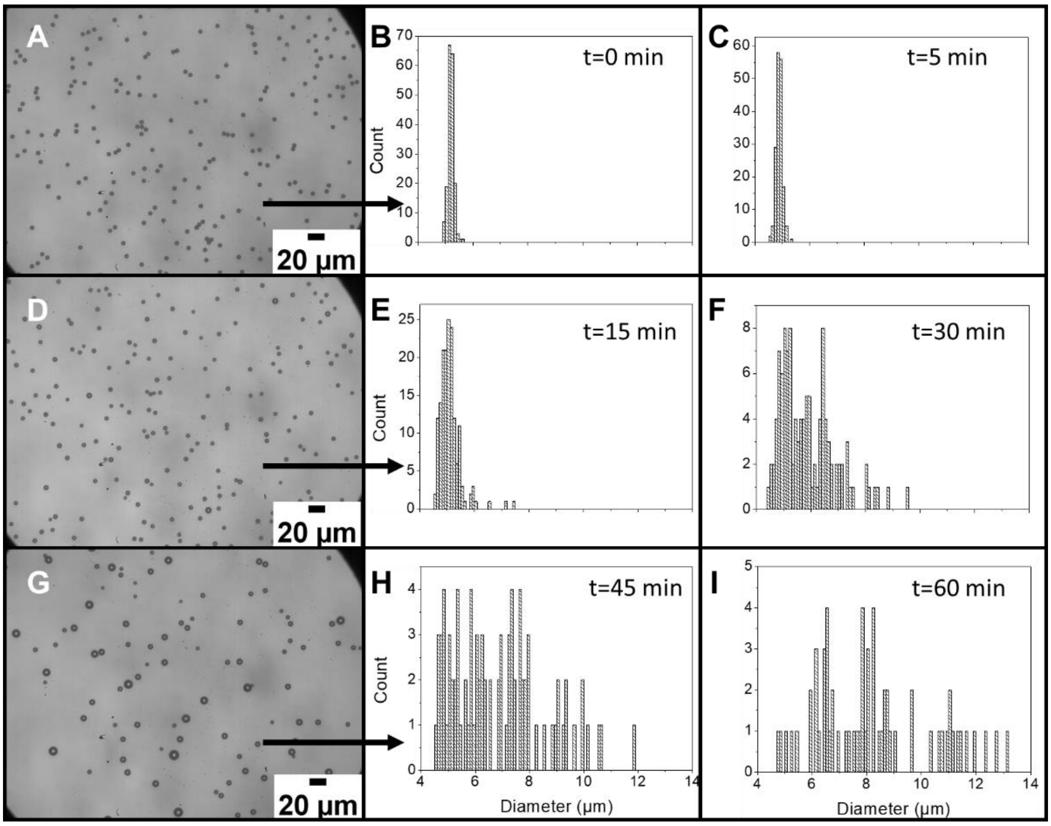

Figure 4.13 – A stability test of typical PVA-shelled monodisperse microbubbles. The size distribution of the collected population was evaluated as a function of time. (A) Optical image of the bubbles at t=0, and (B° its size distribution with a mean diameter of 5.2 µm (CV of 2%). (C) Shows the size distribution of the microbubbles after 5 minutes of collection, with a mean diameter of 4.89 µm (CV of 2.3%). (D) An optical image of the microbubbles after 15 minutes of collection, and (E) shows its size distribution of 5.10 µm (CV of 7.8%). (F) shows the size distribution of the population after 30 minutes, with a mean diameter of 5.9 µm (CV of 17%). (G) Optical image of the microbubble after 45 minutes of collection, (H) with a mean diameter of 6.83µm (CV of 24.7%). (I) Show the size distribution of the microbubbles population after 1 hour from the collection, having a mean diameter of 8.23µm (CV of 25.5 %).

4.5. Final remarks

In the present work, for the first time, we freeze-dried monodisperse microbubbles without degrading their monodispersity. This strategy unlocks the bottleneck of transportation and storage of monodisperse microbubbles in the form of a lyophilisate, i.e., a powder. We solved this problem by developing two different aspects. The first is the optimization of bubble formulation along with a cryoprotectant. The second is maintaining the bubbles, during collection, pre-freezing, and freeze-drying steps, in the form of monolayer spots deposited on a glass surface.

Although we developed this method on a polymer-shelled microbubble, in principle, our method can be applied to obtaining freeze-dried monodisperse lipid or protein-shelled microbubbles.

5. ACOUSTIC CHARACTERIZATION OF FREEZE-DRIED MONODISPERSE MICROBUBBLES

This chapter provides, at first, a literature review of the basic principles of ultrasound imaging, and the elementary aspects of its physics. Secondly, we describe the dynamics of free bubbles and review the models developed throughout the years. Then, the dynamics of coated microbubbles and the models used to characterize them will be addressed. Finally, important concepts for ultrasound contrast agent characterization will be presented and discussed: scattering, absorption, attenuation.

By taking into account the parameters that influence microbubbles' dynamics and acoustic response, we were finally able to characterize a new generation of lyophilized monodisperse contrast agents.

5.1. Fundamentals of Ultrasound

In order to accurately interpret ultrasound images, and the acoustic response of ultrasound contrast agents, a basic understanding of the physical principles involved in ultrasound imaging techniques is crucial. Therefore, this chapter aims to provide an overview for the readers that do not have a background in ultrasound imaging and ultrasound contrast agents.

This sub-section will present a basic description of elementary aspects of the ultrasounds' physics. The goal is to provide the reader with a brief introduction to the ultrasound field. Those interested in a more complete description of the acoustics of waves can refer to the books of Achenbach (1973), and Kinsler *et al.,* (2000), or other dedicated books.

5.1.1. Period, Frequency, and Wavelength

The characteristic variables describing the propagation of a monochromatic wave in time and space are period, T, frequency, f, and wavelength λ. These variables are related to each other as follows:

$$\lambda = \frac{c}{f} = cT \tag{5-1}$$

where *c* is the speed of sound or wave velocity in the medium of propagation.

For clinically used ultrasound, we can find typical values of frequency ranging from 2 to 15 MHz. In soft tissues, the typical sound velocity is *c* ≈1540 m/s, implying that the frequencies utilized in medical ultrasound imaging produce wavelengths ranging from 200 µm to 1 mm (*f=1MHz to f=7.5MHz*).

5.1.2. Phase and Group Velocity

There are two types of sound velocities in a medium that are fundamentally different. The first is the phase velocity, which corresponds to the propagation velocity of a given phase belonging to a single frequency in the periodic wave. If the phase velocity is a function of the frequency or wavelength, the propagating medium is considered to be dispersive, which is the case for all attenuating media: in other words, the different frequencies in a finite signal do not propagate at a constant velocity, which derives from the linearity and causality principles (O Donnell Miller 1980). The second type of velocity is called the group velocity which physically corresponds to the velocity at which a wave packet is carried along the propagation direction (which can be often assimilated to the energy velocity – see e.g., wave propagation and group velocity, Brillouin, 2013).

The phase and group velocity can have different values, depending on the medium in which the wave is propagating. This might occur in a dispersive medium, which can potentially affect the accuracy of the speed of sound measurements (Laugier and Haiat 2011). Thus, being aware of the velocity dispersion is very important to assure accurate measurements. To determine the velocity dispersion (or acoustic dispersion) a broadband transmission method, where the rate of change in phase velocities as the radiated waves pass through a given medium is measured. The phases as a function of the frequencies of the broadband pulse can be accessed by simple Fourier transforming the signal. By knowing the distance that the signal traveled, it is possible to infer the phase velocity for each frequency It is relevant to note that the attenuation coefficient, an important parameter for characterizing ultrasound contrast agents, is related to the velocity of dispersion through the Kramers–Kronig relationship which reflects causality. More specifically, in the dispersion relation for acoustic propagation, the real part of the compressibility is related to the phase velocity, and the imaginary part is related to the attenuation coefficient. By combining this relation with the Kamers-

Kronig relation, it is possible to derive, theoretically, an expression linking the phase velocity and the attenuation coefficient (O Donnell Miller *et al.,* 1980). However, it is worth noting that in practical terms this method can be dangerous since it assumes that the acoustic response is known for an infinite frequency range.

5.1.3. Acoustic pressure

The definition of stress is a force applied by a unit area in a given medium. All stresses can be expressed as a combination of pure shear stress and pure compression (Achenbach, 1973). The combination of compression and shear stress can be expressed in terms of the stress tensor in an anisotropic solid. This is not the case for fluids, which can only support pure compression, called pressure. A compressional wave propagating in fluids results in pressure changes due to the succession of compression and expansion. The difference between the total instantaneous pressure and the ambient pressure is called acoustic pressure or sound pressure. It is important to note that, in fluids, we can only observe longitudinal waves.

5.1.4. Acoustic Impedance

In fluids, the particles of the medium are subjected to displacements around their original position, when exposed to an acoustic wave. The velocity associated with these displacements is called acoustic particle velocity. The sound velocity defined previously must be differentiated from the speed of motion of the particles due to a sound wave. It is possible to derive a relation between both velocities for a plane wave propagating in a lossless infinite medium as follows:

$$p = \rho\, c\, v = Zv \tag{5-2}$$

where p is the acoustic pressure, ρ is the mass density of the medium at rest, c is the speed of sound, and v is the particle velocity. Z defines the characteristic acoustic impedance of the medium, i.e., the product of the density of the medium times the speed of the sound in that medium. In electrical engineering, electrical impedance measures the opposition that a system presents to an electrical current resulting from a voltage applied to the system. In acoustics, a close analogy is made, in which the acoustic impedance represents the opposition that the systems present to an acoustic flow resulting from an acoustic pressure applied to the system.

Acoustic impedance is a very powerful concept in ultrasound imaging, and its effects become noticeable at interfaces between two different tissues, driving the rate of transmission and reflection of a sound wave. This concept will be expanded in the upcoming chapter 5.1.7.

5.1.5. Acoustic Intensity

Acoustic intensity characterizes the energy transported in an ultrasound wave. This intensity is defined as the energy transmitted per unit time and unit area in the direction normal to the considered area. Usually in medical ultrasound, acoustic intensity is measured in W·cm−2, and its value can be related to the sound pressure as follows:

$$I = \frac{p^2}{2Z} \tag{5-3}$$

This relationship for the intensity of a monochromatic wave is only valid at the focus of a focused transducer or in the far-field of an unfocused transducer where the wavefront can be considered as a planar wave (Laugier and Haiat 2011).

5.1.6. The Speed of Sound

The speed of sound is a characteristic of the medium for linear propagation regimes, which are defined by small perturbation or wave amplitude. In this regime, the speed of sound is independent of the wave amplitude, being only a function of the properties and geometrical characteristics of the medium. In such conditions, we can approximate the medium as being a homogeneous effective medium) with and effective elastic modulus, M_e, and effective mass density ρ_e. (Shutilov, 1988). The elastic and geometrical characteristics of the medium govern the effective elastic modulus, which controls the stiffness of the medium concerning a given type of wave. The effective mass density is related to the inertia of the propagating medium. Thus, the speed of the sound c can be expressed as follows:

$$c = \sqrt{\frac{M_e}{\rho_e}} \tag{5-4}$$

In more realistic systems, the speed of the sound can also depend on the amplitude of the wave, as mentioned before, leading to nonlinear wave propagation, creating the necessity to apply a correction to the value of c.

In fluids, the effective mass density is the mass density of the fluid, and the effective elastic modulus is defined by the adiabatic bulk modulus of elasticity, K, which is the inverse of the compressibility. Compressibility is defined as the relative change in volume as a function of pressure change. Therefore, K corresponds to the force opposing compression of the fluid.

As soft tissues are largely composed of water, a fluid model is often used to describe the waves at ultrasonic frequencies, where the speed of the sound's dependency on the temperature is a relevant feature. For example, the speed of sound in water at 20 °C is 1482 m/s, and between the ranges of 20°C and 37°C, it can increase at a rate of 2.5 m/s per 1°C (N. Bilaniuk and G. Wong, 1993). However, this is not the case for all the tissues. The increase in temperature in fat tissues results in a decrease in the speed of sound as presented by (Dunn *et al*., 1978).

5.1.6.1. Speed of the sound in a bubbly medium

The speed of the sound in the liquid can be drastically affected by a small volume fraction of bubbles. In the very low frequency regime (below the Minnaert resonance), the Wood's effective medium model allows predicting $c = 1/\sqrt{\chi_{air}\rho_{water}}$, which physically means that a bubbly liquid has the density of water and the compressibility of air. For an air volume fraction as tiny as 10^{-3}, the effective sound velocity is as small as 200 m/s, i.e., not only less than its value in water but also less than that in air. For larger frequencies, velocity dispersion can be generated by the presence of bubbles, which makes the sound speed of a bubbly liquid frequency-dependent. In general, the driving acoustic pressure is not in phase with the radial displacement of the surface of the bubble, yielding complex and frequency-dependent compressibility of the bubbly fluid, in the frequency domain.

Leighton (1994) provides a calculation of the speed of the sound in bubbly liquids. Reviews of the experimental and theoretical speed of sound are given by Anderson and Hampton (1998) and by Commander and Prosperetti (1989), and rigorous mathematical descriptions can be found in Caflisch *et al*. (1985), Lu *et al.,* (1990), and Hoff (2001).

5.1.7. Specular Reflection and Refraction

As briefly exposed in previous chapters, reflection, refraction, and transmission of sound waves occur at the boundary of two different media having different acoustic impedances.

A specular reflection is characterized by a mirror-like reflection, where the wave bounces back from the surface at the same angles it encountered the surface. For surfaces with irregularities smaller than the wavelength of the sound wave, specular reflection occurs, whereas for surfaces with bigger irregularities the reflection of the sound is diffuse (Ishimaru, 1999). The basis of echography or pulse-echo ultrasound imaging (described in chapter 5.1.11) is formed by exploiting the specular reflection between two organs, typically, and a single scattering of the heterogeneities in the medium. For diagnostic clinical ultrasounds differentiation of fluid-fluid and solid-fluid interfaces is crucial to provide distinctions of soft tissues in the images. The scattering phenomenon is also important for the medical ultrasound field, and it will be discussed in chapter 5.2.5 and 5.2.6. For the simplicity of the following derivations, we will assume that the incident wave is a plane wave in the fluid.

5.1.7.1. Fluid–Fluid Interface

Under the assumption of specular reflection, an incident plane wave will be reflected and transmitted (see Figure 5.1 adapted from Laugier and Haiat 2011). Both reflected and transmitted waves in a fluid must be longitudinal, because it is the only type of wave that exists in inviscid fluids, as mentioned previously. Following Snell's law, the reflection angle θ_1 is equal to the angle of the incident wave and the transmitted wave is refracted away from the direction of the incident wave θ_1 at a refraction angle θ_2 given by:

$$\frac{\sin\,\theta_2}{c_2} = \frac{\sin\,\theta_1}{c_1} \tag{5-5}$$

where c_1 and c_2 are the sound velocities of the first and second media. For the case where the incident wave is normal to the surface, the reflected and transmitted wave will also be normal to the interface. The amplitude reflection coefficient (*r*) is given by the ratio between the reflected and incident acoustic pressure amplitudes. Similarly, the amplitude transmission coefficient (*t*) is given by the ratio between the transmitted and incident acoustic amplitudes. Both coefficients are expressed as a function of the acoustic impedances of the two media as follows:

$$r = \frac{Z_1 - Z_2}{Z_1 + Z_2} t = \frac{2Z_2}{Z_1 + Z_2} \qquad (5\text{-}6)$$

where Z_1 and Z_2 are the characteristic acoustic impedances of the first and second medium for longitudinal waves, respectively

In the same manner, we can define the intensity reflection (*R*) and transmission coefficients (*T*) as the ratio of the reflected and transmitted acoustic intensity to the incident acoustic intensity, respectively:

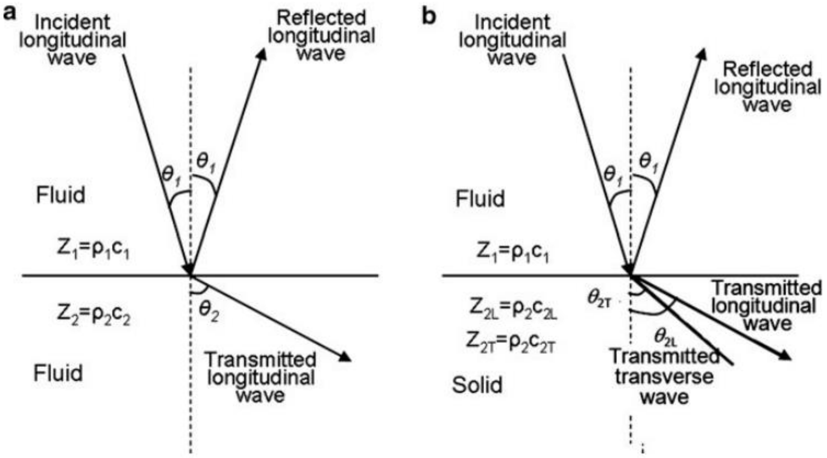

Figure 5.1 – Schematic drawing of reflection and refraction of a sound wave at the boundary (a) between two fluid media and (b) between a fluid and a solid medium (Laugier and Haiat 2011).

$$\mathrm{R} = \left(\frac{\mathrm{Z_1 - Z_2}}{\mathrm{Z_1 + Z_2}}\right)^2 \mathrm{T} = \frac{\mathrm{4Z_1Z_2}}{\mathrm{(Z_1 + Z_2)^2}} \qquad (5\text{-}7)$$

In a lossless medium, energy should be conserved, thus, the sum of transmitted and reflected intensities is equal to 1. The impedance discontinuity, or impedance miss-match, thus defines the amount of energy that will be reflected by the interface. The larger the difference between the acoustic impedances the greater the reflected energy will be. Table 5.1 shows different values of sound velocity, acoustic impedance, and slope of the attenuation coefficient as a function of frequency for selected tissues.

For small discontinuities, such as between two soft tissues, the Z value differs very little from the water value. This means that the majority of the energy is transmitted. Usually, we observe that less than 1% of incident energy is reflected and 99% of incident energy is transmitted in two soft tissues. For this scenario, it is very difficult to differentiate visually between media. Thus, the necessity for ultrasound contrast agents, that create differentiation between blood vessels and tissues with similar acoustic impedance.

Table 5.1: Typical values of sound velocity, acoustic impedance, and attenuation in different tissues for temperatures between 20°C and 37°C (Laugier and Haiat 2011)

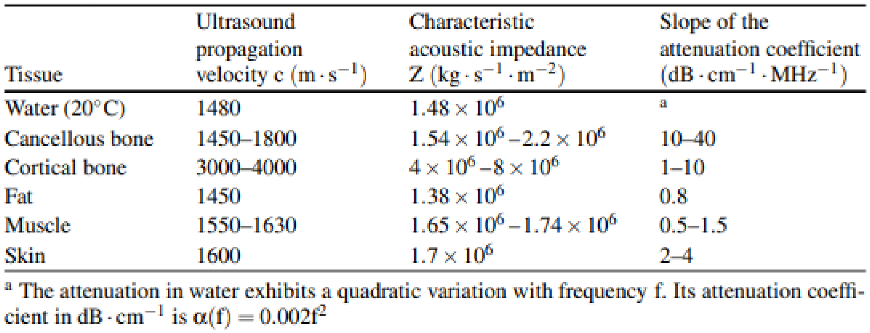

Tissue	Ultrasound propagation velocity c ($m \cdot s^{-1}$)	Characteristic acoustic impedance Z ($kg \cdot s^{-1} \cdot m^{-2}$)	Slope of the attenuation coefficient ($dB \cdot cm^{-1} \cdot MHz^{-1}$)
Water (20°C)	1480	1.48×10^6	[a]
Cancellous bone	1450–1800	$1.54 \times 10^6 - 2.2 \times 10^6$	10–40
Cortical bone	3000–4000	$4 \times 10^6 - 8 \times 10^6$	1–10
Fat	1450	1.38×10^6	0.8
Muscle	1550–1630	$1.65 \times 10^6 - 1.74 \times 10^6$	0.5–1.5
Skin	1600	1.7×10^6	2–4

[a] The attenuation in water exhibits a quadratic variation with frequency f. Its attenuation coefficient in $dB \cdot cm^{-1}$ is $\alpha(f) = 0.002f^2$

5.1.8. Attenuation

The energy content of an ultrasonic wave propagating through a tissue reduces progressively. This loss in energy is driven by several different mechanisms, which together account for the term attenuation. One of the mechanisms is called, in the literature, absorption, and it considers the transformation of mechanical energy into heat. Another important mechanism is called scattering, which accounts for the dispersion of energy from its main propagation direction.

In a first approximation, liquids can be considered as non-attenuating media, because it does not significantly absorb (the absorption length in water is about 35m at 1 MHz) nor scatter ultrasound energy (G. Kossoff, 2000). However, for higher frequencies (*i.e.,* 15 MHz) attenuation can become significant, since it grows as the square of the frequency.

Different materials attenuate ultrasound at different levels and through different mechanisms. Kossoff (2000) provides some examples of attenuation in the context of clinical ultrasound imaging. Soft tissue absorbs a substantial amount of ultrasonic energy but scatters it only slightly. Soft tissue attenuation is measured in dB/cm/MHz units. The liver, for example, attenuates ultrasound at a rate of 0.45 dB/cm/MHz. Thus, a one-way propagation through 5 cm of the liver at 5 MHz reduces the energy content by 11.25 dB, but the energy content is lowered by 22.5 dB in imaging's "back and forth" mode. Bone is also an excellent absorber but also a scatterer of ultrasound. In the particular case of bones, since they are solid with an acoustic impedance very high compared to soft tissues, some of the acoustic energy is converted into a shear wave, which is rapidly absorbed by the bone. Both absorption and scattering of ultrasonic energy are very high for tissues containing air. The attenuation is very significant, and therefore, this type of material, such as lungs, cannot be examined by ultrasound.

Microbubbles are very good scatterers that even in low concentrations can increase the attenuation of sound in water. For ultrasound contrast agents, acoustic attenuation is the basic method used to characterize them, giving information about their resonance frequency and damping, or Q-value. Microbubble attenuation will be described in more detail in the section chapter 5.2.7.

5.1.9. Transducer

The ultrasonic energy is produced by a transducer commonly made of a piezoelectric ceramic, which transforms an applied voltage into an ultrasonic wave. The Curie brothers first characterized the piezoelectric effect in 1880 when they subjected a cut piece of quartz to mechanical stress, resulting in an electric charge on the surface (Kossoff, 2000). Later, they proved the reverse piezoelectric phenomenon: electricity is given to quartz and causes it to vibrate. When these vibrating mechanical sound waves pass through biological tissues, they generate alternating zones of compression and rarefaction.

The acoustic beam pattern produced by the transducer is determined by its size, how it is powered, its characteristic frequency, and how it was built. The thickness of the piezoelectric crystal controls the operating frequency of a transducer. The crystal should work at its natural or resonant frequency for optimal efficiency. This happens when the crystal thickness corresponds to half a wavelength ($\lambda/2$).

As previously stated, wavelength and frequency are inversely connected, which means that a thinner piezoelectric material has a larger resonance frequency. Ultrasound elements are typically between 0.2mm and 1mm thick.

A transducer with a resonance frequency of 2MHz has a thickness of around 1 mm. A transducer operating at a considerably higher frequency (e.g., 7.5MHz) typically has a thickness of 0.3mm.

5.1.9.1. Single Element Circular Transducer

The single element circular transducer is the most basic transducer and is still used in laboratories to characterize medium and microbubble populations. The disc's thickness determines the frequency at which the transducer works. For example, a transducer with a central frequency of 5 MHz is typically roughly 0.4 mm thick. The acoustic wave first propagates in a cylindrical beam with a diameter equal to the transducers over a short distance known as the near-field. The distance between the near-field and far-field areas is related to the square of the transducer's radius and inversely proportional to frequency. Focus transducers can be employed to increase lateral resolution, or a spherical lens can be positioned in front of the transducer (Figure 5.2). Diffraction issues necessitate that focusing can only be accomplished in the transducer's near-field. Another constraint is that the beam cannot be narrowed throughout the near field. The beam width may be reduced only at the focus zone of the transducer (Aldrich, 2007, Abu-Zidan *et al.*, 2011, Kossoff, 2000, Laugier and Haiat, 2011).

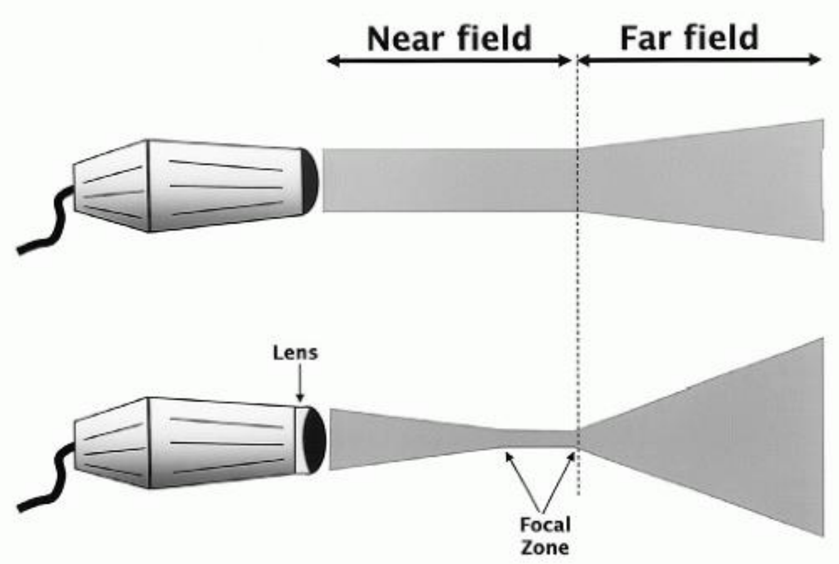

Figure 5.2 – The ultrasonic beam emitted by a transducer can be unfocused (on the left) or focussed using an acoustic lens (on the right) (bottom). Focusing produces a narrower beam but does not affect the length of the near field. The dispersion rate in the far-field is increased due to concentration(illustration from the website Thoracic Key.com).

Using the preceding example of a 5 MHz transducer and setting the focus at half the near-field distance, the beam at the focus point is narrowed by a factor of around 5. The beam width at focus in this design is one-fifth the diameter of the transducer, and the focal zone centered around the focus is around one-fifth the near-field distance. It is feasible to get a greater focus by moving the focus closer to the transducer (limited by the diffraction limit $\lambda/2$), but the focusing zone would be proportionally diminished.

5.1.9.2. Phase-Array Transducer

Phase-array transducers were created to overcome the beam pattern constraints of single disc transducers. An array of piezoelectric crystals is put side by side in one piezoelectric ceramic in these transducers. Typically, these transducers have 128-256 components across the face that are separately linked via one of the ultrasound machine connections. The beam is focused electronically by activating the external components and then progressively energizing the following outer elements until the core disc one is activated. The time delay between the energizing pulses determines the position of the focus. Like a lens, this time delay is often spherical in shape, and the beam comes to focus in the center of this sphere. The focus point is electronically controlled, and various alternative energizing sequences may be utilized to provide a narrow beam over the desired inspection distance. Figure 5.3 depicts the beam pattern of a single disc and a phase-array transducer. The focus zone of a single disc transducer is somewhat shallow, but an annular array transducer produces a significantly superior beam pattern.

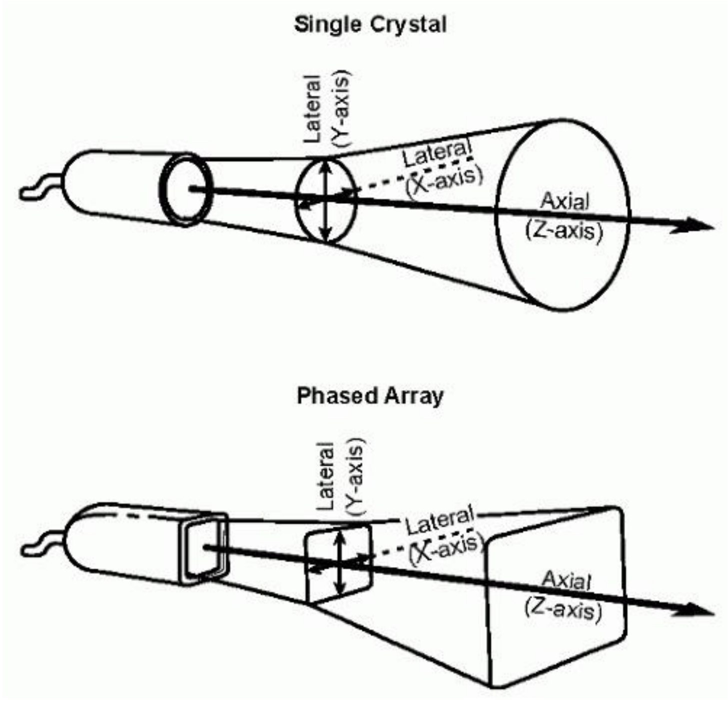

Figure 5.3 – The ultrasonic beam can be shown in three dimensions. A cylindrically formed beam will be emitted by a single-crystal transducer (top). If the transducer face is rectangular (bottom), the beam will also be rectangular. The two illustrations mark the various beam axes (illustration from the website Thoracic Key.com)

5.1.9.3. Linear, curved and Matrix Transducer

Another type of transducer uses a linear array of elements. Such transducers feature a rectangular face with crystals positioned parallel throughout its length. Because the elements are stimulated concurrently, unlike phased-array transducers, the individual scan lines are oriented perpendicular to the face and stay parallel to each other. This produces an unfocused rectangle-shaped beam. Linear-array imaging is frequently employed in abdominal, vascular, and obstetric applications. A sector scan can also be created by curving the face of a linear transducer. This novel concept is currently being implemented in specific portable ultrasound equipment.

A more complicated transducer design is required to accomplish real-time three-dimensional echocardiography. This needs the piezoelectric components to be arranged in a two-dimensional matrix. Each piece represents a scan line needed to build the three-dimensional data collection. If the matrix has 64 by 64 elements, for example, 4,096 scan lines can be formed. A pyramidal-shaped volume (rather than a tomographic slice) of ultrasonic data can be obtained by carefully manipulating the stimulation time. Real-time imaging in three dimensions is feasible by probing the volumetric form multiple times (>20) per second.

5.1.10. Resolution

The resolution, or the capacity to reliably identify two closely located structures or events, is a vital issue for all imaging approaches. When imaging tiny objects like rat and mouse organs, resolution becomes even more crucial. Both spatial and temporal resolution must be addressed in ultrasonic imaging. Axial and lateral resolution are two types of spatial resolution.

Axial resolution is the capacity to differentiate two distinct but closely spaced structures located parallel to the ultrasound beam's propagation axis. The duration and frequency of sound wave pulses affect axial resolution (wavelength). Two distinct structures will be seen as independent structures if the pulse duration is less than the distance between the structures. If the pulse duration exceeds the distance between the structures, only one reflection will be caught, and the picture will only display one structure. Sound waves with higher frequencies have shorter pulse durations and, in general, greater axial resolution.

Lateral resolution is the ability to differentiate between two nearby but distinct objects aligned perpendicular to the axis of the sound wave beam. Beam width and sound wave frequency influence lateral resolution (Coatney, 2001). Greater lateral resolution is provided by narrower beam width. By focusing on the sound waves produced by the transducer, beam width may be reduced. The frequency of the sound wave also influences lateral resolution, with higher frequencies typically boosting resolution. Higher frequency transducers are often recommended for rat and mouse imaging because axial and lateral resolution increases with increasing frequency. One disadvantage of employing higher frequencies is that sound wave penetration reduces as frequency increases. A 5-MHz transducer, for example, may typically image to a depth of 12 to 15 cm, but a 10-MHz transducer may image to a depth of just 3 to 4 cm. As a result, increased frequency restricts penetration depth by increasing axial and lateral resolution.

The capacity to discern two events in time depends on the number of image frames captured every second, which is often stated in Hertz (Hz) or cycles per second. In general, the more frames per unit of time there are, the smoother and more visually pleasant the real-time image. Reduced frame rate factors, such as greater depth of focus, will affect temporal resolution (Coatney, 2001). This is highly critical for structures with high velocities, such as valves. Several widely accessible ultrasound devices have frame rates ranging from 120 to 600 Hz. When imaging target organs that are generally immobile, such as the kidney, temporal resolution is less important.

5.1.11. Ultrasound Imaging

Ultrasound is the most widely used medical imaging technique. It provides low-risk and portable imaging, creates real-time pictures that may be acquired at the bedside, and is less costly than computed tomography (CT) and magnetic resonance imaging (MRI). The operating idea is based on the scattering and reflection of transmitted ultrasonic waves at surfaces and tissue inhomogeneities with variable acoustic impedances.

Diagnostic US exams are often conducted in four modes: A-mode, B-mode or gray scale imaging, M-mode, and Doppler mode (Xu, 2017). Although it is possible to purchase equipment that can only conduct one of these examination modes, modern equipment is often capable of executing all four modes. It is common to gather information from all four modes concurrently and show it in the same image.

The first ultrasonic technology, A-mode, was created in 1930. The transducer emits a single ultrasonic pulse into the medium. As a result, a one-dimensional basic ultrasound image is formed, with a succession of vertical peaks (or amplitudes (A)) generated once the ultrasound beams contact the border of the distinct tissue. The distance between echoed spikes can be determined by dividing the ultrasonic speed in the tissue (1540 m/s) by half the elapsed time. However, it offers little information about the spatial connection of imaged structures. A-mode is used in therapeutic ultrasound to pinpoint the exact targeting of the destructive wave energy on a specific tumor or calculus.

The B-mode is a two-dimensional (2D) image of the region that is scanned simultaneously by a linear array of 100-300 piezoelectric components rather than a single one as in the A-mode. In B-mode imaging, the amplitude of the echo from a sequence of A-scans is transformed into dots of varying brightness. The horizontal and vertical axes show actual tissue distances, whereas the grayscale intensity represents echo strength. The principal mode now employed in ultrasound imaging is B-mode, which can produce an image of a cross-section of the region of interest.

The M-mode is the time-motion display of an ultrasonic wave along a specified ultrasound line. It depicts the heart in a single value. The time axis is used to illustrate all of the reflectors along this line. The M-mode has the benefit of having a very high sample rate, which results in a high temporal resolution, allowing even very fast motions to be captured, displayed, and quantified. The downside is that the ultrasound line is permanently attached to the ultrasound sector's tip. As a result, it may be challenging to align the M-mode perpendicular to the structures presented (e.g., the septum), resulting in inaccurate readings.

This limitation is addressed by reconstructing the M-mode from the 2D image in anatomical M-mode (post-processing). The cursor line can be freely positioned in the anatomical M-mode. However, the temporal resolution is substantially worse than in traditional M-mode.

The Doppler mode derives from the Doppler effect, discovered by Austrian physicist Johann Christian Doppler. The word refers to a shift in the frequency or wavelength of a sound wave caused by relative motion between the source and the receiver. In other words, the sound frequency is constant in a stationary position. If the sound source travels toward the sound receiver, the sound waves must be compressed, resulting in a higher-pitch sound (positive Doppler shift); if the sound source moves away from the receiver, the sound waves must be stretched, resulting in a lower-pitch sound (negative Doppler shift). The magnitude of Doppler shift is determined by the incidence angle between the emitted ultrasonic beam and moving reflectors. There is no Doppler shift at a 90° angle.

The maximum Doppler shift can be noticed when the angle is 0° or 180°. In medical cases, the Doppler changes are generally audible. Color Doppler generates a color-coded mapping of Doppler shifts on a B-mode ultrasound image. The direction of blood flow is determined by whether the motion is toward or away from the transducer. Color Doppler mode is utilized in ultrasound-guided peripheral nerve blocks to determine the existence and character of blood vessels (artery vs. vein) in the area of interest. When the ultrasound beam's direction changes, the arterial flow's color switches from blue to red or vice versa, depending on the convention used. Power Doppler is up to five times more sensitive than color Doppler in measuring blood flow and is less affected by scanning angle. As a result, power Doppler may be utilized to locate tiny blood arteries more consistently. The disadvantage of power Doppler is that it does not offer information on the direction and speed of blood flow.

As previously stated, medical ultrasound imaging relies on echoes, or the scatter and reflection of sound generated by inhomogeneities in the tissue. Ultrasound scatter from blood, on the other hand, is substantially less than scatter from other tissues, often 30 to 60 dB weaker (Hoff, 2001). Although the Doppler mode can differentiate these weak signals from tissue echoes, crucial information for ultrasound imaging and diagnostics is lost. For example, the volume, shape, and movement of blood-filled cavities, particularly the heart's ventricles, blood flow in small, difficult-to-investigate veins, blood perfusion (blood flow through tissue), and more.

To meet these objectives, the scatter of sound from blood should be enhanced by around 30 dB (Hoff, 2001), which can be accomplished using ultrasonic contrast agents. UCA are made up of a suspension of stable microbubbles ranging in size from 0.5 to 10 µm in diameter, allowing them to travel through even the tiniest vascular beds safely. Because of the acoustic impedance mismatch with their liquid surroundings and the resonance characteristic of the bubble vibrations, bubbles are highly echogenic. The interaction of bubbles and ultrasound, as well as the impact of the stabilizing shell, has been extensively researched and will be explained in-depth in the following subsections.

5.2. Fundamentals of Contrast agents for ultrasound imaging

This chapter aims to provide a basic description of the acoustics of ultrasound contrast agents. We aim at introducing the fundamental phenomena involved in the ultrasonic characterization of ultrasound contrast agents. Readers interested in deeper and more complete descriptions of the bubble's dynamics, and ultrasound contrast agents' characterization can refer to the works of Leighton (1994), Hoff (2001), Nanda and Schlief, (1997), and Paradossi *et al.,* (2010).

5.2.1. Dynamic of free gas bubble

Lord Rayleigh (1917) initially characterized the dynamics of an uncoated bubble in free space, which was further modified by Plesset (1949), Noltingk & Neppiras (1950 and 1951), and Poritsky (1952) to account for surface tension and viscosity of the liquid.

The liquid's equations of motion are derived from the conservation equations for mass and momentum and the liquid's equations of state. These equations describe the relationships between changes in pressure, density, and enthalpy in a liquid and are used to develop equations of motion for the bubble surface. For completeness, the set of equations is summarized as:

Equation of state for sound speed c and enthalpy h:

The equations of state establish a link between changes in pressure p, density p, and enthalpy h per unit mass of the liquid. The equations are formulated as partial derivatives under constant entropy, following the common assumption in acoustics that the processes are adiabatic.

$$\left(\frac{\partial \rho}{\partial p}\right)_S = \frac{1}{c^2} \quad , \qquad \left(\frac{\partial h}{\partial p}\right)_S = \frac{1}{\rho} \tag{5-8}$$

where the index S means that the partial derivatives are to be evaluated at constant entropy, *p* is the pressure in the liquid, *ρ* is the density and *h* is the specific enthalpy.

Continuity equation for the liquid (written in spherical coordinates):

$$\left(\frac{\partial \rho}{\partial t} + u\frac{\partial \rho}{\partial r}\right) + \frac{1}{r^2}\frac{\partial}{\partial r}(\rho\, u\, r^2) = 0, \tag{5-9}$$

where $u(r,t)$ is the velocity, r is the radial distance from the bubble center.

Conservation of momentum (Euler equation)

Conservation of momentum is given by the Navier-Stokes equation for the liquid. The flow is purely radial and irrotational, $\nabla \times u = 0$. Bulk viscosity is ignored. Under these conditions, the Navier-Stokes equation is:

$$\rho\left(\frac{\partial u}{\partial t} + (u\nabla)u\right) = -\nabla p + \frac{4}{3}\eta\nabla^2 u \tag{5-10}$$

where η is the viscosity of the liquid.

Using the continuity equation (Eq. 5-9), and equation of state (Eq. 5-8), the Navier-Stoke equation can be written as:

$$\rho \frac{\partial u}{\partial t} + \nabla p = -\frac{4}{3}\frac{\eta}{\rho c^2}\frac{d\nabla p}{dt} \tag{5-11}$$

For liquids of interest, $\omega\eta \ll \rho c$, where ω is the highest frequency involved. The viscosity term on the right side is small to the second order in $1/c$, compared to the ∇p term on the left side. This implies that the contribution from viscosity can be neglected in the bulk of the liquid, and the Navier-Stokes equation is replaced by the Euler equation:

$$\rho \left(\frac{\partial u}{\partial t} + (u\nabla)u\right) + \nabla p = 0 \tag{5-12}$$

So far, the sole assumption employed has been to ignore the viscosity and the thermal conduction in most of the liquid. However, because viscosity contributes to the bubble's surface, it is included in the boundary conditions at the bubble surface.

The fundamental equations are then coupled, with some approximations, to get an equation of motion for the liquid around the bubble. The equations are written as partial derivatives with constant entropy, assuming that the processes are adiabatic, a typical assumption in acoustics. This adiabatic approximation is utilized for the acoustic wave in the liquid surrounding the bubble. The adiabatic model is insufficient for the gas dynamics inside the bubble. The gas acts isothermally rather than adiabatically in most scenarios involving µm-sized bubbles and MHz-frequency ultrasonography. The partial differential equations that describe the liquid's motion can be then combined to produce an ordinary differential equation that describes the bubble radius as a function of time. A review by Prosperetti from 1984 and Hoff (2001) gives the derivations in depth.

5.2.1.1. The Rayleigh-Plesset Equation

Lord Rayleigh (1917) is credited with the earliest research on bubble oscillations. The Rayleigh-Plesset equation is the name given to the following nonlinear differential equation for the bubble surface. This is the most fundamental nonlinear equation of motion for a gas bubble in a liquid. Treating the liquid as incompressible is similar to keeping terms on the zeroth order in the acoustic Mach-number $M = \dot{R}/c$ for the bubble surface. This requires that the bubble wall velocity $\dot{R}(t)$ be minimal in comparison to the liquid's speed of sound c. This assumption is met for modest oscillation amplitudes. The Rayleigh-Plesset model does not account for energy loss due to sound radiation. In an incompressible liquid, sound energy does not propagate. This may appear to be a severe limitation. However, damping from liquid viscosity is included, which is often greater than radiation damping. At low frequencies, radiation damping is modest for tiny bubbles. Acoustic radiation becomes a significant source of damping when ka > 0.1, indicating that acoustic radiation damping becomes essential for frequencies over 5 MHz for bubble diameters greater than around 10 µm.

5.2.1.2. Boundary conditions

As previously stated, the liquid in this model is considered to be incompressible, giving rise to the following equations of state:

$$\rho = constant, \qquad \left(\frac{\partial \rho}{\partial p}\right)_S = 0 \tag{5-13}$$

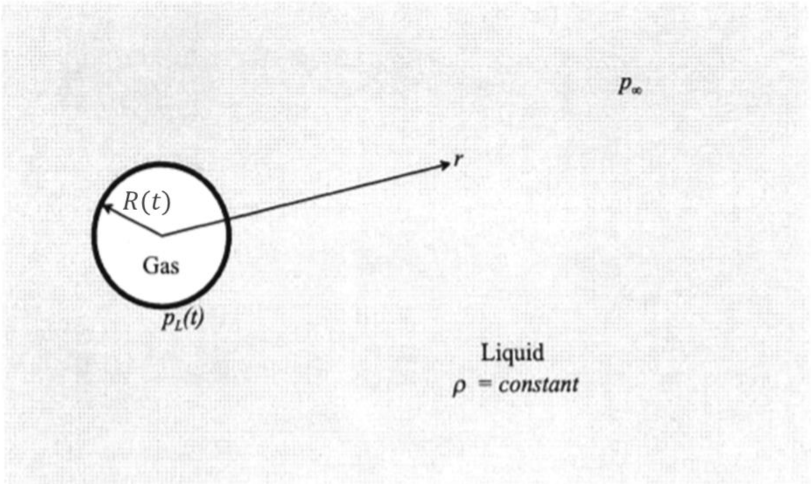

Figure 5.4 – illustration of a bubble in liquid. R(t) is the bubble radius, $p_L(t)$ is the pressure in the liquid at the bubble surface, p_∞ is the pressure in the liquid far from the bubble, and ρ is the density of the liquid (adapted from Hoff (2001)).

Because ρ is constant, the equations for continuity can be reduced as follows:

$$\frac{\partial}{\partial r}(ur^2) = 0 \tag{5-14}$$

Assuming that the bubble remains spherical at all times and pulsates in an infinite body of liquid, the particle velocity in the liquid is always radial and of magnitude $u_r(r,t)$, due to spherical symmetry. Thus, Euler equation (Eq. 5-12) becomes:

$$\frac{\partial u_r(r,t)}{\partial t} + u_r(r,t)\frac{\partial u_r(r,t)}{\partial r} = -\frac{1}{\rho}\frac{\partial p}{\partial r} \tag{5-15}$$

5.2.1.3. Solution at bubble’s surface

Equations (5-14) and (5-15) are solved to obtain a solution for the bubble surface motion at:

$$r(t) = R + \xi(t) \tag{5-16}$$

where ξ(t) is a small displacement of the bubbles surface. At the surface of the bubble the following boundary conditions are proposed:

$$u(r = R) = \left.\frac{\partial \Phi}{\partial r}\right|_{r=R} = \dot{R} \tag{5-17}$$

$$p(r = R) = p_L \tag{5-18}$$

Combining Eq. (5-17) with Eq. (5-14) yields:

$$u_r(r,t) = \frac{R^2\dot{R}}{r^2} \tag{5-19}$$

Introducing Eq. (5-19) into the Eulers equations (Eq. 5-14) one obtains:

$$\ddot{R}\frac{R^2}{r^2} + 2\dot{R}^2\frac{R}{r^2} - 2\dot{R}^2\frac{R^4}{r^5} = -\frac{1}{\rho}\frac{\partial p}{\partial r} \tag{5-20}$$

By integrating Eq. (5-20) from $r = R\ to\ \infty$, the equation of motion for the bubble surface, also known as the Rayleigh equation, is obtained:

$$R\ddot{R} + \frac{3}{2}\dot{R}^2 = \frac{1}{\rho}(p_L - p_\infty) \tag{5-21}$$

The pressure difference at the bubble's surface and the bulk liquid is related to the acceleration, velocity, and radius of the bubble surface by the Eq. (5-21).

Lord Rayleigh's work was supplemented by Plesset in 1949, who added a driving acoustic field to the model. As a result, the pressure p_∞ became $p_\infty = p_0 + p_i(t)$, yielding the Rayleigh-Plesset (RP) equation for oscillating bubbles:

$$\rho \ddot{R} R + \frac{3}{2} \rho \dot{R}^2 = p_L - p_0 - p_i(t) \tag{5-22}$$

where $R, \dot{R}$, and $\ddot{R}$ indicate the bubble's radius, the velocity of the bubble wall, and the acceleration of the bubble wall, respectively, and p_L is the pressure at the bubble surface. p_0 denotes external pressure, and $p_i(t)$ is the driving acoustic pressure. Equation (5-22) is an ordinary differential equation, and its solution is the radius of the bubble as a function of time, *R(t)*, given any driving pressure pulse $p_i(t)$. The nonlinear properties of the bubble response, or echo, are caused by the nonlinearities in the preceding equation. Once the radial dynamics is known, the pressure emitted by the bubble, $p_s(t)$ (also known as the scattered pressure in medical ultrasound literature), can be computed using the conservation of mass and momentum (K. Vokurka, 1985):

$$p_s = \frac{\rho R}{r} \left(2\dot{R}^2 + R\ddot{R} \right) \tag{5-23}$$

where *r* denotes the distance from the bubble, thus, for every given driving pressure pulse $p_i(t)$, the nonlinear echo $p_s(t)$ for an oscillating spherical bubble may be determined.

Noltingk and Neppiras (1950 and 1951) and Poritsky (1952) extended the RP-equation by including the influence of gas within the bubble, constant vapor pressure, surface tension, and liquid viscosity, providing a more complete version:

$$p_L = p_{gas}(t) - \frac{2\sigma_w}{R} - \frac{4\eta \dot{R}}{R} \tag{5-24}$$

where σ_w is the surface tension of the gas-liquid system, and $p_{gas}(t)$ is the internal pressure of the bubble, that can be expressed as $p_{gas}(t) = p_0 \left(\frac{R_0}{R} \right)^{3\kappa}$ through the adiabatic assumption. By combining Eqs. (5-22) and (5-24), one can derive the equation of motion describing the bubble dynamics (often referred to as the Rayleigh-Plesset equation):

$$\rho\left(\ddot{R}R+\frac{3}{2}\dot{R}^2\right)=\left(P_0+\frac{2\sigma_w}{R_0}\right)\left(\frac{R_0}{R}\right)^{3\kappa}\left(1-\frac{3\kappa\dot{R}}{c}\right)-$$

$$P_0-P_i(t)-4\eta\frac{\dot{R}}{R}-\frac{2\sigma_w}{R} \tag{5-25}$$

where ρ is the liquid density, ν is the liquid's kinematic viscosity, c is the liquid's speed of sound, σ_w is the surface tension of the gas-liquid system, and κ is the polytropic exponent of the gas inside the bubble. R_0 indicates the starting bubble radius, R the time-dependent radius of the bubble, and $\dot{R}$ and $\ddot{R}$ the velocity and acceleration of the bubble wall, respectively. During oscillations, the bubble is supposed to be surrounded by an endless medium and stay spherical. The radius of the bubble is small in comparison to the acoustic wavelength. The bubble's gas content remains constant. The damping of bubble dynamics is dictated by viscous damping of the surrounding liquid, and acoustic radiation damping, which is caused by sound radiated away from the bubble (Flynn, 1975a and 1975b), Gilmore (1952), Prosperetti *et al.*, (1988). Thermal damping is not included here for simplicity. Finally, the liquid density is greater than the density of the gas.

5.2.1.4. Linearized equations.

The RP equation that models the behavior of the bubble can be linearized for low driving acoustic pressures. By introducing the dimensionless variable $x(t)=\frac{\xi(t)}{R_0}$ in the Eq. (5- 25), and neglecting surface tension, it is possible to obtain:

$$(1+x)\ddot{x}+\frac{3}{2}\dot{x}^2+\frac{1}{\rho R_0^2}\left[1-(1+x)^{3\kappa}\right]+\frac{\Gamma^{vis}\dot{x}}{1+x}=\frac{-p_\infty(t)}{\rho R_0^2} \tag{5-26}$$

where is $\Gamma^{vis}=\frac{4\eta}{\rho R_0^2}$ .By considering that the bubble's surface is experience small displacements, *x<<1*, Eq. (5-26) can be reduced to:

$$\ddot{x}+\Gamma^{vis}\dot{x}+\frac{3\kappa p_0}{\rho R_0^2}x+\frac{p_\infty(t)}{\rho R_0^2}=0 \tag{5-27}$$

Because of the low excitation level, the bubble wall displacement may be represented as a simple one-dimensional mass-spring oscillator. Minnaert gave the first description of bubble motion as an oscillator in 1933. From energy calculations, he derived the equation for the bubble resonance frequency. Later, Medwin (1977) employed force balance equations, making it easier to account for frictional forces and the reaction to an external pressure field.

The oscillator equation is determined by the mass (*m*), stiffness (*s*), damping (*β*), and applied force (F_{drive}). As a result, the bubble wall's equation of motion can be expressed as:

$$m\frac{d^2x(t)}{dt^2}+\beta\frac{dx(t)}{dt}+sx(t)=F_{driv}(t) \tag{5-28}$$

The resonance frequency of the system (undamped) is provided by approximating the bubble's motion to a simple harmonic oscillator:

$$f_r=\frac{1}{2\pi}\sqrt{\frac{s}{m}} \tag{5-29}$$

The mass of the oscillator is derived from the displacement of the surrounding liquid caused by the surface movement of the bubble, which adds inertia to the system. From a parallel with Eq. (5-27), in dimensioned format, it is possible to obtain the mass value:

$$m=4\pi R_0^3\rho \tag{5-30}$$

where R_0 is the equilibrium radius and ρ is the density of the surrounding liquid. The mechanical oscillator's spring, or stiffness, is derived from the force that resists the volume change of the bubbles caused by the gas core pressure during compression and expansion:

$$s=12\pi\kappa P_0R_0 \tag{5-31}$$

where κ denotes the heat capacity ratio (C_p/C_v) and P_0 the atmospheric pressure. The damping is caused by energy loss owing to viscosity, sound radiation, and heat exchange between gas and liquid:

$$\beta=\delta_{tot}\omega m \tag{5-32}$$

where δ_{tot} represents total damping and ω represents angular frequency.

Combining Eqs. (5-29), (5-30), and (5-31) for a bubble motion with no loss ($\beta=0$) yields the expression for the resonance frequency for a bubble, commonly known as the Minnaert-frequency:

$$f_r = \frac{1}{2\pi R_0}\sqrt{\frac{3\kappa P_0}{\rho}} \tag{5-33}$$

with κ the polytropic exponent of the gas. The liquid around the bubble behaves as a mass, while the gas works like a spring in a mass-spring system. As a result, the bubble resonates to the driving pressure field, and it has a resonance frequency f_r at which a maximum amplitude is seen, as shown in Figure 5.5. The system undergoes damping, as indicated by the width of the resonance curve. The energy loss mechanisms associated with damping can be attributed to acoustic reradiation and viscous damping due to liquid viscosity and thermal damping due to the formation of a thermal boundary layer surrounding the bubble (Prosperetti, 1976). For microbubbles of a typical size of 5 µm, the total dimensionless damping constant, i.e., the sum of all damping contributions, is 0.1. Hence the resonance frequency is extremely close to the bubble's eigenfrequency (Leighton, 1994), $f_r \approx f_0$. Through Eq. (5-33), the eigenfrequency is inversely proportional to the bubble's radius. Minnaert previously calculated the relation $f_0 \cdot R_0 \approx 3\ \mu mMHz$ for an air bubble in water (Minnaert, 1933). As a result, a 3 µm diameter bubble will have an eigenfrequency close to 2 MHz at the center of clinical medical ultrasound imaging.

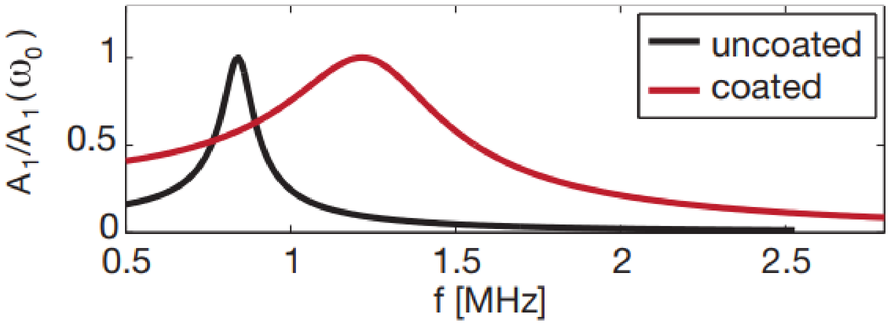

Figure 5.5 – The resonance curves of an uncoated 3.8 µm bubble and a phospholipid-coated bubble of the same size. The coating stiffens the system, resulting in a higher resonance frequency. The coating's viscosity causes higher energy dissipation, or damping, resulting in a broader resonance curve (T. Segers, 2015).

5.2.2. Damping

At low pulsation amplitudes, we demonstrated that a spherical vibrating bubble in an infinite liquid acts as a harmonic oscillator, producing spherical pressure waves as a simple monopole source.

The entire damping of the system in the free gas bubble example is the sum of the individual damping coefficients: reradiation damping, viscosity damping, and thermal damping.

Radiation damping is caused by the bubble behaving as a secondary source, scattering ultrasound, and lowering the system's energy. The reradiation damping coefficient is calculated as follows by Hoff *et al.* (2000):

$$\delta_{rad} = \frac{\frac{3\kappa}{\rho c R_0}\left(P_0 + \frac{2\sigma_W}{R_0}\right)}{\omega_0} = \frac{\omega^2 R_0}{\omega_0 \boldsymbol{c}} \tag{5-34}$$

$$\delta_{rad} \approx \frac{\omega_0 R_0}{c} \text{ , at resonance} \tag{5-35}$$

where ω is the driving frequency, ω_0 is the resonance frequency, R_0 is the bubble radius, and *c* is the speed of sound in the surrounding liquid.

Viscous damping due to the viscosity of the embedding liquid is significant for bubbles diameters in the µm-range.

The mechanical resistance to viscous forces in the liquid is determined only by the bubble's diameter and the viscosity of the surrounding fluid.

$$\delta_{\eta} = \frac{4\eta_L}{\omega_0 \rho R_0^2} \tag{5-36}$$

Thermal damping is obtained by investigating heat transfer inside the gas during oscillations. The liquid is seen as a reservoir of constant temperature.

Thermal damping is affected by the velocity of the bubble surface and the gas properties. Devin (1959) and Eller (1970) provided the model for thermal damping. They investigated temperature changes in the gas by simulating the liquid as a constant-temperature heat reservoir. When using this model for a shelled bubble, the shell is assumed to have the same constant temperature as the surrounding liquid. During the oscillations, heat production in the shell is ignored. This appears to be an acceptable assumption, given that the heat capacity of the shell material is of the same order of magnitude as that of water, which is three orders of magnitude more than that of air (Hoff, 2001; Osterman and Nordling, 1987). As a result, it is anticipated that Devin and Eller's findings for the free bubble can also be applied when a shell is present.

$$\delta_{Th} = \frac{3p_e}{\omega\omega_0\rho R^2}\operatorname{Im}\left(\frac{1}{\Phi}\right) \tag{5-37}$$

where Φ is a function of the thermal properties of the gas, defined as:

$$\Phi(R_0,\omega) = \frac{1}{\gamma}\left(1 + \frac{3(\gamma-1)}{\psi^2}\left(\Psi_{\coth\Psi} - 1\right)\right) \tag{5-38}$$

where γ is the adiabatic constant of the gas, and Ψ is a function defined as:

$$\Psi(R_0, l_D(\omega)) = \frac{1}{2}(1+i)\frac{R_0}{l_D} \tag{5-39}$$

where l_D is the thermal diffusion length:

$$l_D(\omega) = \sqrt{\frac{K_g}{2\omega\rho_g C_p}} \tag{5-40}$$

which is a function of the thermodynamic properties of the gas: K_g is the thermal conductivity of the gas, ρ_g is the gas density, C_p is the heat capacity of gas at constant pressure.

The thermal diffusion length $l_D(\omega)$ expresses the usual thermal diffusion distance during one oscillation cycle. Heat transfer is fast enough to maintain the temperature constant during the oscillation cycle when the bubble is significantly smaller than the thermal diffusion length. Heat transfer is insignificant over the bubble radius when the bubble radius is substantially bigger than the thermal diffusion length.

The bubble oscillation occurs mainly in the transition area between isothermal and adiabatic oscillations for bubble sizes and frequencies utilized in ultrasonic contrast agents. As a result, heat conduction damping must be addressed for common contrast agent bubbles used in medical ultrasound imaging.

At low frequencies, liquid viscosity damping dominates the smallest bubbles, whereas thermal damping dominates the larger bubbles. Radiation damping takes control at high frequencies and becomes the dominant damping mechanism for all bubble sizes. There are several somewhat different definitions of the damping constant δ in the literature. The definition employed here is identical to that used by Church (1995) but differs by ω/ω_0 from those used by Medwin (1977) and Leighton (1994).

Figure 5.6 shows the different damping coefficients that De Jong et al. (2002) determined for different bubble sizes at their resonance frequency. The curves differ from previously published data because they account for the change in thermal diffusivity length for tiny bubbles (Leighton, 1994)). As seen in the image, thermal damping dominates for bubbles greater than 10 µm in diameter, whereas damping owing to fluid viscosity, dominates for bubbles less than 5 µm in diameter. If the surface tension is neglected, the reradiation damping at resonance is constant with the diameter and negligible compared to the thermal and viscous damping for bubbles in this size range. The slight increase for small diameter values is due to the more significant impact of surface tension. The sum of these damping coefficients is roughly 0.15 for bigger bubbles, with minimal change for resonating bubbles with sizes ranging from 4 µm to 50 µm. For small bubbles, total damping increases to 0.5 or higher, with viscous damping accounting for most of the contribution. Because blood's viscosity is three times that of water, the vibration (for example, of a 1 µm bubble) in water will be considerably different from that in the blood.

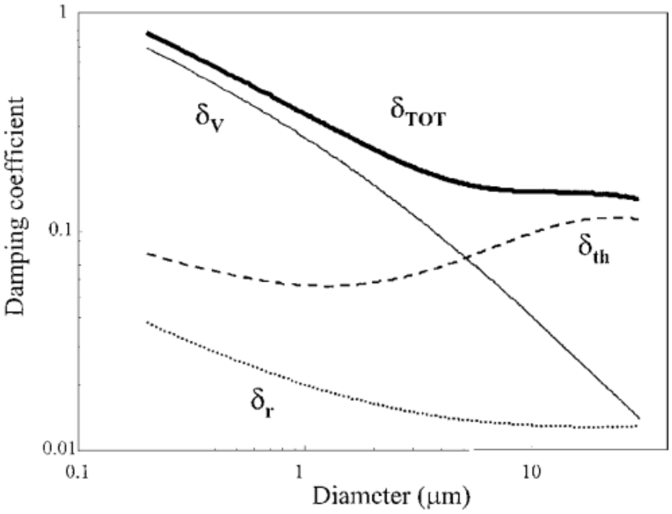

Figure 5.6 – Damping coefficients for an air bubble in water as a function of the diameter calculated at their resonance frequency. δ_{TOT} is the total damping; δ_v is the viscous damping; δ_r is the reradiation damping; δ_{th} is thermal damping (De Jong et al. (2002))

When damping effects are considered, the expected resonance frequency for both free and encapsulated bubbles is lowered, especially for small bubbles (Khismatullin 2004; Doinikov, Haac, et al. 2009). The damped resonance frequency can be calculated using (Doinikov, Haac, et al. 2009)

$$f_{res} = f_0\sqrt{1-\frac{\delta^2}{2}} \tag{5-41}$$

It should be noted that surface tension cannot be ignored for bubbles with a radius of 10 µm. When compared to a free bubble, surface tension increases stiffness. The pressure is increased by $\frac{2\sigma}{R}$ due to surface tension at the gas-liquid contact, making the bubble's equilibrium pressure p_e to be:

$$p_e = p_0 + \frac{2\sigma}{R} \tag{5-42}$$

The surface tension at an air-water interface is approximately 72 mN/m, yielding a one-atmosphere rise in gas pressure for bubbles with diameters in the µm-range. However, the surface tension is significantly lowered if the water is contaminated or includes surface-active chemicals. Because blood includes surface-active protein molecules, its surface tension is substantially lower than that of water.

5.2.3. Oscillation amplitude

By assuming a steady-state response (t → ∞), Eq. (5-28) can be used to get the absolute relative amplitude of oscillation:

$$|x_0| = \frac{F_0}{\sqrt{\left(\omega_0^2-\omega^2\right)^2+(\delta\omega\omega_0)^2}} \tag{5-43}$$

For the case of free gas bubbles, where small damping is observed, the amplitude of oscillations of a bubble driven at a frequency well below its resonance frequency is inversely proportional to the effective mass and the eigenfrequency squared of the system (stiffness-driven). For the case in which the driving frequency is well above the resonance frequency, the oscillation amplitude is inversely proportional to the system's effective mass (inertia-driven). The amplitude of oscillation close to resonance is inversely related to the damping coefficient, the eigenfrequency squared, and the effective mass of the system (T. Leighton 1994).

5.2.4. Dynamic of Coated Bubbles

The majority of ultrasonic contrast agents are made of gas bubbles encased in a shell. The shell keeps the microbubbles stable and prevents the gas from dissolving into the liquid. The gas provides the bubbles with exceptional compressibility, making them effective acoustic scatterers. The shell will make the bubble less compressible, modifying its acoustic characteristics by raising the resonance frequency and providing more viscous damping to the oscillation.

Ultrasound contrast agents are usually encapsulated with a phospholipid, protein, or polymer coating. The coating protects the water from the gas, lowering surface tension and preventing the bubbles from dissolving. For coated bubbles, several Rayleigh-Plesset models have been developed. Church (1995) developed a theoretical model for a covered bubble based on the assumption that the gas core is separated from the liquid by an incompressible, solid elastic layer. Commercial 1st generation Albunex microbubbles feature an albumin shell and are stable at atmospheric pressure for an extended period. According to Overvelde *et al.,* (2010) the shell has a limited thickness, and the elasticity of the shell and the shell viscosity are affected by the stiffness and thickness of the shell.

As a result, in Church's model, the elastic shell is assumed to resist capillary pressure ($P_{g0} = P_0$), stabilizing the bubble against dissolution. The phospholipid shell of second-generation contrast agents is more flexible. The commercially available contrast agents Sonovue® (Bracco), Definity (Lantheus Medical Imaging), and Sonazoid (GE) are made out of a thin monolayer of phospholipids. Several models account for a (phospholipid) coating by assuming a thin viscoelastic shell, such as De Jong *et al.* (1994), Hoff *et al.* (2000), and, more recently, Sarkar *et al.* (2005). The Rayleigh-Plesset type models account for the shell through an effective surface tension, $\sigma(R)$, and the inclusion of a friction term, S_{fric} , owing to shell elasticity and viscosity.

$$\rho\left(\ddot{R}R + \frac{3}{2}\dot{R}^2\right) = P_{g0}\left(\frac{R_0}{R}\right)^{3\kappa}\left(1 - \frac{3\kappa\dot{R}}{c}\right) - P_0 - P_a(t) - 4\nu\rho\frac{\dot{R}}{R} - \frac{2\sigma(R)}{R} - 4S_{fric}\frac{\dot{R}}{R^2} \tag{5-44}$$

Hoff et al. (2001) adapted Church's model to account for the thin shell by reducing Church's equation to a form similar to Eq. (5-44). Table 5.2 shows the effective surface tension and shell viscosity for the various models. The effective surface tension varies with the bubble's radius (see Figure 5.7 taken from

Overvelde *et al.,* (2010) for a visualization of the various shell types). The shell elasticity parameters ($S_p = 2E_s = 6G_s d_{sh0} = 1.1\, N/m$) and shell viscosity parameters ($S_p = 16\pi\kappa_s = 48\pi\mu_s d_{sh0} = 2.7 \cdot 10^{-7}\, kg/s$) are selected to be equivalent in the models, as described by Gorce *et al*. (2000). The slope of the effective surface tension as a function of the bubble radius is similar to the models by De Jong et al. (1994) and Sarkar et al. (2005), in this particular regime. The key difference between the models is the effective surface tension at the initial bubble radius ($\sigma(R_0)$). It equals σ_ω in the De Jong's model and varies in the Sarkar's model. The value chosen was ($\sigma(R_0) = 0.036\, N/m$ for the Sarkar et al. (2005) model in this example.

Table 5.2: Models for the dynamics of coated bubble with elastic shell. The values for the initial gas pressure in the bubble (P_{g0}), the effective surface tension ($\sigma(R)$) and the shell viscosity (S_{fric}) for the models. Uncoated bubbles values are also provided for comparison (Overvelde et al., 2010)

Model	P_{g0} [N/m^2]	$\sigma(R)$ [N/m]	S_{fric} [kg/s]
Rayleigh-Plesset	$P_0 + \frac{2\sigma_w}{R_0}$	σ_w	–
Church [6], Hoff et al. [18]	P_0	$6G_s d_{sh0}\frac{R_0^2}{R^2}\left(1-\frac{R_0}{R}\right)$	$3\mu_s d_{sh0}\frac{R_0^2}{R^2}$
De Jong et al. [7]	$P_0 + \frac{2\sigma_w}{R_0}$	$\sigma_w + S_p\left(\frac{R}{R_0}-1\right)$	$\frac{S_f}{16\pi}$
Sarkar et al. [36]	P_0	$\sigma(R_0) + E_S\left(\frac{R^2}{R_E^2}-1\right)$	κ_s

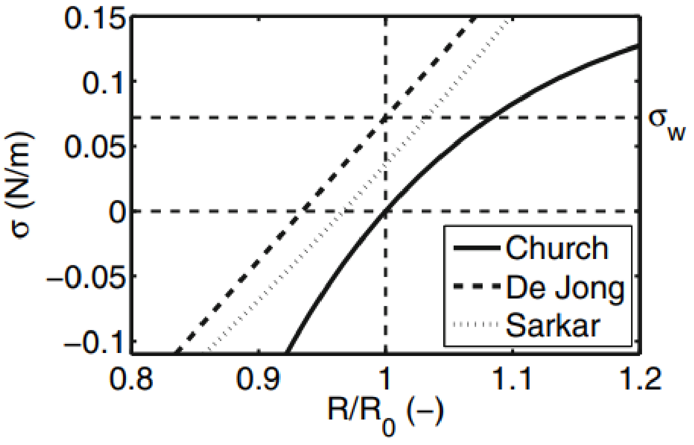

Figure 5.7 – The effective surface tension as a function of the bubble radius (R_0=2 μm) for the models of Church (1995), De Jong (1994), and Sarkar (2005) accounting for the purely elastic shell. Image adpted from Overvelde et al., 2010.

The Church (1995) model, as modified by Hoff et al. (2000), has a lower starting effective surface tension, $\sigma(R_0) = 0\, N/m$, and a different slope. It should be noted that the effective surface tension in these models is not restricted, and it can become negative and greater than σ_{ω}. Marmottant *et al.* (2005) proposed a model that is more appropriate for large amplitude oscillations. The model considers an elastic shell as well as buckling and shell rupture. Compression of the bubble raises the phospholipid concentration when the shell is elastic. Consequently, in the elastic regime, the drop in effective surface tension is a linear function of the area under compression. Further compression causes such high phospholipid concentrations that the shell buckles and the effective surface tension disappears. On the other hand, expansion reduces the phospholipid content and causes rupture. The effective surface tension is expected to relax to σ_w. The effective surface tension for the three regimes is determined by applying Eq. (5-44):

$$\sigma(R) = \begin{cases} 0 & \textit{if } R \leq R_{\textit{buckling}} \\ \chi\left(\frac{R^2}{R_{\textit{buckling}}^2} - 1\right) & \textit{if } R_{\textit{buckling}} \leq R \leq R_{\textit{breakup}}, \\ \sigma_w & \textit{if ruptured and } R \geq R_{\textit{breakup}} \end{cases} \tag{5-45}$$

with χ the shell elasticity and R_{buckling} and R_{breakup} the buckling and breakup radius, respectively. Figure 5.8 depicts the effective surface tension as a function of relative radius for the Marmottant model. A phospholipid monolayer forms the shell of a UCA microbubble. As in the Sarkar model example, the starting surface tension is set to $\sigma(R_0) = 0.036\ N/m$. The combination of the initial surface tension with a shell elasticity of $\chi = \frac{S_p}{2} = 0.55\ N/m$, yields a $R_{buckling} = 0.97\ R_0$ and $R_{breakup} = 1.03\ R_0$. In this scenario, the bubble is considered to break when the surface tension exceeds σ_w. In Eq. (5-44), the shell viscosity is given by $S_{fric} = \kappa_s$.

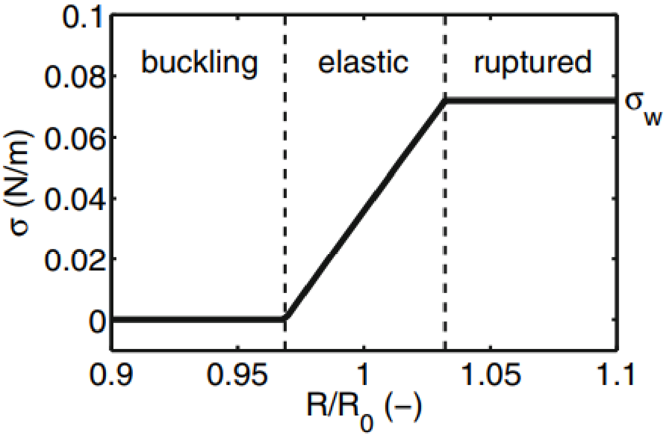

Figure 5.8 – The effective surface tension as a function of the bubble radius (R0=2 µm) including an elastic, buckling, and rupture of the shell regimes for the Marmottant et al. (2005) model. Image from Overvelde et al., 2010.

The elasticity of the shell raises the eigenfrequency of the bubble, while the viscosity of the shell increases the overall damping of the system, as will be presented in the next chapter.

5.2.4.1. Linearized equations

The bubble resonance frequency and damping coefficient are calculated similarly as in chapter 5.21. The eigenfrequency and total damping ($\delta_{tot} = \delta_r + \delta_{vis} + \delta_{th} + \delta_S$) for the De Jong et al. (1994) model are provided by:

$$f_0 = \frac{1}{2\pi}\sqrt{\frac{1}{\rho R_0^2}\left(3\kappa P_0 + (3\kappa - 1)\frac{2\sigma_w}{R_0} + \frac{2S_p}{R_0}\right)} \tag{5-46}$$

$$\delta_{tot} = \frac{\frac{3\kappa}{\rho c R_0}\left(P_0 + \frac{2\sigma_w}{R_0}\right)}{\omega_0} + \frac{4\nu}{\omega_0 R_0^2} + \frac{3p_e}{\omega\omega_0\rho a^2}\operatorname{Im}\left(\frac{1}{\Phi}\right) + \frac{S_f}{4\pi\rho R_0^3\omega_0} \tag{5-47}$$

The eigenfrequency of a coated bubble contains two contributions: one identical to the eigenfrequency of an uncoated bubble and one from the elastic shell. The damping of a shelled bubble is increased by the shell viscosity S_f. The eigenfrequency and the resonance frequency of an uncoated and coated bubble are shown in Figure 5.9. Within the graphical resolution, the uncoated bubble's resonance frequency and eigenfrequency agree. Because of the shell elasticity, the eigenfrequency of a covered bubble is greater than that of an uncoated microbubble. Damping does not affect the resonance frequency for an uncoated bubble and coated bubbles with $R_0 > 1\,\mu m$. The resonance curve of an uncoated and coated microbubble with a resting radius of 2 µm is shown in Figure 5.10.

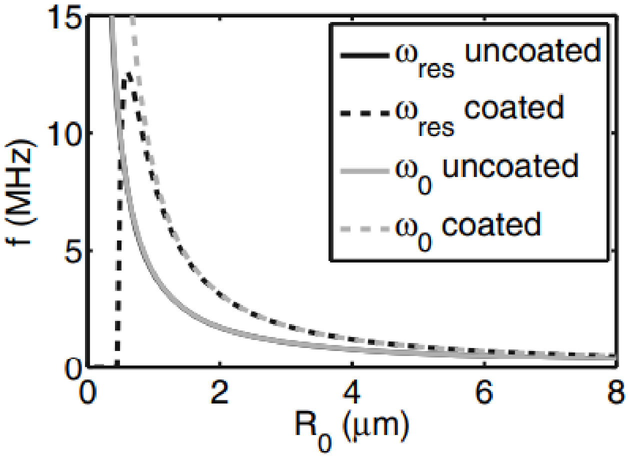

Figure 5.9 – The resonance frequency and the eigenfrequency of uncoated and coated bubbles as a function of the initial radius. The resonance frequency and the natural frequency of the uncoated bubble agree within graphical resolution (Overvelde et al., 2010).

The oscillation amplitude and resonance frequency are normalized to the uncoated bubble's maximum amplitude and resonance frequency, respectively. The damping and eigenfrequency of a coated microbubble increase while the effective mass remains constant. The amplitude of oscillation at resonance is thus reduced when the bubble has a shell (Figure 5.10). The system is stiffness-driven below resonance, neglecting the impact of damping. Because the shell stiffens the system, the oscillation amplitude below resonance is reduced for a coated microbubble. The oscillation amplitude is inversely related to the effective mass of the system much above resonance. As a result, the oscillation amplitude is independent of the shell properties above resonance.

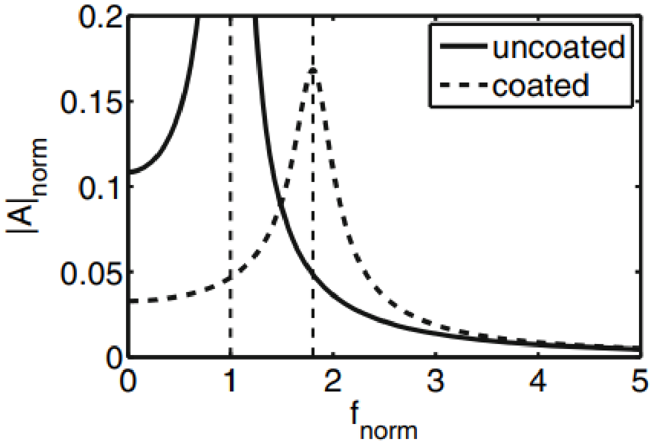

Figure 5.10 – The oscillation amplitude for an uncoated and coated bubble with R0 = 2 µm normalized with the uncoated microbubble's maximum oscillation amplitude. The driving frequency is normalized to the uncoated microbubble resonance frequency (Overvelde et al., 2010).

5.2.5. Scattering and absorption

The acoustical scattering cross-section, which is defined as the ratio between the scattered power $P_S(R_0,\omega)$ and the incident sound intensity $I_i(\omega)$, is commonly used to measure the scattering capabilities of bubbles.

$$\sigma_s(R_0,\omega) = \frac{P_S(R_0,\omega)}{I_i(\omega)} \tag{5-48}$$

When expressed by the amplitudes of the incident and scattered sound, $\hat{p}_s(R_0,\omega)$ and $\hat{p}_i(R_0,\omega)$, the scattering cross-section becomes:

$$\sigma_s(R_0,\omega) = 4\pi R^2 \left|\frac{\hat{p}_s(R_0,\omega)}{\hat{p}_i(R_0,\omega)}\right|^2 \tag{5-49}$$

The scattering cross-section can be described as a harmonic oscillator model.

$$\sigma_s(R_0,\omega) = 4\pi R_0^2 \frac{\Omega^4}{(1-\Omega^2)^2+(\Omega\delta)^2}, \Omega = \frac{\omega}{\omega_0} \tag{5-50}$$

where δ is the damping term, ω is the incident frequency, and ω_0 is the resonance frequency. The extinction cross-section is defined by:

$$\sigma_e(R_0,\omega) = \frac{P_e(R_0,\omega)}{I_i(\omega)} \tag{5-51}$$

where $P_e(R_0,\omega)$ represents the sum of scattered and absorbed power, i.e., the total power loss from the incident sound field, thus, the extinction cross-section can be represented as the sum of scattering and absorbed cross-sections.

$$\sigma_e = \frac{\delta}{\delta_r}\sigma_s \tag{5-52}$$

Inserting Eq. (5-50) into Eq. (5-52) yields

$$\sigma_e = \frac{\delta}{\delta_r}\sigma_s = 4\pi R_0^2 \frac{\Omega^4}{(1-\Omega^2)^2+(\Omega\delta)^2}\frac{\delta}{\delta_r} \tag{5-53}$$

Variation with frequency: The scattering cross-section changes with frequency, as seen in the left figure in Figure 5.11. For frequencies well below resonance, the scattering cross-section increases by 4 orders. For frequencies above resonance, the scattering cross-section is frequency independent. Around and above the resonance frequency, the scatter from a bubble deviates significantly from Rayleigh scattering (Hoff, 2001).

Variation with diameter: Figure 5.11's right diagram shows how the scattering cross-section varies with bubble diameter. The scattering cross-section grows with the sixth power of the diameter for diameters lower than the resonance diameter, ($\sigma_s \propto d^6$). For diameters greater than the resonance diameter, the scattering cross-section increases in proportion to the geometric cross-section of the bubble, ($\sigma_s \propto d^2$).

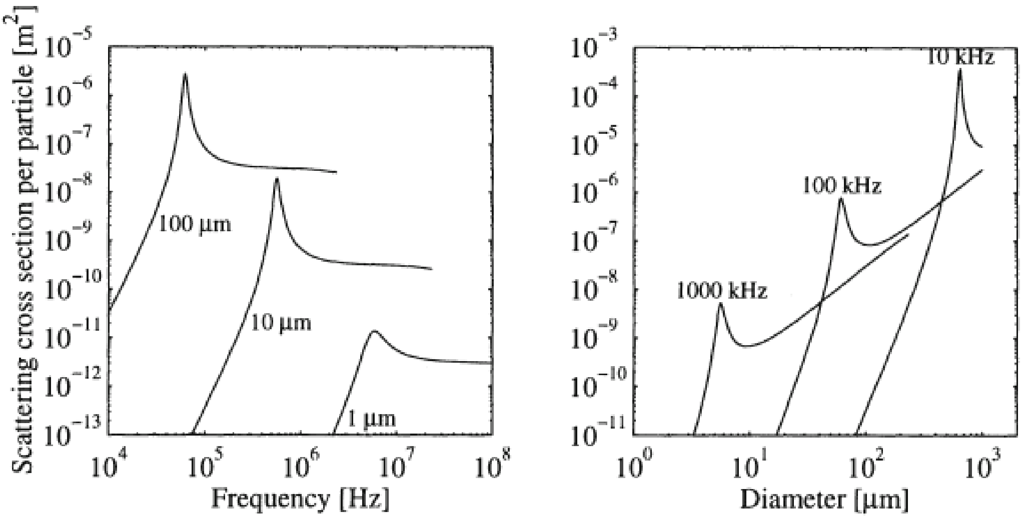

Figure 5.11 – Scattering cross-section as a function of frequency and bubble diameter (Hoff, 2001).

5.2.6. Scattering by bubbles populations

The last section detailed a single bubble's scattering (acoustic response). However, ultrasonic imaging is usually done on collections of particles or complex structures, and interference affects the scattered wave. The echo of specific contrast agents will be no different. The geometry of a set of particles, such as their number density, randomness, or positioning in space or on a plane, modifies the scattered intensity profoundly. The echo from a population of particles within a restricted region is explored in most studies. In this case, the scattered wave can be divided into two components: a term resulting from reflection from the overall structure of the "cloud" of scatterers, known as the coherent scattering contribution, and a term resulting from random fluctuations in acoustical properties within the population of scatterers, known as the incoherent scattering contribution (Mo and Cobbold 1992; Shung and Thieme 1993; Ishimaru 1997). The phase of the scattered wave is arbitrarily distributed for random populations of microbubbles away from the cloud's edge, resulting in incoherent scattering. Because of this statistical independence, the total scattered intensity equals the sum of each scatterer's scattering intensity. It is important to note that this assumption is only valid for diluted media, which is usually referred to as the independent scattering approximation. As a result, the scattered power grows linearly with particle density and depends on the particle's acoustical and geometric features, as explained in the preceding section. This regime also proves that increasing the variation of the scatterer's volume increases backscattering (Cobbold, 2007).

When particle locations are correlated, or multiple scattering occurs, the linear relation between the scattering coefficient, which is the scattering cross-section per unit volume (in $m^{-1}Sr^{-1}$), and particle concentration is lost. In this situation, the backscattering coefficient increases linearly with red blood cell density up to a maximum of around 16% hematocrit (Cobbold 2007) before falling, owing to the loss of randomness in particle location due to geometric restrictions imposed by their limited sizes.

For powerful scatterers, loss of linearity in the backscattering coefficient can be seen at considerably lower concentrations. In this example, scattering from one particle can influence the incident wave on another particle several diameters away. Foldy’s (1945) and Twersky’s (1964) theoretical work on multiple scattering of waves has been discussed in Ishimaru (1997). Chin (2001) briefly examined the problem where multiple scattering becomes important in particle populations in his thesis. The contribution increases with scattering strength (σ_b) rather than total scattering cross-section) and is inversely proportional to the square of the distance between each scatterer. The authors uses the concept of backscattering cross-section, σ_b, which is the scattered power per unit solid angle in the opposite direction to the incident beam (π radians). He proposed that the secondary scattering ratio (SSr) for particles scattered in space is given by Eq.(5- 54), where n_V is the particle density in a volume. It is feasible to derive the same secondary scattering ratio in 2-dimensions as stated in Eq. (5-55) by adapting his formula for scatterers on a plane.

$$SSr_{3D} = \frac{4\pi\sigma_b n_V^{2/3}}{0.5540^2} \tag{5-54}$$

$$SSr_{2D} = 16\pi\sigma_b n_S \tag{5-55}$$

Chin (2001) considers a secondary scattering ratio of 10% to be substantial. The maximum surface densities of particles, before multiple scattering becomes significant, can be estimated using the scattering cross-section obtained in the preceding section. Multiple scattering might be relevant, in the case of microbubbles, even when they are positioned many diameters apart from one other, and are off their resonance frequency. Indeed, repeated scattering can be significant for secondary bubbles tens of microns distant at resonance. It should be noted that scattering mixed with absorption will result in attenuation. Therefore, multiple scattering will affect signal loss via a population of particles.

The phases of scattered waves are not canceled by randomly distributed neighboring particles at the surface of a cloud of scatterers, resulting in a coherent wavefront. This applies to all "continuous" materials, even though they are composed of large concentrations of scatterers far smaller than the wavelength of the ultrasound. The scattering characteristics of individual particles are rarely used to calculate the ultrasonic echo from a continuous material. It is defined more by bulk qualities such as the differential in acoustic impedance at an interface.

5.2.7. Attenuation Coefficient

Microbubbles are very good scatterers that even in low concentrations can increase the attenuation of sound in water. For ultrasound contrast agents, acoustic attenuation is the basic method used to characterize them, giving information about their resonance frequency and damping, or Q-value.

The incoming sound intensity is lowered when passing through the microbubble suspension due to the bubbles' absorption and dispersion. At low bubble concentrations (volume fractions <10^{-3} (Druzhinin and Elghobashi 1998)), the interactions between bubbles are neglected, hence the power attenuated by the bubble suspension is the sum of the power attenuated by the individual bubbles. The unit dB per unit length attenuation coefficient for bubble suspension is given as (Gong, 2013):

$$\alpha(\omega) = 10ln\int_0^\infty \sigma_e(R_0, \omega)n(R_0)dR_0 \tag{5-56}$$

where $n(R_0)$ is the number of bubbles with a radius of R_0.

However, the attenuation measurements do not provide a relationship between attenuation level and the performance of contrast agents. For efficiency assessment of the UCA, acoustic backscatter should be measured. This physical phenomenon and measuring technique will be discussed further in chapter 5.2.9.

5.2.8. Influence of Bubble Size Distribution on Attenuation Coefficient and Resonance Frequency

The resonance frequency of UCA microbubbles is critical. As previously proven, the scattered signal from the microbubble is expected to be maximized when operated at the resonance frequency. Thus, understanding resonance frequency is critical for optimizing ultrasonic contrast imaging and treatment. The resonance frequency of a single microbubble is determined by its starting radius, shell viscoelastic characteristics, surrounding medium material parameters (e.g., density, surface tension, static pressure), and excitation acoustic pressure (Doinikov, Haac, et al. 2009).

Most UCA procedures generate microbubble populations with a broad size distribution. Because the dynamic response of a microbubble depends on its size, it is challenging to detect the resonance frequency of these UCA populations appropriately experimentally. Historically, the acoustic attenuation spectrum of UCA microbubble clouds was measured using ultrasonic spectroscopy (Hoff, Sontum, et al., 2000; He and Zheng, 2001; Yu, Zhang, et al., 2005). The resonance frequency was determined from the frequency-dependent attenuation curve as the frequency at which the observed attenuation achieved a local maximum. However, because the attenuation spectrum for polydisperse microbubbles is relatively broad, the maximum attenuation spans a wide frequency range. As a result, the resonance frequency cannot be determined precisely. If monodisperse microbubbles are used, the link between microbubble size and resonance frequency can be precisely quantified.

Talu et al. (2008) showed that monodispersed microbubbles outperformed polydispersed microbubbles in terms of echo-response, indicating that altering size distribution is an efficient strategy to increase sensitivity in molecular imaging. Based on these findings, Kaya et al. (2009) studied the echo responses of monodisperse lipid microbubbles produced by flow-focusing devices to establish a link between scattered echo, microbubble diameter, and excitation frequency. Both calculations and experimental acoustic data show that the monodisperse microbubble acoustic response increases with microbubble diameter. They suggested that narrowing contrast agent distribution, exciting microbubbles near resonance, or utilizing microbubbles with a larger diameter could boost the sensitivity of US imaging systems.

As demonstrated in chapters 5.2.1 and 5.2.4, the linear resonance frequencies for a single microbubble are determined in theory using Eq. (5-25) (free bubble) and (Eq. 5-44). (encapsulated bubble). Equation (5-56) is also used to get the frequency-dependent attenuation coefficient for a bubble population with a given size distribution. Thus, Gong et al. (2013) calculated the attenuation coefficient for monodisperse lipid-coated microbubbles to identify their resonance frequency. Because the theoretical simulation for lipid-coated microbubbles required unknown shell parameter values (e.g., viscosity and elasticity), the author only does a qualitative study.

Figure 5.12 depicts two Gaussian size distribution examples utilized by the author, with a total of 10^4 suspended microbubbles, a mean radius R0 of 3 µm, and standard deviations of 0.3 and 0.6. The expected attenuation as a function of incident frequency was determined for both free microbubbles and lipid-coated microbubbles with these size distributions and is shown in Figure 5.13.

Figure 5.13 displays the simulation results, where the frequency is normalized by a microbubble's projected linear resonance frequency with a mean radius of R_0. The author presents several conclusions. First, compared to encapsulated microbubbles, free microbubbles are more attenuative and have lower resonance frequencies. This is due to the shell dampening the bubble oscillations, reducing echogenicity, as demonstrated in the previous chapter. Second, increasing the polydispersity of the size distribution reduces the peak magnitude while broadening the attenuation spectrum. Third, the polydispersity of microbubbles causes a drop in the resonance frequency, which increases with polydispersity. Fourth, the polydispersity-induced resonance frequency changes are more significant in encapsulated microbubbles than in free ones.

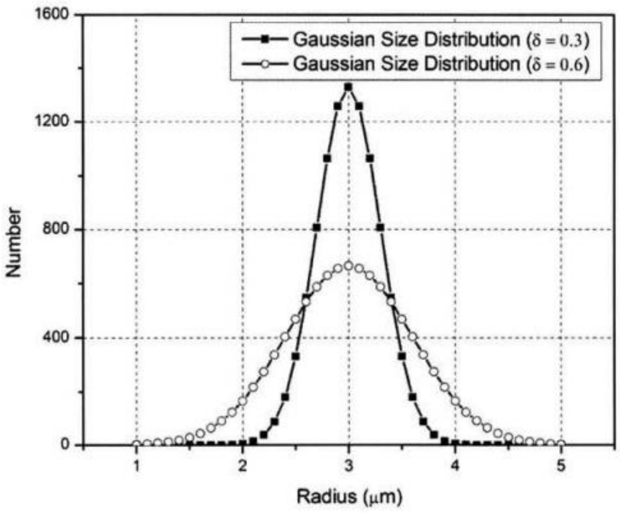

Figure 5.12 – Simulated microbubbles Gaussian size distributions with total number 10^4, mean radius R0 = 3 μm and standard deviation δ = 0.3 and 0.6 (Y. Gong 2013).

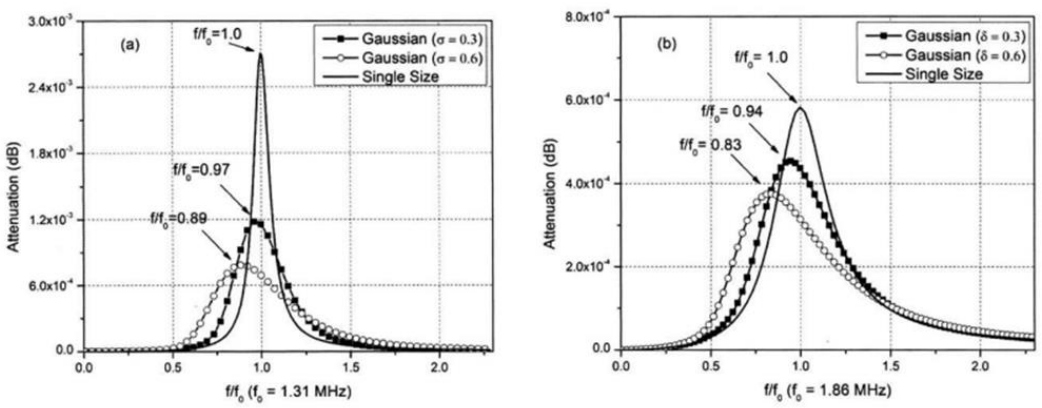

Figure 5.13 – Simulated attenuations as a function of incident frequency for (a) free bubbles, and (b) lipid-coated microbubbles with uniform size distribution and Gaussian size distributions (Figure 5.12), respective (Y. Gong 2013).

As a result, it is proposed that the resonance frequency of UCA microbubbles with Gaussian size distributions does not match the resonance frequency of microbubbles with uniform size distributions. Additional computations were performed to evaluate the effect of polydispersity on resonance frequency for microbubbles of varying sizes. The resonance frequency shift as a function of mean radius for lipid-coated microbubbles with Gaussian size distributions is shown in Figure 5.14 (δ = 0.17). It diminishes as the mean radius increases, implying that smaller microbubbles are more influenced by polydispersity in terms of the resonance frequency. The monodisperse microbubbles in his studies had a mean radius ranging from 1.5-6 μm with a mean δ of 0.17, and the predicted resonance frequency shift is 9%. It demonstrates that monodisperse microbubbles are more precise and suited for studying experimentally the influence of size on the resonance frequency and attenuation coefficient.

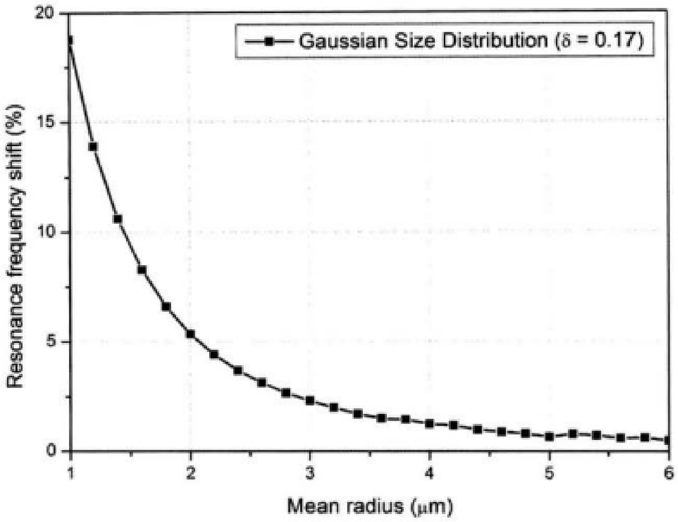

Figure 5.14 – Resonance frequency shift as a function of mean radius for lipid-coated microbubbles with Gaussian size distributions (δ = 0.17) with respect to linear resonance frequency of microbubbles with the uniform sizes (Y. Gong 2013).

Using a similar microfluidic chip structure to Hettiarachchi et al., (2007), the author investigates experimentally two batches of lipid-coated microbubble US contrast agent. The mean diameter of these microbubbles was 4.2 ± 1 µm and 8 ± 1µm, respectively. Next, the frequency-dependent acoustic attenuation coefficient of the two-microbubble batches and a suspension of polydisperse UCA were tested. They discovered that smaller-sized microbubble attenuation happened more frequently. Polydisperse microbubble attenuation occurred over a wider frequency range compared to uniform microbubbles. Furthermore, at low acoustic pressures, the resonance frequency of lipid-shelled microbubbles was studied and decreased with increasing acoustic pressure (Gong et al. 2010). Furthermore, compared to free microbubbles of the same dimension, coated microbubbles exhibited a lower resonance frequency. They also proved that bigger microbubbles had stronger relative resonance frequency changes than smaller ones (Macdonald et al. 2004).

5.2.9. Acoustic backscatter coefficient

Diagnostic ultrasound imaging is based on acoustic backscatter. An ultrasonic pulse is sent into the body, and the echoes it receives are utilized to create a picture of the inside structures. As a result, backscattered power measurement is required to characterize ultrasonic contrast agents.

The theoretical predictions of scattering and attenuation are obtained from the previously described linear scattering model for homogeneously and randomly distributed scatterers. Assuming no multiple scattering, $N\sigma_S(r,f)$ gives the overall scattering cross-section for a large number *N* of randomly distributed identical scatterers (Merzbacher *et al.*, 1977). Similarly, $\sum_r n(r)\sigma_s(r,f)$ gives the total scattering cross-section per unit volume for a cloud of various-sized scatterers, where *n(r)* is the number of scatterers of radius *r* per unit volume. The theoretical differential scattering cross-section per unit volume or differential volumetric scattering cross-section is then derived for scatterers such as tiny microbubbles compared to a wavelength whose scattering behavior is mainly isotropic.

$$\eta(f) = \frac{\sum_r n(r)\sigma_S(r,f)}{4\pi} \tag{5-57}$$

where $\eta(f)$ is measured in units of (cm.sr^{-1}). This is often referred to as the backscatter coefficient (Insana and Brown, 1993). Similarly, attenuation across a layer of scatterers is calculated. The intensity of a plane wave of initial intensity I_0 after passing through a layer of thickness *x* and assuming no multiple scattering is given by:

$$I = I_0 exp\left[-\left(\sum_r n(r)\,\sigma_e(r,f)\right)x\right] = I_0 exp\,[-\alpha_I x] \tag{5-58}$$

where α_I is the theoretical attenuation coefficient for intensity and σ_e is the extinction cross-section of a scatterer of radius *r*, which is defined as the total power extinguished by the scatterer per unit incident intensity at frequency *f*. The total extinction cross-section, $\sum_r n(r)\,\sigma_e(r,f)$, in units of Np/cm, then yields the value α_I. It should be noted that the intensity attenuation coefficient provided here differs by a factor of two from the predicted linear amplitude attenuation coefficient α_a. The amplitude attenuation coefficient is commonly included in the complex wavenumber equation for a propagating plane wave: $\tilde{k} = k + i\alpha_a$. A plane wave's complex pressure amplitude is given by:

$$A(x,t) = A_0\, exp\left[i\left(\tilde{k}x - \omega t\right)\right] =$$

$$A_0 exp\,[-\alpha_A x] exp\,[i(kx - \omega t)] \tag{5-59}$$

Because the intensity of such a wave is proportional to the square of the pressure amplitude, the intensity after propagating *x* distances is as follows:

$$I = I_0 exp\,[-2\alpha_A x] \tag{5-60}$$

Thus, from Eq. (5-58) and (5-60)

$$\alpha_I = 2\alpha_A \tag{5-61}$$

To clarify the notation, the attenuation coefficient, α_{dB}, expressed in dB/cm, is provided by:

$$\alpha_{dB}(f) = \frac{[20\log(A_0/A)]}{x} = \frac{\{20\log[\exp(\alpha_A x)]\}}{x} =$$
$$\alpha_A(20log\ e) = 8.69\alpha_A \tag{5-62}$$

When expressed in terms of the intensity attenuation coefficient, the above expression becomes:

$$\alpha_{dB}(f) = \frac{[10\log(I_0/I)]}{x} = \frac{\{10\log[\exp(\alpha_I x)]\}}{x} =$$
$$\alpha_I(10log\ e) = 4.34\alpha_I \tag{5-63}$$

From Eq. (5-63) and Eq. (5-58), we note that

$$\alpha_I = \textstyle\sum_r n(r)\sigma_e(r \tag{5-64}$$

$$\alpha_A = 0.5\textstyle\sum_r n(r)\sigma_e(r) \tag{5-65}$$

$$\alpha_{dB} = 4.34\textstyle\sum_r n(r)\sigma_e(r) \tag{5-66}$$

The theoretical dependences of backscatter and attenuation on scatterer concentration are shown in Eq. (5-57) and Eqs. (5-64) to (5-66), respectively (in the single scattering approximation) (Marsh *et al.,* 1998). Although the formulas are similar, it is crucial to highlight that the expected backscattered power increases linearly with concentration, but the relative amount of power lost from the incident wave owing to the scatterers rises exponentially. This fundamental distinction is reflected in the units used to describe these quantities: The backscatter coefficient $\eta(f)$ is usually reported linear, whereas the attenuation coefficient α_{dB} is recorded in logarithmic terms in decibels per centimeter.

Thus, twice the concentration of microspheres in a given volume should double the linear value of the backscatter coefficient, i.e., a 3 dB gain. However, the signal power traveling through this same volume will diminish exponentially. These effects compete: the backscattered signal strength increases linearly with increasing dose until the attenuation, which grows much more rapidly, becomes the dominant factor (Marsh *et al.*, 1998). The intensity of the backscattered signal gradually declines beyond this point. This effect has been anticipated in simulations (Hoff *et al.*, 1994, De Jong *et al.*, 1991) and can be one of the primary causes of contrast-induced acoustic shadowing in clinical imaging. It should also be noted that, due to bubble resonances, the attenuation and backscatter of bubble-based contrast agents can be highly frequency-dependent. Therefore, the shadowing effect will be more evident in frequency ranges where the attenuation is highest.

5.2.9.1. Experimental data reduction

Adjusting the returned ultrasonic signal for the electromechanical response of the measuring system, beam diffraction, and the effects of attenuation and interfaces is required to reduce experimentally obtained backscatter data to absolute backscatter coefficient. Some of the approaches presented for determining the backscatter coefficient are briefly reviewed below. The computation of the beam diffraction correction is where these approaches often diverge the most. Siegelman and Reid (1973) presented a method for insonifying a sample using narrow-band sine wave bursts from a planar transducer in the far-field. The effective beam volume is governed laterally by the 3-dB beamwidth and axially by time gating. In this approximation, the field is assumed to be constant everywhere within the cylindrical volume imposed by the time gates and 3-dB beamwidth. O'Donnell and Miller (1981) extended this technique for focused transducers and broadband insonifying pulses. They applied it to samples in the focal area of focused transducers and the far-field of planar transducers. Campbell and Waag (1983) presented a more comprehensive and broad strategy for dealing with a two-transducer scattering system. They rigorously account for the impacts of time-domain gating convolution and beam diffraction in the case of transducers with Gaussian beam sensitivity patterns.

After, Madsen et al. (1984) proposed a method for calculating backscatter coefficients. The diffraction pattern is calculated precisely from knowledge of the transducer face shape to account for variations in beam sensitivity both laterally and axially concerning the insonified volume. Wear et al. (1989) combined several of the earlier methods' simplifications with the more demanding calculations of the Madsen et al. (1984). In this case, the variation in lateral pressure amplitude in the scattering volume due to diffraction was accounted for, whereas both the axial variation in beam intensity and the convolution of the sinc function introduced by time gating were neglected.

To compensate for diffraction effects, treatments that attempt to model the transducer's beam function accurately typically require the evaluation of integrals of the pressure field across the face of the transducer or over the volume occupied by the scatterers; the time required for numerical computation of these quantities may be significant. O'Donnell and Miller's (1981) solution compromise by incorporating several approximations that lower the amount of computation required by many orders of magnitude (Hall, 1996) but at the expense of accurate beam function determination. However, one advantage of this more straightforward approach is that the formulation for reducing the data to backscatter coefficients can be written intuitively as a product of separate terms individually describing the compensation for electromechanical effects and diffraction effects attenuation, and interface losses. This feature is provided in the Wear et al. (1989) formulation, incorporating more precise diffraction modeling. However, it necessitates the computation of several integrals involving the complex pressure field.

Marsh et al., (1998) used in their work a technique first reported by Chen et al., (1997) for measuring the backscatter coefficient. They extend the technique to the specific instance of a spherically focused transducer insonifying an ensemble of scatterers located at the transducer's geometrical focus with a reference measurement obtained from a flat reflector located in the transducer's focal plane. In this case, the authors can reduce complicated integrals of diffraction coefficients over the surface of the transmitting transducer and the volume that the scatterers occupy to simple function evaluations, reducing the amount of computation required while accurately calculating terms associated with beam diffraction effects. We noticed that the approach employs two important approximations similar to those used by Wear et al. (1989). The diffraction correction is generally constant over the length of the gated region, and the influence of the time gate convolution with the backscattered signal is insignificant. The experimentally measured , is then calculated as follows:

$$\eta(f) = \left\{\frac{\langle |V_s(f)|^2\rangle}{\left|V_{ref}(f)\right|^2}\right\}\left\{\frac{r_0^2}{\pi a^2 l E_\infty}\left|D_{ref}(f)\right|^2\right\} \times \left\{\frac{1}{A_S(\alpha_A(f), l, x_0)}\right\}\left\{R\,\frac{T_{ref}^2}{T_S^2}\right\} \tag{5-67}$$

The first contribution in the equation comes from the backscatter measurement and electromechanical compensation, where $\langle |V_s(f)|^2\rangle$ is the average measured power spectrum of the backscatter from the sample, and $\left|V_{ref}(f)\right|^2$ is the power spectrum returned from the reflector placed in the focal plane of the transducer. The ratio between these two values is called the average apparent backscatter transfer function of a sample, $\langle |S(f)|^2 \rangle_{apparent}$.

The second term is the diffraction compensation, where r_0 is the transducer focal length, a is the transducer's radius, E_∞ is a constant with a value of 0.46 (Chen et al. (1997) for details on the determination of this dimensionless constant), l is the length of the insonified volume, given by $l = c\tau/2$ (c is the speed of sound and τ is the gate duration). The remaining factor $D_{ref}(f)$ is the acoustic coupling function given as:

$$D_{ref}(f) = -\{1 - exp\left(-iG_p\right)\left[J_0\left(G_p\right) + iJ_1\left(G_p\right)\right]\} \tag{5-68}$$

$$G_p = ka^2/2r_0 \tag{5-69}$$

where J_n is the Bessel function of the first kind of order n, and k is the wavenumber. The third term of the equation is the attenuation compensation, where A_s shown by the experimentally obtained attenuation coefficient $\alpha_A(f)$ is:

$$A_s(\alpha_A(f), l, x_0) = \ exp\,[-4\alpha_A(f)x_0] \times$$
$$exp\,[-2\alpha_A(f)l]\,\frac{exp\,[2\alpha_A(f)l] - exp\,[-2\alpha_A(f)l]}{4\alpha_A(f)l} \tag{5-70}$$

which is equivalent to the attenuation correction factor given by Sigelmann and Reid (1973) for insonifying pulses much shorter than the time gate selecting the scattering volume. In this analysis, water attenuation was considered to be zero.

The fourth term is the interface loss compensation, where *R* denotes the intensity reflection coefficient for the reference reflector; this component was introduced into the $\eta(f)$ calculation to compensate that the reference measurement was done with a surface that was not a perfect reflector. The term T_{ref}^2 in the calculation to account for the fact that the reference measurement was collected from a reflector positioned beyond the front wall of the specimen chamber.

Estimating the backscatter coefficient is less computationally intensive than other ways that need integral evaluations. Physically, Eq.(5-67) gives a valuable framework for understanding the backscatter coefficient's behavior by dividing it into terms that describe apparent scattering intensity, diffraction correction for the effective beam volume, attenuation correction, and interface losses.

Marsh et al. (1998) demonstrated experimentally that it is possible to compensate for attenuation, region of interest length and position, and measurement system response under carefully controlled conditions, proving a linear relationship of backscatter coefficient to contrast agent concentration. Also, even when no adjustment for beam diffraction is used, a linear relationship exists between backscattered power and concentration. This association appears to hold true (within the available bandwidth) for all of the Albunex® concentrations utilized in their investigation. This linear connection may help with quantitative assessments of cardiac perfusion via RF analysis. The fact that the microsphere size distribution might well be significantly altered in vivo (due to pulmonary filtering, gas diffusion into or out of the microspheres, bolus dilution in the blood, etc.) would change the frequency dependence of the attenuation and backscatter from the agent (De Jong and Hoff, 1993, De Jong et al. 1992, Hoff et al. 1994), but would presumably not affect the linear backscatter-concentration relationship.

6. MATERIALS AND EXPERIMENTAL DESCRIPTION

Acoustic backscatter is the main mechanism used for diagnostic ultrasound imaging. Therefore, the measurement of the backscatter power of the ultrasound contrast agent's population is crucial for their characterization.

This chapter aims to describe the methods used to characterize the backscatter acoustic response of the freeze-dried monodisperse PVA-shelled microbubbles, in comparison with freshly produced microbubbles, and commercially available polydisperse microbubbles Sonovue^{TM}. We describe the backscattering acoustic characterization setup, in which two different geometries for the bubbles' confinement system were used: the 'centimetric cell' and the 'milli-channel'. The method used for measuring the backscatter signal of the bubbles, as well as the deconvolution process are also presented in this chapter. Finally, we present the backscatter acoustic measurements using an universal imaging approach developed at Institut Langevin. This approach is inspired by the advent of multielement technology in acoustics and by the insight that a matrix formalism is a natural way to describe ultrasonic wave propagation between arrays of transducers.

6.1. Acoustic Backscatter Characterization of the Microbubbles

The backscattering measurements were performed with a single focused ultrasound transducer (Imasonics, Voray-sur-l'Ognon, France) with a center frequency of 2.25 MHz, a relative bandwidth of ~50% (i.e., a quality factor of ~2), a focal distance of 38 mm, and a 38 mm aperture. The transducer was used in a pulse-echo mode to be an emitter and a receiver of the signals. The negative acoustic pressure, measured and calibrated using a needle hydrophone (HNR−0500 S/N: 2054, Onda Corporation, USA), was of 150 kPa in a large water container. The pulses consisted of a sinusoidal 5-cycle burst signal with a 1-ms pulse repetition period, generated with a function generator (Tektronix AFG 2021, USA). The measurement covered a frequency range of 0.75 MHz to 3.5 MHz in steps of 0.15MHz, yielding 18 different central frequencies. The sweeping of 5-cycle emitted narrowband pulses at different central frequencies enables to fully exploit the bandwidth of the transducer. A PicoScope (5242D, Pico Technology, UK) was used for data acquisition, with its dedicated software (PicoScope 6, Pico Technology, UK), to monitor and record the detected signal (Figure 6.1A) The acquisition frequency was 20Hz (~1 waveform/45ms), where each waveform (i.e., echo) consisted of 3125 data points with a sampling frequency of 62.5 MSamples/s (16ns sample interval). The bubbles were insonified by a series of 50 narrowband 5-cycles pulses per transmitted frequency, to obtain a statistically relevant scattering signal. A MATLAB computer program was written to fully automate the measurements by transferring the 50 waveforms to a PC and by uploading the new waveform at 0.15MHz higher center frequency and compensated amplitude (explained in detail in chapter 6.1.1), to the arbitrary function generator. A complete measurement over the full range of frequencies took, typically, 2 minutes and in total 900 waveforms.

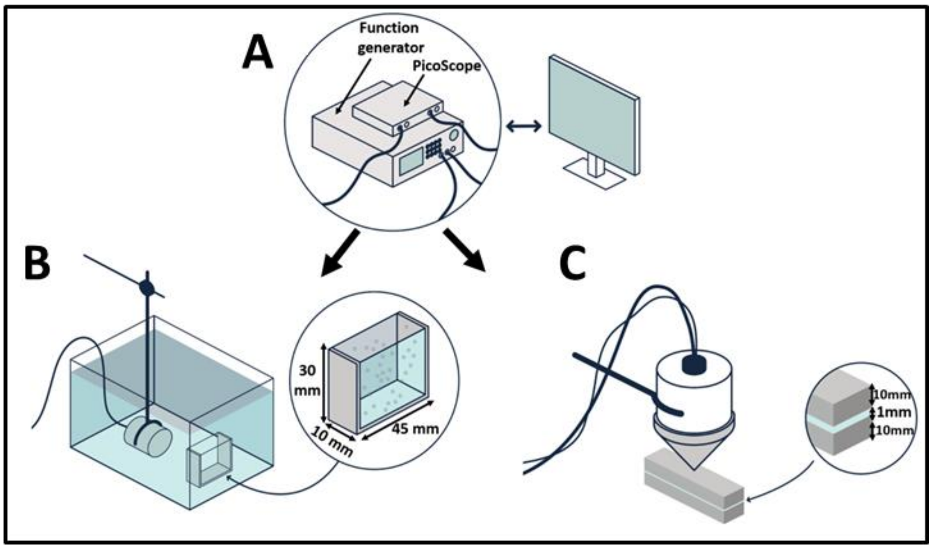

Figure 6.1 – Acoustic characterization setups with different geometries and typical acoustic responses of fresh bubbles and SonoVue. (A) The instrumentation for the data acquisition, monitoring, and recording of the detected signal consist of an arbitrary wave function generator (Tektronix AFG 2021, USA), and a PicoScope (5242D, Pico Technology, UK). (B) Schematic drawing of the centimetric cell used for the backscatter acoustic characterization of the bubbles. The bubbles were injected in a MilliQ water-filled container (45mmX10mmX30mm) which was placed in a degassed DI waterfilled large container. (C) Schematic drawing of the milli-channel for the backscatter acoustic characterization of the bubbles. The focal transducer was coupled with an acoustic gel-filled 3D-printed waveguide.

Each analyzed echo was time-gated at the focal point of the transducer, here referred to as the region of interest (ROI). The ROI was taken between the echoes of the walls in the measurement system (presented below) and typically consisted of 800 points, yielding a frequency resolution in the frequency domain of approximately 78 kHz. (Figure 6.2). Their power spectrum was then calculated (via a Fast Fourier Transform (FFT) algorithm) and averaged with a custom-written

MATLAB code. Figure 6.3 shows an example of the FFT of the emitted pulses (i.e., excitation) across the sweeping frequencies, reflected by the metallic plate, as will be explained in the following sub-section.

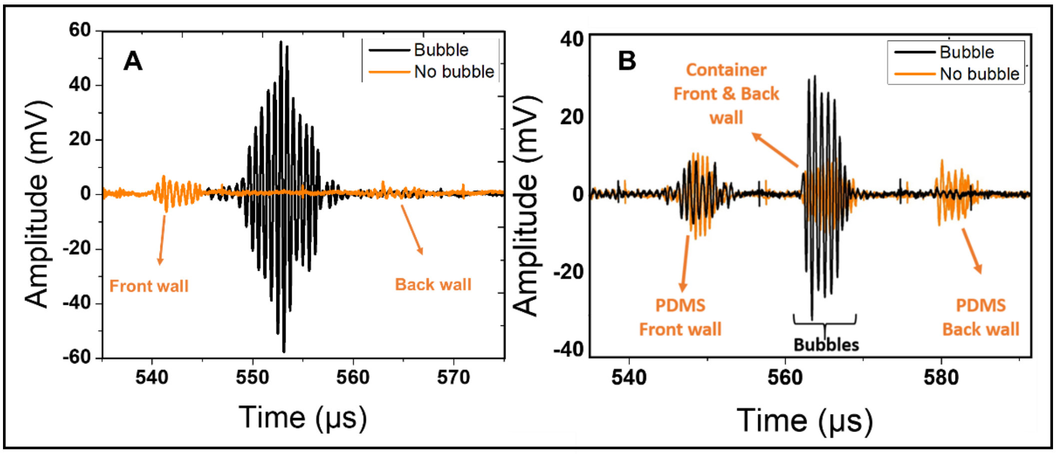

Figure 6.2 – The backscattered echoes show a comparison of 10^6 freshly generated polyvinyl alcohol (PVA) monodisperse microbubbles with a reference measurement (where there are no bubbles) at 1.35 MHz central sweep frequency. (A) The weak front and back wall echoes originated from the mylar windows, while the echoes from the bubbles appeared between these walls, in this 10 mm height cell. (B) The front and back wall echoes originated from the PDMS structure, while the echoes from the confined bubbles merged with the front and back walls of the chamber whose height was 1 mm.

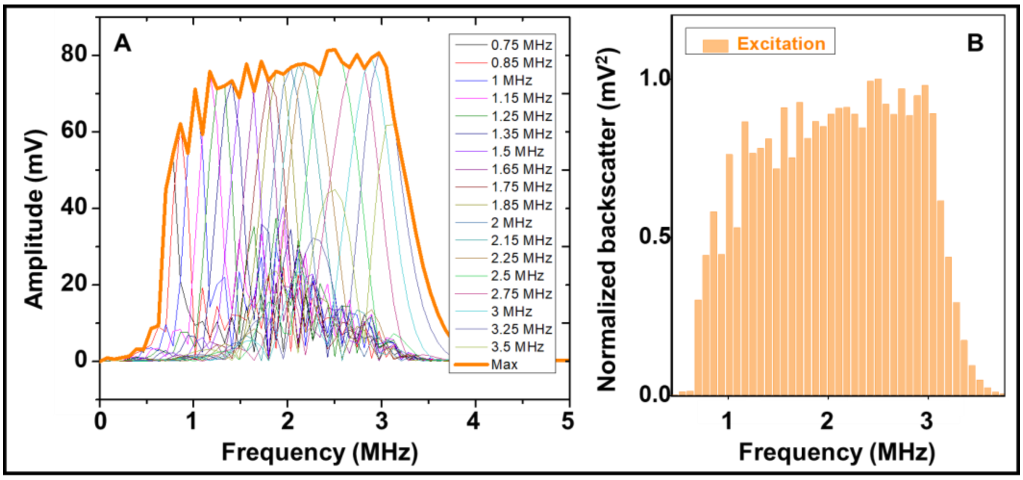

Figure 6.3 – FFT of the emitted pulses (i.e., excitation) across the sweeping frequencies, reflected by the metallic plate. A) The spectrum of the center frequencies emitted through each experiment from 0.75 to 3.5MHz. The maximum amplitude (orange) in each frequency is highlighted. B) The normalized emitted pulse, in which the orange bars illustrate the maximum excitation amplitude in each frequency from 0.75 to 3.5MHz

6.1.1. Method of Measurement and Deconvolution of the Backscattering Signal from the Bubbles

The following method was used to determine the back-scattered signal produced by the bubble. Firstly, measurements are taken without bubbles. Then, a metallic plate is placed in a large water container, positioned orthogonally to the transducer axis in the focal plane. The transducer emits a 5-cycles sinusoidal pulse-wave, whose amplitude, received by the plate, is given by the relation:

$$E(f)= \alpha(f)Vo(f), \quad (6\text{-}1)$$

in which $\alpha(f)$ is the emission transfer function of the transducer and $Vo(f)$ is the applied voltage measured in open circuit. $E(f)$ is the resulting acoustic pressure ‘seen’ by the plate in the degassed deionized water. The metallic plate assumed as a perfect reflector will reflect a wave of the same amplitude, captured by the transducer. The resulting signal $R(f)$, measured by the transducer, will be given by:

$$R(f)= \beta(f)E(f)= \beta(f)\alpha(f)\ Vo(f), \quad (6\text{-}2)$$

in which $\beta(f)$ is the reception transfer function of the transducer. In the procedure we use, we adjust the voltage $Vo(f)$, to obtain a flat response that we normalize to $R(f)= 1$; this implies $\beta(f)\alpha(f)\ Vo(f)= 1$. This quasi-flat response is shown in Figure 6.3A and B. Secondly, we add the bubbles to the measurement systems (described hereinafter), assuming that bubbles are located at the same place as the metallic plate. Thus, the bubbles will also ‘see’ a wave of amplitude $\alpha(f)Vo(f)$. In turn, they scatter a wave of amplitude

$$B(f)=K(f)\alpha(f)Vo(f), \quad (6\text{-}3)$$

where $K(f)$ is the acoustic frequency spectrum of the bubbles. This wave is captured by the transducer and gives rise to a signal $R(f)=\beta(f)B(f)= \beta(f)\alpha(f)\ Vo(f)K(f)$. Since we work with $\beta(f)\alpha(f)\ Vo(f)=1$, this signal will be $K(f)$. Thus, we directly determine the acoustic bubble spectrum with this two-step method.

6.2. Acoustic characterization of the fresh bubbles in two geometries: the ‘centimetric cell’ and the ‘milli-channel’

With the method just described, we investigated the backscatter response of bubbles of different types (mono and polydisperse) in two geometries: a ‘large’ cell which is referred to as the ‘centimetric cell’, shown in Figure 6.1B, and a milli-channel geometry, which is referred to as the ‘confined system’ - in which the fluid is left at rest -, shown in Figure 6.1C. In the centimetric cell, which corresponds to the type of geometry traditionally used in the literature (Hoff 2001), the bubbles were injected in a Milli-Q water-filled container (45mmx10mmx30mm), placed in a degassed deionized (DI) water-filled large water container. The centimetric cell was 3D-printed and Mylar thin films, with approximately 25µm thickness, were glued on both sides of the cell to ensure acoustic transparency. A magnetic stirrer ensured a homogenous bubble distribution. As shown in Figure 6.2A, in the absence of the bubbles, only a weak echo, shown in orange, appears in the temporal signal. It originates from the echo of the Mylar windows (i.e., the walls). In the presence of bubbles, the signal coming from them can easily be identified (Figure 6.2A). These features allow working with excellent signal-to-noise ratios, as currently found in the literature in this type of geometry. In order to avoid discontinuities in the edges of ROI analyzed, the backscattered signals were windowed by a *Hanning* window before being Fourier-Transformed.

The confined system, or ‘milli-channel’ (in which the liquid is at rest), was replicated with PDMS from a mold. The thickness of the PDMS channel is 10 mm, the channel width is 35 mm and its height is 1 mm (Figure 6.1C). In the absence of bubbles, the temporal signal exhibits acoustic reflections of the different interfaces present in the system (see the orange line in Figure 6.2B). In the presence of the bubbles, a strong signal appears. The signal contains two contributions: the one from the milli-channel walls (that can be estimated from the orange line of Figure 6.2B), and the bubbles. In the analysis of the data, we will subtract the wall echo from the response.

6.3. Acoustic Backscatter Characterization: Ultrasound Matrix Imaging

In collaboration with Flavien Bureau (a Ph.D. student of Alexandre Aubry at Institut Langevin), we investigated the backscatter acoustic response of the freeze-dried monodisperse PVA-shelled microbubbles flowing through a Peripheral Vascular Doppler Flow Phantom (Models ATS 524, CIRS, USA), a tissue-mimicking phantom composed of sub-resolution scatterers which generate ultrasonic speckle characteristic of human tissue. The phantom contains a flow channel simulating superficial vasculature located 15 mm below the scan surface. The microbubbles were resuspended and introduced into the phantom flow channel for the measurements.

In order to efficiently isolate and characterize the bubble response, our idea was to use a quite universal imaging approach developed at Institut Langevin. This approach is inspired by the advent of multielement technology in acoustics and by the insight that a matrix formalism is a natural way to describe ultrasonic wave propagation between arrays of transducers.

The matrix approach begins with the experimental acquisition of the reflection matrix *R* associated with the medium to be imaged. This matrix contains the response of the medium recorded by each transducer of the probe, for a set of illuminations. Depending on the problem one is facing, this matrix can be investigated on different bases. The simplest acquisition sequence consists in emitting with one element at a time and for, each emission, recording with all elements the time-dependent field reflected back from the medium (Figure 6.4A). This “canonical basis” was first used to define and exploit the so-called time-reversal operator (Prada and Fink, 2002). It is now commonly used in nondestructive testing, referred to as the full matrix capture sequence (Lambert et al, 2020). A matrix acquired in this way can be written mathematically as $R_{uu}(t) \equiv R(u_{out}, u_{in}, t)$, where u is the position of elements along the array, “in” denoting transmission, and “out” denoting reception.

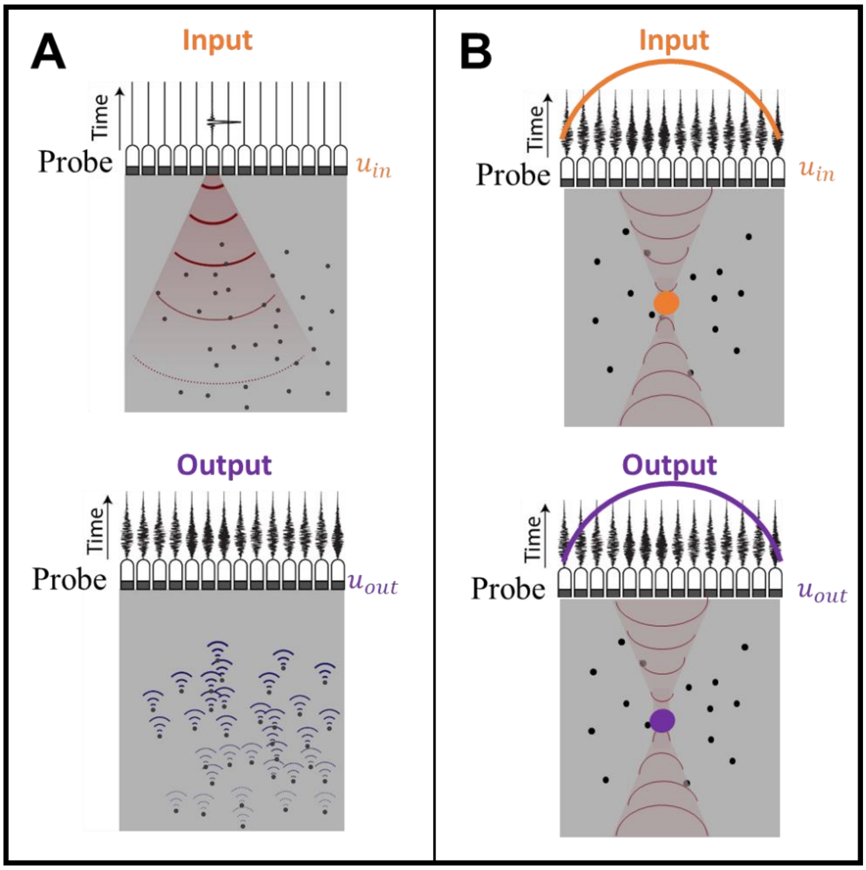

Figure 6.4 – A) Illustration of the recording of the reflection matrix $R_{uu}(t) \equiv R(u_{out}, u_{in}, t)$. One element at a given position u_{in}sends a short pulse and the corresponding echoes are received at each transducer positioned at u_{out} B) Illustration of the time delays applied at the input and output to create the B-mode image confocal image.

Conventional ultrasound imaging relies on confocal beamforming, using the process of delay-and-sum (DAS) beamforming, which is based on a coherent summation of all the measured back-scattered echoes generated by any point of the medium. Each echo is selected by computing the time-of-flight associated with the forward and return travel paths of the ultrasonic wave between the probe and the image voxel. From a physical point of view, time delays in transmission are used to concentrate the ultrasound wave on a focal area whose size is ideally only limited by diffraction. Time delays at reception select echoes coming from this excited area. Thus, the confocal imaging techniques, imply that, for each point of the image, a double-focusing operation is performed. Thus, from the reflection matrix, the classical B-mode image can be formed by applying appropriate time delays to each element in emission and reception (Figure 6.4B) and summing coherently the resulting echoes (delay and sum algorithm):

$$I[r] = \sum_{u_{in}} \sum_{u_{out}} R\left[u_{in}, u_{out}, t_{u_{in}\to r} + t_{r\to u_{out}}\right] \tag{6-4}$$

where $t_{u_{in}\to r}$ is the time that the emitted pulse from transducer u_{in} takes to reach the focus point r, and $t_{r\to u_{out}}$ is the time that the reflected wave takes to reach the transducer u_{out} from the focal point r.

However, the confocal image approach rests on the assumption of a homogeneous medium between the probe and target. Large-scale fluctuations of the wave velocity in the medium can result in wave-front distortion (aberration) and a loss of resolution in the subsequent reflectivity image. Smaller-scale inhomogeneities with a high concentration and/or scattering strength can induce multiple scattering events which can strongly degrade image contrast. Therefore, in contrast with conventional ultrasound imaging that relies on confocal beamforming Figure 6.5A), the idea here is to apply independent focused beamforming procedures at the input and output of the reflection matrix. This process yields a focused reflection (R_F) matrix that contains the responses between virtual transducers synthesized from the transmitted and received focal spots (Figure 6.5B). The R_F matrix holds much more information on the medium than does a conventional ultrasound image. Importantly, the resolution can be assessed locally for any pixel of the image. Mathematically this matrix can be formed as before in the time domain by applying appropriate time delays in emission and reception:

$$\boldsymbol{R_F}[\boldsymbol{r_{in}}, \boldsymbol{r_{out}}, \boldsymbol{z}] = \sum_{u_{in}} \sum_{u_{out}} R\left[u_{in}, u_{out}, t_{u_{in}\to \boldsymbol{r_{in}}} + t_{\boldsymbol{r_{out}}\to u_{out}}\right] \tag{6-5}$$

where r_{in} and r_{out} are the virtual emitters and receivers inside the medium, respectively. Thus, for each depth z, it is possible to obtain the focused reflection matrix R_F that contains the set of impulse responses between virtual transducers r_{in} and r_{out} (Figure 6.6).

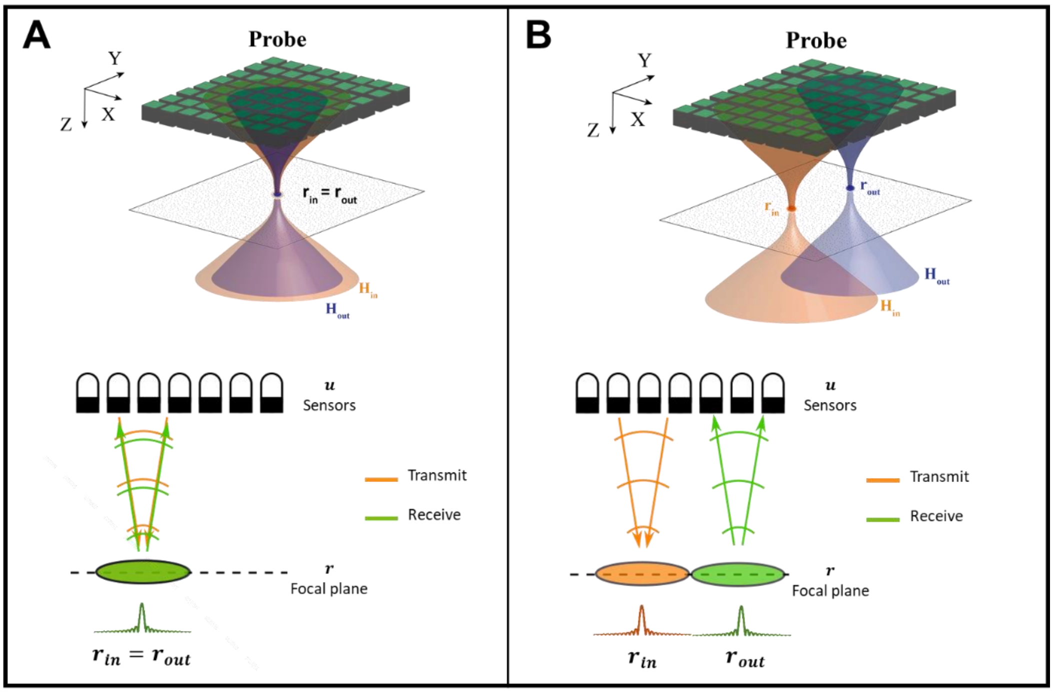

Figure 6.5 – Illustration of the recording of the focused reflection matrix RF. A) shows the confocal image in which the location of the virtual emitters ($\boldsymbol{rin}$) and receivers ($\boldsymbol{rout}$) inside the medium are equal in the focal plane. B) shows the split between the virtual emitters and receivers. While each pixel of a confocal image is associated with the same virtual transducer at emission and reception, the focused reflection matrix also contains the cross-talks between each pixel of the image and, thus, holds much more information than a conventional image.

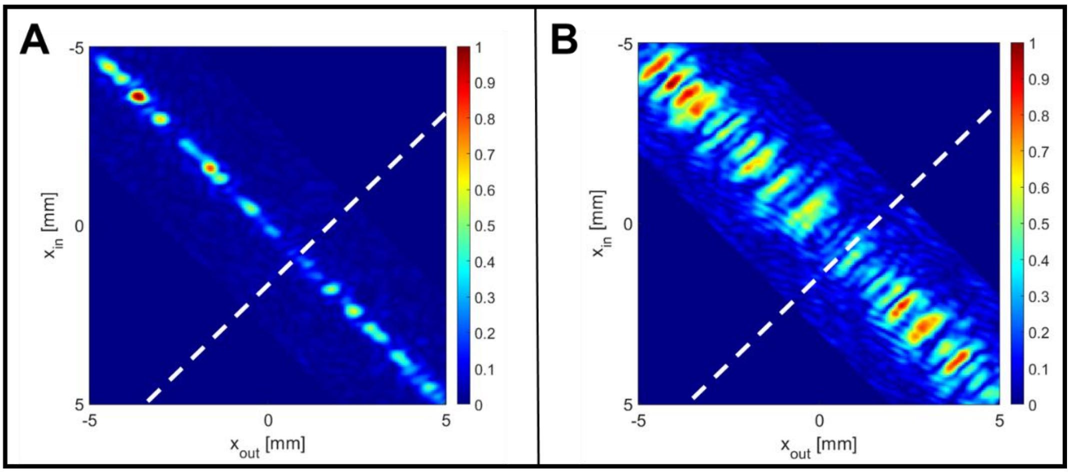

Figure 6.6 – Example of an RF matrix where the dotted white line represents an anti-diagonal. A) Regime dominated by single scattering events, and B) regime dominated by multiple scattering or aberration, due to high off-diagonal intensity values.

R_F contains much more information than a single ultrasound B-mode image. The diagonal of the R_F corresponds to the line at depth z of a confocal ultrasound image, where $r_{in} = r_{out}$. The off-diagonal points can be exploited for assessing the local focusing quality of the ultrasound. The intensity profile along each antidiagonal indeed provides the local image spatial resolution. In a single scattering regime, the focused reflection matrix R_F contains energy only in the vicinity of the diagonal. In presence of aberrations, energy will spread out off the diagonal leading to a decrease in spatial resolution (Figure 6.6). When multiple scattering or electronic noise dominates, energy will not be concentrated around the diagonal anymore but distributed on all matrix elements.

From a practical point of view, in our experiments, the medium of interest was rather probed by a set of plane waves. The experimental setup consisted of an ultrasound matrix probe (Vermon) connected to an ultrafast scanner (Aixplorer®, SuperSonic Imagine, Aix-en-Provence, France). This 2D array of 32x32=1024 transducers with a pitch p=0.5 mm is used to emit 25 plane waves with an angle of incidence ($\theta_{x,in}$,$\theta_{y,in}$) spanning the range from −10° to 10°. The emitted signal is a sinusoidal burst of central frequency fc=3 MHz, with a frequency bandwidth spanning from 2 to 5 MHz. In reception, all elements are used to record the reflected wave field over a time length of about t=150 µs at a sampling frequency of 6 MHz. The probe was placed in contact with the phantom's surface to measure the acoustic response of the bubbles. The transducers u_{out} record the time-dependent reflected wave field for each plane wave emitted with an incident angle θ_{in}. The corresponding signals are then stored in a reflection matrix $R(\theta_{in}, u_{out}, t)$. An ultrasound image can be formed by coherently summing the recorded echoes from each focal point *r* acting as a virtual detector inside the medium (in practice, appropriate time delays are applied to the recorded signals before summation as explained before in order to focus in reception). For that, the reflection matrix has to be projected into a focused basis. This step is greatly simplified by performing beamforming operations in the frequency domain, i.e. applying appropriate phase shifts to all frequency components of the received signals in order to realign them at each focal point. A matrix formalism is particularly suitable for this operation, because, in the frequency domain, the projection of data from the plane-wave or transducer bases to any focal plane can be achieved with a simple matrix product. Consequently, a temporal Fourier transform should be first applied to the experimentally acquired reflection matrix to obtain $R(\theta_{in}, u_{out}, \omega)$, where $\omega = 2\pi f$ is the angular frequency of the waves. The matrix $R(\theta_{in}, u_{out}, \omega)$ can be expressed as follows:

$$R(\theta_{in}, u_{out}, \omega) = G^T(\omega) \times \Gamma \times T \tag{6-6}$$

where the matrix Γ defined in the focused basis, describes the scattering process inside the medium. In the single scattering regime, Γ is diagonal, and its elements correspond to the medium reflectivity $\gamma(r)$. $T = [T(r,\theta)]$ is the transmission matrix between the plane-wave and focused bases. Each column of this matrix describes the incident wave field induced inside the sample by a plane wave of angle θ. $G = [G(u,r)]$ is the Green's matrix between the transducer and focused bases. Each line of this matrix corresponds to the wave front that would be recorded by the array of transducers along vector u if a point source was introduced at a point $r = (x,z)$ inside the sample. The inversion, pseudoinversion, or, more simply, the phase conjugation of the transmission and Green's matrices can enable the reconstruction of a reliable image of the scattering medium, thereby overcoming the aberration and multiple scattering effects induced by the medium itself. However, direct measurement of the transmission and Green's matrices T and G, respectively, would require the introduction of sensors inside the medium, and, therefore, these matrices are not accessible in most imaging configurations. Instead, sound propagation from the planewave or transducer bases to the focal points is usually modeled assuming a homogeneous speed of sound c. The images obtained for each incident plane wave are then summed up coherently and result in a final compounded image with upgraded contrast. The compounded image is thus equivalent to a confocal image that would be obtained by focusing waves on the same point in both the transmit and receive modes. A more detailed description of the technique can be found in Lambert et al., 2019 and 2020.

In order to study the resonance of the bubbles, we formed a time-shift matrix in order to study not only the ballistic time (corresponding to 1 pixel of the image) but multiple times δt around it for each confocal point ($r = r_{in} = r_{out}$):

$$\boldsymbol{R_F}[r, \boldsymbol{\delta t}] = \sum_{\theta_{in}} \sum_{u_{out}} R\left[u_{in}, u_{out}, t_{\theta_{in}\to r} + t_{r\to u_{out}} + \delta t\right] \qquad (6\text{-}7)$$

The spectrum for each focal point can then be obtained by means of a Fourier transform ($\delta t \to f$). Thus, the resonance of bubbles at a given position can be tracked through the following matrix $\boldsymbol{R_F}[r, \boldsymbol{f}]$.

7. RESULTS AND DISCUSSIONS: ACOUSTIC

This chapter aims to study the acoustic behavior of PVA-shelled monodisperse microbubbles. First, we compare the backscatter acoustic response of freshly generated microbubbles to the response of the freeze-dried microbubbles population, in order to verify the impacts of the process on the bubbles' echogenicity, resonance acoustic response, and bandwidth of the resonance curves. We proceed to compare the acoustic behavior of the monodisperse microbubbles to a commercially available polydisperse lipid-shelled microbubble population named Sonovue^{TM}. The experiments were conducted with the setups described in chapter 6.

7.1. Acoustic Backscatter Characterization of the Freeze-dried Monodisperse Microbubbles

As described in chapter 6, the backscatter acoustic characterizations of the microbubbles were performed in two different setups: the "centimetric cell" and the "milli-channel". The measurements were compared as a function of a number of microbubbles semi-quantitatively determined from ~10^8 to ~10^6 with dilution ratios of 1:1 to 1:100 for SonoVue^{TM} in up to 1 ml saline solution provided by the manufacturer. The number of freshly generated 5.4 µm in diameter bubbles (same bubbles as shown in Figure 4.11) was estimated based on the collection time, namely 20 min to 30s, to obtain approximately ~10^7 to ~10^5 bubbles. Note that obtaining a higher number of bubbles than 10^7 with our current device caused long waiting times, making the generated bubbles prone to coalescence in a vial, as demonstrated in the results from chapter 4.4.2.

Here we present the results for ~10^6 bubbles which are collected for 2 min to avoid coalescence before the injection in the measurement chambers. PVA bubbles were diluted with PFC saturated PBS solution to enhance the stability and gently injected into the different measurement containers. Note that the same number of bubbles were injected into both geometries, but water volume in the centimetric cell is roughly two orders of magnitude larger than that of the milli-channel, which makes the bubbles concentrations in the large tank at least one hundred times smaller than that of the confined system.

The responses of freeze-dried and fresh bubbles were evaluated with at least six batches, for which insignificant batch-to-batch variations were observed, regarding the populations' size distribution.

7.1.1. Centimetric Cell: Acoustic Backscatter Characterization

Figure 7.1A shows a typical received time trace from the backscattered response for the PVA-shelled monodisperse microbubbles suspension with a mean diameter of approximately 5.4 µm and a number of bubbles of about 10^6. A time-gated window was applied to the recorded traces with a length of 12 µs as described in chapter 6.1. Figure 7.1B presents typical normalized resonance spectra (black solid line) of fresh bubbles obtained (average of 50 spectra per transmitted frequency) in the "centimetric cell", along with the quasi-flat excitation (orange column), described before (see the preceding chapter). This excitation extends from 0.75 MHz to 3.5 MHz. In all cases where the water was gently stirred in the "centimetric cell", the bubble response exhibits a sharp peak, with ~%5 standard deviations. The resonance frequency of the microbubble inferred from a Gaussian fit (Figure 7.1B) is around 1.4 MHz. It is slightly higher than the Minnaert frequency (around 1.2 MHz for 5.4 µm diameter). The difference can be explained by noting that shelled bubbles resonate at frequencies higher than unshelled bubbles. Concerning the standard deviations of the resonance peaks (STD), the Minnaert law (Minnaert 1933) and more elaborate models (Doinikov and Bouakaz 2011) suggest that the STD of the bubble size distributions and that of the acoustic resonance peak should be equal. This is effectively the case for the centimetric cell.

Figure 7.2A shows the normalized resonance spectra of fresh and freeze-dried bubbles in solid red and black (both were an average of fifty measurements per transmitted pulse frequency and repeated with at least six different batches) in the centimetric cell. We observe an increase of ~5% in the resonance frequency of the freeze-dried microbubble population, which could be related to the decrease of approximately 4-5% in the mean diameter of the population reported in chapter 4. However, we could affirm that within ±5%, the resonance frequencies and the bandwidths of both samples are indistinguishable. More specifically, we also observed a 5% standard deviation in the bandwidth of the signal for the centimetric cell.

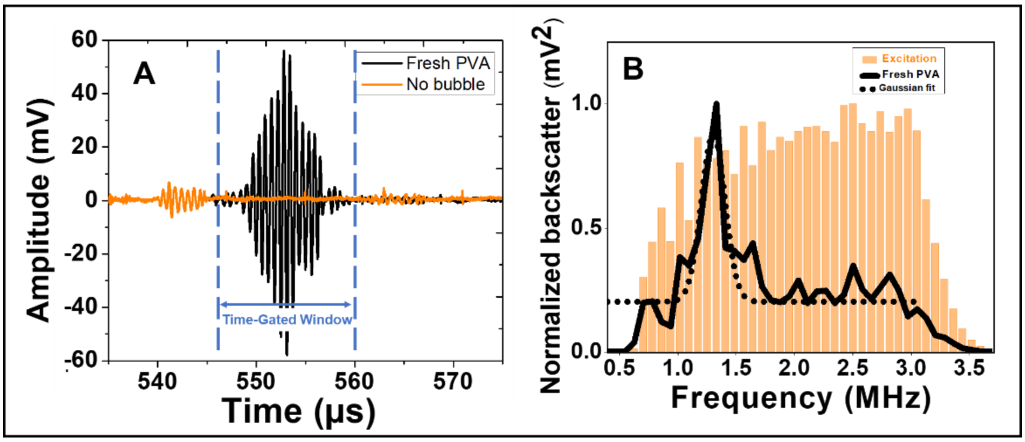

Figure 7.1 – A) The backscattered echoes show a comparison of 10^6 freshly generated polyvinyl alcohol (PVA) monodisperse microbubbles with a reference measurement (where there are no bubbles) at 1.35 MHz central sweep frequency. The weaker front and back wall echoes originated from the mylar windows, while the echoes from the bubbles appeared between these walls, in this 10 mm height cell, where the signal was time-gated with a Hanning window. B) The backscatter acoustic response of 10^6 freshly generated monodisperse PVA-shelled microbubbles with the acoustic excitation presented in the background.

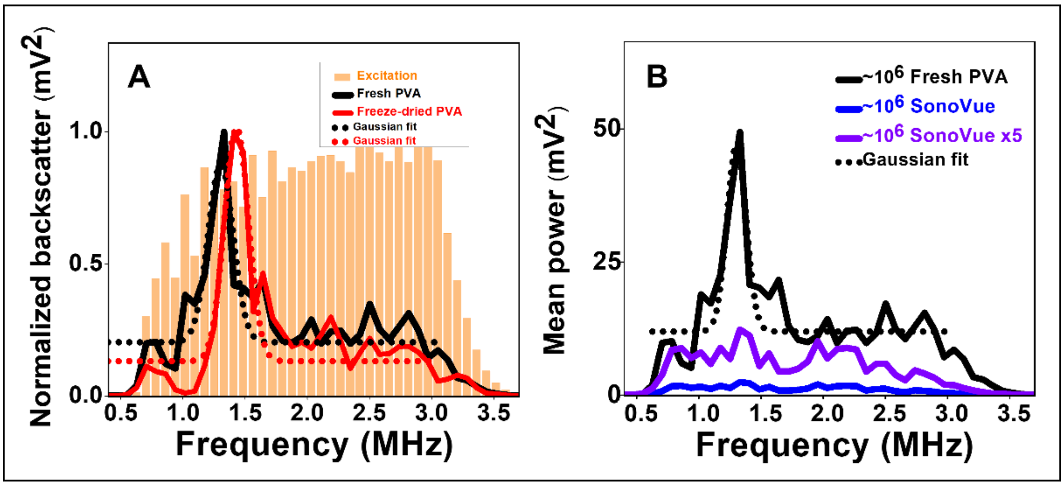

Figure 7.2 – A) Typically obtained normalized backscatter resonance spectra (each is an average over fifty spectra) of the compensated emission, fresh, and freeze-dried bubbles with the same size (5µm in diameter) under the same experimental conditions, obtained in the centimetric cell. B) Shows the backscattered power spectra comparison of ~10^6 SonoVue (magnified by 5), and ~10^6 fresh bubbles (in solid line while the dotted line represents the gaussian fitted spectrum) in the centimetric cell.

Figure 7.2B shows the comparison of the magnitude and bandwidth of the backscatter spectrum from freshly generated monodisperse PVA-shelled microbubbles and polydisperse SonoVue^{TM}, with a similar number of ~10^6 bubbles. The acoustic response of the SonoVue^{TM} population was five times multiplied so we could better visualize the differences between the bandwidth of both samples. The measured peak in the backscattering spectrum for the monodisperse population was significantly higher (20 times) than the peak measured for the polydisperse SonoVue^{TM}. Hoff (2001) noted the same behavior for narrowly distributed microbubbles coated with a surfactant compared to broadly distributed microbubbles coated with either denatured albumin or a polymeric shell (Hoff, 2001). Since the shell material of the monodisperse microbubble population is different from the polydisperse for our study and the one proposed by Hoff, one can argue that the difference in the bandwidth is related to that parameter. However, studies conducted by Serger *et al.,* (2018) and Gong (2013) allowed monodisperse and polydisperse microbubbles to be compared with the same shell material. In both cases, the results showed that the width of the microbubble size distribution could significantly impact the peak in the measured frequency-dependent scattering coefficient.

Figure 7.3A shows the backscatter coefficient for ~3x10^4 bubbles/mL fresh monodisperse PVA-shelled microbbubles bubbles in the centimetric cell, and Figure 7.3B shows the scattered coefficient for 4 different acoustic pressure for a 5.4µm mean diameter lipid-shelled microbubbles population (~5.8x10^3 bubbles/mL) from Segers *et al*., 2018. The backscatter coefficient was calculated as:

$$\eta = \frac{|V_{scat}|^2}{|V_{ref}|^2}\frac{16z^2}{D^2} \tag{7-1}$$

where $|V_{scat}|^2$ is the power spectrum of the recorded scattering signal, and $|V_{ref}|^2$ is the total transmitted power at the transmit frequency measured from the reflection of the transmit pulse from a stainless-steel reflector. The scattering/backscattering coefficient was compensated for the limited aperture

D of the receiving transducer with focal distance z. Both expriments were conducted as described in the chapter 6 with the difference that Segers used a second transducer positioned at 90° from the centimetric cell, recording the scattering signal from the emitter transducer.

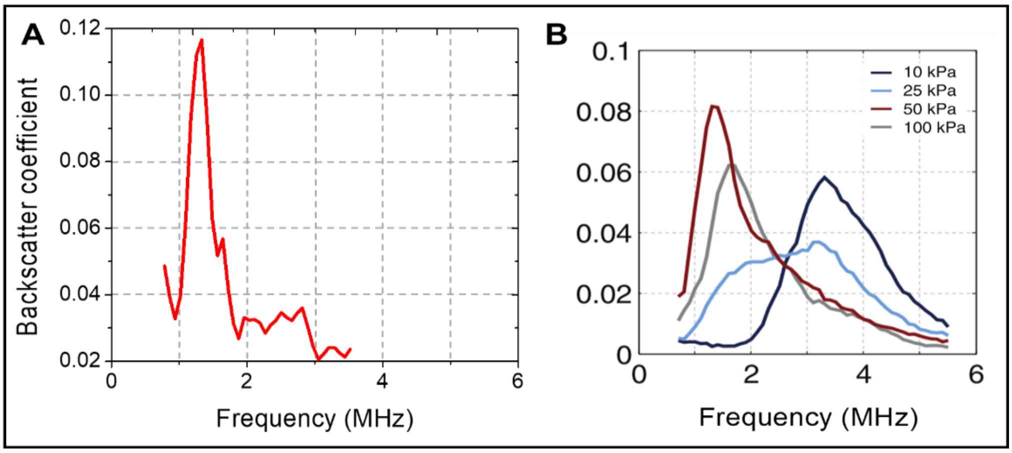

Figure 7.3 – A) Backscatter coefficient for the 5.4µm mean diameter PVA-shelled monodisperse microbubbles. B) Scattering coefficients at the fundamental frequency at peak negative pressures of 10, 25, 50 and 100 kPa for lipid-shelled monodisperse microbubbles (adapted from Segers *et al*., 2018)

It is possible to see that for similar acoustic pressures (100 kPa) the PVA microbubbles showed a narrower bandwidth compared to results presented by Sergers (grey line). This is due to the fact that the PVA-shelled microbubbles presented a CV of 5% compared to a CV of 9% for the lipid-shelled bubbles. These results reinforce the influence of the microbubbles' size distribution over the peak in the measured frequency-dependent scattering/backscattering coefficients.

7.1.2. Milli-Channel: Acoustic Backscatter Characterization

Figure 7.4A shows a typical received time trace corresponding to the backscattered response for the PVA-shelled monodisperse microbubbles suspension with a mean diameter of approximately 5.4 µm and 10^6 bubbles. A time-gated window was selected in the trace, with a length of 12 µs as described in chapter 6.1. Unlike the case of the centimetric cell the front and back wall reflection are merged with the microbubble scattering signal since the height of the chamber is smaller than the pulse length. Therefore, the time-gated window f will include both contributions in this case. The first wall response can be subtracted easily in the frequency domain, however, due to interactions with the scattering signal of the bubbles, the same procedure could not be used for the back wall. Thus, the backscattering acoustic response will contain the contribution of the bubbles and the wall of the chamber.

Figure 7.4B presents typical normalized resonance spectra (black solid line) obtained with fresh bubbles (average of 50 spectra per transmitted frequency) in the milli-channel, along with the quasi-flat excitation (orange column), described before the chapter 6.1. This excitation extends from 0.75 MHz to 3.5 MHz. In all cases where the water was at rest in the milli-channel, the bubble response exhibits a sharp peak, with a ~%10 standard deviation. The resonance frequency we infer from Figure 7.4B with the aid of the Gaussian fit is around 1.4 MHz, which was the same obtained for the backscatter acoustic response of the bubbles in the centimetric cell setup. However, concerning the standard deviations of the resonance peaks (STD), the milli-channel measurement showed a value higher than the size distribution of the population. We hypothesize that the addition of the background signal (the wall of the channel) to the signal of the bubble, creates a broadening of the spectrum, since a pure reflection results in the same bandwidth of the emitted signal. From this perspective, broadening does not occur in the centimetric cell, because wall echoes are much weaker, and excluded from the time-gated window.

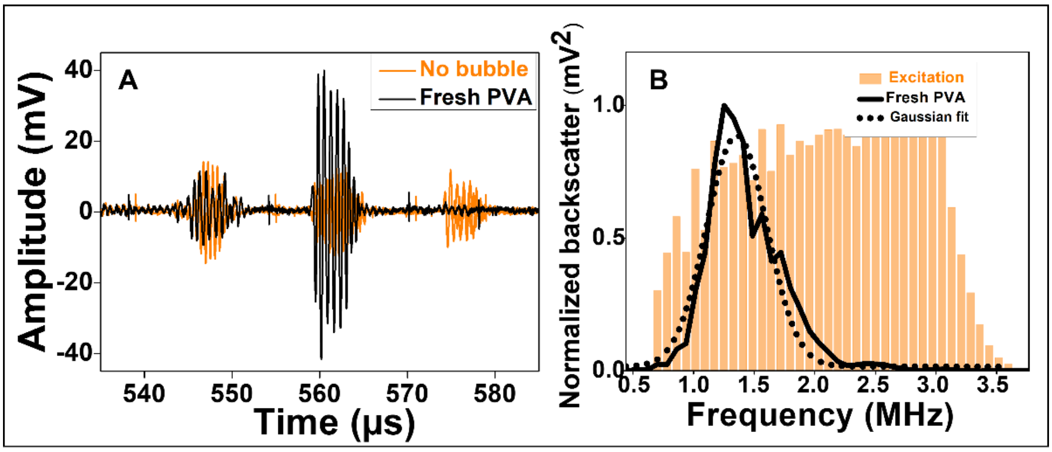

Figure 7.4 – A) The backscattered echoes show a comparison of 10^6 freshly generated polyvinyl alcohol (PVA) monodisperse microbubbles with a reference measurement (where there are no bubbles) at 1.35 MHz central sweep frequency. The front and back wall echoes originated from the PDMS structure, while the echoes from the confined bubbles merged with the front and back walls of the chamber whose height was 1 mm. B) The backscatter acoustic response of 10^6 freshly generated monodisperse PVA-shelled microbubbles with the acoustic excitation presented in the background.

Figure 7.5A shows the normalized resonance spectra of fresh and freeze-dried bubbles in solid red and black. Both result from an average over fifty measurements per transmitted pulse frequency and repeated with at least six different batches. Similar to the centimetric geometry, we observe an increase of ~4% in the resonance frequency of the freeze-dried microbubble population, which could be related to the decrease of approximately 4-5% in the mean diameter of the population as reported in chapter4. However, we could affirm that within ±5%, the resonance frequencies and the bandwidths of both samples are indistinguishable. We also observed a 10% standard deviation in the bandwidth for the milli-channel setup.

The dimension consistency of the bubbles before and after the freeze-drying process, combined with the consistency in their acoustic behavior, allow us to suggest that the freeze-drying process does not alter the shell properties of the bubbles. In any case, from a UCA perspective, we may conclude that freeze-dried and fresh bubbles behave in the same manner.

Figure 7.5B shows the comparison of the magnitude and bandwidth of the backscatter spectrum from freshly generated monodisperse PVA-shelled microbubbles and polydisperse SonoVue, with a similar number of ~10^6 bubbles. The measured peak in the backscattering spectrum for the monodisperse population was approximately 5 times higher than the peak measured for the polydisperse SonoVue. The difference from the results presented for the centimetric cell (20 times higher signal) could be correlated to the wall signal in the milli-channel. As can be seen, the signal from the Sonovue^{TM} population is of the same order of magnitude as the signal without bubbles, indicating that the majority of the signal from Sonovue^{TM} comes from the wall reflection. In a simplified assessment, if a spectral subtraction of the wall reflection signal is implemented, we obtain a peak signal for the monodisperse microbubbles 15 times higher than the polydisperse population. This is a value much closer to the one obtained in the centimetric cell and observed in the literature, as previously mentioned (Serger *et al.,* 2018).

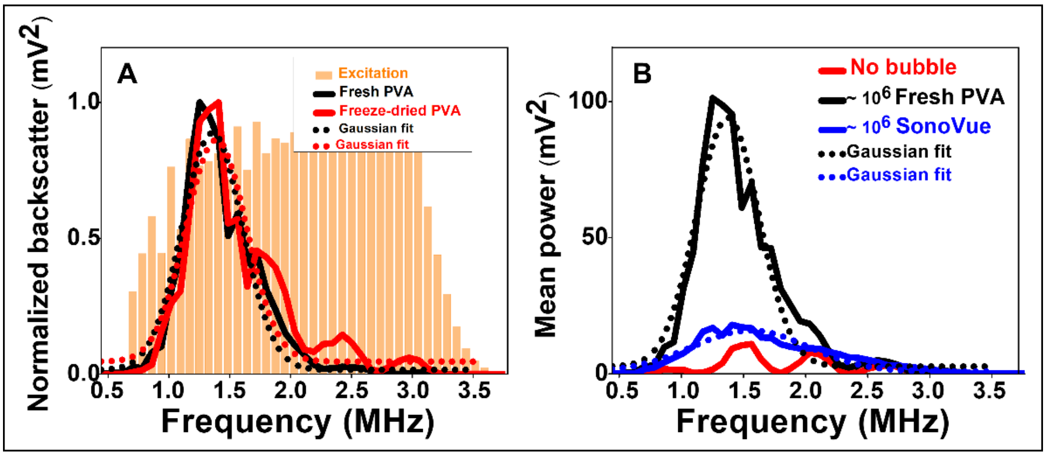

Figure 7.5 – A) Typically obtained normalized backscatter resonance spectra (each is an average over fifty spectra) of the compensated emission, fresh, and freeze-dried bubbles with the same size (5µm in diameter) under the same experimental conditions, obtained in the milli-channel setup. B) Shows the backscattered power spectra comparison of ~10^6 SonoVue and ~10^6 fresh bubbles (in solid line while the dotted line represents the gaussian fitted spectrum) in the centimetric cell.

We proceed to compare the magnitude and bandwidth of the backscattering signal for freshly generated monodisperse microbubbles in a concentration of ~10^6 bubbles with SonoVue in different concentrations (~10^6, ~10^7, and ~10^8 bubbles) The resonance spectra shown in Figure 7.6 indicate that the backscattered power amplitude acoustic response of ~10^6 fresh PVA bubbles, was roughly five times greater than that of ~10^6 bubbles SonoVue, without the spectral subtraction of the walls' reflection. The PVA-shelled microbubbles obtained an equivalent power amplitude with ~10^8 SonoVue bubbles. The typical normalized spectra for fresh PVA bubbles and SonoVue are presented in Figure 7.6.B, which reveals the monodispersity of the fresh bubbles in comparison with polydisperse SonoVue bubbles, with significantly reduced bandwidth in comparison with the wide bandwidth of the polydisperse population and the emitted signal.

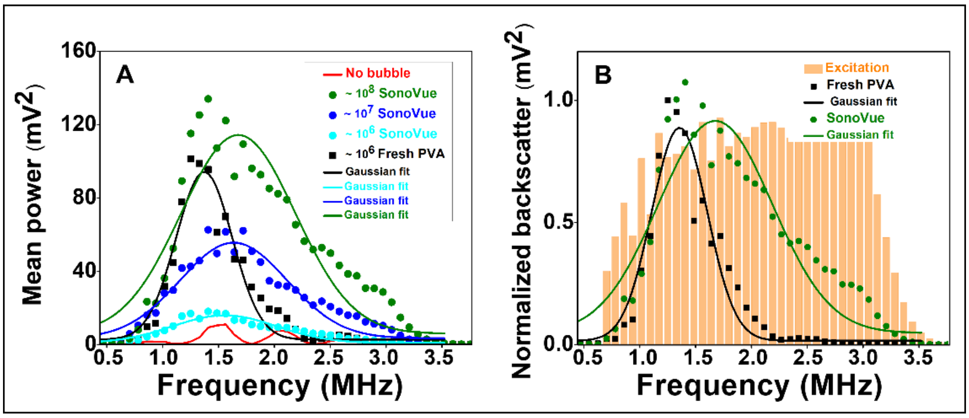

Figure 7.6 – A) Comparison of backscattered power spectra of ~10^6, ~10^7, and ~10^8 SonoVue with ~106 fresh monodisperse microbubblebubbles and reference (where there is no bubble). B) Typical resonance spectrum measured in the confined system (average of 50 spectra) of ~10^8 SonoVue and ~10^6 fresh bubbles with ~%15 % and ~10% standard deviation from the Gaussian center, respectively.

7.2. Acoustic Backscatter Characterization: Ultrasound Matrix Imaging

The matrix approach was applied to the imaging of a freeze-dried PVA-shelled suspension of microbubbles (about 10^6), with a mean diameter of approximately 5.4 µm, inserted in a tissue-mimicking phantom as described in chapter 6.3. Figure 7.7 shows a typical 3D confocal image of the microbubbles flowing inside the phantom, and examples of the cross-sectional views at one point in space. In order to enhance the contrast and better differentiate the microbubbles, a filtering was applied to the images (Figure 7.8): the mean intensity was removed from each frame, yielding an image with only the dynamic elements, e.g., the microbubbles.

In order to study the resonance of the bubbles, a time-shift matrix is formed to study not only the ballistic time (corresponding to 1 pixel of the image) but multiple times δt around it for each confocal point ($r = r_{in} = r_{out}$). The spectrum for each focal point can then be obtained by means of a Fourier transform ($\delta t \rightarrow f$). Figure 7.9A shows the confocal images of the freeze-dried monodisperse microbubbles filtered by removing the mean to extract only the dynamic elements. Figure 7.9B show an example of the signal of a single voxel containing the microbubbles, of which spectrum was obtained through a Fourier transform. The signal consists of the ballistic time of the voxel and $\pm\delta t$ of 20µs. Figure 7.9C shows the mean spectrum of the bubbles inside the tube for multiple pixels in the volume (blue) and the mean speckle spectrum at the same depth as the tube (orange). The mean speckle spectrum is a good approximation to that of the emitted pulse of the transducer. We will use it to deconvolve the bubble signal. Figure 7.9D shows the deconvolved mean signal of the freeze-dried monodisperse microbubbles, with a resonance peak around 1.3MHz.

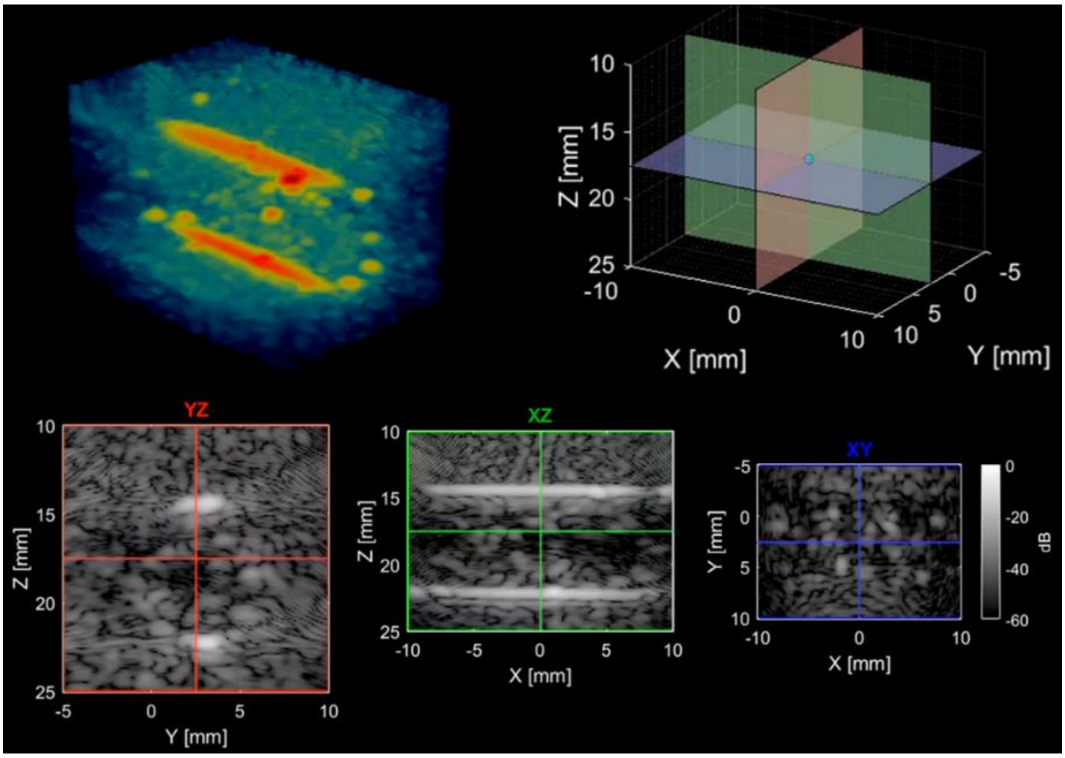

Figure 7.7 – Typical 3D confocal image generated by the matrix image approach in phantom tissue-mimicking setup in the presence of microbubbles (top left).In the bottom is an example of 3 different B-mode planes used to construct the 3D image.

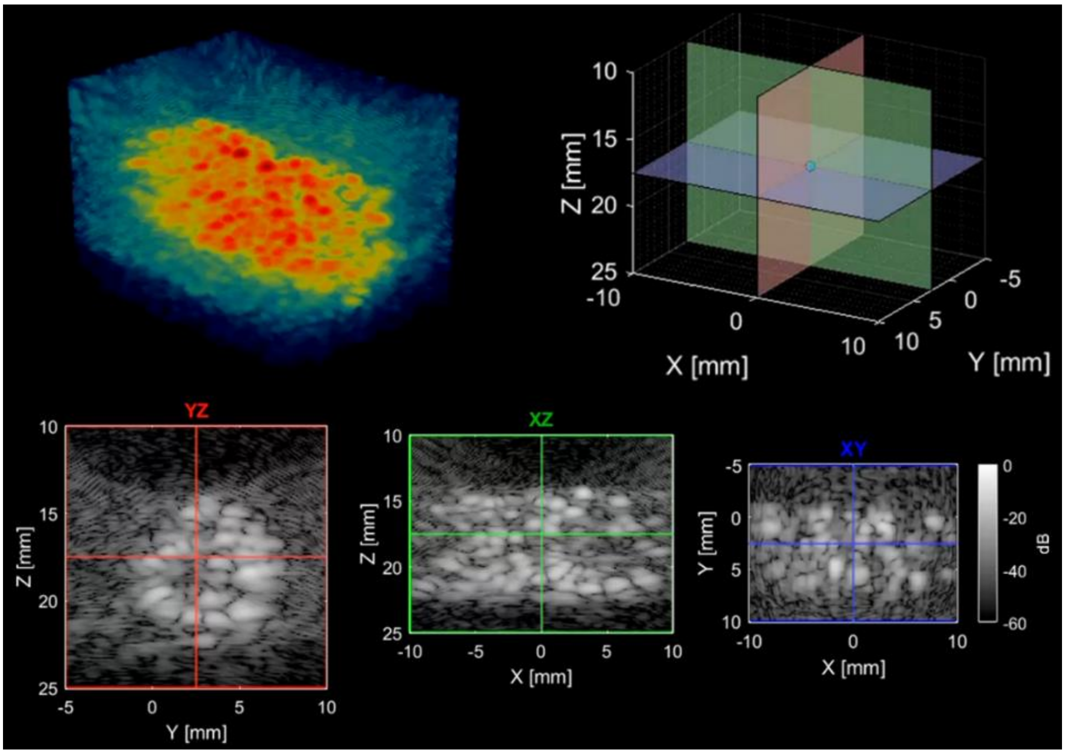

Figure 7.8 – Typical 3D confocal image generated by the matrix imaging approach in phantom tissue-mimicking setup in the presence of microbubbles (top left). A filtering of the mean intensity value was applied in the image in order to highlight the dynamic elements, e.g., microbubbles. In the bottom is an example of 3 different B-mode planes used to construct the 3D image.

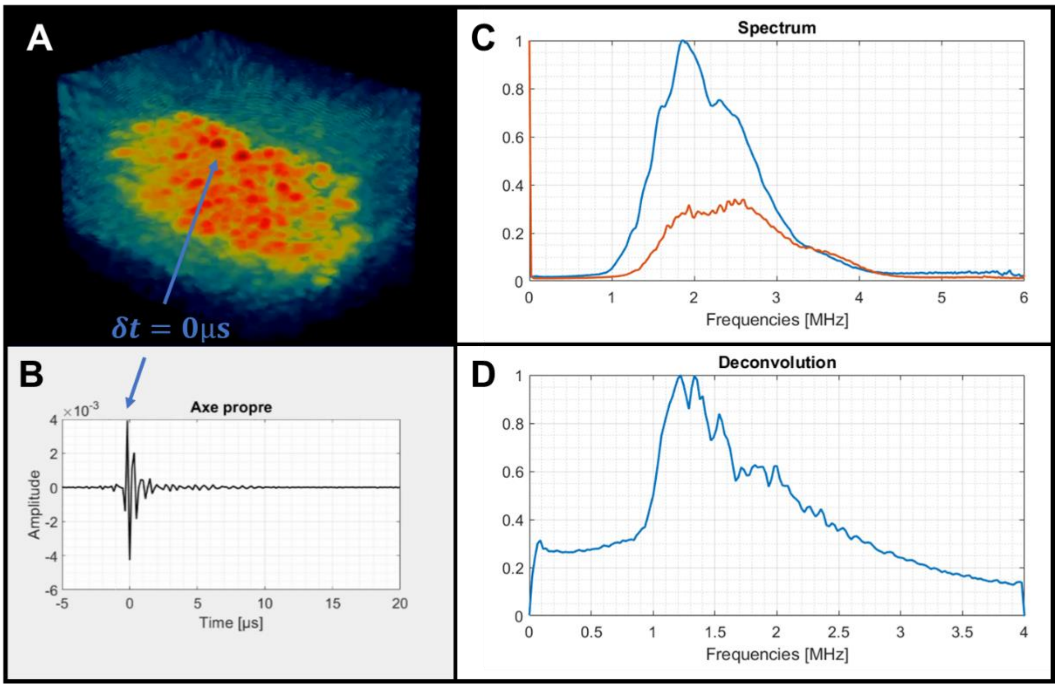

Figure 7.9 – A) 3D confocal image of the freeze-dried monodisperse microbubbles flowing inside the tissue-mimicking phantom. B) Example of the signal of a high intense pixel in the ballistic time, corresponding to the bubble's response. A FFT is applied over the bubbles signal in order to obtain their spectrum. C) Mean spectrum of the microbubbles inside the phantom (blue), and the speckle spectrum at the level of the tube. The speckle signal is assumed to be representative of the signal emitted by the transducer and thus used to deconvolve the microbubble mean spectrum. D) Deconvolved mean spectrum of the freeze-dried monodisperse microbubbles population showing a resonance peak around 1.3MHz.

Figure 7.10 shows the mean backscatter spectrum from freeze-dried monodisperse PVA-shelled microbubbles (left) and polydisperse SonoVue (right), with a similar number of ~10^6 bubbles in the same conditions. It is possible to see that a sharp peak is evident after deconvolution for the monodisperse population while a broad signal appears for the polydisperse population.

These preliminary results reinforce the findings from the backscatter acoustic measurements in the centimetric cell and the milli-channel previously presented. It is possible to see the monodispersity of the freeze-dried PVA-shelled bubble in comparison with polydisperse SonoVue bubbles, with significantly reduced bandwidth in comparison with the wide bandwidth of the polydisperse population.

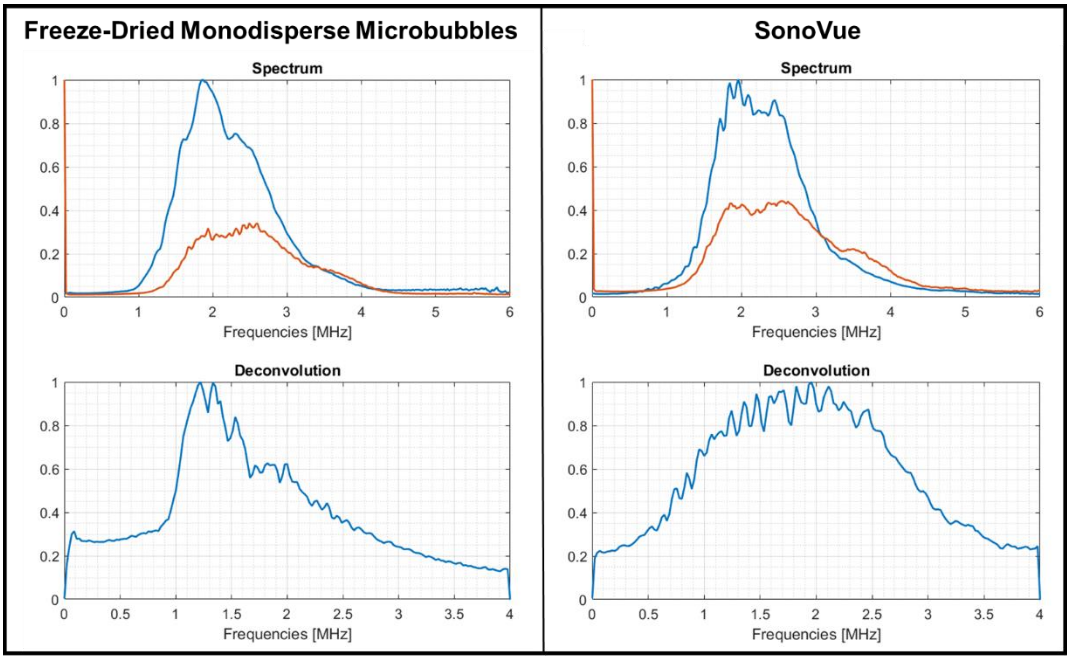

Figure 7.10 – The top left image shows the mean spectrum of the freeze-dried monodisperse microbubbles inside the phantom (blue), and the speckle spectrum at the level of the tube. The images in the bottom left shows the deconvolved mean spectrum of the freeze-dried monodisperse microbubbles population showing a resonance peak around 1.3MHz. The top right image shows the mean spectrum of the polydisperse SonovueTM microbubbles inside the phantom (blue), and the speckle spectrum at the level of the tube. The images in the bottom shows the deconvolved mean spectrum of the polydisperse SonovueTM showing a broad resonance peak with resonance frequency around 2MHz.

7.3. Discussion

7.3.1. Single scattering

In the single scattering regime, the wave backscattered from a random collection of bubbles is simply the sum of the waves scattered by each bubble. The complex backscattered amplitude can then be written as the sum of random phasors. Assuming statistically independent bubble positions, the amplitude and phase of each phasor are independent of each other and of the amplitudes and phases of other elementary phasors. The total intensity scattered off the bubble population is then the sum of the intensity scattered of each individual bubble. Therefore, the scattered power is expected to increase linearly with the density of the bubbles and to depend on the acoustical and geometric properties of the individual bubbles, as shown in chapter 5.2.9. Figure 7.11 confirms the linear relation between the scattered power and the bubbles' concentration for monodisperse PVA-shelled microbubbles.

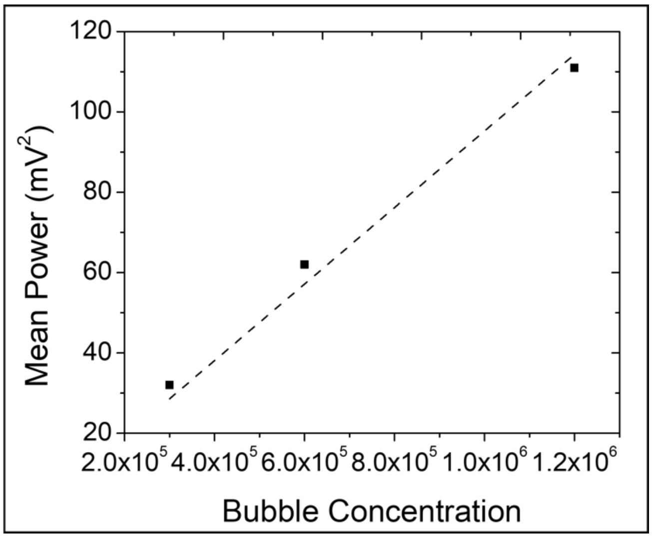

Figure 7.11 – Measured backscattered echo power as a function of freshly generated monodisperse PVA-shelled microbubble concentration in the centimetric cell setup.

7.3.2. Multiple Scattering

The linear relationship between the total backscattering intensity and the intensity scattered by individual bubble is lost when multiple scattering occurs. In other words, the backscattered amplitude is not any more a sum on the bubbles but rather a sum on multiple scattering paths (each involving several bubbles). Thus, in this regime, the signal backscattered by the bubble cloud does not reflect any more the signature of the individual bubble response but instead the response of a set of bubbles coupled via multiple scattering.

In order to evaluate the importance of multiple scattering in our study, we need to evaluate both the scattering and absorption mean free paths. The scattering mean free path is determined by the inverse value of the product of the scattering cross-section, σ_s, and the number density of the scatterer, *n*. When a bubble is excited at its resonance frequency, the scattering cross-section is given by λ^2/π, where λ is the wavelength of the emitted pulse (e.g., $\sigma_s = 0.3\, mm^2$). Assuming a homogeneous distribution of bubbles in the PDMS chamber, the lowest number density of bubbles is 286 bubbles/mm^{-3}.

If we assume that all bubbles are at resonance, this leads to a scattering mean fee path as small as 12 µm. The value is much smaller than the bubble cloud, which indicates that we are possibly in a strongly multiple scattering regime. In such a regime, the resonant frequency of the bubble cloud is expected to be shifted to a higher frequency which depends on the concentration. But we also have to consider the absorption cross-section, σ_a, which is driven by viscous and thermal damping, for the simplified case of a free bubble. The total power removed from the incident acoustic beam is then given by the power that is scattered in addition to the power that is dissipated, yielding to the concept of the extinction cross-section, σ_e. The extinction cross-section can be written as the sum of the absorption and scattering cross-sections, or just as a function of the scattering cross-section, as follows:

$$\sigma_e = \sigma_a + \sigma_s = \frac{\delta_{tot}}{\delta_{rad}}\sigma_s \tag{7-2}$$

where the total damping coefficient is given by the sum of three coefficients respectively associated to radiative damping, liquid viscosity, and thermal diffusion: $\delta_{tot} = \delta_{rad} + \delta_{vis} + \delta_{th}$.

The dimensionless damping coefficients can be obtained by linearizing the Rayleigh-Plesset equation to find as demonstrated in the chapter 5.2.1:

$$\delta_{rad} = \frac{3P_0\kappa}{\rho\omega R_0}, \qquad \delta_{vis} = \frac{4\mu}{\rho\omega {R_0}^2} \tag{7-3}$$

The thermal damping is more difficult to calculate, but for the case of micro-sized bubbles excited by frequencies in the MHz range, it is of the same order of magnitude as the viscous damping (Figure 7.12 adapted from De Jong, 2002). Thus, to account for the thermal damping, typically the viscosity damping in increased by a factor of 2.

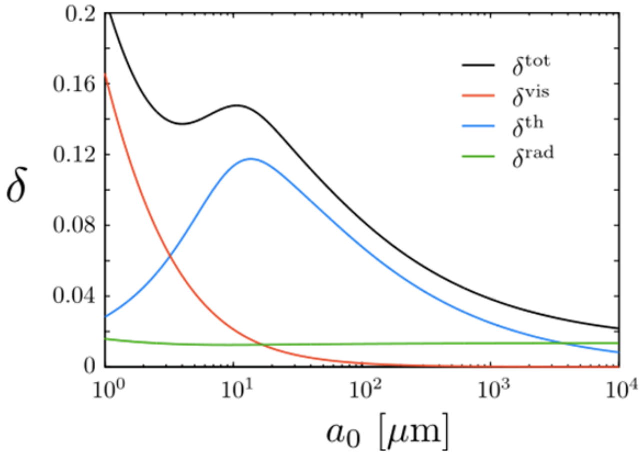

Figure 7.12 – Damping coefficients for air bubbles in water as a function of the diameter calculated at their resonance frequency. $\delta_{tot} =$ total damping; $\delta_{vis} =$ viscous damping; $\delta_{rad} =$ radiative damping; $\delta_{th} =$ thermal damping.

The efficiency of the microbubble as a sound scatterer can be defined as the ratio between the scattered and the consumed powers, or the scattering cross-section and the extinction cross-section (Hoff, 2001):

$$\eta = \frac{\sigma_s}{\sigma_e} = \frac{\delta_{rad}}{\delta_{rad}+\delta_{vis}+\delta_{th}} \qquad (7\text{-}4)$$

For our particular case of microbubbles with diameter in the 5µm range, being insonified by frequencies in the MHz range, viscous and thermal damping dominates over radiation, yielding a scattering efficiency of 0.09. In other words, the absorption cross-section is approximately 10 times the value of the scattering cross-section. Thus, the absorption mean free path is 10 times smaller than the scattering mean free path, leading to the assumption that absorption avoids multiple scattering events and that bubbles are not coupled.

Experimentally, we have shown an almost identical acoustic behavior for the monodisperse microbubbles in the centimetric cell and the milli-channel, which were conducted in concentrations 100 times different from one another. This result, corroborated the assumption made above, indicating that the concentration and wall proximity had no significant effects on the acoustic bubble behavior. In addition, the backscattering response of the bubbles increases linearly with concentration (Figure 7.11). Such behavior also indicates that the measurements were not affected by multiple scattering.

7.3.2.1. Focused Reflection Matrix

In this section we turn our attention to the points far from the confocal elements (R_{xx} $(r_{in} \neq r_{out})$). Because each matrix R_{xx} is investigated at the ballistic time ($t = 2z/c$), the only possible physical origin of echoes between distant virtual transducers at points far from the diagonal would be the existence of multiple-scattering paths occurring at depths shallower than the focal depth.

For our experimental configuration, multiple scattering can be investigated by examining the spatial signal intensity profile of the anti-diagonals in the reflection matrix. Each intensity profile comprises three contributions: the single scattering component, the multiple scattering component, and the electronic noise. The single scattering signals mainly lie along the near-confocal elements of the R_{xx} (diagonal of the matrix). The average multiple scattering contribution can be split into three terms: speckle, incoherent, and coherent contributions. When a pulsed plane wave with wavevector k_0 is transmitted into a multiple-scattering medium, the backscattered intensity $I(k_0, k)$, in the direction given by k can be decomposed into all possible pairs of paths (i, j) in the medium (Figure 7.13), i.e.,$I(k, k_0) = \sum_{i,j} A_i(k_0, k) A_j^*(k_0, k)$. Each pair belongs to one of the three previously mentioned contributions. The first is the speckle contribution (Figure 7.13A). It is caused by the collision of paths with no 'common history in the medium,' i.e., no specific phase relationship. As a result, after averaging over disorder, the resulting intensity pattern vanishes. The second contribution represents the incoherent contribution. It is related to paths that follow the same sequence of scatterers in the medium and are, therefore, in phase irrespective of emergence direction (Figure 7.13B). It produces an isotropic intensity distribution after averaging over disorder. This contribution is incorporated into the 'diffusion approximation,' detailed in Tourin *et al.* (2000). Finally, there is the coherent contribution in Figure 7.13C. Indeed, regardless of the scatterer configuration, a given beam path and its reciprocal counterpart always interfere constructively in the backscattering direction because they are necessarily in phase under the assumption of medium reciprocity. It explains why, after configuration averaging, a coherent backscattering peak appears. Experimentally, the averaged intensity is twice as large in the backscattering direction than in the other directions only if the single-scattering contribution is subtracted since the latter is not subject to coherent interference scattering.

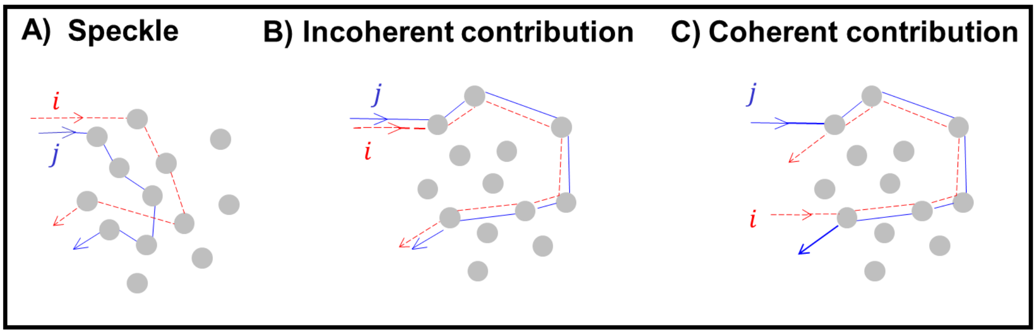

Figure 7.13 – The backscattered intensity can be decomposed onto all possible pairs of paths in the medium. These path pairs can be classified into one of the three categories symbolized in the figure. (A) Speckle contribution; (B) incoherent contribution; (C) coherent contribution (adapted from A.Tourin et al., 2000).

Referred to as coherent backscattering (CBS), this interference phenomenon was originally discovered on the plane-wave basis in optics (van Albada *et al.,* 1991; van Albada and Lagendijk, 1985), this phenomenon also occurs on a point-to-point basis, whether the points be real sensors (Tourin *et al.*, 1997) or created via focused beam forming (Lambert *et al.*, 2019). On the point-to-point basis, contributions from multiple scattering give the backscattered intensity profile the following shape: a narrow, steep peak (the CBS peak) in the vicinity of the source location (diagonal of the matrix R_{xx}), which sits on top of a wider pedestal (the incoherent contribution). Finally, the contribution from electronic noise can decrease the contrast of an ultrasound image in the same way as multiple scattering. Noise contributes to a roughly constant background level to the backscattered intensity profiles.

Figure 7.14A shows a cross-sectional confocal image of the tissue-mimicking phantom positioned in the center of the tube containing the freeze-dried monodisperse PVA-shelled microbubbles. Figure 7.14B shows a focused reflection matrix inside the tube representing the red line in the confocal image. Figure 7.14D shows a typical reflection matrix slightly below the back wall of the tube, represented by the blue line in the confocal image Figure 7.14C and E are the antidiagonal intensity of the red and blue lines in the confocal image, respectively.

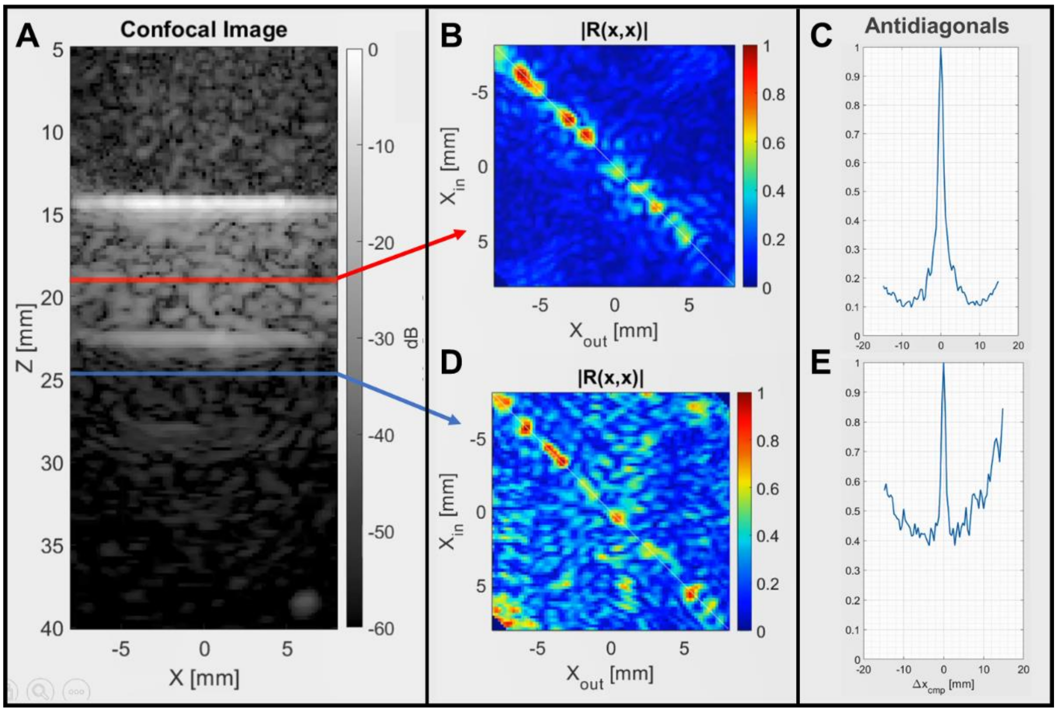

Figure 7.14 – A) Transversal 2D confocal image of the tissue-mimicking phantom with the presence of freeze-dried monodisperse PVA-shelled microbubbles. The red and blue lines represent the regions where the focused reflection matrix from images B and D were taken. B) Focused reflection matrix inside the tube where the monodisperse microbubbles are present. C) Is the Antidiagonal signal intensity for the region represented by the red line in image A. D) Focused reflection matrix inside the below the backwall of the tube without the presence of any microbubbles. E) Is the Antidiagonal signal intensity for the region represented by the blue line in image A.

The high intensity of the signal at the diagonal of R_{xx}, in the Figure 7.14B and C, indicates that the measurement is dominated by single scattering events. Figure 7.14D and E corroborates these results by displaying the reflection matrix in a position where there is no single scattering from the bubbles. It is possible to see that in this position multiple scattering, as expected, dominates. These preliminary results reinforce the assumptions made in the previous chapter. Despite having a scattering mean free path extremely small, absorption dominates over scattering for µm-sized bubbles, resulting in a single scattering regime. In other words, the signal backscattered by the bubble cloud would reflect the signature of the individual bubble response.

7.3.2.2. Linear Hoff-Church Model for Polymeric-shelled Microbubbles

In 1995, Church derived a model describing the dynamics of shelled gas microbubbles from the classical Rayleigh–Plesset equation. The bulk Newtonian liquid is separated from the gas core by a continuous layer of an incompressible, solid elastic shell with damping. The Laplace pressure tends to force the dissolution of the microbubbles, which is counteracted by the elastic surface layer that resists the strains generated by it. The proposed model also includes viscous damping:

$$\rho_S R_1 \ddot{R}_1 \left[1 + \left(\frac{\rho_L - \rho_S}{\rho_S}\right)\frac{R_1}{R_2}\right] + \rho_S \dot{R}_1^2 \left\{\frac{3}{2} + \left(\frac{\rho_L - \rho_S}{\rho_S}\right)\left[\frac{4R_2^3 - R_1^3}{2R_2^3}\right]\frac{R_1}{R_2}\right\} = P_{G,eq}\left(\frac{R_{01}}{R_1}\right)^{3\gamma} - P_\infty(t) - \frac{2\sigma_1}{R_1} - \frac{2\sigma_2}{R_2} - \frac{4\dot{R}_1}{R_1}\left[\frac{V_S\eta_S + R_1^3\eta_L}{R_2^3}\right] - 4\frac{V_S G_S}{R_2^3}\left(1 - \frac{R_{01}}{R_1}\right) \quad (7\text{-}5)$$

Here R_1 and R_2 are respectively the inner and outer radii of the elastic shell, R_{01} are R_{02} are corresponding ambient radii, ρ_s is the shell density, σ_1 is the surface tension of the gas-shell interface, σ_2 is the surface tension of the shell-liquid interface, $P_{G,eq} = P_0$ for the surface layer permeable to gas, η_s and η_L are the shell and liquid shear viscosities, respectively, and G_s is the shell shear modulus. Hoff (2001) simplified Church's equation for the case of a bubble whose shell thickness is thin, and linearized the model for very small radius displacements, yielding:

$$f_0 = \frac{\omega_0}{2\pi} = \frac{1}{2\pi R}\sqrt{\frac{1}{\rho_L}\left(3\kappa p_e + 12 G_s \frac{d_{se}}{R}\right)} \quad (7\text{-}6)$$

where f_0 is the resonance frequency of the bubble, R is the bubble's radius, ρ_L is the density of the surrounding liquid, κ is the polytropic gas constant, G_s is the shear modulus, and d_{se} is the thickness of the shell.

From Hoff and Church's equations, combined with the resonance response obtained from the backscattering acoustic measurement, the Youngs modulus of the PVA-shelled microbubble is approximately 1 MPa. The value is 3.5 times smaller than the value obtained by Paradossi *et al.* (2009) (3.5 MPa). The difference can be explained by two factors. First, the PVA used by the authors had a molecular weight 3 times larger than the one used in our study. Also, their formulation consists of cross-liking the PVA shell, which makes the shell thicker and stiffer. As demonstrated by Bermejo and Ugarte (2009), the mechanical properties of cross-linked polymer networks depend strongly on both the network topology and cross-linking density. They studied the influence of cross-linking degrees on-chain packing and hydrogen-bond structure for PVA. They observed that their 90% cross-linked PVA formulation had 3 times higher Young's modulus compared to the pure PVA formulation.

It is worth noticing that the approximation made in this analysis is only valid for low acoustic pressure, where the microbubbles behave linearly to the excitation.

7.4. Final Remarks

In this chapter, we tracked the resonance frequency of resuspended PVA bubbles over a few minutes, using the acoustic setup of Figure 6.1. During this time, billions of oscillations occur. We did not observe any significant change in the resonance frequency. This behavior suggests an acceptable shell Physico-chemical stability since it is known that the shell constitution substantially contributes to the value of the resonance frequency (de Jong et al. 2002). In collaboration with Flavien Bureau and Alexandre Aubry from the Institut Langevin, we were able to use the ultrasound matrix image approach to assess the microbubbles' backscatter acoustic response. It was possible to verify that the monodispersity and the echogenicity of the bubbles were kept after the freeze-drying process. The focused reflection matrix used to evaluate the presence of multiple scattering events confirmed that the bubbles were being measured in a single scattering regime. In addition, although the lyophilisates were transported to different laboratories to perform acoustic measurements with our collaborators, we did not observe any degradation in the acoustic performances. Last but not least, the lifetime of the lyophilisate is at least one year. This was obtained by using a lyophilisate stored at ambient conditions at room temperature for one year. In this study, we found that neither morphologies, nor diameter distributions, nor resonance frequencies significantly evolved during storage.

It must be pointed out that the microfluidic technology is capable of producing monodisperse microbubbles tunable in size, e.g., down to 1 µm in diameter (Gnyawali et al. 2017). These small bubbles are well-suited to address *in vivo* applications on small animals, where higher frequencies (e.g., 10-15 MHz) can be used compared to experiments on humans due to the limited penetration depth. To facilitate the use of large sizes of microbubbles in small animals, radial modulation imaging can be used to detect large microbubbles, e.g., 5 µm in diameter, at high frequency by using dual ultrasonic excitations such as 1 MHz and 15 MHz (Muleki Seya et al. 2020). In radial modulation imaging bubble oscillation is induced by low amplitude, low-frequency modulation pulse. Two broadband high-frequency imaging pulses are also transmitted to hit the bubble at two different times corresponding to two different bubble oscillatory states. The responses of the bubble to the two imaging pulses do not cancel out upon subtraction, as opposed to the responses from the tissue, which should not change under exposure to the modulation wave.

The ultrasound image matrix approach has not only the potential to measure multiple scattering, measure the speed of sound and correct aberrations in the ultrasound image, but also to track individual microbubbles in a volume. By retrieving the resonance frequency of each individual bubble in volume, it has the possibility to correlate their eigenfrequency with the ambient pressure in the surroundings through relations such as the Minneart law (Minneart 1933). That way, together with the monodisperse microbubbles, this technology would provide the complete hemodynamics of an individual in a non-invasive manner, becoming a promising tool for the diagnostic of cardiovascular diseases.

8. CONCLUSION

Over the last decade, significant progress has been achieved in manufacturing monodisperse microbubbles and their use as UCAs. According to the scientific literature, bubble monodispersity increases image contrast and allows bubbles to be used in early diagnosis, therapy, and sensing applications. The polydispersity of existing clinical UCAs makes using bubbles in such novel applications difficult. However, no technology has yet been developed that allows for the storage and transportation of monodisperse microbubbles. Alternative freeze-drying methods are unrealistic compared to clinical UCAs, which are storable, transportable, and simple to use. Aside from economic and regulatory considerations, this may have hampered the progress of monodisperse bubbles through the clinics, despite their better features in some relevant aspects compared to commercial polydisperse bubbles.

For the first time, monodisperse microbubbles has been freeze-dried without losing their monodispersity. This technique solves the bottleneck of transporting and storing monodisperse microbubbles as a lyophilisate or powder. We solved this difficulty by focusing on two distinct factors. The first is microbubble composition and buffer solution formulation optimization, which includes selecting a shell molecule, a surfactant, and a cryoprotectant. While the shell and surfactant increase bubble stability, cryoprotectant shields bubbles during freezing and freeze-drying cycles. PVA works as shell material, surfactant, and cryoprotectant in our case. Second, by the resuspension of the bubbles, monolayer and localized freeze-drying of microbubbles ensure a monodisperse population—the latter results in less interaction between the bubbles. Consequently, failure in step one results in the destruction of the bubbles after freeze-drying, whereas failure in step two results in polydisperse freeze-dried bubbles. We believe that a variety of features of our lyophilisates and our resuspended bubbles may be important for several applications, and it is worth to pursue further investigations. Although we developed this approach on a polymer-shelled microbubble, it may be extended to freeze-dried monodisperse lipid or protein-shelled microbubbles in theory.

Fresh and freeze-dried PVA bubbles with the same size and gas core were acoustically described under the identical experimental circumstances in our studies. We observed the identical backscattered acoustic response under such settings within experimental error. These results round out the optical observations of bubble sizes and morphologies throughout the freeze-drying process and lead to the conclusion that freeze-drying, as we go, conserves bubble attributes. Because the shell constitution is known to have a significant role in determining the resonance frequency, this behavior suggests acceptable shell Physico-chemical stability (de Jong *et al*., 2002). Furthermore, the lyophilisates were maintained at room temperature for a year before moving to different facilities for acoustic measurements. We discovered that neither morphologies, diameter distributions, nor resonance frequencies changed substantially during storage. Furthermore, we compared the backscattered acoustic response of SonoVue and monodisperse PVA bubbles in the confined system. We discovered that monodisperse bubbles' maximum acoustic backscattered response was approximately seven times higher than SonoVue bubbles at a similar concentration. SonoVue produced a nearly flat response compared to the monodisperse bubbles' response, which was defined as narrow bandwidth in the centimetric cell. Our findings might aid in the entrance of monodisperse bubbles into the domain of UCAs, allowing for new activities and the development of innovative non-invasive measures.

It should be noted that microfluidic technology can manufacture monodisperse microbubbles with controllable sizes, for example, down to 1 µm in diameter (Gnyawali *et al*., 2017). Due to the restricted penetration depth, tiny bubbles are suited for in vivo applications on small animals where high frequencies (e.g., 10-15 MHz) are often favored. Radial modulation imaging may be used to detect big microbubbles, such as 5 µm in diameter, at high frequency by employing dual ultrasonic excitations such as 1 MHz and 15 MHz to ease the use of large sizes of microbubbles in small animals (Muleki-Seya *et al*., 2020).

Contrary to popular belief, employing microfluidic devices to generate monodisperse bubbles does not compromise the ability to achieve throughputs consistent with global research and clinical demands. The global output of contrast agent microbubbles is estimated to be on the scale of 10^{17} per year. A microfluidic device constantly working at a frequency of 10 kHz (assuming efficient maintenance conditions such as automated material refilling and cleaning) generates 10^{11} bubbles each year by preventing disruption in production using the anti-clogging system. By parallelizing 1,000 times, this would result in 10^{14} each year. It should be noted that parallelizing is not a simple task. Furthermore, obtaining one million microbubbles per second from a single microfluidic device would demand the adoption of only a few devices (van Elburg *et al*., 2021). When we consider that monodisperse bubbles require one hundred times fewer bubbles due to their high echogenicity (Segers *et al*., 2018b; Sirsi *et al*., 2010; Helbert *et al.*, 2020), the production we can achieve with microfluidic devices is compatible with the domain's needs on a global scale. Indeed, before freeze-drying, we must spread the bubbles on surfaces that may require considerable area. Calculations reveal that in an industrial process where bubbles are generated and then transported to the freeze-drier, the space required to distribute the bubbles would be pretty restricted.

This work concentrated on developing and characterizing what can become a new generation of contrast agents that can be stored for months and transported at any place, resuspended, and used directly in clinical applications. Hopefully, the exciting results obtained here will be helpful in future works to improve ultrasound contrast imaging, either by creating improved contrast agents or by creating measurement techniques that can extract quantitative information from the agents.

8.1. FUTURE WORK

The novel technique for freeze-drying monodisperse microbubbles developed and presented in this thesis can facilitate the penetration of monodisperse bubbles in the domain of UCAs, to perform new tasks and develop novel non-invasive measurements. However, much work still has to be done regarding their characterization and possible applications.

From the characterization aspect, *in vivo* stability of the microbubbles should be investigated. Preliminary studies were conducted in blood serum, where the microbubbles remained stable and monodisperse for more than 20 minutes. Currently, our bubbles are being studied in an egg Ex-vivo model in partnership with Sorbonne University. Preliminary results indicate that the bubbles are stable after injection. However, their capacity to sustain monodispersity when exposed to a complex medium such as the circulatory system of small rodents should be investigated.

From the acoustic characterization point of view, attenuation measurements should be conducted for different bubbles concentration and different acoustic pressure. That way, the backscatter coefficient for the monodisperse microbubbles can be corrected, yielding a more accurate description of the dynamics of the bubble and full exploitation of the linear relationship of the backscatter coefficient to contrast agent concentration.

Regarding the potential applications of the freeze-dried monodisperse microbubbles, experiments concerning the monodispersity of microbubbles with different shell materials (lipids, proteins, etc.) should be conducted. Thus, confirming that the technique developed can be expanded through the classical materials available for UCA production.

Ambient pressure measurements based on the resonance peak of the microbubbles populations' backscatter signal would be a significant step toward non-invasive pressure measurements. The static ambient pressure variation experiments are being conducted with the milli-channel setup presented in this work. Also, in collaboration with the Institut Langevin, experiments for pressure measurement are in the beginning phase using the matrix approach. The resuspended bubbles will be injected into a tissue-mimicking phantom, described in chapter 6.3, with different flow rates, and the bubble's resonance peak will be tracked through the matrix approach technique. This approach of wave imaging is based on the concept of the distortion matrix, in which the operator essentially connects any focal point inside the medium with the distortion that a wavefront emitted from that point experiences due to heterogeneities. A time-reversal analysis of the distortion matrix enables the estimation of the transmission matrix that links each sensor and image voxel (Lambert *et al.*, 2020). This way, the bubbles can be seen in a 3-D space, where their resonance frequency can be obtained. This could result in a pressure map of the flow, having the potential, in the future, to provide non-invasively the whole hemodynamics of the circulatory system.

BIBLIOGRAPHY

[1] Abdelwahed, W., Degobert, G., & Fessi, H. (2006). Investigation of nanocapsules stabilization by amorphous excipients during freeze-drying and storage. European journal of pharmaceutics and biopharmaceutics, 63(2), 87-94.

[2] Abou-Saleh, R. H., Armistead, F. J., Batchelor, D. V., Johnson, B. R., Peyman, S. A., & Evans, S. D. (2021). Horizon: Microfluidic platform for the production of therapeutic microbubbles and nanobubbles. Review of Scientific Instruments, 92(7), 074105.

[3] Abou-Saleh, R. H., Delaney, A., Ingram, N., Batchelor, D. V., Johnson, B. R., Charalambous, A., ... & Evans, S. D. (2020). Freeze-dried therapeutic microbubbles: Stability and gas exchange. ACS Applied Bio Materials, 3(11), 7840-7848.

[4] Abu-Zidan, F. M., Hefny, A. F., & Corr, P. (2011). Clinical ultrasound physics. Journal of Emergencies, Trauma and Shock, 4(4), 501.

[5] Achenbach, J. (2012). Wave propagation in elastic solids. Elsevier.

[6] Aldrich, J. E. (2007). Basic physics of ultrasound imaging. Critical care medicine, 35(5), S131-S137.

[7] Anderson, A. L., & Hampton, L. D. (1980). Acoustics of gas-bearing sediments I. Background. The Journal of the Acoustical Society of America, 67(6), 1865-1889.

[8] Anna, S. L., Bontoux, N., & Stone, H. A. (2003). Formation of dispersions using “flow focusing” in microchannels. Applied physics letters, 82(3), 364-366.

[9] Atherton, T. J., & Kerbyson, D. J. (1999). Size invariant circle detection. Image and Vision computing, 17(11), 795-803.

[10] Becher, H., Zähler, K., Grube, E., Schlief, R., & Lüderitz, B. (1988). Improving color Doppler echocardiography of the right heart chambers following intravenous injection of SHU 454. Zeitschrift fur Kardiologie, 77(4), 227-232.

[11] Bermejo, J. S., & Ugarte, C. M. (2009). Influence of cross-linking density on the glass transition and structure of chemically cross-linked PVA: a

molecular dynamics study. Macromolecular theory and simulations, 18(6), 317-327.

[12] Bhattacharya, S. (2018). Cryoprotectants and their usage in cryopreservation process. Cryopreservation Biotechnology in Biomedical and Biological Sciences, 7-18.

[13] Bilaniuk, N., & Wong, G. S. (1993). Speed of sound in pure water as a function of temperature. The Journal of the Acoustical Society of America, 93(3), 1609-1612.

[14] Björnmalm, M., Yan, Y., & Caruso, F. (2014). Engineering and evaluating drug delivery particles in microfluidic devices. Journal of Controlled Release, 190, 139-149.

[15] Blanken, N., Wolterink, J. M., Delingette, H., Brune, C., Versluis, M., & Lajoinie, G. (2022). Super-Resolved Microbubble Localization in Single-Channel Ultrasound RF Signals Using Deep Learning. IEEE transactions on medical imaging.

[16] Bloch, S. H., Dayton, P. A., & Ferrara, K. W. (2004). Targeted imaging using ultrasound contrast agents. IEEE Engineering in Medicine and Biology Magazine, 23(5), 18-29.

[17] Böhmer, M. R., Schroeders, R., Steenbakkers, J. A., de Winter, S. H., Duineveld, P. A., Lub, J., ... & Stapert, H. R. (2006). Preparation of monodisperse polymer particles and capsules by ink-jet printing. Colloids and Surfaces A: Physicochemical and Engineering Aspects, 289(1-3), 96-104.

[18] Borden, M. A., & Longo, M. L. (2002). Dissolution behavior of lipid monolayer-coated, air-filled microbubbles: Effect of lipid hydrophobic chain length. Langmuir, 18(24), 9225-9233.

[19] Brillouin, L. (2013). Wave propagation and group velocity (Vol. 8). Academic press.

[20] Bureau, F., Lambert, W., Cobus, L., Frappart, T., Fink, M., & Aubry, A. (2020, December). Matrix approach of aberration correction in medical ultrasound imaging. In Forum Acusticum (pp. 1427-1428).

[21] Burkard, M. E., & Van Liew, H. D. (1994). Oxygen transport to tissue by persistent bubbles: theory and simulations. Journal of Applied Physiology, 77(6), 2874-2878.

[22] C. Devin. Survey of thermal, radiation and viscous damping of pulsating air bubbles in water. J. Acoust. Soc. Am., 31:1654- 1667, 1959

[23] Caflisch, R. E., Miksis, M. J., Papanicolaou, G. C., & Ting, L. (1985). Effective equations for wave propagation in bubbly liquids. Journal of Fluid Mechanics, 153, 259-273.

[24] Campbell, J. A., & Waag, R. C. (1983). Normalization of ultrasonic scattering measurements to obtain average differential scattering cross sections for tissues. The Journal of the Acoustical Society of America, 74(2), 393-399.

[25] Carroll, B. A., Turner, R. J., Tickner, E. G., Boyle, D. B., & Young, S. W. (1980). Gelatin encapsulated nitrogen microbubbles as ultrasonic contrast agents. Investigative radiology, 15(3), 260-266.

[26] Cavalieri, F., El Hamassi, A., Chiessi, E., & Paradossi, G. (2005). Stable polymeric microballoons as multifunctional device for biomedical uses: synthesis and characterization. Langmuir, 21(19), 8758-8764.

[27] Cavalieri, F., El Hamassi, A., Chiessi, E., Paradossi, G., Villa, R., & Zaffaroni, N. (2006). Tethering functional ligands onto shell of ultrasound active polymeric microbubbles. Biomacromolecules, 7(2), 604-611.

[28] Cavalieri, F., Finelli, I., Tortora, M., Mozetic, P., Chiessi, E., Polizio, F., ... & Paradossi, G. (2008). Polymer microbubbles as diagnostic and therapeutic gas delivery device. Chemistry of Materials, 20(10), 3254-3258.

[29] Cerroni, B., Cicconi, R., Oddo, L., Scimeca, M., Bonfiglio, R., Bernardini, R., ... & Paradossi, G. (2018). In vivo biological fate of poly (vinylalcohol) microbubbles in mice. Heliyon, 4(9), e00770.

[30] Chang, L. L., Shepherd, D., Sun, J., Ouellette, D., Grant, K. L., Tang, X. C., & Pikal, M. J. (2005). Mechanism of protein stabilization by sugars during freeze-drying and storage: native structure preservation, specific interaction, and/or immobilization in a glassy matrix?. Journal of pharmaceutical sciences, 94(7), 1427-1444.

[31] Chaudhari, R. V., & Hofmann, H. (1994). Coalescence of gas bubbles in liquids. Reviews in Chemical Engineering, 10(2), 131-190.

[32] Chen, X., Phillips, D., Schwarz, K. Q., Mottley, J. G., & Parker, K. J. (1997). The measurement of backscatter coefficient from a broadband pulse-echo system: A new formulation. IEEE transactions on ultrasonics, ferroelectrics, and frequency control, 44(2), 515-525.

[33] Chesters, A. (1991). Modelling of coalescence processes in fluid-liquid dispersions: a review of current understanding. Chemical engineering research and design, 69(A4), 259-270.

[34] Chin, C. T. (2001). Modelling the behaviour of microbubble contrast agents for diagnostic ultrasound. Ph. D. thesis] University of Toronto, Canada.

[35] Chlon, C., Guédon, C., Verhaagen, B., Shi, W. T., Hall, C. S., Lub, J., & Böhmer, M. R. (2009). Effect of molecular weight, crystallinity, and hydrophobicity on the acoustic activation of polymer-shelled ultrasound contrast agents. Biomacromolecules, 10(5), 1025-1031.

[36] Choi, J. J., Feshitan, J. A., Baseri, B., Wang, S., Tung, Y. S., Borden, M. A., & Konofagou, E. E. (2009). Microbubble-size dependence of focused ultrasound-induced blood–brain barrier opening in mice in vivo. IEEE Transactions on Biomedical Engineering, 57(1), 145-154.

[37] Choi, J. J., Pernot, M., Small, S. A., & Konofagou, E. E. (2007). Noninvasive, transcranial and localized opening of the blood-brain barrier using focused ultrasound in mice. Ultrasound in medicine & biology, 33(1), 95-104.

[38] Church, C. C. (1995). The effects of an elastic solid surface layer on the radial pulsations of gas bubbles. The Journal of the Acoustical Society of America, 97(3), 1510-1521.

[39] Cobbold, R. S. C. (2007). Ultrasound imaging arrays In: Foundations of biomedical ultrasound.

[40] Commander, K. W., & Prosperetti, A. (1989). Linear pressure waves in bubbly liquids: Comparison between theory and experiments. The Journal of the Acoustical Society of America, 85(2), 732-746.

[41] Convery, N., & Gadegaard, N. (2019). 30 years of microfluidics. Micro and Nano Engineering, 2, 76-91.

[42] Cootney, R. W. (2001). Ultrasound imaging: principles and applications in rodent research. Ilar Journal, 42(3), 233-247.

[43] Coulaloglou, C. A., & Tavlarides, L. L. (1977). Description of interaction processes in agitated liquid-liquid dispersions. Chemical Engineering Science, 32(11), 1289-1297.

[44] Dalvi, S. V., & Joshi, J. R. (2015). Modeling of microbubble dissolution in aqueous medium. Journal of colloid and interface science, 437, 259-269.

[45] D'Arrigo, J. S., & Imae, T. (1992). Physical characteristics of ultrastable lipid-coated microbubbles. Journal of colloid and interface science, 149(2), 592-595.

[46] Dayton, P. A., & Rychak, J. J. (2007). Molecular ultrasound imaging using microbubble contrast agents. Frontiers in Bioscience-Landmark, 12(13), 5124-5142.

[47] de Jong, N. (1993). Acoustic properties of ultrasound contrast agents.

[48] De Jong, N., Bouakaz, A., & Frinking, P. (2002). Basic acoustic properties of microbubbles. Echocardiography, 19(3), 229-240.

[49] De Jong, N., Cornet, R., & Lancée, C. D. (1994). Higher harmonics of vibrating gas-filled microspheres. Part one: simulations. Ultrasonics, 32(6), 447-453.

[50] de Jong, N., Hoff, L., Skotland, T., & Bom, N. (1992). Absorption and scatter of encapsulated gas filled microspheres: theoretical considerations and some measurements. Ultrasonics, 30(2), 95-103.

[51] De Jong, N., Ten Cate, F. J., Lancee, C. T., Roelandt, J. R. T. C., & Bom, N. (1991). Principles and recent developments in ultrasound contrast agents. Ultrasonics, 29(4), 324-330.

[52] De La Vega, J. C., Elischer, P., Schneider, T., & Häfeli, U. O. (2013). Uniform polymer microspheres: monodispersity criteria, methods of formation and applications. Nanomedicine, 8(2), 265-285.

[53] Demené, C., Robin, J., Dizeux, A., Heiles, B., Pernot, M., Tanter, M., & Perren, F. (2021). Transcranial ultrafast ultrasound localization microscopy of brain vasculature in patients. Nature biomedical engineering, 5(3), 219-228.

[54] Dhanaliwala, A. H., Chen, J. L., Wang, S., & Hossack, J. A. (2013). Liquid flooded flow-focusing microfluidic device for in situ generation of monodisperse microbubbles. Microfluidics and nanofluidics, 14(3), 457-467.

[55] Dixon, A. J., Li, J., Rickel, J. M. R., Klibanov, A. L., Zuo, Z., & Hossack, J. A. (2019). Efficacy of sonothrombolysis using microbubbles produced by a catheter-based microfluidic device in a rat model of ischemic stroke. Annals of biomedical engineering, 47(4), 1012-1022.

[56] Doinikov, A. A., & Bouakaz, A. (2011). Review of shell models for contrast agent microbubbles. IEEE transactions on ultrasonics, ferroelectrics, and frequency control, 58(5), 981-993.

[57] Doinikov, A. A., Haac, J. F., & Dayton, P. A. (2009). Resonance frequencies of lipid-shelled microbubbles in the regime of nonlinear oscillations. Ultrasonics, 49(2), 263-268.

[58] Doubliez, L. (1991). The drainage and rupture of a non-foaming liquid film formed upon bubble impact with a free surface. International journal of multiphase flow, 17(6), 783-803.

[59] Dressaire, E., Bee, R., Bell, D. C., Lips, A., & Stone, H. A. (2008). Interfacial polygonal nanopatterning of stable microbubbles. Science, 320(5880), 1198-1201.

[60] Druzhinin, O. A., & Elghobashi, S. (1998). Direct numerical simulations of bubble-laden turbulent flows using the two-fluid formulation. Physics of Fluids, 10(3), 685-697.

[61] Duffy, D. C., McDonald, J. C., Schueller, O. J., & Whitesides, G. M. (1998). Rapid prototyping of microfluidic systems in poly (dimethylsiloxane). Analytical chemistry, 70(23), 4974-4984.

[62] Duineveld, P. C. (1994). Bouncing and coalescence phenomena of two bubbles in water. In Bubble Dynamics and Interface Phenomena (pp. 447-456). Springer, Dordrecht.

[63] Eisenbrey, J. R., Albala, L., Kramer, M. R., Daroshefski, N., Brown, D., Liu, J. B., ... & Wheatley, M. A. (2015). Development of an ultrasound sensitive oxygen carrier for oxygen delivery to hypoxic tissue. International journal of pharmaceutics, 478(1), 361-367.

[64] Eller, A. I. (1970). Damping constants of pulsating bubbles. The Journal of the Acoustical Society of America, 47(5B), 1469-1470.

[65] Elton, G. A. H., & Picknett, R. G. (1957). The coalescence of aqueous droplets with an oil/water interface. In Second International Congress of Surface Activity (pp. 288-294). London: Butterworths.

[66] Epstein, P. S., & Plesset, M. S. (1950). On the stability of gas bubbles in liquid-gas solutions. The Journal of Chemical Physics, 18(11), 1505-1509.

[67] Errico, C., Pierre, J., Pezet, S., Desailly, Y., Lenkei, Z., Couture, O., & Tanter, M. (2015). Ultrafast ultrasound localization microscopy for deep super-resolution vascular imaging. Nature, 527(7579), 499-502.

[68] Esposito, C., McDonald, M. E., Machado, P., Savage, M., Fischman, D., Mehrotra, P., ... & Dave, J. K. (2020, September). Estimating central cardiac pressures noninvasively in patients using ultrasound contrast agents. In 2020 IEEE International Ultrasonics Symposium (IUS) (pp. 1-4). IEEE.

[69] Fairbank, W. M., & Scully, M. O. (1977). A new noninvasive technique for cardiac pressure measurement: resonant scattering of

ultrasound from bubbles. IEEE Transactions on Biomedical Engineering, (2), 107-110.

[70] Farook, U., Stride, E., & Edirisinghe, M. J. (2009). Stability of microbubbles prepared by co-axial electrohydrodynamic atomisation. European Biophysics Journal, 38(5), 713-718.

[71] Feinstein, S. B., Shah, P. M., Bing, R. J., Meerbaum, S., Corday, E., Chang, B. L., ... & Fujibayashi, Y. (1984). Microbubble dynamics visualized in the intact capillary circulation. Journal of the American College of Cardiology, 4(3), 595-600.

[72] Ferrara, K., Pollard, R., & Borden, M. (2007). Ultrasound microbubble contrast agents: fundamentals and application to gene and drug delivery. Annual review of biomedical engineering, 9(1), 415-447.

[73] Feshitan, J. A., Chen, C. C., Kwan, J. J., & Borden, M. A. (2009). Microbubble size isolation by differential centrifugation. Journal of colloid and interface science, 329(2), 316-324.

[74] Flynn, H. G. (1975). Cavitation dynamics. I. A mathematical formulation. The Journal of the Acoustical Society of America, 57(6), 1379-1396.

[75] Flynn, H. G. (1975). Cavitation dynamics: II. Free pulsations and models for cavitation bubbles. The Journal of the Acoustical Society of America, 58(6), 1160-1170.

[76] Foldy, L. L. (1945). The multiple scattering of waves. I. General theory of isotropic scattering by randomly distributed scatterers. Physical review, 67(3-4), 107.

[77] Franks, F. (1998). Freeze-drying of bioproducts: putting principles into practice. European journal of Pharmaceutics and BioPharmaceutics, 45(3), 221-229.

[78] Frinking, P. J., Tardy, I., Théraulaz, M., Arditi, M., Powers, J., Pochon, S., & Tranquart, F. (2012). Effects of acoustic radiation force on the binding efficiency of BR55, a VEGFR2-specific ultrasound contrast agent. Ultrasound in medicine & biology, 38(8), 1460-1469.

[79] Frinking, P., Segers, T., Luan, Y., & Tranquart, F. (2020). Three decades of ultrasound contrast agents: a review of the past, present and future improvements. Ultrasound in medicine & biology, 46(4), 892-908.

[80] Furuta, Y., Oikawa, N., & Kurita, R. (2016). Close relationship between a dry-wet transition and a bubble rearrangement in two-dimensional foam. Scientific reports, 6(1), 1-8.

[81] Gale, B. K., Jafek, A. R., Lambert, C. J., Goenner, B. L., Moghimifam, H., Nze, U. C., & Kamarapu, S. K. (2018). A review of current methods in microfluidic device fabrication and future commercialization prospects. Inventions, 3(3), 60.

[82] Gañán-Calvo, A. M. (2006). Jetting–dripping transition of a liquid jet in a lower viscosity co-flowing immiscible liquid: the minimum flow rate in flow focusing. Journal of Fluid Mechanics, 553, 75-84.

[83] Ganán-Calvo, A. M., & Gordillo, J. M. (2001). Perfectly monodisperse microbubbling by capillary flow focusing. Physical review letters, 87(27), 274501.

[84] Gao, Z., Kennedy, A. M., Christensen, D. A., & Rapoport, N. Y. (2008). Drug-loaded nano/microbubbles for combining ultrasonography and targeted chemotherapy. Ultrasonics, 48(4), 260-270.

[85] Garstecki, P., Fuerstman, M. J., Stone, H. A., & Whitesides, G. M. (2006). Formation of droplets and bubbles in a microfluidic T-junction—scaling and mechanism of break-up. Lab on a Chip, 6(3), 437-446.

[86] Garstecki, P., Gańán-Calvo, A. M., & Whitesides, G. M. (2005). Formation of bubbles and droplets in microfluidic systems. Bulletin of the Polish Academy of Sciences: Technical Sciences, 53(4).

[87] Garstecki, P., Gitlin, I., DiLuzio, W., Whitesides, G. M., Kumacheva, E., & Stone, H. A. (2004). Formation of monodisperse bubbles in a microfluidic flow-focusing device. Applied Physics Letters, 85(13), 2649-2651.

[88] Garstecki, P., Stone, H. A., & Whitesides, G. M. (2005). Mechanism for flow-rate controlled breakup in confined geometries: A route to monodisperse emulsions. Physical review letters, 94(16), 164501.

[89] Gilmore, F. R. (1952). The growth or collapse of a spherical bubble in a viscous compressible liquid.

[90] Gnyawali, V., Moon, B. U., Kieda, J., Karshafian, R., Kolios, M. C., & Tsai, S. S. (2017). Honey, I shrunk the bubbles: microfluidic vacuum shrinkage of lipid-stabilized microbubbles. Soft Matter, 13(22), 4011-4016.

[91] Gong, Y. (2013). Acoustic characterization of ultrasound contrast agents with lipid-coated monodisperse microbubble. Boston University.

[92] Gong, Y., Cabodi, M., & Porter, T. (2010). Relationship between size and frequency dependent attenuation of monodisperse populations of lipid coated microbubbles. Bubble Science, Engineering & Technology, 2(2), 41-47.

[93] Gorce, J. M., Arditi, M., & Schneider, M. (2000). Influence of bubble size distribution on the echogenicity of ultrasound contrast agents: A study of SonoVue™. Investigative radiology, 35(11), 661-671.

[94] Goss, S. A., Johnston, R. L., & Dunn, F. (1978). Comprehensive compilation of empirical ultrasonic properties of mammalian tissues. The Journal of the Acoustical Society of America, 64(2), 423-457.

[95] Gramiak, R., & Shah, P. M. (1968). Echocardiography of the aortic root. Investigative radiology, 3(5), 356-366.

[96] Grayburn, P. (1997). Perflenapent emulsion (echogen®): A new long-acting phase-shift agent for contrast echocardiography. Clinical cardiology, 20(S1), 12-18.

[97] Grishenkov, D., Kari, L., Brodin, L. Å., Brismar, T. B., & Paradossi, G. (2011). In vitro contrast-enhanced ultrasound measurements of capillary microcirculation: comparison between polymer-and phospholipid-shelled microbubbles. Ultrasonics, 51(1), 40-48.

[98] Grishenkov, D., Pecorari, C., Brismar, T. B., & Paradossi, G. (2009). Characterization of acoustic properties of PVA-shelled ultrasound contrast agents: linear properties (part I). Ultrasound in medicine & biology, 35(7), 1127-1138.

[99] Grishenkov, D., Pecorari, C., Brismar, T. B., & Paradossi, G. (2009). Characterization of acoustic properties of PVA-shelled ultrasound contrast agents: ultrasound-induced fracture (part II). Ultrasound in medicine & biology, 35(7), 1139-1147.

[100] H. Ybema, L. Kolkman-Roodbeen, M. P. Te Booy, and H. Vromans, Pharm. Res. 12, 1260 (1995)

[101] Hall, C. S. (1996). Measurements of ultrasonic backscatter coefficient and attenuation coefficient for anisotropic inhomogenous media and suspensions of solid and gaseous microspheres. Washington University in St. Louis.

[102] Hamilton, A. J., Huang, S. L., Warnick, D., Rabbat, M., Kane, B., Nagaraj, A., ... & McPherson, D. D. (2004). Intravascular ultrasound molecular imaging of atheroma components in vivo. Journal of the American College of Cardiology, 43(3), 453-460.

[103] Hamilton, A., Huang, S. L., Warnick, D., Stein, A., Rabbat, M., Madhav, T., ... & McPherson, D. (2002). Left ventricular thrombus enhancement after intravenous injection of echogenic immunoliposomes: studies in a new experimental model. Circulation, 105(23), 2772-2778.

[104] Hatley, R. H., Franks, F., & Day, H. (1986). Subzero-temperature preservation of reactive fluids in the undercooled state: II. The effect on the oxidation of ascorbic acid of freeze concentration and undercooling. Biophysical chemistry, 24(2), 187-192.

[105] He, P., & Zheng, J. (2001). Acoustic dispersion and attenuation measurement using both transmitted and reflected pulses. Ultrasonics, 39(1), 27-32.

[106] Helbert, A., Gaud, E., Segers, T., Botteron, C., Frinking, P., & Jeannot, V. (2020). Monodisperse versus polydisperse ultrasound contrast agents: In vivo sensitivity and safety in rat and pig. Ultrasound in Medicine & Biology, 46(12), 3339-3352.

[107] Hernot, S., & Klibanov, A. L. (2008). Microbubbles in ultrasound-triggered drug and gene delivery. Advanced drug delivery reviews, 60(10), 1153-1166.

[108] Hoff, L. (2001). Acoustic characterization of contrast agents for medical ultrasound imaging. Springer Science & Business Media.

[109] Hoff, L., Sontum, P. C., & Hovem, J. M. (2000). Oscillations of polymeric microbubbles: Effect of the encapsulating shell. The Journal of the Acoustical Society of America, 107(4), 2272-2280.

[110] Holm, S., Myhrum, M., & Hoff, L. (1994). Modelling of the ultrasound return from Albunex microspheres. Ultrasonics, 32(2), 123-130.

[111] Howarth, W. J. (1964). Coalescence of drops in a turbulent flow field. Chemical Engineering Science, 19(1), 33-38.

[112] Hu, S., & Li, W. X. (2018). Influence of particle size distribution on lifetime and thermal stability of Ostwald ripening of supported particles. ChemCatChem, 10(13), 2900-2907.

[113] Insana, M. F., & Brown, D. G. (1993). Acoustic scattering theory applied to soft biological tissues. Ultrasonic scattering in biological tissues, 75-124.

[114] Ishihara, K., Kitabatake, A., Tanouchi, J., Fujii, K., Uematsu, M., Yoshida, Y., ... & Shirae, K. (1988). New approach to noninvasive manometry based on pressure dependent resonant shift of elastic microcapsules in ultrasonic frequency characteristics. Japanese Journal of Applied Physics, 27(S1), 125.

[115] Ishimaru, A. (1997). Wave propagation and scattering in random media: Oxford University Press.

[116] Izumida, Y., Sugiura, S., Oda, T., Satake, M., & Nakajima, M. (2005). Production of quasi-monodisperse emulsions with large droplets using a micromachined device. Journal of the American Oil Chemists' Society, 82(1), 73-78.

[117] Jeffreys, G. V., & Davies, G. A. (1971). Coalescence of liquid droplets and liquid dispersion. In Recent Advances in Liquid–Liquid Extraction (pp. 495-584). Pergamon.

[118] Jennings, T. A. (1999). Lyophilization: introduction and basic principles. CRC press.

[119] Jin-Fei, Y., Dong, Z., Xiu-Fen, G., Yan-Jun, G., Zhe-Min, Z., & Xue-Ming, L. (2005). Frequency dependences of sound attenuation and phase velocity in suspensions containing encapsulated microbubbles. Chinese Physics Letters, 22(4), 892.

[120] Kabalnov, A. S., & Shchukin, E. D. (1992). Ostwald ripening theory: applications to fluorocarbon emulsion stability. Advances in colloid and interface science, 38, 69-97.

[121] Kabalnov, A., Bradley, J., Flaim, S., Klein, D., Pelura, T., Peters, B., ... & Weers, J. (1998). Dissolution of multicomponent microbubbles in the bloodstream: 2. Experiment. Ultrasound in medicine & biology, 24(5), 751-760.

[122] Kabalnov, A., Klein, D., Pelura, T., Schutt, E., & Weers, J. (1998). Dissolution of multicomponent microbubbles in the bloodstream: 1. Theory. Ultrasound in medicine & biology, 24(5), 739-749.

[123] Katiyar, A., Sarkar, K., & Jain, P. (2009). Effects of encapsulation elasticity on the stability of an encapsulated microbubble. Journal of Colloid and Interface Science, 336(2), 519-525.

[124] Kaul, S. (2002). Instrumentation for contrast echocardiography: technology and techniques. The American journal of cardiology, 90(10), 8-14.

[125] Kaul, S. (2008). Myocardial contrast echocardiography: a 25-year retrospective. Circulation, 118(3), 291-308.

[126] Kaya, M., Feingold, S., Streeter, J., Hettiarachchi, K., Lee, A. P., & Dayton, P. A. (2009, September). Acoustic characterization of individual monodisperse contrast agents with an optical-acoustical system. In 2009 IEEE International Ultrasonics Symposium (pp. 1813-1816). IEEE.

[127] Keitel, G., & Onken, U. (1982). Inhibition of bubble coalescence by solutes in air/water dispersions. Chemical Engineering Science, 37(11), 1635-1638.

[128] Kelvin, W. (1871). The influence of wind on waves in water supposed frictionless. Phil. Mag, 42(4), 368-374.

[129] Khismatullin, D. B. (2004). Resonance frequency of microbubbles: Effect of viscosity. The Journal of the Acoustical Society of America, 116(3), 1463-1473.

[130] Kim, A. D., & Ishimaru, A. (1999). A Chebyshev spectral method for radiative transfer equations applied to electromagnetic wave propagation and scattering in a discrete random medium. Journal of Computational Physics, 152(1), 264-280.

[131] Kim, Y. S., Rhim, H., Choi, M. J., Lim, H. K., & Choi, D. (2008). High-intensity focused ultrasound therapy: an overview for radiologists. Korean journal of radiology, 9(4), 291-302.

[132] Kinsler, L. E., Frey, A. R., Coppens, A. B., & Sanders, J. V. (2000). Fundamentals of acoustics. John wiley & sons.

[133] Klibanov, A. L. (2005). Ligand-carrying gas-filled microbubbles: ultrasound contrast agents for targeted molecular imaging. Bioconjugate chemistry, 16(1), 9-17.

[134] Klibanov, A. L. (2007). Ultrasound molecular imaging with targeted microbubble contrast agents. Journal of Nuclear Cardiology, 14(6), 876-884.

[135] Klibanov, A. L., Rychak, J. J., Yang, W. C., Alikhani, S., Li, B., Acton, S., ... & Kaul, S. (2006). Targeted ultrasound contrast agent for molecular imaging of inflammation in high-shear flow. Contrast media & molecular imaging, 1(6), 259-266.

[136] Kok, M. P., Segers, T., & Versluis, M. (2015). Bubble sorting in pinched microchannels for ultrasound contrast agent enrichment. Lab on a Chip, 15(18), 3716-3722.

[137] KOOIMAN, K. et al. DSPC or DPPC as main shell component influences ligand distribution and binding area of lipid-coated targeted microbubbles. European Journal of Lipid Science and Technology, v. 116, n. 9, p. 1217–1227, 2014

[138] Kooiman, K., Böhmer, M. R., Emmer, M., Vos, H. J., Chlon, C., Shi, W. T., ... & van Wamel, A. (2009). Oil-filled polymer microcapsules for

ultrasound-mediated delivery of lipophilic drugs. Journal of controlled release, 133(2), 109-118.

[139] Kooiman, K., Roovers, S., Langeveld, S. A., Kleven, R. T., Dewitte, H., O'Reilly, M. A., ... & Holland, C. K. (2020). Ultrasound-responsive cavitation nuclei for therapy and drug delivery. Ultrasound in Medicine & Biology, 46(6), 1296-1325.

[140] Kossoff, G. (2000). Basic physics and imaging characteristics of ultrasound. World journal of surgery, 24(2), 134-142.

[141] Kwan, J. J., & Borden, M. A. (2010). Microbubble dissolution in a multigas environment. Langmuir, 26(9), 6542-6548.

[142] Kwan, J., & Borden, M. (2010, October). Microbubble shell break-up and collapse during gas exchange. In 2010 IEEE International Ultrasonics Symposium (pp. 897-899). IEEE.

[143] Lambert, W., Cobus, L. A., Couade, M., Fink, M., & Aubry, A. (2020). Reflection matrix approach for quantitative imaging of scattering media. Physical Review X, 10(2), 021048.

[144] Larina, I. V., Evers, B. M., Ashitkov, T. V., Bartels, C., Larin, K. V., & Esenaliev, R. O. (2005). Enhancement of drug delivery in tumors by using interaction of nanoparticles with ultrasound radiation. Technology in cancer research & treatment, 4(2), 217-226.

[145] Lasic, D. D., & Papahadjopoulos, D. (Eds.). (1998). Medical applications of liposomes. Elsevier.

[146] Laugier, P., & Haïat, G. (2011). Introduction to the physics of ultrasound. Bone quantitative ultrasound, 29-45.

[147] Lee, C. Y., Chang, C. L., Wang, Y. N., & Fu, L. M. (2011). Microfluidic mixing: a review. International journal of molecular sciences, 12(5), 3263-3287.

[148] Lee, J. C., & Hodgson, T. D. (1968). Film flow and coalescence-I Basic relations, film shape and criteria for interface mobility. Chemical Engineering Science, 23(11), 1375-1397.

[149] Lee, M., Lee, E. Y., Lee, D., & Park, B. J. (2015). Stabilization and fabrication of microbubbles: applications for medical purposes and functional materials. Soft matter, 11(11), 2067-2079.

[150] Leighton, T. G. (1994). The Acoustic Bubble.| Academic. Press, London, 234-243.

[151] Lemlich, R. (1978). Prediction of changes in bubble size distribution due to interbubble gas diffusion in foam. Industrial & Engineering Chemistry Fundamentals, 17(2), 89-93.

[152] Leong-Poi, H., Christiansen, J., Klibanov, A. L., Kaul, S., & Lindner, J. R. (2003). Noninvasive assessment of angiogenesis by ultrasound and microbubbles targeted to αv-integrins. Circulation, 107(3), 455-460.

[153] Li, M. L., Kuo, Y. C., & Yeh, C. K. (2010). Amplitude-modulation chirp imaging for contrast detection. Ultrasound in medicine & biology, 36(9), 1535-1545.

[154] Liao, Y., & Lucas, D. (2010). A literature review on mechanisms and models for the coalescence process of fluid particles. Chemical Engineering Science, 65(10), 2851-2864.

[155] Liu, Y., Miyoshi, H., & Nakamura, M. (2006). Encapsulated ultrasound microbubbles: therapeutic application in drug/gene delivery. Journal of controlled release, 114(1), 89-99.

[156] Lu, N. Q., Prosperetti, A., & Yoon, S. W. (1990). Underwater noise emissions from bubble clouds. IEEE journal of oceanic engineering, 15(4), 275-281.

[157] Luo, W., Zhou, X., Tian, X., Ren, X., Zheng, M., Gu, K., & He, G. (2006). Enhancement of ultrasound contrast agent in high-intensity focused ultrasound ablation. Advances in therapy, 23(6), 861-868.

[158] Ma, J., Lee, S. M. Y., Yi, C., & Li, C. W. (2017). Controllable synthesis of functional nanoparticles by microfluidic platforms for biomedical applications–a review. Lab on a Chip, 17(2), 209-226.

[159] MacDonald, C. A., Sboros, V., Gomatam, J., Pye, S. D., Moran, C. M., & McDicken, W. N. (2004). A numerical investigation of the resonance of gas-filled microbubbles: resonance dependence on acoustic pressure amplitude. Ultrasonics, 43(2), 113-122.

[160] Macé, E., Montaldo, G., Cohen, I., Baulac, M., Fink, M., & Tanter, M. (2011). Functional ultrasound imaging of the brain. Nature methods, 8(8), 662-664.

[161] Madsen, E. L., Insana, M. F., & Zagzebski, J. A. (1984). Method of data reduction for accurate determination of acoustic backscatter coefficients. The Journal of the Acoustical Society of America, 76(3), 913-923.

[162] Mahue, V., Mari, J. M., Eckersley, R. J., & Tang, M. X. (2011). Comparison of pulse subtraction Doppler and pulse inversion

Doppler. IEEE transactions on ultrasonics, ferroelectrics, and frequency control, 58(1), 73-81.

[163] Malloggi, F., Pannacci, N., Attia, R., Monti, F., Mary, P., Willaime, H., ... & Poncet, P. (2010). Monodisperse colloids synthesized with nanofluidic technology. Langmuir, 26(4), 2369-2373.

[164] Maresca, D., Payen, T., Lee-Gosselin, A., Ling, B., Malounda, D., Demené, C., ... & Shapiro, M. G. (2020). Acoustic biomolecules enhance hemodynamic functional ultrasound imaging of neural activity. NeuroImage, 209, 116467.

[165] Marmottant, P., Van Der Meer, S., Emmer, M., Versluis, M., De Jong, N., Hilgenfeldt, S., & Lohse, D. (2005). A model for large amplitude oscillations of coated bubbles accounting for buckling and rupture. The Journal of the Acoustical Society of America, 118(6), 3499-3505.

[166] Marsh, J. N., Hughes, M. S., Hall, C. S., Lewis, S. H., Trousil, R. L., Brandenburger, G. H., ... & Miller, J. G. (1998). Frequency and concentration dependence of the backscatter coefficient of the ultrasound contrast agent Albunex®. The Journal of the Acoustical Society of America, 104(3), 1654-1666.

[167] Medwin, H. (1977). Counting bubbles acoustically: a review. Ultrasonics, 15(1), 7-13.

[168] Mensink, M. A., Frijlink, H. W., van der Voort Maarschalk, K., & Hinrichs, W. L. (2017). How sugars protect proteins in the solid state and during drying (review): Mechanisms of stabilization in relation to stress conditions. European Journal of Pharmaceutics and Biopharmaceutics, 114, 288-295.

[169] Merzbacher, E., Feagin, J. M., & Wu, T. H. (1977). Superposition of the radiation from N independent sources and the problem of random flights. American Journal of Physics, 45(10), 964-969.

[170] Minnaert, M. (1933). XVI. On musical air-bubbles and the sounds of running water. The London, Edinburgh, and Dublin Philosophical Magazine and Journal of Science, 16(104), 235-248.

[171] Mitchell, D. E., Fayter, A. E., Deller, R. C., Hasan, M., Gutierrez-Marcos, J., & Gibson, M. I. (2019). Ice-recrystallization inhibiting polymers protect proteins against freeze-stress and enable glycerol-free cryostorage. Materials horizons, 6(2), 364-368.

[172] Mo, L. Y. L., & Cobbold, R. S. (1992). A unified approach to modeling the backscattered Doppler ultrasound from blood. IEEE transactions on biomedical engineering, 39(5), 450-461.

[173] Mobley, J., Marsh, J. N., Hall, C. S., Hughes, M. S., Brandenburger, G. H., & Miller, J. G. (1998). Broadband measurements of phase velocity in Albunex® suspensions. The Journal of the Acoustical Society of America, 103(4), 2145-2153.

[174] Muleki-Seya, P., Xu, K., Tanter, M., & Couture, O. (2019). Ultrafast radial modulation imaging. IEEE Transactions on Ultrasonics, Ferroelectrics, and Frequency Control, 67(3), 598-611.

[175] Nanda, N. C., Schlief, R., & Goldberg, B. B. (Eds.). (2012). Advances in echo imaging using contrast enhancement. Springer Science & Business Media.

[176] Needles, A., Couture, O., & Foster, F. S. (2009). A method for differentiating targeted microbubbles in real time using subharmonic micro-ultrasound and interframe filtering. Ultrasound in medicine & biology, 35(9), 1564-1573.

[177] Neppiras, E. A., & Noltingk, B. E. (1951). Cavitation produced by ultrasonics: theoretical conditions for the onset of cavitation. Proceedings of the Physical Society. Section B, 64(12), 1032.

[178] Noltingk, B. E., & Neppiras, E. A. (1950). Cavitation produced by ultrasonics. Proceedings of the Physical Society. Section B, 63(9), 674.

[179] O'Donnell, M., & Miller, J. G. (1981). Quantitative broadband ultrasonic backscatter: An approach to nondestructive evaluation in acoustically inhomogeneous materials. Journal of Applied Physics, 52(2), 1056-1065.

[180] O'Donnell, Matthew, E. T. Jaynes, and J. G. Miller. "Kramers–Kronig relationship between ultrasonic attenuation and phase velocity." The Journal of the Acoustical Society of America 69.3 (1981): 696-701.

[181] Oddo, L., Cerroni, B., Domenici, F., Bedini, A., Bordi, F., Chiessi, E., ... & Paradossi, G. (2017). Next generation ultrasound platforms for theranostics. Journal of colloid and interface science, 491, 151-160.

[182] Ojha, T., Pathak, V., Drude, N., Weiler, M., Rommel, D., Rütten, S., ... & Lammers, T. (2019). Shelf-life evaluation and lyophilization of PBCA-based polymeric microbubbles. Pharmaceutics, 11(9), 433.

[183] Oliveira, A. F., Pessoa, A. C., Bastos, R. G., & de la Torre, L. G. (2016). Microfluidic tools toward industrial biotechnology. Biotechnology Progress, 32(6), 1372-1389.

[184] OOLMAN, T. O., & BLANCH, H. W. (1986). Bubble coalescence in stagnant liquids. Chemical Engineering Communications, 43(4-6), 237-261.

[185] Osterman, J., & Nordling, C. (1987). Physics Handbook.

[186] Overvelde, M., Garbin, V., Dollet, B., de Jong, N., Lohse, D., & Versluis, M. (2011). Dynamics of coated microbubbles adherent to a wall. Ultrasound in medicine & biology, 37(9), 1500-1508.

[187] Overvelde, M., Garbin, V., Sijl, J., Dollet, B., De Jong, N., Lohse, D., & Versluis, M. (2010). Nonlinear shell behavior of phospholipid-coated microbubbles. Ultrasound in medicine & biology, 36(12), 2080-2092.

[188] Paradossi, G., Pellegretti, P., & Trucco, A. (Eds.). (2010). Ultrasound contrast agents: Targeting and processing methods for theranostics. Springer Science & Business Media.

[189] Peyman, S. A., Abou-Saleh, R. H., McLaughlan, J. R., Ingram, N., Johnson, B. R., Critchley, K., ... & Evans, S. D. (2012). Expanding 3D geometry for enhanced on-chip microbubble production and single step formation of liposome modified microbubbles. Lab on a Chip, 12(21), 4544-4552.

[190] Peyratout, C. S., & Daehne, L. (2004). Tailor-made polyelectrolyte microcapsules: from multilayers to smart containers. Angewandte Chemie International Edition, 43(29), 3762-3783.

[191] Phillips, L. C., Klibanov, A. L., Wamhoff, B. R., & Hossack, J. A. (2012). Intravascular ultrasound detection and delivery of molecularly targeted microbubbles for gene delivery. IEEE transactions on ultrasonics, ferroelectrics, and frequency control, 59(7), 1596-1601.

[192] Pikal, M. J., Shah, S., Roy, M. L., & Putman, R. (1990). The secondary drying stage of freeze drying: drying kinetics as a function of temperature and chamber pressure. International journal of pharmaceutics, 60(3), 203-207.

[193] Pinton, G., Aubry, J. F., Bossy, E., Muller, M., Pernot, M., & Tanter, M. (2012). Attenuation, scattering, and absorption of ultrasound in the skull bone. Medical physics, 39(1), 299-307.

[194] Plesset, M. S. (1949). The dynamics of cavitation bubbles.

[195] Podell, S., Burrascano, C., Gaal, M., Golec, B., Maniquis, J., & Mehlhaff, P. (1999). Physical and biochemical stability of Optison®, an injectable ultrasound contrast agent. Biotechnology and applied biochemistry, 30(3), 213-223.

[196] Poehlmann, M., Grishenkov, D., Kothapalli, S. V., Härmark, J., Hebert, H., Philipp, A., ... & Fery, A. (2014). On the interplay of shell structure with low-and high-frequency mechanics of multifunctional magnetic microbubbles. Soft Matter, 10(1), 214-226.

[197] Poritsky, H. (1952). The growth or collapse of a spherical bubble or cavity in a viscous fluid. In Proc. US First National Congress, Appl. Mech., ASME (Vol. 313).

[198] Postema, M., Marmottant, P., Lancée, C. T., Hilgenfeldt, S., & De Jong, N. (2004). Ultrasound-induced microbubble coalescence. Ultrasound in medicine & biology, 30(10), 1337-1344.

[199] Prada, C., Kerbrat, E., Cassereau, D., & Fink, M. (2002). Time reversal techniques in ultrasonic nondestructive testing of scattering media. Inverse problems, 18(6), 1761.

[200] Prosperetti, A. (1976). Viscous effects on small-amplitude surface waves. The Physics of Fluids, 19(2), 195-203.

[201] Prosperetti, A. (1984). Bubble phenomena in sound fields: part one. Ultrasonics, 22(2), 69-77.

[202] Prosperetti, A., Crum, L. A., & Commander, K. W. (1988). Nonlinear bubble dynamics. The Journal of the Acoustical Society of America, 83(2), 502-514.

[203] Qian, J. Y., Li, X. J., Wu, Z., Jin, Z. J., & Sunden, B. (2019). A comprehensive review on liquid–liquid two-phase flow in microchannel: Flow pattern and mass transfer. Microfluidics and Nanofluidics, 23(10), 1-30.

[204] Rayleigh, L. (1917). VIII. On the pressure developed in a liquid during the collapse of a spherical cavity. The London, Edinburgh, and Dublin Philosophical Magazine and Journal of Science, 34(200), 94-98.

[205] Roovers, S., Segers, T., Lajoinie, G., Deprez, J., Versluis, M., De Smedt, S. C., & Lentacker, I. (2019). The role of ultrasound-driven microbubble dynamics in drug delivery: From microbubble fundamentals to clinical translation. Langmuir, 35(31), 10173-10191.

[206] Sackmann, E. K., Fulton, A. L., & Beebe, D. J. (2014). The present and future role of microfluidics in biomedical research. Nature, 507(7491), 181-189.

[207] Samad, A., & Devarajan, P. V. (2010). Freeze thaw: a simple approach for prediction of optimal cryoprotectant for freeze drying. Aaps Pharmscitech, 11(1), 304-313.

[208] Sarkar, K., Katiyar, A., & Jain, P. (2009). Growth and dissolution of an encapsulated contrast microbubble: effects of encapsulation permeability. Ultrasound in medicine & biology, 35(8), 1385-1396.

[209] Sarkar, K., Shi, W. T., Chatterjee, D., & Forsberg, F. (2005). Characterization of ultrasound contrast microbubbles using in vitro experiments and viscous and viscoelastic interface models for encapsulation. The Journal of the Acoustical Society of America, 118(1), 539-550.

[210] Schneider, M. (1999). Characteristics of sonovue™. Echocardiography, 16, 743-746.

[211] Schneider, M., Arditi, M., Barrau, M. B., Brochot, J., Broillet, A., Ventrone, R., & Yan, F. (1995). BR1: a new ultrasonographic contrast agent based on sulfur hexafluoride-filled microbubbles. Investigative radiology, 30(8), 451-457.

[212] Schneider, M., Brochot, J., Puginier, J., & Yan, F. (1997). U.S. Patent No. 5,686,060. Washington, DC: U.S. Patent and Trademark Office.

[213] Searles, J. A., Carpenter, J. F., & Randolph, T. W. (2001). Annealing to optimize the primary drying rate, reduce freezing-induced drying rate heterogeneity, and determine T'g in pharmaceutical lyophilization. Journal of pharmaceutical sciences, 90(7), 872-887.

[214] Segers, T., De Rond, L., De Jong, N., Borden, M., & Versluis, M. (2016). Stability of monodisperse phospholipid-coated microbubbles formed by flow-focusing at high production rates. Langmuir, 32(16), 3937-3944.

[215] Segers, T., Gaud, E., Versluis, M., & Frinking, P. (2018). High-precision acoustic measurements of the nonlinear dilatational elasticity of phospholipid coated monodisperse microbubbles. Soft matter, 14(47), 9550-9561.

[216] Segers, T., Kruizinga, P., Kok, M. P., Lajoinie, G., De Jong, N., & Versluis, M. (2018). Monodisperse versus polydisperse ultrasound contrast

agents: Non-linear response, sensitivity, and deep tissue imaging potential. Ultrasound in medicine & biology, 44(7), 1482-1492.

[217] Segers, T., Lohse, D., Versluis, M., & Frinking, P. (2017). Universal equations for the coalescence probability and long-term size stability of phospholipid-coated monodisperse microbubbles formed by flow focusing. Langmuir, 33(39), 10329-10339.

[218] Shi, W., Forsberg, F., Raichlen, J., Needleman, L., & Goldberg, B. (1999). Pressure dependence of subharmonic signals from contrast microbubbles. Ultrasound in medicine & biology, 25(2), 275-283.

[219] Shih, R., Bardin, D., Martz, T. D., Sheeran, P. S., Dayton, P. A., & Lee, A. P. (2013). Flow-focusing regimes for accelerated production of monodisperse drug-loadable microbubbles toward clinical-scale applications. Lab on a Chip, 13(24), 4816-4826.

[220] Shinnar, R., & Church, J. M. (1960). Statistical theories of turbulence in predicting particle size in agitated dispersions. Industrial & Engineering Chemistry, 52(3), 253-256.

[221] Shung, K. K., & Thieme, G. A. (1992). Ultrasonic scattering in biological tissues. CRC press.

[222] Shutliov, V. A., Alferieff, M. E., & Beyer, R. T. (1990). Fundamental physics of Ultrasound.

[223] Sigelmann, R. A., & Reid, J. M. (1973). Analysis and measurement of ultrasound backscattering from an ensemble of scatterers excited by sine-wave bursts. The Journal of the Acoustical Society of America, 53(5), 1351-1355.

[224] Simon, M. (2004). Koaleszenz von Tropfen und Tropfenschwärmen. Technische Universität Kaiserslautern, Chair of Separation Science and Technology.

[225] Simpson, D. H., Chin, C. T., & Burns, P. N. (1999). Pulse inversion Doppler: a new method for detecting nonlinear echoes from microbubble contrast agents. IEEE transactions on ultrasonics, ferroelectrics, and frequency control, 46(2), 372-382.

[226] Sirsi, S., Feshitan, J., Kwan, J., Homma, S., & Borden, M. (2010). Effect of microbubble size on fundamental mode high frequency ultrasound imaging in mice. Ultrasound in medicine & biology, 36(6), 935-948.

[227] Soetanto, K. S. K., Chan, M. C. M., & Okujima, M. O. M. (1997). Change in size and number of sodium laurate microbubbles with time in

saline at different air concentrations. Japanese journal of applied physics, 36(5S), 3238.

[228] Solis, C., Forsberg, F., & Wheatley, M. A. (2010). Preserving enhancement in freeze-dried contrast agent ST68: Examination of excipients. International journal of pharmaceutics, 396(1-2), 30-38.

[229] Song, R., Peng, C., Xu, X., Wang, J., Yu, M., Hou, Y., ... & Yao, S. (2018). Controllable formation of monodisperse polymer microbubbles as ultrasound contrast agents. ACS applied materials & interfaces, 10(17), 14312-14320.

[230] Sontum, P. C. (2008). Physicochemical characteristics of Sonazoid™, a new contrast agent for ultrasound imaging. Ultrasound in medicine & biology, 34(5), 824-833.

[231] Squires, T. M., & Quake, S. R. (2005). Microfluidics: Fluid physics at the nanoliter scale. Reviews of modern physics, 77(3), 977.

[232] Sridhar, S., Patel, A., & Dalvi, S. V. (2016). Estimation of storage stability of aqueous microbubble suspensions. Colloids and Surfaces A: Physicochemical and Engineering Aspects, 489, 182-190.

[233] Streeter, J. E., Gessner, R., Miles, I., & Dayton, P. A. (2010). Improving sensitivity in ultrasound molecular imaging by tailoring contrast agent size distribution: in vivo studies. Molecular imaging, 9(2), 7290-2010.

[234] Stride, E. (2009). Physical principles of microbubbles for ultrasound imaging and therapy. Cerebrovascular Diseases, 27(Suppl. 2), 1-13.

[235] Stride, E., & Edirisinghe, M. (2008). Novel microbubble preparation technologies. Soft matter, 4(12), 2350-2359.

[236] Stride, E., Segers, T., Lajoinie, G., Cherkaoui, S., Bettinger, T., Versluis, M., & Borden, M. (2020). Microbubble agents: New directions. Ultrasound in medicine & biology, 46(6), 1326-1343.

[237] Sukhorukov, G. B., Fery, A., Brumen, M., & Möhwald, H. (2004). Physical chemistry of encapsulation and release. Physical Chemistry Chemical Physics, 6(16), 4078-4089.

[238] Sutton, J. T., Raymond, J. L., Verleye, M. C., Pyne-Geithman, G. J., & Holland, C. K. (2014). Pulsed ultrasound enhances the delivery of nitric oxide from bubble liposomes to ex vivo porcine carotid tissue. International journal of nanomedicine, 9, 4671.

[239] Tabeling, P. (2005). Introduction to microfluidics. Oxford University Press on Demand.

[240] Tabeling, P. (2009). A brief introduction to slippage, droplets and mixing in microfluidic systems. Lab on a Chip, 9(17), 2428-2436.

[241] Talu, E., Hettiarachchi, K., Powell, R. L., Lee, A. P., Dayton, P. A., & Longo, M. L. (2008). Maintaining monodispersity in a microbubble population formed by flow-focusing. Langmuir, 24(5), 1745-1749.

[242] Talu, E., Hettiarachchi, K., Zhao, S., Powell, R. L., Lee, A. P., Longo, M. L., & Dayton, P. A. (2007). Tailoring the size distribution of ultrasound contrast agents: possible method for improving sensitivity in molecular imaging. Molecular imaging, 6(6), 7290-2007.

[243] TESE

[244] Tourin, A., Derode, A., Roux, P., Van Tiggelen, B. A., & Fink, M. (1997). Time-dependent coherent backscattering of acoustic waves. Physical review letters, 79(19), 3637.

[245] Tourin, A., Fink, M., & Derode, A. (2000). Multiple scattering of sound. Waves in random media, 10(4), R31.

[246] Tremblay-Darveau, C., Williams, R., & Burns, P. N. (2014). Measuring absolute blood pressure using microbubbles. Ultrasound in medicine & biology, 40(4), 775-787.

[247] Tu, L., Liao, Z., Luo, Z., Wu, Y. L., Herrmann, A., & Huo, S. (2021, December). Ultrasound-controlled drug release and drug activation for cancer therapy. In Exploration (Vol. 1, No. 3, p. 20210023).

[248] Twersky, V. (1964). Acoustic bulk parameters of random volume distributions of small scatterers. The Journal of the Acoustical Society of America, 36(7), 1314-1329.

[249] Tzvetkov, G., Graf, B., Fernandes, P., Fery, A., Cavalieri, F., Paradossi, G., & Fink, R. H. (2008). In situ characterization of gas-filled microballoons using soft X-ray microspectroscopy. Soft Matter, 4(3), 510-514.

[250] Unger, E. C., Hersh, E., Vannan, M., Matsunaga, T. O., & McCreery, T. (2001). Local drug and gene delivery through microbubbles. Progress in cardiovascular diseases, 44(1), 45-54.

[251] Upadhyay, A., & Dalvi, S. V. (2019). Microbubble formulations: synthesis, stability, modeling and biomedical applications. Ultrasound in medicine & biology, 45(2), 301-343.

[252] Upadhyay, A., Yagnik, B., Desai, P., & Dalvi, S. V. (2018). Microbubble-mediated enhanced delivery of curcumin to cervical cancer cells. ACS omega, 3(10), 12824-12831.

[253] Van Albada, M. P., & Lagendijk, A. (1985). Observation of weak localization of light in a random medium. Physical review letters, 55(24), 2692.

[254] van Albada, M. P., van Tiggelen, B. A., Lagendijk, A., & Tip, A. (1991). Speed of propagation of classical waves in strongly scattering media. Physical review letters, 66(24), 3132.

[255] Van Elburg, B., Collado-Lara, G., Bruggert, G. W., Segers, T., Versluis, M., & Lajoinie, G. (2021). Feedback-controlled microbubble generator producing one million monodisperse bubbles per second. Review of scientific instruments, 92(3), 035110.

[256] Van Liew, H. D., & Burkard, M. E. (1995). Behavior of bubbles of slowly permeating gas used for ultrasonic imaging contrast. Investigative radiology, 30(5), 315-321.

[257] Van Liew, H. D., & Burkard, M. E. (1995). Bubbles in circulating blood: stabilization and simulations of cyclic changes of size and content. Journal of Applied Physiology, 79(4), 1379-1385.

[258] Van Neer, P. L., Matte, G., Danilouchkine, M. G., Prins, C., Van Den Adel, F., & De Jong, N. (2010). Super-harmonic imaging: development of an interleaved phased-array transducer. IEEE transactions on ultrasonics, ferroelectrics, and frequency control, 57(2), 455-468.

[259] van Winden, E. C. (2003). Freeze-drying of liposomes: theory and practice. Methods in enzymology, 367, 99-110.

[260] van Winden, E. C., & Crommelin, D. J. (1999). Short term stability of freeze-dried, lyoprotected liposomes. Journal of controlled release, 58(1), 69-86.

[261] van Winden, E. C., Zhang, W., & Crommelin, D. J. (1997). Effect of freezing rate on the stability of liposomes during freeze-drying and rehydration. Pharmaceutical research, 14(9), 1151-1160.

[262] Vokurka, K. (1986). Comparison of Rayleigh's, Herring's, and Gilmore's models of gas bubbles. Acta Acustica united with Acustica, 59(3), 214-219.

[263] Vrij, A. (1966). Possible mechanism for the spontaneous rupture of thin, free liquid films. Discussions of the Faraday Society, 42, 23-33.

[264] Weaire, D. L., & Hutzler, S. (2001). The physics of foams. Oxford University Press.

[265] Wear, K. A., Milunski, M. R., Wickline, S. A., Perez, J. E., Sobel, B. E., & Miller, J. G. (1989). Differentiation between acutely ischemic

myocardium and zones of completed infarction in dogs on the basis of frequency-dependent backscatter. The Journal of the Acoustical Society of America, 85(6), 2634-2641.

[266] Wei, P., Cornel, E. J., & Du, J. (2021). Ultrasound-responsive polymer-based drug delivery systems. Drug Delivery and Translational Research, 11(4), 1323-1339.

[267] Weller, G. E., Lu, E., Csikari, M. M., Klibanov, A. L., Fischer, D., Wagner, W. R., & Villanueva, F. S. (2003). Ultrasound imaging of acute cardiac transplant rejection with microbubbles targeted to intercellular adhesion molecule-1. Circulation, 108(2), 218-224.

[268] Whitesides, G. M. (2006). The origins and the future of microfluidics. nature, 442(7101), 368-373.

[269] Xu, D. (2017). Physics of ultrasound. In Hadzic's Textbook of Regional Anesthesia and Acute Pain Management (pp. 503-524). McGraw-Hill, USA.

[270] Xu, S., Nie, Z., Seo, M., Lewis, P., Kumacheva, E., Stone, H. A., ... & Whitesides, G. M. (2005). Generation of monodisperse particles by using microfluidics: control over size, shape, and composition. Angewandte Chemie, 117(5), 734-738.

[271] Yang, Y., Biviano, M. D., Guo, J., Berry, J. D., & Dagastine, R. R. (2020). Mass transfer between microbubbles. Journal of colloid and interface science, 571, 253-259.

[272] Yan-Jun, G., Dong, Z., Xiu-Fen, G., & Kai-Bin, T. (2006). The viscoelasticity of lipid shell and the hysteresis of subharmonic in liquid containing microbubbles. Chinese Physics, 15(7), 1526.

[273] Yeh, C. K., Su, S. Y., Shen, C. C., & Li, M. L. (2008). Dual high-frequency difference excitation for contrast detection. IEEE transactions on ultrasonics, ferroelectrics, and frequency control, 55(10), 2164-2176.

[274] Zhang, D., Gong, Y., Gong, X., Liu, Z., Tan, K., & Zheng, H. (2007). Enhancement of subharmonic emission from encapsulated microbubbles by using a chirp excitation technique. Physics in Medicine & Biology, 52(18), 5531.

[275] Zhang, H., Zhu, Y., & Shen, Y. (2018). Microfluidics for cancer nanomedicine: from fabrication to evaluation. Small, 14(28), 1800360.

[276] Zúñiga, R. N., & Aguilera, J. M. (2009). Structure–fracture relationships in gas-filled gelatin gels. Food Hydrocolloids, 23(5), 1351-1357

RÉSUMÉ

Les avantages de l'utilisation d'agents de contraste ultrasonores (ACU) à distribution de taille monodisperse ont été mis en évidence. Caractérisées par un coefficient de variation (CV) de leur diamètre inférieur à 5%, les microbulles monodisperses (MBM) ont le potentiel d'améliorer la qualité des images ultrasonores (amélioration du rapport signal/bruit et réduction des effets d'ombre). Elles facilitent également le contrôle de la fréquence de résonance fondamentale (FRF) des microbulles, ouvrant des possibilités dans les domaines de l'imagerie moléculaire et des mesures de pression non invasives. En outre, les MBM peuvent optimiser l'administration de médicaments, et de gènes

Cependant, contrairement aux bulles polydisperses (MBP), la lyophilisation de MBM fraîches, sans détérioration de leur monodispersité, reste un défi. Ainsi, les MBM ne peuvent être ni stockées ni transportées. Cela représente un goulot d'étranglement pour leur utilisation dans des applications cliniques. Les tentatives faites pour résoudre ce problème ont utilisé des solvants toxiques, ce qui soulève des problèmes de réglementation.

L'objectif était de développer une nouvelle technique de lyophilisation des MBM qui ne dégrade pas leur distribution de taille, ni leurs propriétés acoustiques, et ce sans utiliser de solvants toxiques. La première étape a consisté à fabriquer des dispositifs microfluidiques de focalisation du flux pour produire des microbulles avec une distribution de taille monodisperse (CV<5%). L'optimisation de la formulation des microbulles et des matériaux cryoprotecteurs a été réalisée. La caractérisation géométrique de deux microbulles avec des diamètres moyens de 40µm et 5µm a été menée. Des images de toutes les étapes du processus de lyophilisation des microbulles ont été capturées et analysées, pour contrôler la distribution de taille et le taux de production. Le développement d'une nouvelle technique de récupération a permis de réduire considérablement l'interaction entre les bulles pendant la lyophilisation. De cette manière, il a été possible de préserver la monodispersité pendant le processus de lyophilisation (CV <6%).

Une caractérisation de la réponse acoustique des MBM lyophilisées et enveloppées de PVA a été réalisée et comparée avec celles de microbulle fraîchement produites et de MBP disponibles dans le commerce (SonovueTM). La réponse acoustique en rétrodiffusion a été évaluée dans deux configurations différentes : la cellule centimétrique (grand récipient), et le "milli-channel" (système confiné). En utilisant un transducteur acoustique focalisé avec une fréquence de 2.25MHz, les FRF et amplitudes, avant et après le processus de lyophilisation, ont été comparées pour des bulles de 5µm de diamètre. Il a été constaté que la variation de l'amplitude et de la FRF des bulles se situait dans la plage d'incertitude expérimentale, ce qui suggère que leurs propriétés acoustiques ont été préservées. Nous avons observé qu'il existe une dépendance linéaire entre la concentration de la population de microbulles et l'amplitude du coefficient de rétrodiffusion. Une comparaison de la réponse acoustique a été effectuée pour des MBM et MBP. Nous avons observé une amplitude du signal de réponse des MBM de 8 à 10 fois supérieure à celle des MBP. Il a été possible d'observer une plus faible incertitude dans le suivi du pic de résonance des bulles et une plus petite largeur de bande pour les MBM. Enfin, en utilisant une approche « d'imagerie matricielle par ultrasons », la réponse acoustique de la MBP et MBM a été évaluée dans un fantôme simulant les tissus. Les résultats préliminaires renforcent les conclusions des mesures acoustiques menées dans la cellule centimétrique et le canal millimétrique.

Nous avons proposé une nouvelle génération d'ACU se présentant sous la forme d'une poudre lyophilisée stable qui peut être transportée et stockée pendant des mois et remise en suspension monodisperse pour être utilisée dans des cliniques.

MOTS CLÉS

Microbulles; microfluidique; lyophilisees; monodisperse; ultrason; alcool polyvinylique

ABSTRACT

The advantages of using ultrasound contrast agents (UCA) with monodisperse size distribution have been highlighted. Characterized by a coefficient of variation (CV) lower than 5%, monodisperse microbubbles (MMB) have the potential to improve the quality of ultrasound images. It also facilitates microbubble resonance frequency monitoring, opening possibilities in the areas of molecular imaging, non-invasive pressure measurements, and drug and gene delivery.

But, contrarily to polydisperse microbubbles bubbles (PMB), freeze-drying monodisperse populations of fresh microbubbles, without deteriorating their monodispersity, remains a challenge. Thus, MMB can neither be stored nor transported. This represents a bottleneck for their use in clinical applications. Attempts made to solve the problem have used toxic solvents, raising regulatory issues

The present work presents a new freeze-drying technique for MMB that did not degrade their size distribution, or their acoustic properties, without the use of toxic solvents. As the first step of the project, flow-focusing microfluidic devices were fabricated to produce microbubbles with highly monodisperse size distribution (CV<5%). During this step, the optimization of the microbubble formulation and cryoprotectant materials was performed. Geometric characterization of two microbubbles population with mean diameters of 40µm and 5µm was performed. Images of all stages of the freeze-drying process of the microbubbles were captured and analyzed, aiming the control of the size distribution and production rate. The steps of the freeze-drying process consisted of production, collection, freezing, lyophilization, and resuspension. The development of a new retrieval technique, where the microbubbles were stored in monolayers, resulted in a drastic reduction of the interaction between the bubbles during lyophilization. In this way, it was possible to preserve the monodispersity, resulting in a CV <6% for the resuspended microbubbles.

In the second stage of the project, a characterization of the backscatter acoustic response (BSAR) of the freeze-dried monodisperse PVA-shelled microbubbles (FDMD), in comparison with fresh MMB, and PMB was conducted. Firstly, the BSAR of the microbubbles was evaluated in two different setups: the centimetric cell (large container), and the ‘milli-channel’ (confined system in which the liquid is at rest). Using a focused acoustic transducer with a frequency of 2.25MHz, the backscattering acoustic responses of the microbubbles, before and after the freeze-drying process was compared for the bubble population of 5μm diameter. The variation of amplitude and fundamental resonance frequency of the bubbles were within the experimental uncertainty range, suggesting that their acoustic properties were preserved. We also observed, in agreement with the literature, that there is a linear dependence between the concentration of the microbubble population and the amplitude of the backscatter coefficient. Also, in agreement with the literature, we observed an amplitude in the response signal of the monodispersed bubbles of 8 to 10 times higher than that for the polydispersed ones, for the same in vitro concentration. It was observed a lower uncertainty in monitoring the fundamental resonance peak of the bubbles and a smaller bandwidth for the FDMD. Finally, using the ultrasound matrix imaging approach, developed at Institut Langevin, the BSAR of the FDMD and PMB was evaluated in a phantom mimicking tissue. The results reinforced the findings obtained the centimetric cell and the milli-channel.

We successfully presented a new technique developed to freeze-dry monodisperse microbubbles without degrading their geometrical and acoustic properties. Thus, we proposed a new generation of ultrasound contrast agents in the form of a stable freeze-dried powder that can be transported and stored for months and resuspended for use in clinical applications.

KEYWORDS

Microbubbles; microfluidic; lyophilized; monodisperse; ultrasound; polyvinyl alcohol